# Investigation of pulse duration reduction and intensity increase of Petawatt-class laser systems

Petrisor Gabriel Bleotu

INSTITUT POLYTECHNIQUE DE PARIS

UNIVERSITATEA DIN BUCUREȘTI
VIRTUTE ET SAPIENTIA

INSTITUT POLYTECHNIQUE DE PARIS

NNT : 2023IPPAX108

Thèse de doctorat

# Investigation of pulse duration reduction and intensity increase of Petawatt-class laser systems

Thèse de doctorat de l'Institut Polytechnique de Paris et l'Université de Bucarest
préparée à Extreme Light Infrastructure-Nuclear Physics

École doctorale n°626 Ecole doctorale de l'Institut Polytechnique de Paris (EDIPP)
Spécialité de doctorat : Physique

Thèse présentée et soutenue à Bucharest, le 29.11.2023, par

**PETRIȘOR GABRIEL BLEOTU**

Composition du Jury :

| | |
|---|---|
| Emmanuele d'Humières<br>Professeur, CELIA - Université Bordeaux | Président |
| Emmanuele d'Humières<br>Professeur, CELIA - Université Bordeaux | Rapporteur |
| Niculae Puscas<br>Professeur, Politehnica University of Bucharest | Rapporteur |
| Mihai Stafe<br>Professor, Politehnica University of Bucharest | Examinateur |
| Adrian Petris<br>Directeur du recherche, National Institute for Laser, Plasma and Radiation Physics | Examinateur |
| Gérard Mourou<br>Professeur émérite, École Polytechnique | Examinateur |
| Julien Fuchs<br>Directeur du recherche, École Polytechnique | Directeur de thèse |
| Daniel Ursescu<br>Directeur du recherche, Horia Hulubei National Institute for R&D in Physics and Nuclear Engineering | Co-directeur de thèse |

*Dedication,*

*I dedicate this thesis to Nobel Laureate, Professor Gérard Mourou, the person who paved my road in the field of high-power lasers and to my family Robert, Constantin and Elena Bleotu who unconditionally support me to achieve my dreams.*

*Dedic această teză laureatului Nobel, Profesorului Gérard Mourou, persoana care mi-a deschis drumul în domeniul laserelor de mare putere, și familiei mele, Robert, Constantin și Elena Bleotu, care m-au susținut necondiționat în realizarea viselor mele.*

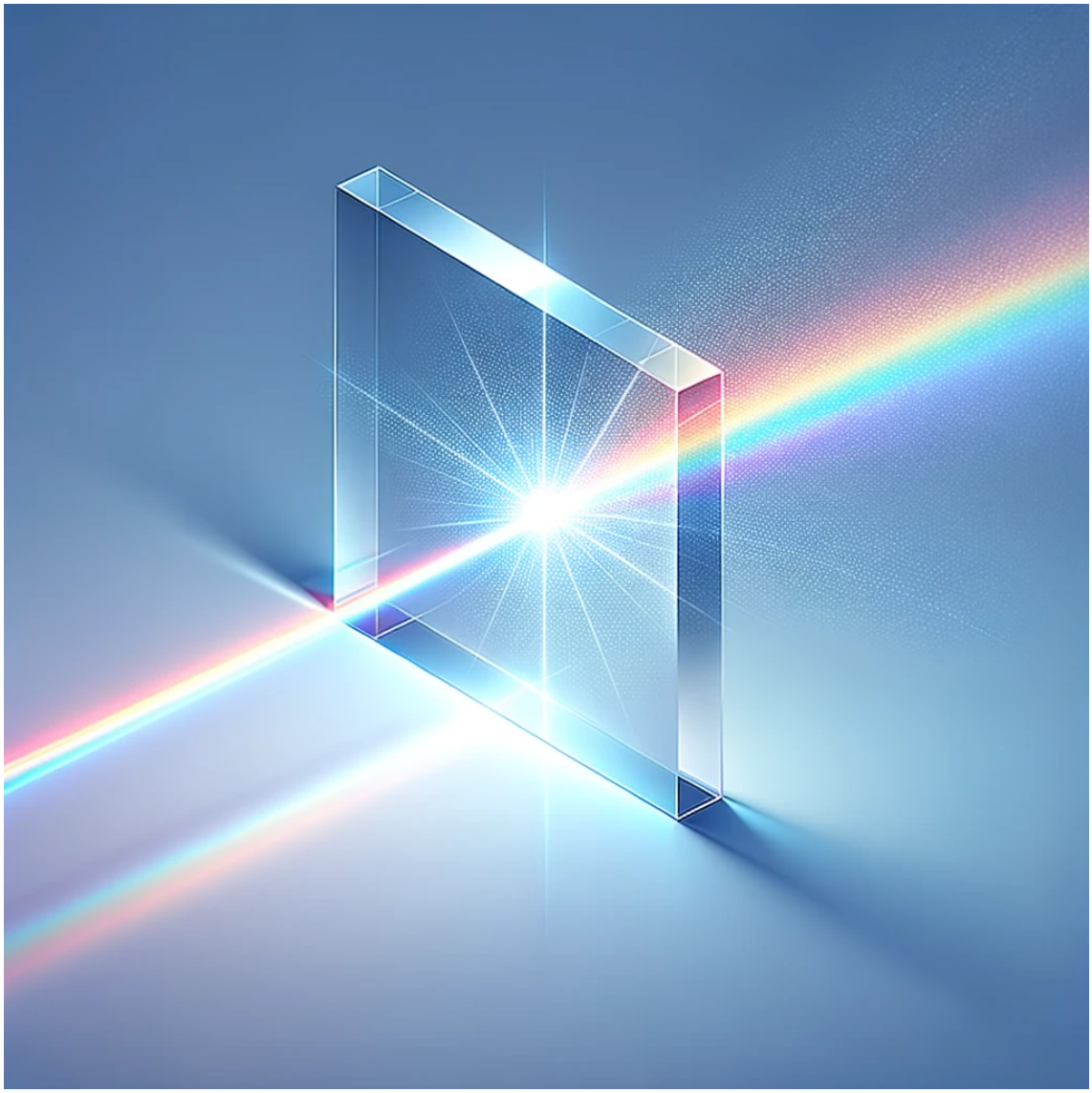

# Contents

CHAPTER 1

# Chapter 1 Introduction

The motivation for this thesis arises from the need to advance future development of peak power energy laser systems to pave the road for a better understanding of fundamental physics, Universe genesis, quantum vacuum properties, materials science etc.. In pursuing these multifaceted applications, a major goal is the increase of the maximum attainable peak power achievable by laser systems developed around the world in the last decades (e.g. ELI, Apollon, SULF, XCELS...). The post-compression of existing femtosecond (fs) pulses toward the fundamental limit of a single-cycle of their carrier wavelength has been proposed as a shortcut to the morphing of TW into PW-class laser systems [1].
The post-compression comes as an unexpensive and efficient method to increase the pulse peak power instead of using further amplification stages. To reach the shortest pulse durations requires going to shorter UV and X-ray wavelengths, but the actual challenge is to drive these pulses using modern day laser facilities [2]. Meeting this challenge will open up an entirely new realm of fundamental and applied physics both directly and by driving Exawatt, X-ray pulses with extremely short, sub-attosecond timescales, which are far from traditional laser regimes. Despite the fact that multiple solutions for peak power enhancement such as coherent combination [3], plasma amplification [4, 5], post compression or post compression combined with nonlinear amplification have been proposed by numerous research groups [6, 7, 8, 9], the problem of generating few-cycle laser radiation of a petawatt (PW) peak power level has not been solved to this day.
This thesis investigates a method of post-compression that relies on the careful control of the self-phase modulation used here to increase the laser pulse bandwidth, as well as the control of the needed group delay dispersion compensation of the broadband pulses. The proposed method (Thin Film Compression [1]) emerges as the most reliable way to reach sub 10 fs pulse duration for high power laser systems, for the existing PW and 10 PW laser systems [10, 11].
The emphasis of our investigation will reside in a comprehensive exploration of the interaction between high intensity laser pulses with thin transparent media in order to generate ultra-short pulses, close to single cycle. A complete characterization of these materials is necessary in order to choose the right optical materials that satisfy the high intensity pulses problems. In this thesis, I will present the results obtained using the post-compression technique applied at four different high-power laser facilities.

## Context

## Summary

The motivation for this thesis arises from the need to advance the development of peak power energy laser systems. The post-compression of existing femtosecond (fs) pulses toward the fundamental limit of a single-cycle of their carrier wavelength has been proposed as a shortcut to the morphing of TW into PW-class laser systems.

**Chapter I** summarises the need for ultra-short and ultra-intense laser pulses while putting the accent on the actual status of high-power laser systems. This chapter includes a review of the post-compression methods that might lead to a realistic Exawatt class laser implementation.

**Chapter II** is dedicated to the theoretical aspects of this thesis. The first part focuses on nonlinear effects, particularly nonlinear refractive index (NRI) and Self-Phase Modulation (SPM) leading to spectral broadening of ultrashort pulses. The latter part of this chapter discusses dispersion phenomena, different orders of dispersion, relevant dispersive materials commonly used in high-power laser systems (HPLS), and methods to compensate for dispersion. These concepts form the foundation of the thesis. To bring these theoretical concepts to experiments, simulations were developed using the PyNLO library within a Python environment. These simulations are designed to replicate the generation of ultra-short laser pulses and their subsequent propagation through nonlinear media.

**Chapter III** outlines the comprehensive characterization of optical materials, covering dispersion, transmission, roughness, vacuum compatibility, and providing a detailed analysis of the nonlinear refractive index and laser-induced damage threshold. Additionally, a dispersion management system (DMS) is designed to compress the newly simulated spectrally broadened pulses. The results were summarized in a table that covers the properties of 10 different glasses and plastic optical materials.

**Chapter IV** presents a detailed description of the experimental results obtained from four experimental campaigns dedicated to post-compression of ultrashort pulses. It showcases the utilization of plastics and glasses in post-compression experiments involving high-energy laser pulses, successfully achieving compression levels ranging from terawatt (TW) to petawatt (PW) peak power. The chapter also addresses new challenges pertaining to the metrology of post-compressed laser pulses, such as spatio-temporal couplings, encircled energy, nonlinear absorption in chirped mirrors (CM), and wavefront correction, providing detailed insight into these aspects.

Using the key parameters such as dispersion, nonlinear refractive index, and damage threshold, it is shown also that the propagation of ultra-short laser pulses through optical materials can provide sub 6 fs laser pulses.

**Chapter V** wraps up the thesis by presenting the main conclusions drawn from the research. It includes various summary tables, two novel methods to estimate the NRI, 3 complementary methods to perform LIDT measurements, and the prediction of reaching sub 6 fs at Joule-level energy. I showed for the first time experimental results for the stability of such post-compressed laser pulses while higher orders of dispersion are compensated, therefore demonstrating the potential to generate a 5-fold compression factor when 2 J and 2 mm BK7 are used.

This chapter also discusses future perspectives, including the potential implementation of the results of the work for electron acceleration, as well as simulations involving secondary sources of radiation.

## Résumé

L'intérêt de cette thèse découle de la nécessité de faire progresser le développement des systèmes laser à énergie de pointe. La post-compression des impulsions femtosecondes (fs) existantes vers la limite fondamentale d'un cycle unique de leur longueur d'onde porteuse est la méthode qui a été proposée comme raccourci pour la transformation de systèmes laser de classe TW en PW.

**Le chapitre I** explique brièvement l'importance des impulsions laser ultra-courtes et ultra-intenses tout en mettant l'accent sur l'état actuel des systèmes laser de haute puissance. Ce chapitre comprend une revue des méthodes de post-compression qui pourraient conduire à une mise en fonctionnement réaliste d'un laser de classe Exawatt.

**Le chapitre II** est consacré aux aspects théoriques de cette thèse. La première partie se concentre sur les effets non linéaires, en particulier l'indice de réfraction non linéaire (NRI) et l'auto-modulation de phase (SPM) conduisant à un élargissement spectral des impulsions ultracourtes. La dernière partie de ce chapitre traite des phénomènes de dispersion, des différents ordres de dispersion, des matériaux dispersifs pertinents couramment utilisés dans les systèmes laser haute puissance (HPLS) et des méthodes de compensation de la dispersion. Ces concepts constituent le fondement de la thèse.

Pour appliquer ces concepts théoriques aux expériences, des simulations ont été développées à l'aide de la bibliothèque PyNLO dans un environnement Python. Ces simulations sont conçues pour reproduire la génération d'impulsions laser ultra-courtes puis leur propagation dans des milieux non linéaires.

**Le chapitre III** donne la caractérisation complète des matériaux optiques, couvrant la dispersion, la transmission, la rugosité, la compatibilité sous vide et fournissant une analyse détaillée de l'indice de réfraction non linéaire et du seuil de dommages induits par le laser. De plus, un système de gestion de la dispersion (DMS) est conçu pour compresser les impulsions spectralement élargies nouvellement simulées. Les résultats ont été résumés dans un tableau qui couvre les propriétés de 10 verres et matériaux optiques plastiques différents.

**Le chapitre IV** propose une description détaillée des résultats expérimentaux obtenus à partir de quatre campagnes expérimentales dédiées à la post-compression d'impulsions ultracourtes. Il présente l'utilisation de plastiques et de verres dans des expériences de post-compression impliquant des impulsions laser à haute énergie, atteignant avec succès des niveaux de compression allant de la puissance maximale du térawatt (TW) au pétawatt (PW). Le chapitre aborde également les nouveaux défis liés à la métrologie des impulsions laser post-comprimées, tels que les couplages spatio-temporels, l'énergie encerclée, l'absorption non linéaire dans les miroirs chirpés (CM) et la correction du front d'onde, fournissant un aperçu détaillé de ces aspects.

En utilisant des paramètres clés tels que la dispersion, l'indice de réfraction non linéaire et le seuil de dommage, il est également démontré que la propagation d'impulsions laser ultra-courtes à travers des matériaux optiques peut fournir des impulsions laser inférieures à 6 fs.

**Le chapitre V** achève la thèse en présentant les principales conclusions tirées des recherches menées. Il comprend divers tableaux récapitulatifs, deux nouvelles méthodes pour estimer le NRI, 3 méthodes complémentaires pour effectuer des mesures LIDT et la prédiction de l'atteinte de moins de 6 fs à une énergie de niveau Joule. J'ai obtenu, ce qui constitue une première, des résultats expérimentaux sur la stabilité de telles impulsions laser post-comprimées pendant que des ordres de dispersion plus élevés sont compensés, démontrant ainsi le potentiel de générer un facteur de compression par 5 lorsque 2 J et 2 mm BK7 sont utilisés.

Ce chapitre aborde également les perspectives futures, notamment la possible mise en œuvre des résultats des travaux sur l'accélération des électrons, ainsi que les simulations impliquant des sources secondaires de rayonnement.

## Rezumat

Motivația cercetarilor prezentate in această teză reiese din necesitatea de a avansa în dezvoltarea sistemelor laser cu pulsuri ultra-intense. Post-compresia pulsurilor cu durata de ordinul femtosecundelor (fs) existente a fost propusă ca un mod de a transforma sisteme laser de clasa TW în sisteme laser de clasă PW.

**Capitolul I** explică nevoia de pulsuri laser ultra-scurte și ultra-intense, pornind de la starea actuală a sistemelor laser de mare putere. Acest capitol include o trecere în revistă a metodelor de post-compresie care ar putea duce la o implementare realistă a unui sistem laser de clasa Exawatt.

**Capitolul II** este dedicat aspectelor teoretice ale acestei teze. Prima parte se concentrează pe efectele neliniare, în special pe indicele de refracție neliniar (NRI) și automodularea de fază (SPM) care conduc la lărgirea spectrală a pulsurilor ultra-scurte. Ultima parte a acestui capitol discută fenomenele de dispersie, diferitele ordine de dispersie, materialele dispersive și metodele de compensare a dispersiei. Aceste concepte teoretice stau la baza acestei teze de doctorat. Pentru a aduce aceste concepte teoretice în experimente, au fost dezvoltate simulări folosind biblioteca PyNLO într-un mediu de programare ce utilizeaza limbajul Python. Aceste simulări sunt concepute pentru a descrie generarea de pulsuri laser ultra-scurte și propagarea lor ulterioară prin medii neliniare.

**Capitolul III** descrie caracterizarea proprietăților materialelor optice: dispersia, transmisia, rugozitatea, compatibilitatea cu vidul, și oferă o analiză detaliată a indicelui de refracție neliniar și a pragului de distrugere indus de laser. În plus, un sistem de management al dispersiei (DMS) este proiectat pentru a comprima pulsurile lărgite spectral, nou simulate. Rezultatele au fost rezumate într-un tabel care acoperă proprietățile a 10 materiale optice de tip sticlă sau plastic.

**Capitolul IV** prezintă o descriere detaliată a rezultatelor experimentale obținute în urma a patru campanii experimentale dedicate post-compresiei pulsurilor ultra-scurte. Prezintă utilizarea materialelor plastice și a sticlelor în experimente de post-compresie care implică pulsuri laser de înaltă energie, atingând cu succes niveluri de compresie variind de la putere de vârf de terawatt (TW) la petawatt (PW). Capitolul abordează, de asemenea, noile provocări legate de metrologia pulsurilor laser post-comprimate, cum ar fi cuplajele spațio-temporale, energia în focus, absorbția neliniară în oglinzi cu derivă de frecventa (CM) și corecția frontului de undă, oferind o perspectivă detaliată asupra acestor aspecte.

Folosind parametrii cheie precum dispersia, indicele de refracție neliniar și pragul de distrugere, se arată, de asemenea, că propagarea pulsurilor laser ultra-scurte prin materiale optice poate furniza pulsuri laser cu durată de sub 6 fs.

**Capitolul V** încheie teza prin prezentarea principalelor rezultate obținute și concluzii ale cercetărilor efectuate. Include diverse tabele cu rezultatele principale, două metode noi pentru a estima NRI, 3 metode complementare pentru a efectua măsurători LIDT și predicția atingerii a sub 6 fs la energie de 2 Joule. Am arătat, pentru prima dată, rezultate experimentale pentru stabilitatea unor astfel de pulsuri laser post-comprimate în timp ce ordinele mai mari de dispersie sunt compensate, demonstrând astfel potențialul de a genera un factor de compresie temporală a pulsurilor de 5 atunci când sunt utilizați 2 J și 2 mm BK7.

Acest capitol discută, de asemenea, perspective de viitor, inclusiv implementarea potențială a rezultatelor lucrării pentru accelerarea electronilor, precum și simulări care implică surse secundare de radiație.

## 1.1 Ultra-short laser pulses

### 1.1.1 The need for ultra-short laser pulses

Ultra-short laser pulses have found applications in various fields of science and technology, including femtochemistry, biology, communications, metrology, attosecond science, and harmonic generation, particularly in situations requiring a few-cycle regime. I will provide a few detailed examples:

The first one is **femtochemistry**, the domain where Ahmed Zewail was awarded the Nobel prize. Femtochemistry investigates the chemical reactions dynamics and ultrafast processes that occur within femtoseconds. It has provided a deeper understanding of the rapid dynamics associated with photo-dissociation reactions, unveiling the intricate mechanisms and timescales associated with bond breaking processes. Femtochemistry based experiments such as Pump-probe and ultrafast spectroscopy, electron diffraction and imaging led to the understanding of dynamics of photo-dissociation, solvation dynamics, ultrafast electron transfer and reaction control [12, 13]. This newfound knowledge holds also significant implications for various fields including atmospheric chemistry, photo-biology, and photo-voltaics.

The advent of **frequency combs**, made possible by the utilization of femtosecond laser pulses, has brought a paradigm shift in various scientific and technological domains. These combs, characterized by their distinct comb-like spectra and precise frequency references, have catalyzed remarkable advancements in precision metrology, spectroscopy, optical communications, astronomy, and quantum information processing.

Ongoing research endeavors in the field of frequency combs are focused on pushing the boundaries of their capabilities. This includes expanding the comb spectrum into the mid-infrared and terahertz regions, enhancing stability and compactness, and exploring novel applications in fields such as biology and materials science [14, 15]. However, several challenges are yet to be addressed, including streamlining the complexity and cost of frequency comb systems, improving power scalability, and mitigating issues related to noise and stabilization. By overcoming these obstacles, the potential for further developments in frequency comb technology holds promising prospects for scientific discoveries and technological innovations in the future.

Non-thermal **materials processing** refers to the utilization of femtosecond laser pulses to achieve precise modifications in materials without causing substantial heat transfer to the surrounding regions. This stands in contrast to traditional laser processing methods that frequently lead to thermal damage. By delivering energy at an ultrafast rate and in a localized manner, femtosecond lasers minimize the accumulation of heat, enabling exceptional control over the outcomes of materials processing.

Surface processing encompasses various techniques such as micromachining, micro- and nanostructuring, and nano-ablation, which focus on modifying the surface of materials. On the other hand, volume processing involves methods like two-photon polymerization and three-dimensional (3D) processing, specifically targeting the modification and fabrication of structures within transparent materials [16, 17].

Ongoing research and development endeavors in non-thermal femtosecond laser processing are dedicated to expanding the capabilities of this technique and tackling current challenges. These efforts encompass the refinement of processing parameters, the enhance-

ment of throughput, the improvement of efficiency, and the development of advanced control techniques. Challenges that need to be overcome include achieving scalability for industrial applications, ensuring cost-effectiveness, and seamlessly integrating femtosecond laser processing into existing manufacturing processes [18].

### 1.1.2 Ultra-short laser pulses generation

A laser pulse is called short ($10^{-12}s$, ps) or ultra-short ($10^{-15}s$) when the duration is close to the duration given by the Fourier limit (i.e. to the duration retrieved from the Fourier transform of the spectrum). The Fourier limit binds the pulse duration and the spectral bandwidth in an inversely proportional relation, as stated in Eq. (1.1) and thus the shortest pulse duration is retrieved for a broadest bandwidth at constant spectral phase.

$$\Delta\tau * \Delta\omega = k \tag{1.1}$$

where $\Delta\tau$ is the pulse duration, $\Delta\omega$ is the spectral bandwidth, and $k$ is a constant (ex. k= 0.441 for a Gaussian shaped pulse).

The limit to pulse duration is imposed by the carrier frequency (i.e. a single cycle pulse at wavelength of 800 nm has a duration around 3 fs and around 325 nm bandwidth). Approaching this spectral bandwidth and properly compressing it, provides the shortcut to the hundreds of PW or to Exawatt regime in the most efficient way.

A visual example of the electric field for a 25 fs and a for 3 fs laser pulse is presented in Figure 1.1.

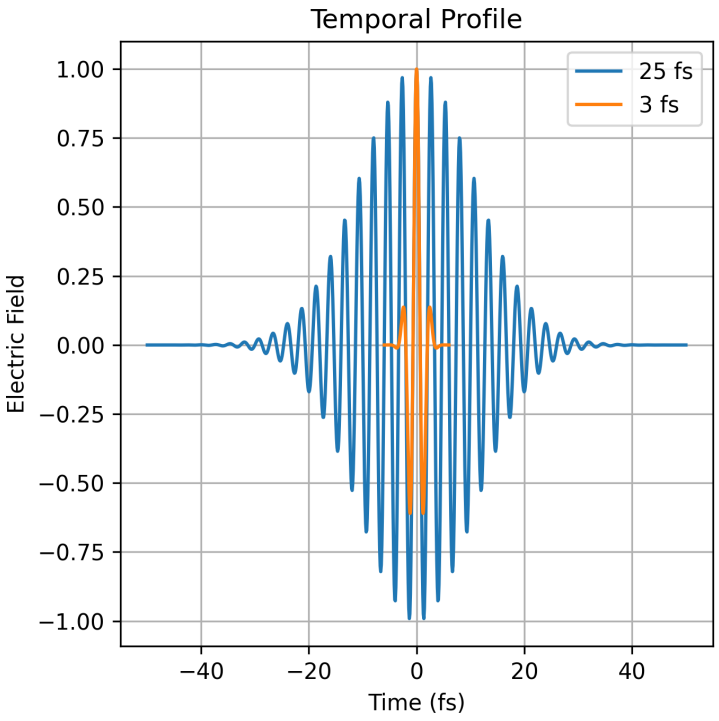


Figure 1.1: Comparison of electric field temporal evolution for a 25 fs and for a 3 fs laser pulse.

The laser pulse duration is also related to the pulse irradiance $I$ ($W/m^2$) or laser pulse intensity given by:

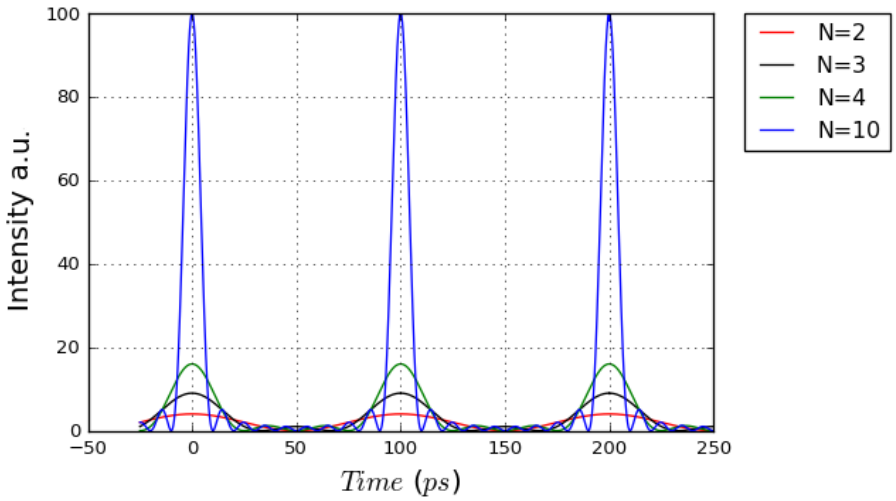


Figure 1.2: Intensity as a function of the number of longitudinal modes, in phase, generated in the resonant cavity of a laser oscillator.

$$I = E/(\tau \cdot S) \tag{1.2}$$

where $\tau$ is the pulse duration at FWHM, $S$ is the spot area measured at $1/e^2$ of the maximum beam intensity and $E$ is the energy of the pulse.

Another way to express the intensity of focused electromagnetic field [7] is:

$$I = \frac{E}{\tau \cdot \lambda^2} \left( \frac{\theta_{pulse}}{\theta_{dif}} \right)^2 \tag{1.3}$$

where $\lambda$ is the wavelength, $\theta_{pulse}$ is the pulse divergence and $\theta_{dif}$ is the diffraction-limited divergence.

At present, ultra-short pulses can be generated in commercial oscillators based on the mode-locking process and a dispersion compensation set-up. An efficient mode-locking consists in a stable resonant cavity, a large bandwidth amplification media and hundreds of thousands (i.e. for Ti:sapphire) phase coupled longitudinal modes (N). The coupling of the longitudinal modes is related to the length of the cavity and bandwidth. The shortest pulse duration is extracted when all the modes are in phase. For the simplicity of the illustration, four examples of ps range laser pulses are shown in Figure 1.2.

Reaching the close-to flat spectral phase condition required dispersion compensation through prisms or using a more controlled way, via chirped mirrors. Nowadays, these lasers are employed as parts of the FRONT-ENDS of the big High Power Lasers Systems (HPLS's).

These small lasers/table-top systems/ oscillators can reach a spectral bandwidth larger than 200 nm and are commercially available. The broad gain bandwidth of Titanium-doped sapphire lasers has been successfully utilized to generate few-cycle pulses at KHz and even MHz repetition rates. As drawbacks, Ti:Sa oscillators have limitations in terms of average output power and pulse energy. They can only be operated at hundreds of Watts average power and sub-$\mu J$ pulse energies. As a result, they are only the first building brick for the advancement of the next generation of femtosecond technology, which aims to scale up both average and peak power levels.

## 1.2 Ultra-intense laser pulses

To obtain ultra-intense laser pulses, 3 main operations are required: the increase of the pulse energy (which requires large size amplification crystals > 20 cm, i.e. at ELI-NP, Apollon, extra pumping lasers, high damage threshold, large size mirrors, extra space for the optics), the shortening of the pulse duration (which requires efficient compression, large size gratings, acousto-optic programmable dispersive filter (Dazzler [19]) and the reduction of laser pulse diameter (which requires high quality focusing optics, good alignment, wavefront sensor and deformable mirror). This thesis aims to advance the pulse duration shortening, as the fastest and cheapest solution to be implemented.

### 1.2.1 The need for ultra-intense laser pulses

With the development of pulsed high-power lasers, using them for applications in areas such as astrophysics, particles physics, relativistic optics, medicine, attophysics, Quantum electrodynamics (QED), etc. can be highlighted [5, 20, 21]. As high-power lasers continue to develop rapidly, it raises the fundamental question of the maximum laser intensity that researchers can achieve ($10^{23} W/cm^2$ -@ Extreme Light Infrastructures (ELI)).

I will describe in short few applications:

In an ideal vacuum condition, **the Schwinger field** represents the upper limit for laser intensity, denoted as $E_s = 2\pi m_e^2 c^3/eh$, which is approximately $1.32 \cdot 10^{18} V/m$ [22]. **QED** is the first and the most precisely tested field theory, at least in the perturbative regime (electron g-2 factor) [23]. It served as a development framework for all other field theories. The importance of QED is tremendous: it predicts the electron (muon) anomalous magnetic moment, Compton & Dellbrück scattering, and generally speaking, it precisely predicts all processes involving electrons and photons up to the energy level where the Weak interactions become significant ($\sim$ 80 GeV).

It is predicted that high intensity laser pulses can generate high field strength through various methods like tight focusing, coherent combining, or other techniques. This enables them to convert a significant number of virtual particle pairs into real particles.

Challenging applications such as **pair production** ($e^- - e^+$) in vacuum or yet untested predictions of QED, such as light-by-light scattering or vacuum birefringence require intensities higher than $10^{26} W/cm^2$ [24, 25, 26, 27].

Nevertheless a number of beyond Standard Model (BSM) theories have been proposed and tested via extreme laser intensities (Dark Matter searches, Axion searches etc.).

Particle accelerators are indispensable tools for pushing the boundaries of scientific research and exploring the fundamental constituents of matter. Traditional accelerators, such as synchrotrons and the linear ones, have been pivotal in generating high-energy particle beams. However, the advent of high-power laser technology has opened a new era for particle acceleration and their applications. Different methods, experimental setups, diagnostics or targets designed have been proposed [28, 29, 30, 31].

The most common techniques related to **particle acceleration using high power lasers** are summarized below and further useful reviews can be found in [32, 33, 34].

- *Plasma Acceleration*: Plasma-based acceleration techniques leverage the unique properties of plasmas to achieve high acceleration gradients. The plasma can support strong electric fields, allowing for efficient particle acceleration. Various plasma-based schemes, such as laser wakefield acceleration, plasma beat-wave acceleration, and plasma bubble acceleration, are being explored for different particle types and energy ranges [31].

- *Laser Wakefield Acceleration* (LWFA): In LWFA, an intense laser pulse propagates through a plasma, creating a wakefield behind it. Electrons injected into this wakefield can gain significant energy by surfing the wake. This technique offers high acceleration gradients and has the potential to produce compact and high-energy particle beams [35].

- *Direct Laser Acceleration* (DLA): DLA involves directly accelerating charged particles using the electric field of the laser pulse. It typically employs ultrafast laser pulses to generate strong electric fields, which propel particles forward. DLA has the advantage of providing high-quality particle beams with low emittance and high control over the acceleration process [36].

- *Plasma Acceleration*: Plasma-based acceleration techniques leverage the unique properties of plasmas to achieve high acceleration gradients. Plasma can support strong electric fields, allowing for efficient particle acceleration. Various plasma-based schemes, such as laser wakefield acceleration, plasma beat-wave acceleration, and plasma bubble acceleration, are being explored for different particle types and energy ranges [31].

- *Laser-Driven Dielectric Accelerators* (LDA): LDA utilizes specially designed dielectric structures that interact with the laser pulse to achieve acceleration. These structures, known as photonic or dielectric waveguides, can generate strong accelerating fields and confine the laser energy, enabling efficient energy transfer to particles. LDA offers potential for miniaturization and integration with other components. Recent studies, beside secondary sources acceleration, show the applicability for radiobiology [37].

- *Laser-Driven Ion Acceleration*: Laser-driven ion acceleration focuses on accelerating ions to high energies using intense laser pulses. Different mechanisms, such as Target Normal Sheath Acceleration (TNSA) [28] and Radiation Pressure Acceleration (RPA) [38], are utilized to achieve ion acceleration. This technique has applications in medical physics, nuclear physics, and ion beam-driven fast ignition for inertial confinement fusion.

Some of the advantages of particles acceleration with high intensity lasers are related to the compactness, cost-effectiveness and high gradient acceleration (shorter distance). On the other side, the energy spread and beam quality, repetition rate (laser systems typically have lower repetition rate compared to classical accelerators) and scalability are still in an optimization process. Scaling laser-driven accelerators (using post-compression) to secondary sources higher energies [39] is an active area of research [21], warranting further development and optimization.

As a promising medical application, in 2014, Vincent Favaudon and his team showed that by using the ultra high dose rate therapy (FLASH-RT) the toxicity at the healthy tissue level is reduced [40]. Albeit, **FLASH irradiation** implies the delivering of an ultra high dose in a very short period of time (i.e. $\geqslant 100$ Gy/s), with specific beam parameters, maintaining the efficiency wanted on the tumor growth, it has the benefit of sparing the healthy tissue as much as possible.

For example, a new platform for ultra-high dose rate radio biological research has been designed using the BELLA PW laser (35 J, 52 $\mu m$, 45 fs, 0.2 Hz, $10^{19} W/cm^2$) proton beamline [41]. It is mentioned that the high mean dose rate should be $>$ 40 Gy/s, with doses belonging to more than 10 Gy and delivering time $<$100 ms. In another experiment the acceleration was performed by focusing the PW arm of Vulcan Laser at an intensity of

order $5{\cdot}10^{20} W/cm^2$ onto a 25 $\mu m$-thick aluminum foil [42, 43]. At the moment both FLASH electrons and protons are under development showing promising results. Implementing post-compression method for the particle acceleration will be an advantage for the future FLASH applications. More details can be found in the review [44].

Although high-intensity lasers are yet to reach the level of maturity and widespread adoption seen in classical accelerators, their unique characteristics and potential applications make them a subject of significant interest for research and exploration. Continued advancements in ultra-short and ultra-intense laser technology will likely unlock further capabilities, expanding their scope of applications and facilitating breakthroughs in radiation sources, imaging techniques, and particle physics research.

### 1.2.2 Laser pulses amplification

#### 1.2.2.1 Chirped pulse amplification (CPA)

A significant advancement took place in 1985 with the introduction of the Chirped Pulse Amplification (CPA) principle, enabling the generation of short and intense laser pulses [45]. For this topic and for its major contribution in science, G. Mourou and D. Strickland received the Nobel prize in 2018. During '80s, a major challenge was the damage threshold of the amplification medium. Intense laser pulses could create filaments and cause optical damage.

The solution came in the form of the CPA method (See Figure 1.3), which efficiently extracts energy from solid-state amplifiers (typically Ti:Sapphire or Nd:Glass). This method involves temporally stretching the pulse from the oscillator by a factor of $10^3 - 10^5$ before amplification to avoid the accumulation of nonlinear effects (i.e. B-integral) and damage. Subsequently, the amplified pulse is compressed back to its original duration.

The main architecture of a CPA-based laser system typically includes a stable oscillator that produces a train of pulses with durations in the tens of femtosecond range, followed by an optical stretcher using gratings or prisms, to increase the pulse duration to the hundreds of picoseconds range through the dispersion process. Amplification is achieved using regenerative amplifiers (RAs) and multiple pass amplifiers (MPAs), providing energies ranging from mJ in RAs up to hundreds of joules in MPAs.

Finally, a compressor, consisting of gratings with an opposite sign of dispersion compared to the stretcher, is employed to compress the pulse to its optimal duration. This compression process takes into consideration the dispersion introduced by the stretcher, amplifiers and all other subsequent materials from Pockel cells, Dazzler etc. This topic will be addressed in detail in Chapter 2.

For high power laser systems (HPLSs), the compression process is one of the weakest points. This aspect will be constantly brought forward in the following sections as a drawback of many HPLs. At the moment, the compression is successfully achieved using gratings, chirped mirrors (CM), prisms or GRISMs [46]. When large beams (>30 cm) are needed, tiled, folded or mosaic shaped gratings can be developed as a solution for compression in HPLSs .

The need for such complex arrangements is due to: (1) the size limit of very large gratings, and (2) the limit imposed by the diffraction grating damage threshold and their diffraction efficiency. For HPLs, the laser induced damage threshold (LIDT) of optics, amplification crystals and gratings is a very important parameter which should be taken into account when ultra-short and high energy pulses are required [47, 48].Thus, a dedicated section regarding LIDT will be addressed in Chapter 3. The actual efficiency of the compressors is between 60-74 %, which is still sufficient to compress pulses with 10 PW peak power [21].

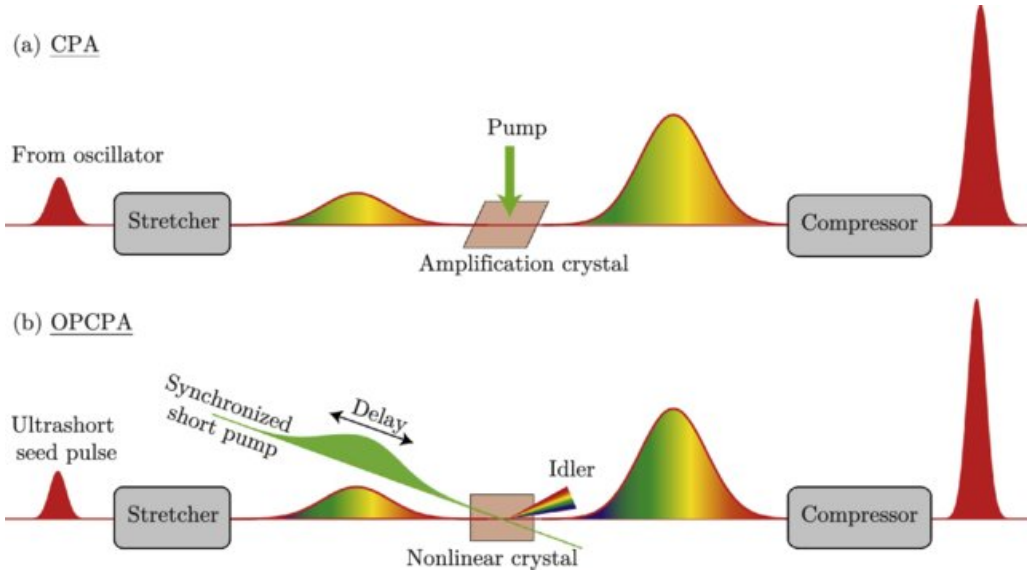


Figure 1.3: CPA and OPCPA working principal. Figure extracted from ref. [49]

#### 1.2.2.2 Optical Parametric Chirped Pulse Amplification (OPCPA)

Two additional techniques for pulse amplification are Optical Parametric Chirped Pulse Amplification (OPCPA) (See Figure 1.3) and Fiber Optics Amplifiers (FOA). OPCPA is based on the process of colinear or non-colinear parametric amplification in nonlinear crystals (such as KDP, BBO, and LBO) pumped by picosecond laser pulses [50, 51].

OPCPA offers several advantages over CPA, including a wide gain bandwidth, low spontaneous luminescence level, large gain coefficient, absence of self-excitation, and lower thermal loads. However, OPCPA also presents challenges such as pump and seed pulse synchronization, spatio-temporal shaping of the pump beam, manufacturing of large crystals for high-energy amplifiers, phase matching, and energy conservation of the pump, signal, and idler pulses [52].

Derivatives from OPCPA are non-collinear OPCPA (NOPCPA) where larger bandwidth can be amplified, quasi-collinear OPCPA using partially deuterated KDP (P-DKDP) crystals [53] can reach hundreds of PW or the most novel technique wide-angle non-collinear OPCPA alongside post-compression can reach the Exawatt class [6, 54]. A detailed sub section (1.2.4) will be dedicated to the Exawatt laser concept.

#### 1.2.2.3 Fiber Optics Amplifiers (FOA)

The scaling of power and energy in single-fiber laser systems has encountered significant limitations with respect to the coupling in the fiber as well as to nonlinear effects and damage of the fiber. To surpass these limitations and achieve higher power and energy levels, the combination of output powers from multiple lasers has emerged as a leading strategy. Among the various techniques available for combining lasers, coherent beam combining (CBC) of fiber amplification channels holds great promise. This approach enables the realization of ultra-high-power and energy lasers with beam qualities that provide pulses with focusing profiles close to diffraction-limit [55].

Currently, multipetawatt laser systems like ELI-NP or Apollon, employ a combination of CPA and OPCPA. However, the peak power of these systems limits the maximum repetition rate to one shot per minute. A potential solution to this limitation is anticipated through the utilization of FOA properties to develop International Coherent Amplification

Network (I/XCAN) within the collaboration between the Ecole Polytechnique and the Thales company [56].

The ICAN aims to coherently combine amplified pulses from multiple optical fibers into a single petawatt-scale pulse with repetition rates in the KHz range. This advancement holds promise for applications such as particle acceleration in the GeV range and radioactive waste treatment.

By leveraging FOA technology within the ICAN framework, it is expected that high-power laser systems can achieve both high peak powers and higher repetition rates, thereby enabling a broader range of applications to be implemented.

#### 1.2.2.4 Metrology and control of amplified laser pulses

One can conclude that the most important output parameters of high intense laser pulses that should be further addressed are: energy, spectrum, pulse duration, focus quality, spatio-temporal couplings.

I divide the metrology and the control of the amplified laser pulses in 4 categories that include the main devices that are involved in this process. This classification covers the main laser key components and diagnostics used in the laser facilities presented in Table 1.1.

- **Temporal control** (Pulse duration and Spectrum) [57]
  - Acousto-Optic Programmable Dispersion Filter – AOPDF (DAZZLER-Fastlite)
  - Acousto-Optic Programmable Gain Control Filter – AOPGCF (MAZZLER)
  - CPA and OPCPA
  - Reflective Optical Filters (ROF)
  - Cross-polarized wave generation – XPW

  The most important devices to measure **the spectra** are: Optical spectrometer, Spatially resolved spectrometer and to measure **the pulse duration** are: Autocorrelator, Wizzler, FROG, Spider, D-scan [58]:

- **Intensity contrast control**
  - Saturable absorber intensity filters
  - Cross-polarized wave generation – XPW
  - CPA and OPCPA
  - Plasma Mirrors (used in 1 or 2 configurations in terms of their number)

  Devices such as third-order autocorrelator i.e. Tundra are able to measure the contrast in ns or ps.

- **Spatial control** (Energy, Focus and Strehl ratio)
  - Energymeter/Powermeter
  - Deformable Mirrors (DMr)
  - Wavefront sensor (WS)

- **Spatio-Temporal Couplings control** [59]
  - Fourier transform spectroscopy interferometry -INSIGHT, TERMITES

- Digital holography-STRIPED-FISH
- Spectrally resolved Spider- SEA-SPIDER
- Wavelength resolved wavefront- HAMSTER

Mastering the temporal, spatial, spatio-temporal and energy control of ultra-short and ultra-intense laser pulses is a critical step in defining correctly *the intensity in focus*.

### 1.2.3 High power lasers (HPLs) in the world

Since the demonstration of CPA in 1985 till present, a large number of laser facilities across the world have been built and upgraded. This section follows, on short, 3 main review papers [60, 61, 62] published till 2021, a book [51] and my bibliographic study for adding the last 4 years of HPLs advancements. A complete description of the most important laser facilities, the description of their achronims, their operating parameters, state-of-the-art results and their future upgrades and perspectives can be found in the above mentioned reviews.

A PW class laser can be obtained with different pulse parameters. The HPLs evolution during time, can be seen in the following enumeration:

- 1 MJ in 1 ns (i.e. similar laser facilities: NIF, LMJ)
- 1 kJ in 100 ps (i.e. OMEGA-EP)
- 500 J in 500 fs (i.e. VULCAN)
- 25 J in 25 fs (i.e. ELI-NP)
- 1 J in 1 fs (17 fs, the shortest pulse duration proposed @APOLLON laser)

  or, as a perspective for the Exawatt class

- 1 J in 1 as (2023, record of 53 attoseconds (as) [63])

The actual HPLs can be grouped in few categories based on the amplification method (Nd:Glass, Ti:Sapphire, OPCPA), output energy (kJ -> MJ), peak power (TW -> 10 PW) and proposed perspectives (10 PW -> EW) as follows:

#### 1.2.3.1 Amplification method

The evolution of the amplification started with Q-switch (1962), Mode-locking (1964) and reached the best within CPA (1985), Ti:sapphire mode-locking oscillators (1991) and OPCPA (1992). For instance, the first PW class laser was NOVA at LLNL [64] where a new front end and a vacuum compressor were developed to generate 680 J in 440 fs $\approx$ 1.5 PW. Other laser systems such as PEARL (0.56 PW) use large apertures DKDP crystals for amplification.

To reach PW power and above ranges, novel technologies based on OPCPA (i.e. temperature-insensitive OPCPA [65]), Nd:Glass and Ti:sapphire architectures, coherent combining (CC) [66], multiple fiber beams [55], plasma amplifiers-Raman or Brillouin scattering [4, 67] or post compression [7, 24] have been proposed.

#### 1.2.3.2 High energy laser systems

Most high-energy laser systems rely on amplification media such as Nd:Glass, primarily because of their ability to store significant amounts of energy. However, these amplifiers have certain limitations that need to be considered. One drawback is their relatively large size, which can pose challenges in terms of system design and practical implementation. Additionally, the low repetition rate of Nd:Glass lasers is a result of thermal effects that require substantial cooling time between successive laser pulses. For instance, at NIF, there are days when only a few shots per day are performed due to the time required for amplification or changing the target.

The pumping mechanism for Nd:Glass lasers typically involves the use of flash lamps, which provide the necessary energy to excite the amplifying medium and initiate the amplification process. This pumping method has been widely employed in various high-energy laser systems.

Table 1.1 presents a few examples of high-energy laser systems based on Nd:Glass and Ti:Sapphire amplifiers, showcasing their output specifications related to energy and peak power.

On the other side, PW laser based on Ti: Sapphire come with the advantages of relative small size, high repetition rate (0.1-10 Hz), table top, broadband (30 fs ). The pumping is achieved using frequency doubled ($2\omega$ / 532 nm) Nd:Glass or Nd:YAG lasers.

An important aspect is addressed in Figure 1.4, where it becomes evident that although the peak power of the majority of lasers falls within the range of 1 TW to 1 PW, their average peak power typically remains at the Watt (W) scale. The primary applications of these laser systems are related to laser-driven fusion concepts, high-harmonic generation (HHG), particle acceleration and medical applications (such as radioisotope production, hadron and boron neutron capture therapies, and radiography), among others.

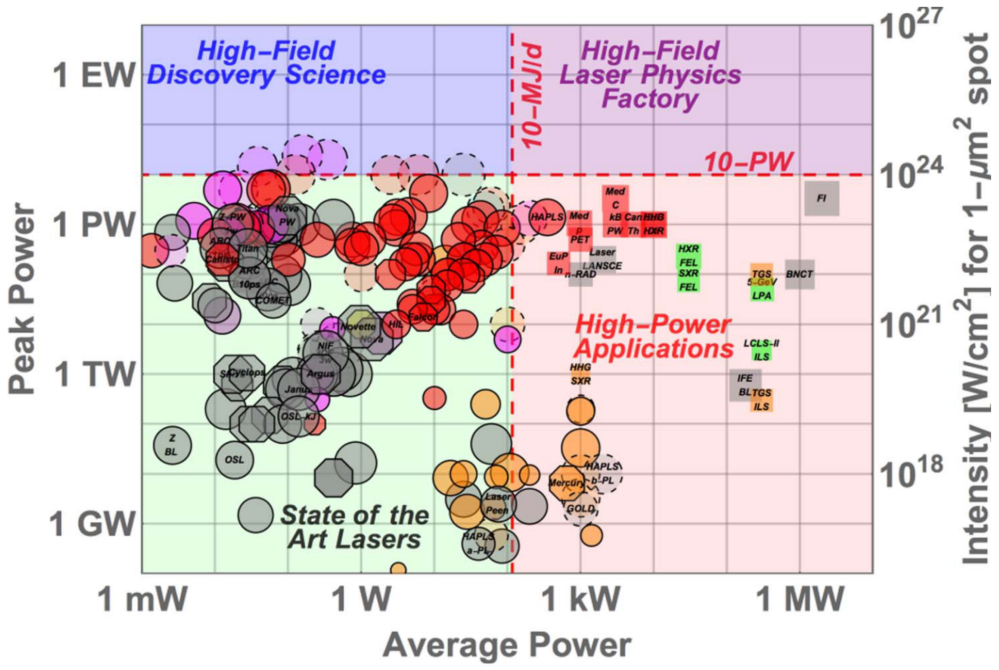


Figure 1.4: Peak power versus average power and their possible to be reached intensities. Figure extracted from Ref. [61]

Improvements such as active feedback spectral phase control, the adoption of a dual

| **Nd:Glass amplification** | | | | | |
|---|---|---|---|---|---|
| **Sub-kJ class** | | **kJ class** | | **MJ class** | |
| Gekko-XII, Japan (2004) | 0.42 | OMEGA EP, USA (2006) | 2.60 | NIF, USA (192 beams) (2018) | 1.8 |
| Titan, USA (2006) | 0.30 | PETAL, France (2008) | 1.50 | LMJ, France (176 beams) (2017) | 1.4 |
| SG-II-U, SIOM, China (2008) | 0.15 | LFEX, Japan (2012) | 10.00 | VNIIED*, Russia (192 beams) | 2.8 |
| Z-Petawatt, USA (2008) | 0.50 | NIF-ARC, USA (2015) | 13.60 | Shenguang-IV* (48 beams) | 0.2 |
| Texas Petawatt, USA (2010) | 0.17 | Vulcan 2020*, UK (6 beams) | 2.00 | | |
| PHELIX, Germany (2010) | 0.40 | L4*, Czech Republic (2019) | 1.50 | | |
| Orion AWE, UK (2013) | 0.50 | SG-II, China (2018) | 6.00 | | |
| **Ti:Sapphire amplification** | | | | | |
| **Sub-PW class** | | **PW class** | | **10 PW class** | |
| J-KAREN, Japan (2003) | 0.85 | ELI-NP, Romania (2022) | 1.00 | ELI-NP, Romania (2022) | |
| HERCULES, USA (2004) | 0.30 | BELLA, USA (2018) | 1.30 | SULF*, China (2018) | |
| SILEX-I, China (2005) | 0.27 | XL-III, China (2018) | 1.20 | Apollon*, France (2019) | |
| Astra-Gemini, UK (2009) | 0.50 | Apollon, France (2018) | 1.00 | PEARLX*, Russia | |
| CETAL*, Romania (2010) | 0.70 | VEGA, Spain (2018) | 1.00 | $>$ **10 PW** | |
| Scarlet, USA (2018) | 0.40 | J-KAREN-P*, Japan (2018) | 1.00 | ELI-NP, Romania | 10.2 |
| Diocles*, USA (2012) | 0.70 | Shengguang, China (2013) | 2.00 | Vulcan 2020*, UK | 20 |
| LOA, France (2018) | 0.50 | CoReLS, S. Korea (2021) | 4.20 | LLP*, China | 15 |
| XingGuang-III, China (2018) | 0.70 | ELI-BL, Czech Rep. (2019) | 1.00 | EPOCH* | 25 |
| J-KAREN-P*, Japan (2019) | 0.30 | ELI-ALPS, Hungary (2018) | 2.00 | | |
| SACLA, Japan (2019) | 0.50 | Vulcan PW*, UK (2018) | 1.00 | | |
| Scapa, UK (2018) | 0.35 | ILE, Japan (2018) | 2.00 | | |
| TIFR, India (2019) | 0.15 | PEnELOPE, Germany (2018) | 1.00 | | |
| * Denotes that the facility is proposing an upgrade to the mentioned value or they operates at lower power. The year represents the last update extracted from the reviews [60, 61, 62] and the source: https://www.easymapmaker.com/map/ICUIL_World_Map_v3 | | | | | |

Table 1.1: High power lasers systems based on Nd:Glass and Ti:Sapphire amplification media, across the world. The numbers next to facility name represent the corresponding pulse energy (kJ/MJ) and the peak power in PW, respectively.

compressor geometry (Diocles), utilization of large gratings (NIF), integration of high-energy pump lasers (e.g., Atlas 100 @ HERCULES, ELI-NP), elimination of lens-based telescopes (TEXAS PW), contrast enhancement through cross-polarized wave techniques (XPW) (as seen in Scarlet, ELI-NP), the introduction of a plasma mirror before the target (GEKKO XII), and the implementation of double plasma mirrors (CoReLS) have all been implemented as part of upgrade initiatives.

#### 1.2.3.3 High repetition rate laser systems

Significant advancements have been achieved within the ELI (Extreme Light Infrastructure) projects, including ELI-NP, which boasts the world's highest peak power of 10 PW with a rate of 1 shot per minute. ELI ALPS, another notable project, has achieved the shortest pulse duration of 6 fs, 100 KHz, 5 mJ, and PW peak power at 10 Hz repetition rate. The ELI Beamlines project has set a remarkable record for the highest repetition rate, with 1 PW at 10 Hz and a goal of 10 PW, 1.5 kJ, and 1 shot per minute. A comprehensive description of these key pillars of the ELI initiative can be found in the referenced lecture [68].

Future perspectives in this field are emerging through the EPOCH facility in Japan, which plans to achieve 16 KJ, 16 Hz, 1 ns, and 160 beams, or via fibers (known as FOAs), such as the I/X CAN project in France, which aims to establish 10,000 channels. FOAs have demonstrated, albeit on a smaller scale, their applicability in areas such as particle accelerators, nuclear waste transmutation, and space debris mitigation [3].

As for drawbacks, it is worth noting the use of multiple combining elements arranged in a cascade configuration, which increases the level of complexity with the number of fibers involved. Additionally, the small size of the fibers, typically on the $\mu m$ scale, allows only pulse energy in the mJ range, posing a further challenge in this context.

#### 1.2.3.4 High intensity laser systems

It is evident that a multitude of high-peak-power lasers have been constructed, and substantial technological endeavors have been devoted to realize their original designs. The first experimental proof of peak power surpassing a 10 PW beam has been achieved at ELI-NP. This facility is currently the only one operational at 10 PW in the world as of 2023. [69].

Intensities exceeding $10^{23} W/cm^2$ are expected also at ELI-NP, utilizing a 10 PW beam and the existing F=2.7 off-axis parabolic mirrors. As of 2023, this facility remains the sole operational 10 PW laser system worldwide performing experiments at this level [69], but news from the 10 PW laser facility at SIOM, China are expected to appear in the near future, too [54].

Table 1.1 provides insights into other facilities on the brink of reaching the 10 PW milestone; however, they have encountered technological challenges, delaying their progress beyond their initially proposed timelines. Furthermore, experimentalists and engineers are striving to push the boundaries in the 10 PW realm (see table 1.1, column: $>$ 10 PW).

The principal constraints in the development of High-Peak-Power Lasers (HPLs) encompass the following:

- **Optics Aperture:** This pertains to the size of optics elements such as plane mirrors, parabolic mirrors, and diffraction gratings, which often reach meter-scale dimensions.
- **Bandwidth:** The demand for broadband optics, frequently substantial in size, poses a significant challenge.

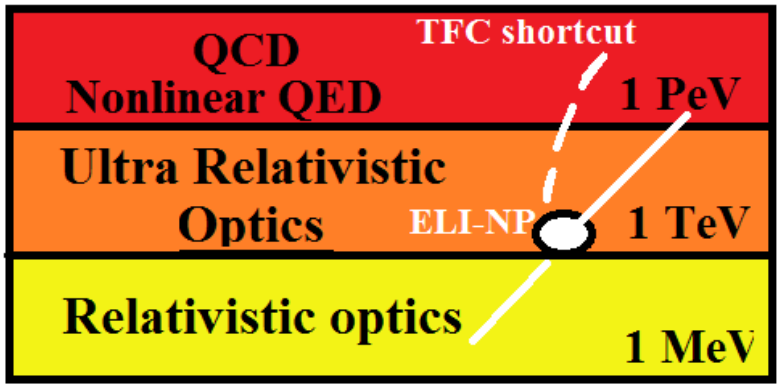


Figure 1.5: Thin Film compression(TFC)-a road shortcut to Exawatt lasers, where QCD denotes Quantum chromodynamics

- **B-Integral**: The accumulation of nonlinear phase during laser propagation through materials.
- **Laser-Induced Damage Threshold:** Ensuring the laser's components can withstand high peak power without damage.
- **Multiplexing Limits:** Particularly for fiber-based systems, ensuring spatio-temporal overlap.

In addition, key technologies aimed at increasing laser peak power and the repetition rate of HPLs are related to:

- **Temporal Contrast Improvements:** Achieved through the application of plasma mirrors and frequency doubling post-compressed beams.
- **Plasma Optics:** Tied spatially to the repetition rate of the laser (RRL), and a proposed solution involves liquid plasma targets.
- **Advanced Optics:** Addressing size, laser-induced damage threshold (LIDT), wavefront quality, and broadband characteristics.
- **Laser Diagnostics:** Including full-aperture and single-shot diagnostics.

In summary, the quest for achieving high peak power levels involves two primary approaches: increasing pulse energy or reducing pulse duration. Both avenues contribute to achieving higher peak powers. Notably, reducing pulse duration appears to be a more efficient means of accomplishing this, particularly including them after the diffraction gratings compressor (refer to Figure 1.5).

However, it is vital to acknowledge that both approaches present unique challenges. Coherent combination offers an alternative solution, but achieving coherence in both spatial and temporal domains introduces significant technological complexity. Progress in technology and a deeper understanding of the underlying principles are imperative to overcome these challenges and ultimately attain the ambitious goal of Exawatt power.

### 1.2.4 Exawatt concept

In the pursuit of reaching the Exawatt ($10^{18}$ W) power level, many attempts with respect to simulations, concepts and novel designs for laser parts have been proposed (See Table 1.2).

Table 1.2: Exawatt class lasers concepts and methods

| **Author** | **Year** | **Method** | **Predicted Peak power (EW)** | **Laser parameters** | **Details** |
|---|---|---|---|---|---|
| Malkin [4] | 1999 | Stimulated Raman backscattering for amplification and compression in plasma (BRA) | 30-40 | 1.5 MJ, 200 $cm^2$ | Theoretical calculations for laser pulse amplification in plasma. $\pi$ pulse scheme, which fully depletes the pumping beam while undergoing amplification and contraction; The advantage of avoiding gratings, but the plasma must be uniform over a length given by half of the laser pulse length |
| Tajima [2] | 2002 | OPCPA for NIF/LMJ like laser multiple (2500) CPAs | 1-100 | 10 kJ-1MJ, 10 fs | Proposals for Exawatt and Zeptowatt class lasers and their applications |
| Hays [70] | 2007 | Nd-doped laser glasses for high-energy CPA | 0.12 | 15 kJ, 120 fs | Proposal of 2 novel laser glasses (Nd:phosphate and Nd:silicate ) used with an OPCPA to generate high energy and broadband laser pulses. The peak power is achieved using 8 beamlines of such configuration |
| Mourou [5] | 2012 | Combination of 3 compression methods: CPA, OPCPA and Backward Raman Amplification (BRA) in the $C^3$ concept | 1 | ns-fs, MJ | Introduction of the $C^3$ for Cascaded Conversion Compression concept; the concept of Multiple-Beam-Pumping shows that the energy from several beams can be transferred to one signal seed pulse; Efficiency was estimated between 24 and 50% |
| Voronin [71] | 2013 | Spectral Broadening and cascade of nine nonlinear elements separated by eight spatial filters | 0.35 | 4.2 fs | Detailed analysis of the spatio-temporal dynamics: dispersion, pulse self-steepening, small-scale self-focusing, ionization, self-phase modulation of multi-petawatt laser; Overall energy loss due to the spatial filtering 15%. |

| | | | | | |
|---|---|---|---|---|---|
| Mourou [1] | 2014 | Thin Film Compression (TFC) $\lambda^3$ concept | 0.1-1 | 1kJ, 2 fs | A proposal for 2 compression stages (25 fs -2 fs) while using thin film (500 and 100 um) for SPM, Deformable mirrors for wavefront corrections, parabolic mirrors for beam expansion, and pinholes to clean the beam; Efficiency >50%; compression using the relativistic mirror may lead to attoseconds or zeptoseconds [72] |
| Barty [73] | 2016 | Large beams splitting and coherently recombining before compressor | 1.2 | 250kJ, 20 ns-100 fs | Development of the beam splitting setup and their recombination process |
| Li [74] | 2019 | proposal of wideangle non-collinear optical parametric chirped-pulse amplification (WNOPCPA) | 0.1 | 370 J, 3 fs | Analysis of the amplification process through WNOPCPA using type I LBO crystal; Simulations for the grating compressor; |
| Liu [75] | 2021 | Multistep pulse compressor (MPC) and spatio temporal focus | 0.1 | 1.5 kJ, 2 ns-14.5 fs | MPC for achieving high-energy 100 PW using a single beam and multiple compression steps. MPC typically includes a prism pair for pre-compression, 4 gratings for main compression, and a spatio-temporal focusing self-compressor for post-compression |
| Li [6] | 2021 | WNOPCPA is combined with the thin-plate post-compression and CMs | 0.58 | 971 J, 1.65 fs | Simulations for the amplification process, WNOPCPA; Post-compression (fused silica, m size), dispersion compensation using CMs |
| Wang [76] | 2022 | Front-end developed for the 100 PW | 0.1 | 5.26 J, 13.4 fs, 0.1 Hz | 3 stages of OPCPA based on LBO crystals; Temporal, spectral, and contrast measurements were provided. Compression efficiency reached 67%. Another Front-end optimization setup [77] |

| | | | | | |
|---|---|---|---|---|---|
| Hur [78] | 2022 | Spatially varying dispersion of a plasma plume with a density gradient | 7.3 | 2.35 ps-10.3 fs | 1-D PIC Simulations of laser pulses compression with linearly chirped pulse using parabolic plasma density profiles, 99.2 efficiencies; Amplification by a factor of 170 times larger |
| Han [79] | 2023 | Generation and possibility to compress 400 nm bandwidth | 0.1 | 1.5 kJ, 15 fs | Development of broadband gratings ( 400 nm, 90% efficiency) |
| Ches-nut [80] | 2023 | Spatio temporal analysis via chirped pulse juxtaposed with beam amplification (CPJBA) | 0.2 | 250 kJ, 20 ns-100 fs | Development and dispersion analysis of 6 grating compressor |

To achieve a sub-optical-cycle Exawatt (EW)-class laser, there are additional challenges that need to be considered in addition to the well-known factors such as optics dimensions, dispersion control, wavefront control, high-gain/energy amplification, spectral narrowing, temporal contrast, beam smoothing, beam pointing, and beam focusing.

A more recent concern that has emerged is the spatio-temporal and spectral coupling distortion caused by the deformation of the compressor gratings. Although this issue is technically controllable, it should be carefully addressed to ensure optimal performance and maintain the desired laser characteristics [6].

New concepts such as $\lambda^3$ regime offers perspectives which are linked to the focus volume, where the highest intensity can be achieved for a given pulse energy. In order to further amplify the intensity, a transition towards shorter wavelengths becomes essential. This transition allows for shorter pulse durations and enables tighter focusing, thus facilitating the enhancement of the intensity.

From Table 1.2 it can be seen that the amplification and compression in plasma offers the highest gain factor (170) [78] and eliminates the gratings [4] but more studies are needed to be performed.

Moreover, a detailed description of the applications of Exawatt and zeptoseconds can be found in [2, 81]. Main bottlenecks that influence the current and the future PW class lasers and their possible solutions are further discussed in Ref. [54].

On the other hand, post compression along side WNOPCPA seems to be the most accessible way to reach EW. Thus, in the following section, I will describe the actual status of the thin film compression/post compression, for the low energy case and in details for the high energy (>100 mJ) case.

## 1.3 Review of the experimental methods to realize post compression

### 1.3.1 Broadening and post compression of low energy laser pulses

To shorten the pulse duration, a large spectral broadening is required along with control over the spectral phase over the entire spectrum, and an efficient re-compression method.

The first sub-10 fs pulses have been generated through self-phase modulation (SPM) (1 MW, 8 fs, 5 KHz) in solid-core fibers followed by the compression of the resulting chirped pulses [82].

Efficient spectral broadening was obtained through SPM effect in fibers [83], hollow core fibers filled with gas i.e. Krypton, Argon [84], nonlinear crystals [85, 86], glasses [8, 87] and most recently in plastics [1, 88, 89, 90, 91].

When it comes to the latest generation of high-power femtosecond (fs) sources, the use of capillaries is somewhat limited due to significant transmission losses in waveguides with core diameters smaller than 100 $\mu m$. However, generating the necessary nonlinear effects for pulses with peak powers in the MW range requires relatively small diameters [92].

To address this challenge, an alternative method for achieving spectral broadening within this power range is the utilization of hollow-core photonic crystal fibers (HC-PCF), featuring a cladding structure based on the kagome lattice [93]. These HC-PCFs offer a promising solution by allowing for efficient nonlinear effects while maintaining sufficient transmission for higher peak-power pulses.

Post compression has been also realized using deformable mirror ($\tau_{out}$ =15 fs ) [94], pulse shaping ($\tau_{out}$ =2.2 fs ) [95]; it has been proved both in experiment and theory that the negatively chirped laser pulse can be reshaped and self-compressed in a piece of glass plate [96], and by using self-compression in solid thin fused silica plates (6 plates) and spatial filtering, 8.8 fs have been measured input laser pulses with 40 fs and 0.8 mJ [97].

### 1.3.2 Self-compression of low energy laser pulses

Self-compression is a complex phenomenon observed during the propagation of strong femtosecond laser pulses in nonlinear media [97]. It involves a delicate interplay of various linear and nonlinear effects that influence the pulse duration. In essence, self-compression occurs when factors causing positive dispersion counteract those leading to negative dispersion.

One critical factor affecting self-compression is material dispersion, which depends on the wavelength of the input pulses [98]. In many studies, researchers have focused on regions where the medium exhibits negative dispersion within the wavelength range of the input pulses. This negative dispersion balances the positive dispersion induced by the Kerr effect. Key parameters include the interaction medium, its solid density, the central wavelength of the laser, and the input intensity.

In the case of laser pulse propagation, the plasma effect primarily occurs at the trailing edge of the pulse due to ionization at the leading edge [98]. Plasma accumulation toward the trailing edge induces a negative refractive index, pushing shorter wavelength components forward, similar to negative dispersion behavior. Additionally, the self-steepening effect decelerates the pulse's back part, resulting in super-continuum generation, self-compression, and pulse splitting during propagation.

In solid-state materials, self-compression mechanisms are similar to those in gases, but significant differences exist in dispersion, Kerr effect, and photon ionization parameters, which are more pronounced in solids [98].

The interplay of SPM and plasma effects is crucial in solid-state materials [98]. SPM introduces positive dispersion, counteracting self-compression, while the plasma effect acts as if it provides negative dispersion, facilitating pulse compression. Balancing these opposing effects is essential for successful self-compression.

SPM introduces new spectral components alongside ionization spectral broadening, contributing to broader spectra and shorter pulses during self-compression [98].

Achieving dispersion matching for self-compression in solids requires precise control to balance linear and nonlinear effects [7]. Without careful control, pulse splitting can occur, hindering self-compression.

One solution for high-energy, close-to-single-cycle laser pulses involves spectrum broadening in multiple thin plates [7]. This approach suppresses filamentation by strategically positioning plates relative to the laser focus, maintaining spectral coherence. Precise plate positioning leads to the compensation of the negative dispersion from the plasma effect with the positive dispersion during propagation.

In single laser pulse self-compression, relativistic mass variation and ponderomotive effects are crucial [99]. These factors lead to longitudinal self-compression of the pulse.

Ponderomotive nonlinearity modifies the refractive index due to density changes induced by the ponderomotive force [99]. This force moves electrons from lower to higher intensity regions, enhancing nonlinear characteristics and the on-axis refractive index of the pulse.

Spatial dimensions of the laser pulse can be altered by relativistic self-focusing and pulse self-compression, impacting both transverse and axial extensions of the pulse [99].

### 1.3.3 Post compression of high energy laser pulses

For the high-energy regime ($E > 500$ mJ), issues related to ionization, self-focusing, material damage, and the size of nonlinear materials become critical factors [1, 88, 90]. This thesis aims to investigate the feasibility of generating a broad spectral bandwidth through SPM in bulk materials using high-energy laser pulses.

SPM is a nonlinear process, which will be further detailed in Chapter 2, based on the intensity-dependent refractive index change when an intense beam propagates through the medium ($n(t,r) = n_0 + n_2 \cdot I(t,r)$). In essence, the refractive index variation with incident irradiance induces a phase modulation over time for each frequency component within the pulse. The medium's response introduces a phase shift to the incoming wave, resulting in the generation of new frequencies. The nonlinear response ($n_2$) varies among different materials based on their chemical composition, leading to distinct nonlinear refractive indices (NRIs), which influence SPM generation.

In addition to the generation of new frequencies in nonlinear crystals, fibers, and gas-filled hollow capillaries, which have found effective applications in low-energy laser systems with Gaussian beam profiles, thin and flat plastic materials offer a novel perspective for generating ultrashort pulses in large-aperture, Joule-level laser systems with super-Gaussian or flat-top beam profiles [1, 88, 90]. These beam profile types enable a uniform energy distribution across the material surface, mitigating the occurrence of hot spots and filamentation commonly associated with Gaussian profiles. Understanding the properties of optical and plastic materials, along with their capabilities, presents both a challenge and an opportunity for achieving the single-cycle regime, as further discussed in Chapter 3.

#### 1.3.3.1 Thin Film Compression (TFC)

With their main advantages as low cost, short manufacturing time and large variety of sizes along with their optical characteristics being similar to glasses (i.e. FS or N-BK7 in

terms of refractive index, transmission) plastics were introduced and proposed for the first time in the Thin Film Compression method which is illustrated in Figure 1.6 [1].

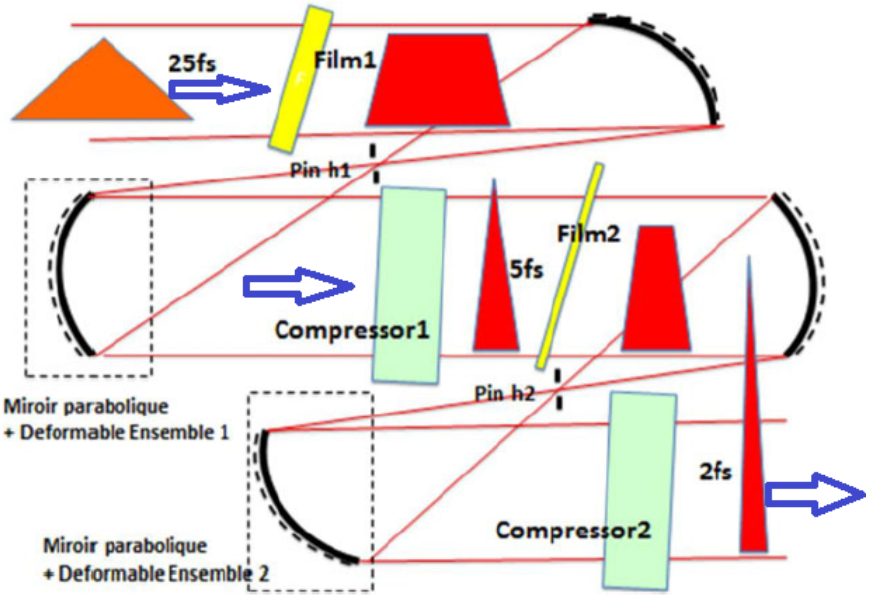


Figure 1.6: Thin film compression method (TFC): Using the SPM effect, new frequencies are generated followed by the laser pulse re-compression. Figure extracted and modified from ref. [1]

The TFC method is using thin plastic films with hundreds of micrometers thickness for SPM. The plastic materials should have a high optical quality and are preferably positioned at the Brewster angle to minimize the losses through reflections. A series of chirped mirrors (CM) with a specific value of Group Delay Dispersion (GDD) are used to compress the pulse duration after the spectrum broadening. The chirped mirrors are manufactured from multiple dielectric layers with spaces of varying depth designed to reflect multiple wavelengths. The introduced GDD by the CM has a negative magnitude thus allowing the compensation of the positive dispersion introduced by the material. The perfect compensation of the GDD leads to a compressed pulse close to the Fourier limit. A more detailed section, in Chapter II, will address the dispersion introduced by the CMs.

#### 1.3.3.2 Challenges

Post-compression of high-energy laser pulses was found to be constrained by the damage threshold of optical materials and chirped mirrors, and the quality of these materials plays a critical role in wavefront and focus quality. Careful measurement of nonlinearities, particularly those leading to SPM, at the laser's central wavelength (e.g., $\lambda_{central} = 800$ nm) is essential. The successful implementation of the technique, as well as the development of effective diagnostics, are pivotal for achieving precise control over post-compression. Furthermore, optimization through simulations and exploring various applications are imperative steps in advancing this technique on a global scale.

This thesis comprehensively addresses these aspects, encompassing theoretical frameworks, simulation studies, and experimental findings. The primary focus of this research is on post-compression of high-energy laser pulses to attain few-cycle durations, with an emphasis on utilizing both glass and plastic materials. A series of experiments has been conducted to gain profound insights into the underlying principles and key challenges associated with this field, with the ultimate goal of making substantial advancements.

## 1.4 Structure of manuscript

Chapter II is dedicated to the theoretical underpinnings of this thesis, focusing on nonlinear effects, particularly SPM, nonlinear refractive index, and dispersion effects. These concepts form the foundation of the thesis. The latter part of this chapter discusses dispersion phenomena, different orders of dispersion, relevant dispersive materials commonly used in high-power laser systems (HPLS), and methods to compensate dispersion.

This part of the thesis extensively covers theoretical aspects pertaining to SPM and the various parameters that contribute to this phenomenon. The goal was to establish the simplest yet most accurate model to describe SPM, incorporating several underlying assumptions. The nonlinear refractive index, another pivotal factor, is thoroughly scrutinized, including the fitting models associated with it. Furthermore, the thesis delves into the specific scenario of a large nonlinear phase shift and assesses the impact of high-order nonlinearities.

To bring these theoretical concepts to experiments, simulations were developed using the PyNLO library within a Python environment. These simulations are designed to replicate the generation of ultra-short laser pulses and their subsequent propagation through nonlinear media.

Chapter III introduces the theoretical models and simulations developed for this research, along with the techniques used to implement them in an experimental setup. This chapter outlines the comprehensive characterization of optical materials, covering dispersion, roughness, vacuum compatibility, and providing a detailed analysis of the nonlinear refractive index and laser-induced damage threshold. Additionally, a computational dispersion management system (DMS) is designed to compress the newly simulated spectrally broadened pulses. Using the key parameters such as dispersion, nonlinear refractive index, damage threshold, I computed the propagation of ultra-short laser pulses through optical materials and I showed the possibility of reaching close to single cycle regime.

Chapter IV presents a comprehensive description of the experimental results obtained from four experiments relevant to the thesis topic. It showcases the utilization of plastics and glasses in post-compression experiments involving high-energy laser pulses, successfully achieving compression levels ranging from terawatt (TW) to petawatt (PW) peak power. The chapter also addresses new challenges pertaining to the metrology of post-compressed laser pulses, such as spatio-temporal couplings, encircled energy, nonlinear absorption in chirped mirrors (CM), and wavefront correction, providing detailed insights into these aspects.

Chapter V wraps up the thesis by presenting the main conclusions drawn from the research. It also discusses future perspectives, including potential implementations of original ideas emerging from the work, as well as simulations involving secondary sources acceleration.

# Bibliography


[1] G. Mourou, S. Mironov, et al. "Single cycle thin film compressor opening the door to Zeptosecond-Exawatt physics". en. In: *The European Physical Journal Special Topics* 223.6 (May 2014), pp. 1181–1188. URL: http://link.springer.com/10.1140/epjst/e2014-02171-5 (visited on 02/06/2019).

[2] T. Tajima and G. Mourou. "Zettawatt-exawatt lasers and their applications in ultrastrong-field physics". In: *Physical Review Special Topics - Accelerators and Beams* 5.3 (Mar. 2002). Publisher: American Physical Society, p. 031301. URL: https://link.aps.org/doi/10.1103/PhysRevSTAB.5.031301 (visited on 06/28/2023).

[3] Gerard Mourou, William Brocklesby, et al. "The future is fibre accelerators". In: *Nature Photonics* 7 (Apr. 2013), pp. 258–261.

[4] V. M. Malkin, G. Shvets, et al. "Fast Compression of Laser Beams to Highly Overcritical Powers". In: *Physical Review Letters* 82.22 (May 1999). Publisher: American Physical Society, pp. 4448–4451. URL: https://link.aps.org/doi/10.1103/PhysRevLett.82.4448 (visited on 06/22/2023).

[5] G. A. Mourou, N. J. Fisch, et al. "Exawatt-Zettawatt pulse generation and applications". In: *Optics Communications* 285.5 (Mar. 2012), pp. 720–724. URL: http://www.sciencedirect.com/science/article/pii/S0030401811012338 (visited on 02/06/2019).

[6] Zhaoyang Li, Yoshiaki Kato, et al. "Simulating an ultra-broadband concept for Exawatt-class lasers". en. In: *Scientific Reports* 11.1 (Jan. 2021). Number: 1 Publisher: Nature Publishing Group, p. 151. URL: https://www.nature.com/articles/s41598-020-80435-6 (visited on 01/13/2021).

[7] E. A. Khazanov, S. Yu Mironov, et al. "Nonlinear compression of high-power laser pulses: compression after compressor approach". en. In: *Physics-Uspekhi* 62.11 (Nov. 2019). Publisher: IOP Publishing, p. 1096. URL: https://iopscience.iop.org/article/10.3367/UFNe.2019.05.038564/meta (visited on 11/09/2020).

[8] S. Yu. Mironov, S. Fourmaux, et al. "Thin plate compression of a sub-petawatt Ti:Sa laser pulses". en. In: *Applied Physics Letters* 116.24 (June 2020), p. 241101. URL: http://aip.scitation.org/doi/10.1063/5.0008544 (visited on 06/22/2020).

[9] Ji in Kim, Jin Woo Yoon, et al. "Post-compression of a 100-TW Ti:sapphire laser (Conference Presentation)". In: *High-power, High-energy Lasers and Ultrafast Optical Technologies*. Vol. PC12577. SPIE, June 2023, PC125770G. URL: https://www.spiedigitallibrary.org/conference-proceedings-of-spie/PC12577/PC125770G/Post-compression-of-a-100-TW-Ti-sapphire-laser-Conference/10.1117/12.2669875.full (visited on 06/13/2023).

[10] S. Gales, K. A. Tanaka, et al. “The extreme light infrastructure—nuclear physics (ELI-NP) facility: new horizons in physics with 10 PW ultra-intense lasers and 20 MeV brilliant gamma beams”. en. In: *Reports on Progress in Physics* 81.9 (Aug. 2018). Publisher: IOP Publishing, p. 094301. URL: https://doi.org/10.1088/1361-6633/aacfe8 (visited on 02/11/2021).

[11] François Lureau, Guillaume Matras, et al. “High-energy hybrid femtosecond laser system demonstrating 2 × 10 PW capability”. en. In: *High Power Laser Science and Engineering* 8 (2020). Publisher: Cambridge University Press. URL: https://www.cambridge.org/core/journals/high-power-laser-science-and-engineering/article/highenergy-hybrid-femtosecond-laser-system-demonstrating-2-10-pw-capability/C10005F3B8BA78E4FA3EF9EAF06C3BFB (visited on 12/17/2020).

[12] A. H. Zewail, M. Dantus, et al. “Femtochemistry: recent advances and extension to high pressures”. en. In: *Journal of Photochemistry and Photobiology A: Chemistry* 62.3 (Jan. 1992), pp. 301–319. URL: https://www.sciencedirect.com/science/article/pii/101060309285061X (visited on 06/09/2023).

[13] Ahmed H. Zewail. “Femtochemistry: Atomic-Scale Dynamics of the Chemical Bond”. en. In: *The Journal of Physical Chemistry A* 104.24 (June 2000), pp. 5660–5694. URL: https://pubs.acs.org/doi/10.1021/jp001460h (visited on 06/14/2023).

[14] Victor Torres-Company and Andrew M. Weiner. “Optical frequency comb technology for ultra-broadband radio-frequency photonics”. In: *Laser & Photonics Reviews* 8.3 (2014). _eprint: https://onlinelibrary.wiley.com/doi/pdf/10.1002/lpor.201300126, pp. 368–393. URL: https://onlinelibrary.wiley.com/doi/abs/10.1002/lpor.201300126 (visited on 07/01/2023).

[15] Tara Fortier and Esther Baumann. “20 years of developments in optical frequency comb technology and applications”. en. In: *Communications Physics* 2.1 (Dec. 2019), p. 153. URL: https://www.nature.com/articles/s42005-019-0249-y (visited on 07/01/2023).

[16] Koji Sugioka. “Progress in ultrafast laser processing and future prospects”. en. In: *Nanophotonics* 6.2 (Mar. 2017). Publisher: De Gruyter, pp. 393–413. URL: https://www.degruyter.com/document/doi/10.1515/nanoph-2016-0004/html (visited on 06/14/2023).

[17] Koji Sugioka and Ya Cheng. “Ultrafast lasers—reliable tools for advanced materials processing”. en. In: *Light: Science & Applications* 3.4 (Apr. 2014). Number: 4 Publisher: Nature Publishing Group, e149–e149. URL: https://www.nature.com/articles/lsa201430 (visited on 06/14/2023).

[18] Ingolf V Hertel, Razvan Stoian, et al. “On the physics of material processing with femtosecond lasers”. en. In: ().

[19] Pierre Tournois. “Acousto-optic programmable dispersive filter for adaptive compensation of group delay time dispersion in laser systems”. en. In: *Optics Communications* 140.4 (Aug. 1997), pp. 245–249. URL: https://www.sciencedirect.com/science/article/pii/S0030401897001533 (visited on 07/01/2023).

[20] I. C. E. Turcu, S. Balascuta, et al. “Strong field physics and QED experiments with ELI-NP 2 *10PW laser beams”. en. In: *AIP Conference Proceedings*. Vol. 416. Sinaia, Romania: 1645, 2015, pp. 416–420. URL: http://aip.scitation.org/doi/abs/10.1063/1.4909613 (visited on 07/16/2019).

[21] G. Wormser, C. Barty, et al. *The White Book of ELI Nuclear Physics Bucharest-Magurele, Romania*. Vol. 68. Romanian Report in Physics, Dec. 2010. URL: http://www.eli-np.ro/whitebook.php.

[22] Yitong Wu, Liangliang Ji, et al. "On the upper limit of laser intensity attainable in nonideal vacuum". EN. In: *Photonics Research* 9.4 (Apr. 2021). Publisher: Optica Publishing Group, pp. 541–547. URL: https://opg.optica.org/prj/abstract.cfm?uri=prj-9-4-541 (visited on 06/09/2023).

[23] Tatsumi Aoyama, Masashi Hayakawa, et al. "Erratum: Tenth-order electron anomalous magnetic moment: Contribution of diagrams without closed lepton loops [Phys. Rev. D 91, 033006 (2015)]". In: *Physical Review D* 96.1 (July 2017). Publisher: American Physical Society, p. 019901. URL: https://link.aps.org/doi/10.1103/PhysRevD.96.019901 (visited on 07/02/2023).

[24] Gerard A. Mourou, Toshiki Tajima, et al. "Optics in the relativistic regime". en. In: *Reviews of Modern Physics* 78.2 (Apr. 2006), pp. 309–371. URL: https://link.aps.org/doi/10.1103/RevModPhys.78.309 (visited on 02/12/2021).

[25] Stepan S. Bulanov, Timur Zh Esirkepov, et al. "On the Schwinger limit attainability with extreme power lasers". In: *Physical Review Letters* 105.22 (Nov. 2010). arXiv: 1007.4306, p. 220407. URL: http://arxiv.org/abs/1007.4306 (visited on 08/10/2019).

[26] C. Bamber, S. J. Boege, et al. "Studies of nonlinear QED in collisions of 46.6 GeV electrons with intense laser pulses". In: *Physical Review D* 60.9 (Oct. 1999), p. 092004. URL: https://link.aps.org/doi/10.1103/PhysRevD.60.092004 (visited on 08/10/2019).

[27] Jonathan A. Wheeler, Gérard Mourou, et al. "Science of High Energy, Single-Cycled Lasers". In: *Reviews of Accelerator Science and Technology* 10.01 (Aug. 2019). Publisher: World Scientific Publishing Co., pp. 227–244. URL: https://www.worldscientific.com/doi/abs/10.1142/S1793626819300123 (visited on 09/17/2020).

[28] S. Keppler, N. Elkina, et al. "Intensity scaling limitations of laser-driven proton acceleration in the TNSA-regime". en. In: *Physical Review Research* 4.1 (Jan. 2022), p. 013065. URL: https://link.aps.org/doi/10.1103/PhysRevResearch.4.013065 (visited on 02/08/2022).

[29] D. Doria, M. O. Cernaianu, et al. "Overview of ELI-NP status and laser commissioning experiments with 1 PW and 10 PW class-lasers". en. In: *Journal of Instrumentation* 15.09 (Sept. 2020). Publisher: IOP Publishing, pp. C09053–C09053. URL: https://doi.org/10.1088/1748-0221/15/09/c09053 (visited on 02/12/2021).

[30] J. Park, J. H. Bin, et al. "Target normal sheath acceleration with a large laser focal diameter". In: *Physics of Plasmas* 27.12 (Dec. 2020). Publisher: American Institute of Physics, p. 123104. URL: https://aip.scitation.org/doi/full/10.1063/5.0020609 (visited on 04/18/2022).

[31] M. Borghesi, J. Fuchs, et al. "Fast Ion Generation by High-Intensity Laser Irradiation of Solid Targets and Applications". In: *Fusion Science and Technology* 49.3 (Apr. 2006). Publisher: Taylor & Francis _eprint: https://doi.org/10.13182/FST06-A1159, pp. 412–439. URL: https://doi.org/10.13182/FST06-A1159 (visited on 07/02/2023).

[32] M. Roth and M. Schollmeier. "Ion Acceleration—Target Normal Sheath Acceleration". en. In: *CERN Yellow Reports* (Feb. 2016). Artwork Size: 231 Pages Publisher: CERN, Geneva, 231 Pages. URL: https://e-publishing.cern.ch/index.php/CYR/article/view/222 (visited on 07/02/2023).

[33] Andrea Macchi, Marco Borghesi, et al. "Ion acceleration by superintense laser-plasma interaction". In: *Reviews of Modern Physics* 85.2 (May 2013). Publisher: American Physical Society, pp. 751–793. URL: https://link.aps.org/doi/10.1103/RevModPhys.85.751 (visited on 09/06/2023).

[34] A. Măgureanu, L. Dincă, et al. "Target Characteristics Used in Laser-Plasma Acceleration of Protons Based on the TNSA Mechanism". In: *Frontiers in Physics* 10 (2022). URL: https://www.frontiersin.org/articles/10.3389/fphy.2022.727718 (visited on 09/11/2023).

[35] P. Sprangle, G. Joyce, et al. "Laser wakefield acceleration and relativstic optical guiding". In: *AIP Conference Proceedings* 175.1 (Nov. 1988), pp. 231–239. URL: https://doi.org/10.1063/1.37621 (visited on 07/02/2023).

[36] A. E. Hussein, A. V. Arefiev, et al. "Towards the optimisation of direct laser acceleration". en. In: *New Journal of Physics* 23.2 (Feb. 2021). Publisher: IOP Publishing, p. 023031. URL: https://dx.doi.org/10.1088/1367-2630/abdf9a (visited on 07/02/2023).

[37] Kazuyoshi Koyama, Shohei Otsuki, et al. "Parameter study of a laser-driven dielectric accelerator for radiobiology research". en. In: *Journal of Physics B: Atomic, Molecular and Optical Physics* 47.23 (Nov. 2014). Publisher: IOP Publishing, p. 234005. URL: https://dx.doi.org/10.1088/0953-4075/47/23/234005 (visited on 07/02/2023).

[38] A. Macchi, C. Livi, et al. "Radiation pressure acceleration: perspectives and limits". en. In: *Journal of Instrumentation* 12.04 (Apr. 2017), p. C04016. URL: https://dx.doi.org/10.1088/1748-0221/12/04/C04016 (visited on 07/02/2023).

[39] C. Caizergues, S. Smartsev, et al. "Phase-locked laser-wakefield electron acceleration". en. In: *Nature Photonics* 14.8 (Aug. 2020). Number: 8 Publisher: Nature Publishing Group, pp. 475–479. URL: https://www.nature.com/articles/s41566-020-0657-2 (visited on 04/20/2023).

[40] Vincent Favaudon, Laura Caplier, et al. "Ultrahigh dose-rate FLASH irradiation increases the differential response between normal and tumor tissue in mice". eng. In: *Science Translational Medicine* 6.245 (July 2014), 245ra93.

[41] Jianhui Bin, Lieselotte Obst-Huebl, et al. "A new platform for ultra-high dose rate radiobiological research using the BELLA PW laser proton beamline". en. In: *Scientific Reports* 12.1 (Jan. 2022). Number: 1 Publisher: Nature Publishing Group, p. 1484. URL: https://www.nature.com/articles/s41598-022-05181-3 (visited on 06/16/2023).

[42] Pankaj Chaudhary, Deborah C. Gwynne, et al. "Development of a portable hypoxia chamber for ultra-high dose rate laser-driven proton radiobiology applications". In: *Radiation Oncology* 17.1 (Apr. 2022), p. 77. URL: https://doi.org/10.1186/s13014-022-02024-3 (visited on 06/16/2023).

[43] Pankaj Chaudhary, Giuliana Milluzzo, et al. "Cellular irradiations with laser-driven carbon ions at ultra-high dose rates". In: *Physics in Medicine & Biology* 68 (Jan. 2023), p. 025015.

[44] Jake Atkinson, Eva Bezak, et al. “The current status of FLASH particle therapy: a systematic review”. eng. In: *Physical and Engineering Sciences in Medicine* 46.2 (June 2023), pp. 529–560.

[45] Donna Strickland and Gerard Mourou. “Compression of amplified chirped optical pulses”. In: *Opt. Commun* (1985), pp. 219–221.

[46] I. V. Yakovlev. “Stretchers and compressors for ultra-high power laser systems”. English. In: *Quantum Electronics (Woodbury, N.Y.)* 44.5 (2014), pp. 393–414. URL: http://inis.iaea.org/Search/search.aspx?orig_q=RN:46081353 (visited on 08/10/2019).

[47] Laurent Gallais and Jean-Yves Natoli. “Optimized metrology for laser-damage measurement: application to multiparameter study”. en. In: *Applied Optics* 42.6 (Feb. 2003), p. 960. URL: https://www.osapublishing.org/abstract.cfm?URI=ao-42-6-960 (visited on 09/09/2020).

[48] L. Gallais, J. Natoli, et al. “Statistical study of single and multiple pulse laser-induced damage in glasses”. en. In: *Optics Express* 10.25 (Dec. 2002), p. 1465. URL: https://www.osapublishing.org/oe/abstract.cfm?uri=oe-10-25-1465 (visited on 09/04/2020).

[49] Christoph Heyl, Cord Arnold, et al. “Introduction to macroscopic power scaling principles for high-order harmonic generation”. In: *Journal of Physics B: Atomic, Molecular and Optical Physics* 50 (Jan. 2017), p. 013001.

[50] A. Dubietis, G. Jonušauskas, et al. “Powerful femtosecond pulse generation by chirped and stretched pulse parametric amplification in BBO crystal”. en. In: *Optics Communications* 88.4 (Apr. 1992), pp. 437–440. URL: https://www.sciencedirect.com/science/article/pii/0030401892900708 (visited on 06/14/2023).

[51] R Dabu. *Lumina extrema. Lasere de mare putere - 2015*. URL: https://www.librariaeminescu.ro/ro/isbn/973-27-2561-0/Razvan-Dabu_-_Lumina-extrema-Lasere-de-mare-putere.html (visited on 09/27/2019).

[52] Razvan Dabu. “Femtosecond Laser Pulses Amplification in Crystals”. en. In: *Crystals* 9.7 (July 2019). Number: 7 Publisher: Multidisciplinary Digital Publishing Institute, p. 347. URL: https://www.mdpi.com/2073-4352/9/7/347 (visited on 06/19/2023).

[53] Razvan Dabu. “Optical Parametric Chirped Pulse Amplification at Critical Wavelength Degeneracy – a proposed solution for 100-PW Femtosecond Lasers Development”. en. In: *Frontiers in Optics* (2020), p. 2.

[54] Zhaoyang Li, Yuxin Leng, et al. “Further Development of the Short-Pulse Petawatt Laser: Trends, Technologies, and Bottlenecks”. en. In: *Laser & Photonics Reviews* n/a.n/a (). _eprint: https://onlinelibrary.wiley.com/doi/pdf/10.1002/lpor.202100705, p. 2100705. URL: https://onlinelibrary.wiley.com/doi/abs/10.1002/lpor.202100705 (visited on 10/31/2022).

[55] Hossein Fathi, Mikko Närhi, et al. “Towards Ultimate High-Power Scaling: Coherent Beam Combining of Fiber Lasers”. en. In: *Photonics* 8.12 (Dec. 2021). Number: 12 Publisher: Multidisciplinary Digital Publishing Institute, p. 566. URL: https://www.mdpi.com/2304-6732/8/12/566 (visited on 06/23/2023).

[56] Ihsan Fsaifes, Louis Daniault, et al. “Coherent beam combining of 61 femtosecond fiber amplifiers”. EN. In: *Optics Express* 28.14 (July 2020). Publisher: Optica Publishing Group, pp. 20152–20161. URL: https://opg.optica.org/oe/abstract.cfm?uri=oe-28-14-20152 (visited on 07/02/2023).

[57] Yi Cai, Zhenkuan Chen, et al. “The Development of the Temporal Measurements for Ultrashort Laser Pulses”. en. In: *Applied Sciences* 10.21 (Jan. 2020). Number: 21 Publisher: Multidisciplinary Digital Publishing Institute, p. 7401. URL: https://www.mdpi.com/2076-3417/10/21/7401 (visited on 07/02/2023).

[58] Ian A. Walmsley and Christophe Dorrer. “Characterization of ultrashort electromagnetic pulses”. EN. In: *Advances in Optics and Photonics* 1.2 (Apr. 2009). Publisher: Optica Publishing Group, pp. 308–437. URL: https://opg.optica.org/aop/abstract.cfm?uri=aop-1-2-308 (visited on 08/28/2023).

[59] Christophe Dorrer. “Spatiotemporal Metrology of Broadband Optical Pulses”. In: *IEEE Journal of Selected Topics in Quantum Electronics* 25.4 (July 2019). Conference Name: IEEE Journal of Selected Topics in Quantum Electronics, pp. 1–16.

[60] Colin Danson, David Hillier, et al. “Petawatt class lasers worldwide”. en. In: *High Power Laser Science and Engineering* 3 (Jan. 2015). Publisher: Cambridge University Press, e3. URL: https://www.cambridge.org/core/journals/high-power-laser-science-and-engineering/article/petawatt-class-lasers-worldwide/77B55882D24E72D26E233B691A8376D2 (visited on 06/09/2023).

[61] Colin N. Danson, Constantin Haefner, et al. “Petawatt and exawatt class lasers worldwide”. en. In: *High Power Laser Science and Engineering* 7 (Jan. 2019). Publisher: Cambridge University Press, e54. URL: https://www.cambridge.org/core/journals/high-power-laser-science-and-engineering/article/petawatt-and-exawatt-class-lasers-worldwide/D85E3F002CBFC286C08076E127BB5F5C (visited on 06/09/2023).

[62] Sterling Backus, Charles G. Durfee III, et al. “High power ultrafast lasers”. In: *Review of Scientific Instruments* 69.3 (Mar. 1998), pp. 1207–1223. URL: https://doi.org/10.1063/1.1148795 (visited on 06/09/2023).

[63] H. Y. Kim, M. Garg, et al. “Attosecond field emission”. In: *Nature* 613.7945 (Jan. 2023), pp. 662–666. URL: https://doi.org/10.1038/s41586-022-05577-1.

[64] M. D. Perry, D. Pennington, et al. “Petawatt laser pulses”. EN. In: *Optics Letters* 24.3 (Feb. 1999). Publisher: Optica Publishing Group, pp. 160–162. URL: https://opg.optica.org/ol/abstract.cfm?uri=ol-24-3-160 (visited on 06/21/2023).

[65] Daolong Tang, Jingui Ma, et al. “Temperature- and wavelength-insensitive parametric amplification enabled by noncollinear achromatic phase-matching”. en. In: *Scientific Reports* 6.1 (Oct. 2016). Number: 1 Publisher: Nature Publishing Group, p. 36059. URL: https://www.nature.com/articles/srep36059 (visited on 06/23/2023).

[66] Ding Wang and Yuxin Leng. “A method for aligning a femtosecond multi-petawatt coherent beam combining system”. en. In: *Applied Physics B* 127.3 (Feb. 2021), p. 41. URL: https://doi.org/10.1007/s00340-021-07589-7 (visited on 03/02/2021).

[67] M. Maier, W. Kaiser, et al. “Intense Light Bursts in the Stimulated Raman Effect”. In: *Physical Review Letters* 17.26 (Dec. 1966). Publisher: American Physical Society, pp. 1275–1277. URL: https://link.aps.org/doi/10.1103/PhysRevLett.17.1275 (visited on 06/22/2023).

[68] Daniel Ursescu. *Ultra-intense laser pulses and the High Power Laser System at Extreme Light Infrastructure – Nuclear Physics*. arXiv:2105.05494 [physics]. May 2021. URL: http://arxiv.org/abs/2105.05494 (visited on 06/22/2023).

[69] Christophe Radier, Olivier Chalus, et al. "10 PW peak power femtosecond laser pulses at ELI-NP". en. In: *High Power Laser Science and Engineering* 10 (2022). Publisher: Cambridge University Press. URL: https://www.cambridge.org/core/journals/high-power-laser-science-and-engineering/article/10-pw-peak-power-femtosecond-laser-pulses-at-elinp/7F68E8E791BE58DAD69566A9DD53A96B (visited on 07/12/2022).

[70] Greg R. Hays, Erhard W. Gaul, et al. "Broad-spectrum neodymium-doped laser glasses for high-energy chirped-pulse amplification". EN. In: *Applied Optics* 46.21 (July 2007). Publisher: Optica Publishing Group, pp. 4813–4819. URL: https://opg.optica.org/ao/abstract.cfm?uri=ao-46-21-4813 (visited on 06/30/2023).

[71] Aleksandr A. Voronin, Aleksei M. Zheltikov, et al. "Subexawatt few-cycle lightwave generation via multipetawatt pulse compression". en. In: *Optics Communications* 291 (Mar. 2013), pp. 299–303. URL: https://linkinghub.elsevier.com/retrieve/pii/S0030401812012230 (visited on 03/07/2022).

[72] N. M. Naumova, J. A. Nees, et al. "Relativistic Generation of Isolated Attosecond Pulses in a ${\ensuremath{\lambda}}^{3}$ Focal Volume". In: *Physical Review Letters* 92.6 (Feb. 2004). Publisher: American Physical Society, p. 063902. URL: https://link.aps.org/doi/10.1103/PhysRevLett.92.063902 (visited on 06/28/2023).

[73] C. P. J. Barty. "The Nexawatt: A Strategy for Exawatt Peak Power Lasers Based on NIF and NIF-like Beam Lines". In: *J. Phys.: Conf. Ser.* 717 (2016). Publisher: IOP Publishing. URL: https://cyberleninka.org/article/n/1401583 (visited on 04/18/2022).

[74] Zhaoyang Li and Junji Kawanaka. "Possible method for a single-cycle 100 petawatt laser with wide-angle non-collinear optical parametric chirped pulse amplification". EN. In: *OSA Continuum* 2.4 (Apr. 2019). Publisher: Optica Publishing Group, pp. 1125–1137. URL: https://opg.optica.org/osac/abstract.cfm?uri=osac-2-4-1125 (visited on 06/23/2023).

[75] Jun Liu, Xiong Shen, et al. "Multistep pulse compressor for 10s to 100s PW lasers". EN. In: *Optics Express* 29.11 (May 2021). Publisher: Optica Publishing Group, pp. 17140–17158. URL: https://opg.optica.org/oe/abstract.cfm?uri=oe-29-11-17140 (visited on 06/28/2023).

[76] Wang Xinliang, Xingyan Liu, et al. "13.4 fs, 0.1 Hz OPCPA Front End for the 100 PW-Class Laser Facility". In: *Ultrafast Science* 2022 (June 2022), pp. 1–8.

[77] Hao Xue, Meizhi Sun, et al. "High-Contrast Frontend for Petawatt-Scale Lasers Using an Optically Synchronized Picosecond Optical Parametric Chirped Pulse Amplification". en. In: *Photonics* 9.12 (Dec. 2022). Number: 12 Publisher: Multidisciplinary Digital Publishing Institute, p. 945. URL: https://www.mdpi.com/2304-6732/9/12/945 (visited on 06/23/2023).

[78] Min Sup Hur, Bernhard Ersfeld, et al. "Laser pulse compression by a density gradient plasma for exawatt to zettawatt lasers". en. In: (), p. 12.

[79] Yuxing Han, Zhaoyang Li, et al. "400nm ultra-broadband gratings for near-single-cycle 100 Petawatt lasers". en. In: *Nature Communications* 14.1 (June 2023). Number: 1 Publisher: Nature Publishing Group, p. 3632. URL: https://www.nature.com/articles/s41467-023-39164-3 (visited on 06/23/2023).

[80] K. D. Chesnut and C. P. J. Barty. "Ideal spatio-temporal pulse distribution for exawatt-scale lasers based on simultaneous chirped beam and chirped pulse amplification". EN. In: *Optics Express* 31.4 (Feb. 2023). Publisher: Optica Publishing Group, pp. 5687–5698. URL: https://opg.optica.org/oe/abstract.cfm?uri=oe-31-4-5687 (visited on 02/03/2023).

[81] Gerard Mourou. "Nobel Lecture: Extreme light physics and application". en. In: *Reviews of Modern Physics* 91.3 (July 2019), p. 030501. URL: https://link.aps.org/doi/10.1103/RevModPhys.91.030501 (visited on 10/31/2022).

[82] W. H. Knox, R. L. Fork, et al. "Optical pulse compression to 8 fs at a 5-kHz repetition rate". en. In: *Applied Physics Letters* 46.12 (June 1985), pp. 1120–1121. URL: https://pubs.aip.org/aip/apl/article/46/12/1120-1121/49468 (visited on 06/14/2023).

[83] R. H. Stolen and Chinlon Lin. "Self-phase-modulation in silica optical fibers". In: *Physical Review A* 17.4 (Apr. 1978), pp. 1448–1453. URL: https://link.aps.org/doi/10.1103/PhysRevA.17.1448 (visited on 09/27/2019).

[84] Xiaowei Song and Jingquan Lin. "Spectral broadening of femtosecond laser pulse through ionizing-gas-filled capillary". en. In: *Optik* 124.6 (Mar. 2013), pp. 501–504. URL: https://linkinghub.elsevier.com/retrieve/pii/S0030402612000605 (visited on 02/06/2019).

[85] S Yu Mironov, V N Ginzburg, et al. "Using self-phase modulation for temporal compression of intense femtosecond laser pulses". en. In: *Quantum Electronics* 47.7 (July 2017), pp. 614–619. URL: http://stacks.iop.org/1063-7818/47/i=7/a=614?key=crossref.05447f7085d35235d951af5ca02eabd4 (visited on 02/06/2019).

[86] Andrey Shaykin, Vladislav Ginzburg, et al. "Use of KDP crystal as a Kerr nonlinear medium for compressing PW laser pulses down to 10 fs". en. In: *High Power Laser Science and Engineering* 9 (2021). Publisher: Cambridge University Press, e54. URL: https://www.cambridge.org/core/journals/high-power-laser-science-and-engineering/article/use-of-kdp-crystal-as-a-kerr-nonlinear-medium-for-compressing-pw-laser-pulses-down-to-10-fs/47F400B9C1E38C4DA0B2BDAC33C6AE23 (visited on 01/04/2023).

[87] R. R. Alfano and S. L. Shapiro. "Observation of Self-Phase Modulation and Small-Scale Filaments in Crystals and Glasses". In: *Physical Review Letters* 24.11 (Mar. 1970), pp. 592–594. URL: https://link.aps.org/doi/10.1103/PhysRevLett.24.592 (visited on 08/10/2019).

[88] S Yu Mironov, J Wheeler, et al. "100 J-level pulse compression for peak power enhancement". en. In: *Quantum Electronics* 47.3 (Mar. 2017), pp. 173–178. URL: http://stacks.iop.org/1063-7818/47/i=3/a=173?key=crossref.bc537e9b520e19d80018dbb8797b98f9 (visited on 02/06/2019).

[89] D. M. Farinella, J. Wheeler, et al. "Focusability of laser pulses at petawatt transport intensities in thin-film compression". en. In: *Journal of the Optical Society of America B* 36.2 (Feb. 2019), A28. URL: https://www.osapublishing.org/abstract.cfm?URI=josab-36-2-A28 (visited on 01/29/2020).

[90] P.-G. Bleotu, J. Wheeler, et al. "Post-compression of high-energy, sub-picosecond laser pulses". en. In: *High Power Laser Science and Engineering* 11 (2023), e30. URL: https://www.cambridge.org/core/product/identifier/S2095471923000105/type/journal_article (visited on 05/02/2023).

[91] Daniel Ursescu, Dan Matei, et al. “First HPLS Experiments at ELI-NP: Spectral Broadening in Thin Films”. en. In: *Frontiers in Optics* (2020), p. 2.

[92] Marcus Seidel, Gunnar Arisholm, et al. “All solid-state spectral broadening: an average and peak power scalable method for compression of ultrashort pulses”. EN. In: *Optics Express* 24.9 (May 2016). Publisher: Optica Publishing Group, pp. 9412–9428. URL: https://opg.optica.org/oe/abstract.cfm?uri=oe-24-9-9412 (visited on 06/14/2023).

[93] John C. Travers, Wonkeun Chang, et al. “Ultrafast nonlinear optics in gas-filled hollow-core photonic crystal fibers [Invited]”. EN. In: *JOSA B* 28.12 (Dec. 2011). Publisher: Optica Publishing Group, A11–A26. URL: https://opg.optica.org/josab/abstract.cfm?uri=josab-28-12-A11 (visited on 06/14/2023).

[94] Erik Zeek, Kira Maginnis, et al. “Pulse compression by use of deformable mirrors”. EN. In: *Optics Letters* 24.7 (Apr. 1999). Publisher: Optical Society of America, pp. 493–495. URL: https://www.osapublishing.org/ol/abstract.cfm?uri=ol-24-7-493 (visited on 12/04/2020).

[95] Francisco Silva, Benjamín Alonso, et al. “Strategies for achieving intense single-cycle pulses with in-line post-compression setups”. EN. In: *Optics Letters* 43.2 (Jan. 2018). Publisher: Optica Publishing Group, pp. 337–340. URL: https://opg.optica.org/ol/abstract.cfm?uri=ol-43-2-337 (visited on 06/08/2023).

[96] Jun Liu, Xiaowei Chen, et al. “Spectrum reshaping and pulse self-compression in normally dispersive media with negatively chirped femtosecond pulses”. EN. In: *Optics Express* 14.2 (Jan. 2006). Publisher: Optica Publishing Group, pp. 979–987. URL: https://opg.optica.org/oe/abstract.cfm?uri=oe-14-2-979 (visited on 06/28/2023).

[97] Yitan Gao, Yabei Su, et al. “Generation of annular femtosecond few-cycle pulses by self-compression and spatial filtering in solid thin plates”. en. In: *Optics Express* 29.19 (Sept. 2021), p. 29789. URL: https://www.osapublishing.org/abstract.cfm?URI=oe-29-19-29789 (visited on 09/06/2021).

[98] Michaël Hemmer, Matthias Baudisch, et al. “Self-compression to sub-3-cycle duration of mid-infrared optical pulses in dielectrics”. EN. In: *Optics Express* 21.23 (Nov. 2013). Publisher: Optica Publishing Group, pp. 28095–28102. URL: https://opg.optica.org/oe/abstract.cfm?uri=oe-21-23-28095 (visited on 07/28/2023).

[99] Arohi Jain, Devki Nandan Gupta, et al. “Self-compression of a high-intensity laser pulse ina double-ionizing gas”. en. In: *Physics of Plasmas* (2022), p. 10.

CHAPTER 2

# Chapter 2 Dispersion and Self-Phase Modulation

In the previous chapter, I conducted an examination of the current state of the world's most significant lasers, shedding light on the potential of Exawatt-class lasers. Among the critical parameters, spectral broadening and post-compression emerge as effective strategies for enhancing the peak power of existing high power laser systems.
To delve deeper into spectral broadening, in this chapter, I presented an elaborate theoretical study of the underlying phenomena, which includes dispersion, self-phase modulation (SPM), the B-integral, and the nonlinear refractive index. These phenomena are intricately linked to the materials employed and the input laser parameters.
Therefore, throughout this chapter, I delved into the theory of SPM, investigated the dispersion contributors, and scrutinized various techniques for quantifying nonlinear effects.

## 2.1 Dispersion of optical laser pulses

The pulse duration is retrieved using the Fourier transform (FT) functions derived by Joseph Fourier for signals. The Fourier transform of signals in time domain, $t$, to their spectral components, $\omega$, can be performed with the following relations from Ref. [1]:

$$F(\omega) = \frac{1}{2\pi} \int_{-\infty}^{\infty} f(t) e^{-j\omega t} dt \tag{2.1}$$

The inverse Fourier transformation (IFT) extracts the signal, in time, out of the spectrum:

$$f(t) = \int_{-\infty}^{\infty} F(\omega) e^{j\omega t} d\omega \tag{2.2}$$

The easiest way to model signals is to consider a Gaussian profile, based on the general statement that a Fourier transform of a Gaussian signal has a Gaussian shape too. Considering a Gaussian signal with pulse duration $\tau_p$:

$$f(t) = e^{-\frac{t^2}{2\tau_p^2}}, \tag{2.3}$$

and using the Fourier transform (FT) formula of eq. 2.1 the signal in the spectral domain is given by:

$$F(\omega) = \frac{\tau_p}{\sqrt{2\pi}} e^{-\frac{\omega^2 \tau_p^2}{2}} \tag{2.4}$$

Thus, the spectral width scales with the inverse of the time duration $\tau_p$. The relation between the spectral FWHM ($\triangle\omega$) and the FWHM of the time duration ($\triangle t$) can easily be calculated as follows:

$$\Delta t = 2\tau_p \sqrt{\ln 2} \Delta\omega = 2\frac{\sqrt{\ln 2}}{\tau_p} \tag{2.5}$$

Multiplication of these FWHM gives the relation between the spectral width and the time duration of Gaussian shaped signals:

$$\triangle\omega \cdot \Delta t = 4 \ln 2 \tag{2.6}$$

After generating an ultra-short pulse, it becomes critically important to preserve the spectral phase relation. Disruptions in the spectral phase can lead to changes in the pulse duration. For example, when light goes through a dispersive medium like glass, the red spectral components move faster than the blue ones. Consequently, the pulse becomes elongated, with different spectral components reaching the detector at distinct moments. This temporal separation of spectral components is referred to as "chirp." The term "chirp" draws an analogy from the melodious notes of a bird's song, wherein many birds produce a sequence of tones within a single call, progressing from low to high tones. The simplest way to introduce chirp in a laser pulse is by passing the pulse through transparent materials, such as glass.

Optical materials introduce a complex spectral phase ($\phi_{\text{mat}}(\lambda)$), due to their wavelength ($\lambda$) dependency of the refractive index ($n(\lambda)$). This spectral phase is proportional with the length of the material ($l_{\text{mat}}$) as:

$$\phi_{\text{mat}}(\lambda) = \frac{2\pi n(\lambda) l_{mat}}{\lambda} \tag{2.7}$$

When considering that linear spectral phase disturbances do not affect the pulse duration, it becomes difficult to identify the particular spectral phase disruptions that can adversely alter the pulse's shape. Therefore, it is preferable to begin with an initial pulse in the time domain and explore how its shape changes after passing through a dispersive system. Any arbitrary pulse in the time domain can be expressed as follows:

$$E(t) = \xi(t)e^{i[\omega_0 t+\sigma(t)]} \tag{2.8}$$

Here the slowly varying envelope is $\xi(t)$ and the central carrier frequency is $\omega_0$, while the $\sigma(t)$ is the temporal phase. In case of a Gaussian pulse where $\xi(t) = \xi_0 e^{-\left(t^2/\tau^2\right)}$ and $\sigma(t) = 0$, the expression for the input pulse changes to:

$$E(t) = \xi_0 e^{-\left(t^2/\tau^2\right)} e^{i\omega_0 t} \tag{2.9}$$

The FT of a Gaussian pulse provides the amplitude and phase in frequency domain as,

$$G(\omega) = \int_{-\infty}^{\infty} E(t)e^{-i\omega t}dt = g(\omega)e^{i\eta(\omega)} \tag{2.10}$$

where $g(\omega)$ and $\eta(\omega)$ are the spectral amplitude and phase, respectively. The output in the spectral domain can be written as:

$$G'(\omega) = G(\omega)S(\omega) = g(\omega)s(\omega)e^{i[\eta(\omega)+\phi(\omega)]} \tag{2.11}$$

In this context, the complex transfer function $S(\omega)$ encompasses both the spectral transfer function ($s(\omega)$) and the system's contribution of spectral phase ($\phi(\omega)$). The primary focus lies on the spectral phase contribution ($\phi(\omega)$) due to its substantial impact on the resulting pulse shape in the time domain once the system's output is considered. The spectral transfer function ($s(\omega)$) characterizes the spectral amplification or attenuation within the system. Notably, the term $s(\omega)$ doesn't influence the spectral phase relationship. Therefore, when designing a dispersion-free system, this aspect is not taken into consideration. The temporal configuration of the pulse, denoted as $E'(t)$ after passing through the system, can then be determined using the inverse Fourier transform:

$$E'(t) = \frac{1}{2\pi}\int_{-\infty}^{\infty} G'(\omega)e^{i\omega t}d\omega \tag{2.12}$$

It is important to note that once a dispersion-free system is established, the output pulse retains the same shape as the input pulse.

The nature of this spectral phase disturbance is contingent upon the refractive indices of the utilized materials. These material attributes are intricate functions of wavelength, presenting a high degree of complexity. To manage this complexity, a Taylor expansion can be employed for the spectral phase. While this approach impacts calculation precision, it effectively reduces the intricacy to a manageable extent. Endeavors to bypass this simplification have yielded formulations that prove excessively intricate for analytical or computational solutions, such as with software tools like Python, PYNLO. Fortunately, the accuracy achieved through the Taylor approximation is satisfactory for the purpose of optimizing the setup to minimize dispersion. The subsequent expression showcases the Taylor series representation of the spectral phase:

$$\phi(\omega) = \phi(\omega_0) + \phi'(\omega_0)(\omega-\omega_0) + \frac{1}{2}\phi''(\omega_0)(\omega-\omega_0)^2 + \frac{1}{6}\phi'''(\omega_0)(\omega-\omega_0)^3 + \dots \tag{2.13}$$

The primary focus is on investigating the distortion of the light pulse within the temporal domain. The key disruption in this context involves specific spectral components advancing more rapidly through a medium, leading to an increase of the pulse duration. Consequently, our primary concern revolves around the time it takes for these spectral components to pass through the medium. The phase shift induced by the material is given by:

$$\phi(\omega) = \frac{L_{mat} n(\omega)}{c} \cdot \omega \tag{2.14}$$

where the travel time through the optical medium is $T(\omega) = \frac{L_{\mathrm{m}}\, n(\omega)}{c}$. The transit time through a dispersive medium becomes:

$$T(\omega) = \frac{\delta\phi(\omega)}{\delta\omega} \tag{2.15}$$

The transit time of a quasi monochromatic wave can be written as:

$$T(\omega) = \frac{\delta\phi(\omega)}{\delta\omega} = \phi'(\omega_0) + \phi''(\omega_0)(\omega - \omega_0) + \frac{1}{2}\phi'''(\omega_0)(\omega - \omega_0)^2 + \dots \tag{2.16}$$

The derivatives of the spectral phase with respect to frequency: $\phi', \phi''$ and $\phi'''$ are known as the group delay dispersion (GDD), group velocity dispersion (GVD), third order dispersion (TOD), etc. The linear element of the spectral phase (first order) only introduces a delay in time. However, the higher-order components introduce distinct travel durations for various spectral elements centered around the central frequency. This phenomenon causes the dispersal of the pulse power within the temporal domain. In cases where a Gaussian-shaped pulse lacks GVD and higher-order dispersion, it earns the label of "Fourier transform limited". This designation stems from the fact that the IFT of the Gaussian pulse yields an output that mirrors the initial pulse's shape, indicating a lack of distortion.

## 2.2 Dispersion management

In the realm of high-power laser systems, which serves as the foundation for this research, a pivotal challenge arises: the necessity to manage dispersion in order to achieve ultrashort laser pulse durations while maintaining a consistent spectral phase across a wide range of frequencies. To accomplish this goal, it is important to compensate the dispersion introduced by materials and stretcher, by utilizing the compressor's dispersion. This approach enables the generation of laser pulses with durations approaching the Fourier limit, representing an ideal scenario. However, achieving this desired outcome, especially for femtosecond-range pulses with high energy, presents challenges due to the intricate task of compensating for the diverse dispersion factors introduced by individual components.

Spectral manipulation plays a crucial role in adjusting the pulse duration within the amplification chain, optimizing energy amplification without compromising the integrity of optical elements. The compressed pulse can subsequently reach its minimal duration, striking a balance between energy amplification and temporal confinement.

Dispersion management systems (DMS) prove invaluable in assessing and counteracting dispersion effects encountered when passing through materials with pronounced dispersion properties, such as various types of glass (FS, BK7), Ti:Sapphire, $TeO_2$, or Terbium Gallium Garnet (TGG). In the following sections, my focus will be on a comprehensive analysis of the significant terms within this expansion, particularly delving into the second to fourth orders of dispersion.

While contemporary stretchers and diffraction grating compressors offer the ability to finely control the spectral phase up to the third order, residual spectral phase remains

uncompensated. This residual phase can lead to sub-optimal pulse durations that exceed the theoretical limit prescribed by the Fourier principle. Additionally, it might introduce intensity peaks, commonly referred to as pre-pulses, thereby influencing the interaction between the laser and its target in experimental setups. Consequently, precise calculation and compensation for this residual phase constitute primary objectives of this study.

A Fourier-limited pulse duration is achieved when all dispersion orders are compensated, and the final spectral phase is set to zero. This study provides an in-depth analysis of high-order dispersion and how to control dispersion orders and spectral phase.

For a CPA laser system, the following relation holds for perfect dispersion compensation to retrieve a FTL (Fourier Transform Limited) laser pulse:

$$\phi^n_{materials}(\omega) + \phi^n_{stretcher}(\omega) + \phi^n_{amplifier}(\omega) + \phi^n_{compressor}(\omega) = 0 \tag{2.17}$$

n= 0, 1, 2...- represent the order of dispersion for materials, stretcher, amplification medium and compressor.

When post-compression is introduced, at least two new dispersion contribution factors, denoted as materials2 and chirped mirrors (CM), need to be incorporated into the previous equations. The term *materials2* refers to the optical material selected for spectral broadening.

$$\phi^n_{materials}(\omega) + \phi^n_{stretcher}(\omega) + \phi^n_{amplifier}(\omega) + \phi^n_{compressor}(\omega) + \phi^n_{materials2}(\omega) + \phi^n_{CM}(\omega) = 0 \tag{2.18}$$

To elevate the capacity for correcting spectral phase within the ultra-short laser systems, innovative components such as GRISM [2], Chirped Mirrors [3] and devices like the Dazzler have been effectively integrated into various facilities.

While these advancements offer the advantage of fine-tuning for low-order dispersion, they exhibit limitations when addressing higher dispersion orders, specifically those beyond the fourth. These limitations arise from the interaction length of light within the devices and the optical components, resulting in a constrained dynamic range.

Therefore, I will provide a short overview of the control (within Carrier Envelope Phase (CEP)) as well as the sources of significant high order of dispersion, including optical materials, stretchers, compressors, prisms, and Chirped mirrors. These elements are typically encountered within a CPA laser system.

### 2.2.1 Carrier Envelope Phase (CEP)

A stable solution for the fine-tuning applied to low energy lasers class is related to CEP stabilization which allows for single cycle regime by carefully controlling the high orders of dispersion and phase.

In short, the electric field of a laser pulse can be conceptualized as a sinusoidal oscillation referred to as the carrier, which is modulated by a slowly evolving envelope function. As this pulse traverses a medium, alterations in the relative alignment between the carrier wave and envelope may occur due to chromatic dispersion and optical nonlinearities. Consequently, a disparity arises between the phase velocity and the group velocity. This discrepancy gives rise to the carrier-envelope offset (CEO) phase, alternatively termed as the carrier-envelope phase (CEP). Specifically, the CEO phase is quantified as the distinction between the optical phase of the carrier wave and the position of the envelope.

The carrier-envelope offset frequency can be detected through methods like utilizing an interferometer. This involves creating a beat note between the higher-frequency extremity of the comb spectrum and the frequency-doubled lower-frequency extremity. This

technique proves effective when the optical spectrum encompasses an entire octave of frequencies.

The carrier-envelope phase plays a pivotal role in shaping the accuracy of endeavors involving high-energy and attosecond experiments, along with ultrafast spectroscopy measurements.

Companies like FASTLITE, Menlo Systems, and Sphere manufacture phase stabilization devices of this kind. While these devices exhibit significant advancements in low-energy laser systems, there are overarching limitations when employed in high-power laser systems. In such systems, where the pulse duration (20-30 fs, for PW class) is not solely contingent on the Carrier-Envelope Phase (CEP), and another issue arises concerning the damage threshold of the measuring equipment. The incorporation of CEP in High-Power Laser Systems (HPLS) will be explored in the final chapter of this thesis, where enhancements to post-compression will also be addressed.

### 2.2.2 Dispersion of the materials

Higher-order phase dispersion for various materials can be determined by differentiating the Sellmeier equations, which are available at *www.refractiveindex.info*. This formula will be utilized in the subsequent chapters to calculate the Group Delay Dispersion (GDD), Third Order Dispersion (TOD), and Fourth Order Dispersion (FOD) of the optical materials employed in our experiments.

The phase introduced by the optical materials is expressed as follows:

$$\phi_{mat}(\lambda) = \frac{2\pi n(\lambda) L_{mat}}{\lambda} \tag{2.19}$$

Deriving this equation as a function of the refractive index $n$, dependent of $\lambda$, the high order phase equations were retrieved:

$$\frac{d^2\phi}{d\omega^2} = \phi^2(\omega) = \frac{\lambda^3 n^{(2)} L_{mat}}{2\pi c^2}(fs^2) \tag{2.20}$$

$$\frac{d^3\phi}{d\omega^3} = \phi^3(\omega) = \frac{-\lambda^4[3n^{(2)}L_{mat}] + \lambda n^{(3)} L_{mat}}{4\pi^2 c^3}(fs^3) \tag{2.21}$$

$$\frac{d^4\phi}{d\omega^4} = \phi^4(\omega) = \frac{\lambda^5[12n^{(2)}L_{mat}] + 8\lambda n^{(3)} L_{mat} + \lambda^2 n^{(4)} L_{mat}}{8\pi^3 c^4}(fs^4) \tag{2.22}$$

where $n(\lambda)$ is the refractive index, $n^{(i)}$ is the order of the derivative with i= 2, 3, 4, ... and $L_{mat}$ is the length of the material.

The cumulative phase introduced by the optical materials is relatively low compared to the phase introduced by the stretcher and compressor. The primary determinants for this phase are the refractive index of the material and the length of the material. The materials that contribute to a higher magnitude of dispersion and phase include the amplification material, Ti:Sapphire, Faraday rotators like Terbium Gallium Garnet (TGG), Pockels cells such as Dideuterium Phosphate (DKDP), and acousto-optic modulators, specifically $TeO_2$. This is because their accumulated path length results from multiple passes through the optical components, leading to a more significant overall phase contribution.

### 2.2.3 Dispersion in stretchers and compressors

In an ideal Chirped Pulse Amplification laser system, the GDD of the stretcher, materials, and of the amplifier should be perfectly matched by the GDD and TOD of the

compressor. However, in real-world CPA laser systems, the dispersion of the compressor never exactly matches the dispersion of the preceding components. Consequently, extensive efforts have been dedicated to designing complex stretcher-amplifier-compressor systems with a net dispersion very close to zero. Additionally, to achieve perfect spectral bandwidth enlargement and compression, components such as acousto-optic modulators and different stretcher-compressor designs with low aberrations have been introduced into laser systems. Alongside factors like the separation between gratings and incident angles, another critical parameter is the groove density.

Gratings are manufactured with a specific groove/line density, typically measured in grooves per millimeter (gr/mm), and this parameter plays a crucial role in controlling the dispersion of light. In general, higher groove densities lead to improved spectral resolution.

Therefore, when considering these three critical factors—incidence angle, distance, and groove density—you can calculate the phase terms by evaluating the distance traveled by the central wavelength ($\lambda_{central}$) according to the grating law:

$$sin(\theta) + sin(i) = \frac{p\lambda}{d} \tag{2.23}$$

$$\phi_{comp}(\omega) = 2 * \left( \frac{\omega g}{c} + \frac{\omega L_R * cos(\theta(\omega))}{c} \right) \tag{2.24}$$

where $\phi_{comp}(\omega)$ is the phase accumulated after 1 pass through the gratings. By using the Taylor expansion around $\omega_0$ the higher order phase can be expressed as:

$$\phi^2_{comp}(\omega) = -\frac{8\pi^2 c L_{comp}}{\omega_0^3 d^2 * cos^2(\theta(\omega_0))} \tag{2.25}$$

$$\phi^3_{comp}(\omega) = -\frac{3}{\omega_0} \left( 1 - \frac{2\pi c * sin(\theta(\omega_0))}{\omega_0 d * cos^2(\theta(\omega_0))} \right) * \phi^2_{comp}(\omega) \tag{2.26}$$

Here: $i$ and $\theta$ are the angle of incidence and the angle of diffraction at wavelength $\lambda$, $p$ is the diffraction order (-1 for this case), $d$ is the spacing of the grating spacing with the observation that (line density: N = 1 / d ), $L_R$ is the perpendicular distance between the two gratings, $L_{comp}$ the distance between the gratings for the central wavelength and $c$ is the speed of the light.

These terms need to be optimized to compensate as effectively as possible for the corresponding terms of the input stretched pulse phase. The same equations apply to the stretcher based on two anti-parallel gratings, but with a "-1" multiplier on each term due to negative magnification.

For a comprehensive description of optical pulse compression using diffraction gratings, detailed information can be found in Reference [4] since 1969, and this concept has also served as the basis for the Chirped Pulse Amplification (CPA) method, as outlined in Reference [5].

### 2.2.4 Dispersion introduced by DAZZLER

An important component within high-power laser systems is the DAZZLER, a programmable acoustic-optical dispersive (AODPF) filter. This innovative device enables precise modeling of arbitrary phase and amplitude profiles by leveraging an acoustic wave's interaction with an optical wave. The spectral amplitude of the diffraction impedance undergoes modulation based on the strength of the acoustic signal within the crystal.

This crystal type exhibits a dual behavior with fast ordinary and slow extraordinary axes, allowing different wavelengths to experience time delays contingent on the input

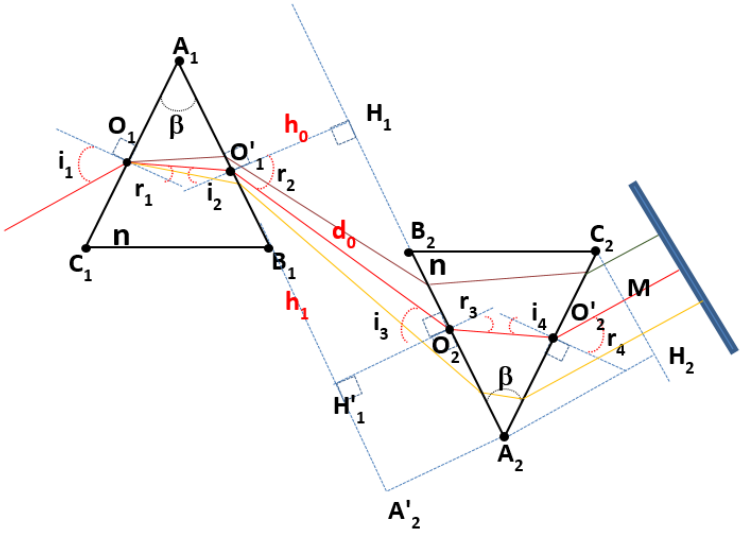


Figure 2.1: Geometrical optical path for 3 different wavelengths (colors) in prism

acoustic signal. Despite the ability of oscillators to generate Fourier pulses of limited duration (5-10 fs) subsequent to traversing the amplifier environment, which narrows the gain spectral band, it is important to note that the peripheral wavelengths would not undergo amplification to the same extent as the central wavelengths.

The initiation of the acoustic wave within the crystal transpires through a piezoelectric transducer, enabling fine corrections through controlled dispersion up to the fourth order, all stemming from its interface. These DAZZLER devices are supplied in a comprehensive package, incorporating a user-friendly graphical interface. This interface empowers users to define the spectral shape of the acoustic wave, introducing a Gaussian "hole" within a spectrum characterized by a super Gaussian profile defined by specific parameters such as depth, width, and position.

By inputting solely the values corresponding to the central wavelength within the interface, it becomes possible to estimate the complete phase using a Taylor expansion approach.

### 2.2.5 Dispersion introduced by prisms

Prism combinations offer the advantage of introducing controlled dispersion up to the 5th order, and they can also be used to compensate for dispersion introduced by other materials or in stretcher/compressor setups.

The key parameters of this system include:

**Incidence Angle (i)**: This angle allows fine-tuning of the 4th and 5th orders of dispersion.

**Entry Position (p)**: This parameter refers to the relative position of entry, denoted as "O1" in Figure 2.1, within the prism.

**Distance (d)**: The distance between the prisms, which influences the modification of the 4th order of dispersion.

Additionally, other prism parameters to consider are the angle of the prism (apex) and the material they are made of.

To calculate the phase introduced by a pair of prisms, it's important to estimate the optical path length for each wavelength. By considering the optical path length for each wavelength, the number of passes through a single prism or the number of prisms ($nr_{prisms}$) the final thickness $L_{prism}$ can be calculated as follows:

$$L_{prism}(\lambda) = nr_{prisms} * 2 * [n(\lambda)(O_1O_1' + O_2O_2') + O_1'O_2 + O_2'M] \tag{2.27}$$

$$\phi_{prism}(\lambda) = \frac{2\pi L_{prism}}{\lambda} \tag{2.28}$$

By deriving Eq.2.28 with respect to $\omega$ the higher order phase were retrieved. The global phase introduced by a pair of prisms is obtained by implementing the $\phi_{prism}$ in Eq. 2.16.

**Some remarks related to the using of prism:** At high intensities, nonlinear effects in the material become significant, with the critical point being the last pass through the prism. This phenomenon can introduce nonlinear changes in the optical properties of the material.

Fine-tuning of the overall dispersion is achievable due to the opposite sign of material dispersion, which can help in optimizing the dispersion compensation.

The GDD is typically negative in this setup, resulting from the combination of angular dispersion (which is negative) and the prism material's positive dispersion, particularly in the visible and near-infrared (NIR) spectrum.

After the first pass through the prism, the wavelengths will be dispersed, whereas after the second pass, the rays will exit the prism in a parallel fashion. This parallel exit minimizes spatial separation between different spectral components.

To minimize reflection losses in a prism compressor, it is advisable to use an apex angle ($\beta$) such that when the incident angle reaches the first surface at Brewster s angle, the refracted ray at the central wavelength ($\lambda_{central}$) exits the second surface at the same angle. This alignment reduces the reflection losses at the prism surfaces.

### 2.2.6 Dispersion introduced by Chirped Mirrors

Chirped mirrors (CMs) have emerged as a transformative technology in the field of laser optics, enabling the compression of high-power laser pulses to durations in the sub-femtosecond range. In this section, I will briefly address the challenges associated with chirped mirror design, manufacturing, and alignment, as well as highlight current trends and potential future developments in this field.

Chirped mirrors are a revolutionary technology that achieves pulse compression by manipulating the spectral phase of laser pulses. The initial reports on the design and implementation of chirped mirrors can be found in references such as [3] and [6]. Since their inception, they have been widely used to compress ultra-short laser pulses, as discussed in Chapter 1, and have found applications in ultrafast laser spectroscopy, laser micro-machining, high harmonics generation, and more.

Chirped mirrors belong to the category of dispersive optics designed to introduce controlled variations in the group delay of different frequency components within a laser pulse. This variation leads to spectral broadening, which can be compensated for using a complementary dispersive element. When properly designed, chirped mirrors can achieve negative dispersion, enabling the recompression of the pulse. The fundamental principle behind chirped mirror technology is the generation of a linear chirp in the laser pulse, reflecting the variation in frequency or wavelength over time.

Chirped mirrors offer several advantages over traditional pulse compression techniques, such as grating pairs or prism pairs:

- Compactness - they are more compact and mechanically more stable compared to bulk grating compressors

- Dispersion control - offer precise control over the spectral phase of the pulse, allowing for fine-tuning of the compression process.
- Broadband compression - can handle broad spectral bandwidths (>200 nm), enabling the compression of complex laser spectra
- Customizable dispersion - they present tunable dispersion, enabling flexibility for various applications.

Indeed, chirped mirrors offer significant advantages in pulse compression; however, they do come with their own set of challenges, particularly when dealing with low-energy laser pulses. Here are a few challenges specific to low-energy laser pulses:

- Dispersion Management: Designing chirped mirrors with precise dispersion profiles over a wide bandwidth is challenging and requires advanced modeling techniques.
- Alignment: Proper alignment of chirped mirror setups is critical to achieve optimal compression. Stability and sensitivity to misalignment are factors that must be carefully managed.
- Incidence angle (AOI): In general, they work in pair at low incidence angle ($< 11°$) which can imply limitations of space in the interaction chamber. Novel designs includes AOI of 45°.
- Size: At the moment, maximum size is limited at 10", which do not favor the compression of 10 PW scale laser pulses, full aperture.
- Laser Induced Damage Threshold: They are limited, in mean value, at 0.25 J/cm$^2$ [7].
- Nonlinear Absorption in the layers: recently, this problem has been reported [8] but not completely studied.

Advanced multi-layer coating designs are being explored to achieve better control over dispersion and to address limitations in single-layer designs [9]. Up to now, CM can be used to introduce positive or negative GDD and TOD for a broadband spectrum from UV to Mid-IR.

### 2.2.7 Dispersion orders

The comprehensive description of these derivatives for materials, stretchers, and compressors, along with their effects, can be found in the third chapter titled "Effets des différents ordres de dispersion / The effects of different dispersion orders" in Gilles Cheriaux's PhD thesis [10]. In this chapter, the author begins with the Taylor series and derives equations that describe the electric field, temporal characteristics, and provides clear graphical representations of each dispersion order. Different materials are characterized in terms of their dispersion properties, and detailed tables containing their dispersion values are presented.

The zeroth-order phase remains constant in both the temporal and spectral domains and is typically referred to as the absolute phase. It represents the relative phase of the carrier wave with respect to the pulse envelope.

First-order effects result in linear shifts in time or frequency, which can be measured using a spectrometer. It is important to note that these first-order shifts do not impact

the pulse duration; The second-order and higher-order effects that significantly shape the pulse's temporal profile.

The second-order effect introduces positive or negative chirp, indicating frequency modulation acquired as the pulse passes through a medium. This establishes the relationship between frequency and time.

$$\tau_{out} = \tau_{in}\sqrt{1 + \left(\frac{4 * ln(2) * GDD}{\tau_{in}^2}\right)^2} \tag{2.29}$$

The pulse duration can be deduced from this order if the Group Delay Dispersion (GDD) is the primary or sole contributor (see Eq. 2.29). This analysis also requires a Gaussian spectral/temporal profile as input.

When traversing a medium with third-order dispersion, the pulse's temporal shape deviates from Gaussian. The term $\phi^{(3)}$ $(\omega_0)$ primarily imparts pulse asymmetry, leading to post-pulses (positive $\phi^{(3)}$) or pre-pulses (negative $\phi^{(3)}$). While the Full Width at Half Maximum (FWHM) is minimally affected by this dispersion, intensity redistributes towards the pulse's edges. Skillfully selecting third-order signs allows for concentrating residual energy within pre/post-pulses. These subsidiary pulses can attain ample intensity to generate plasma during target interactions. Consequently, the primary pulse's energy deposits into the plasma rather than the target. The pre-pulses' intensities, relative to the main pulse, hinge on third-order characteristics and duration. Such pre-pulses can be advantageous in applications requiring plasma creation for ions, electrons, protons, etc., which subsequently get accelerated by the primary pulse.

Fourth-order dispersion essentially acts as a pedestal on the pulse's temporal profile and modestly increases pulse duration. An autocorrelation between two pulses exhibiting this dispersion showcases a disruption in the gradient, evident on the display. This order's spectral phase impact resembles second-order dispersion, albeit with minor differences.

Fifth-order effects yield effects on pulse profiles akin to third-order dispersion, including pre-pulse/post-pulse emergence. Its influence on pulse duration is generally negligible for low-power lasers but becomes significant at the Terawatt (TW) and Petawatt (PW) power levels.

In conclusion, fourth and fifth-order dispersion primarily affect pulse contrast and energy distribution outside the main pulse envelope. However, compensating for dispersion-induced phase changes involves introducing phase shifts of opposing signs from another same-parity order (positive fourth-order offsets negative second-order, and third-order counters fifth-order). The GDD and TOD terms are adjustable via the compressor/stretcher's two degrees of freedom: grating distance and angle of incidence.

An interesting study showed that it is also possible to achieve near-transform-limited pulses without the traditional approach of zeroing out successive orders of dispersion by balancing higher-order dispersion terms against one another [11]. The grating mismatch makes it possible to use an aberration-free stretcher design to compensate for large material path lengths. Previously, the difficulty with such high groove density gratings has been the tight alignment tolerances that are due to their highly dispersive nature.

The minimum pulse width actually occurs when the $2^{nd}$ order GDD is nonzero. This is based on the fact that small amounts of $2^{nd}$ order group-delay dispersion correct for residual 4th order dispersion. The net result is a shorter pulse width, but a slight asymmetry in the pulse intensity, as the new grating spacing has left residual third-order dispersion.

| High order spectral phase | | | |
|---|---|---|---|
| $\phi^{(2)}(\omega_0)$ | $\phi^{(3)}(\omega_0)$ | $\phi^{(4)}(\omega_0)$ | $\phi^{(5)}(\omega_0)$ |
| $\phi^{(2)}_s(\omega) < 0$ | $\phi^{(3)}_s(\omega) < 0$ | $\phi^{(4)}_s(\omega) > 0$ | $\phi^{(5)}_s(\omega) < 0$ |
| $\phi^{(2)}_m(\omega) > 0$ | $\phi^{(3)}_m(\omega) > 0$ | $\phi^{(4)}_m(\omega) < 0 \; or > 0$ | $\phi^{(5)}_m(\omega) > 0$ |
| $\phi^{(2)}_p(\omega) < 0 \; or > 0$ | $\phi^{(3)}_p(\omega) < 0 \; or > 0$ | $\phi^{(4)}_p(\omega) < 0 \; or > 0$ | $\phi^{(5)}_p(\omega) < 0 \; or > 0$ |
| $\phi^{(2)}_c(\omega) < 0$ | $\phi^{(3)}_c(\omega) > 0$ | $\phi^{(4)}_c(\omega) < 0$ | $\phi^{(5)}_c(\omega) > 0$ |
| $\phi^{(2)}_{CM}(\omega) < 0 \; or > 0$ | $\phi^{(3)}_{CM}(\omega) < 0 \; or > 0$ | - | - |

Figure 2.2: Dispersion orders sign for s-stretcher, m-materials, p-prisms,c-compressor, and CM-chirped mirrors

### 2.2.8 Discussions and personal contribution

The SPM theory was implemented in a programming code to simulate the propagation of laser pulses through various materials and analyze their effects on the temporal and spectral aspects of the pulses. These simulations, which also incorporated the nonlinear refractive index $n_2$, were utilized in Chapter Four to estimate the observed broadening in experiments conducted at facilities like ELI-NP (two experimental campaigns), LASERIX, and APOLLON.

The outcomes related to dispersion from this chapter were used to develop a Python code capable of extracting up to the fifth order of dispersion and spectral phase for a predefined list of materials. This list covers 12 materials commonly employed in large CPA (Chirped Pulse Amplification) systems, including Fused silica (FS), BK7, MgF2, CaF2, SF11, SF57, TGG, Al2O3 (Ti:Sapphire), DKDP, $TeO_2$, with variations for their two orientations on the ordinary and extraordinary axes. The dispersion signs associated with each of these optical components are presented in Figure 2.2.

#### 2.2.8.1 Applications of prism compressor

Combining negative dispersion resulting from wavelength-dependent refraction in a pair of prisms with positive material dispersion has proven effective and convenient as a method for managing overall Group Delay Dispersion. An advancement in prism utilization was reported in the paper [12], demonstrating that ultra-short laser pulses can be compressed using a single prism with four passes through it.

The code I developed was used to simulate the dispersion introduced by the windows and leakage mirrors in High-Power Laser Systems (HPLS) and to pre-compensate for the dispersion introduced in a misaligned oscillator. These preliminary results provide a solution to a real HPLS issue, specifically the measurement of laser pulse duration in both the experimental area and the diagnostics bench simultaneously.

When passing through these optics (leakage mirrors, windows), the laser pulse accumulates positive dispersion. To maintain the same duration in the experimental area, the same material with the same thickness as the sampling optics should be added (e.g., after the stretcher) in the laser pulse path. Depending on the peak irradiance, the thickness of the windows increases, leading to a significant increase in pulse duration. This can reduce the possibility of accurately measuring the pulse duration (e.g., WIZZLER can measure pulses with durations less than two times its Fourier limit (FL)). This addition of material

| Power | Thickness (mm) | | *GDD* $\Phi^2(\lambda)$ $(fs^2)$ | *TOD* $\Phi^3(\lambda)$ $(fs^3)$ | Output pulse duration (fs) *FL=25 fs* |
|---|---|---|---|---|---|
| | Window | Leakage mirror | | | |
| **100 TW** | 15 (Silica) | 20 @45° (BK7/Silica) | 1565 | 1190 | **> 160** |
| **1 PW** | 40 (BK7) | 60 @45° (FS) | 4748 | 3659 | **> 490** |
| **10 PW** | 65 (FS) | 80 @45° (Silica) | 6298 | 4960 | **> 650** |

Figure 2.3: GDD and TOD values calculation for retrieving the pulse duration on both experiment area and diagnostic bench at the same time

helps to determine the duration in the experimental area but at the cost of a longer duration on the diagnostic bench (see Figure 2.3, last column). This introduced GDD is then subtracted in the laser front-end to ensure the correct measurement of the laser pulse on the diagnostic bench.

The final retrieved temporal shape demonstrates the capability to simultaneously measure the pulse duration in the experimental area.

To prove the capability of on-shot measurement, a prism compressor with four passes was designed (Fig. 2.4). By varying the setup parameters ($\alpha$, p, d), I can introduce different quantities of negative dispersion (negative GDD and TOD) to obtain a pulse duration close to its FL.

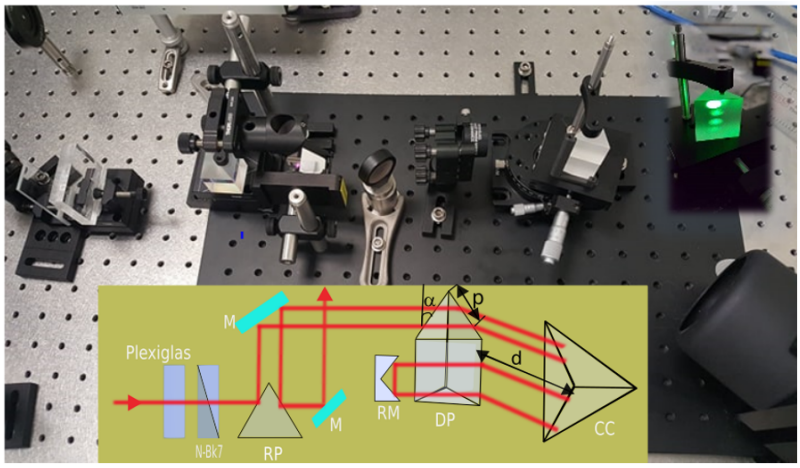


Figure 2.4: Single prism compressor setup, Inset - the four passes through the prism using a green laser

To test the capability of the setup, an ultra-short laser pulse (Avesta Oscillator) was stretched from 24.5 fs to 172 fs and re-compressed to 25.6 fs using the following parameters: angle of incidence 50.8°, insertion position 6 mm from the tip, distance between the prism and the corner cube of 20 cm. The same output pulse duration can be achieved by maintaining one of the parameters fixed and correct from the others.

In conclusion, the proposed prism compressor can re-compress the pulse duration after the insertion of 43 mm of glass introducing GDD and TOD equivalent for diagnostic bench of 100 TW laser system. Due to its compactness, the setup can be easily implemented before the WIZZLER on the diagnostic bench solving the sampling problem. In this way, the pulse duration in both the experiment and on the diagnostic bench can be measured on-shot. The prism compressor can compensate for larger material dispersion, making it a perfect candidate for 1 PW and 10 PW diagnostics benches of HPLS.

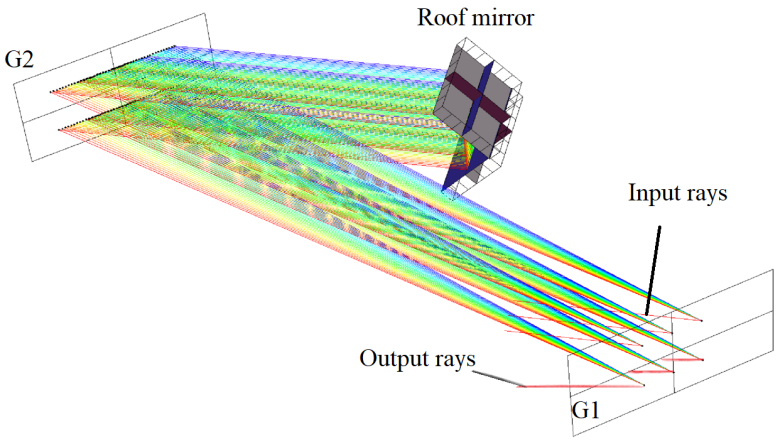


Figure 2.5: Two gratings compressor (G1 and G2) designed with 1500 grooves/mm; 800 nm central wavelength; 60 nm bandwidth

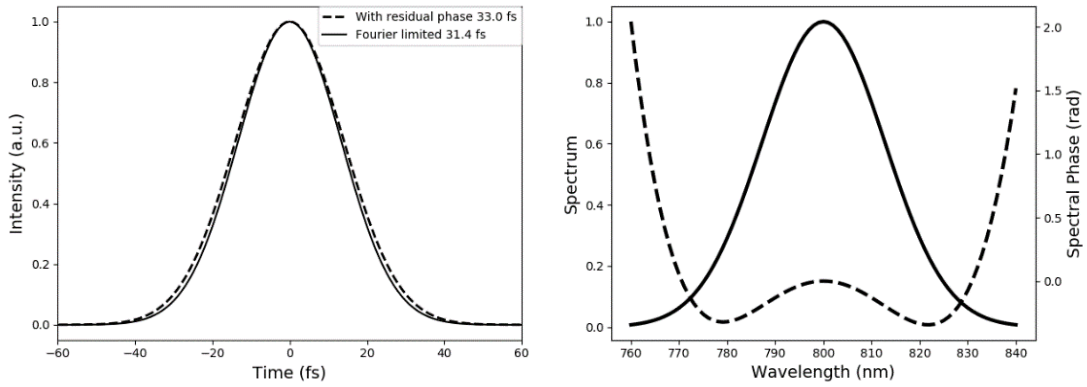


Figure 2.6: Left: Compressed pulse after upgrade; Right: Spectral phase of the compressed pulse after upgrade. Figures extracted from Ref. [13]

#### 2.2.8.2 Compressor design for a TW laser upgrade

The same algorithm was used to simulate the dispersion introduced by a CPA laser system (Avesta, 800 nm, 10 Hz, 4 mJ) and for an external amplifier in order to upgrade the actual laser system. I was involved in designing the compressor (see Figure 2.5) and calculus and compensation of the dispersion and phase (see Figure 2.6). The results were published in Ref. [13].

## 2.3 SPM general theory

Self-phase modulation (SPM) is a phenomenon that occurs when a laser beam interacts with a medium during its propagation, resulting in the phase modulation influence on the beam itself. This phenomenon is rooted in the strong intensity of the laser beam, which can induce significant changes in the refractive index of the medium it travels through. These changes cause a reciprocal response from the medium, leading to a phase shift in the incident wave and giving rise to SPM [14, 15].

Because a laser beam has a finite cross-sectional area and, consequently, a spatially varying intensity profile, the SPM that occurs on the beam exhibits a corresponding spatial dependence. This spatial SPM leads to a deformation of the wavefront, resulting in the laser

beam undergoing apparent self-diffraction. This self-diffraction, stemming from spatial SPM, is a fundamental aspect of well-known nonlinear optical effects like self-focusing and self-defocusing.

When dealing with pulsed laser input, the temporal fluctuations in laser intensity lead to time-based SPM effects. Since the time derivative of the phase corresponds to the angular frequency of the wave, SPM also manifests as frequency modulation. As a result, the output laser beam exhibits self-induced broadening of its spectral content.

The concept of SPM was first proposed by Shimizu in 1967 as an explanation for the observed spectral broadening of the output resulting from the self-focusing of a Q-switched laser pulse in liquids with significant optical Kerr constants [16]. In other studies, it was observed spectral broadening in the form of small-scale trapped filaments of light.

Alfano and Shapiro (1970) demonstrated that the use of picosecond laser pulses can lead to extensive spectral broadening (up to 10k $cm^{-1}$) in nearly any transparent condensed medium, thanks to the SPM phenomenon [17]. In the case of transparent materials, it is suggested that self-focusing plays a significant role in driving the SPM process.

### 2.3.1 SPM equations - global effects

The theory and the equations which describe the SPM theory and the beam propagation through an optical medium were extracted and adapted from [15, 16, 18, 19]. This theory was first developed to understand the linear and nonlinear mechanisms of air/ atmosphere, in low and high intensity cases, and was further extended to other media.

The interplay of diffraction, nonlinear self-focusing and ionization has an important role in the propagation of laser and plasma filaments. Moreover, the involvement of nonlinear effects stemming from bound electrons, stimulated Raman scattering, and the formation of plasma further contribute significantly to the extensive spectral broadening and subsequent generation of white light as a consequence of the laser pulse.

Thus, the complete model (3D) presented in [16] includes the effects of diffraction, dispersion, ionization, pulse energy depletion due to ionization, stimulated molecular Raman scattering, nonlinearities associated with bound electrons, spatial inhomogeneity in air density, plasma wakefields, and relativistic electron motion. Further expansive instances encompassing phenomena such as beam focusing, compression, ionization, and the generation of white light in the vicinity of the focal region are meticulously examined through the numerical solution of the complete set of three-dimensional, nonlinear propagation equations.

Starting from the wave equation of a laser electric field ***E(r,t)*** where **r**=(x,y,z)- the 3D coordinates and $t$ is the time:

$$\left(\nabla_{\perp}^{2} + \frac{\partial^2}{\partial z^2} - \frac{1}{c^2}\frac{\partial^2}{\partial t^2}\right) E = S_L + S_{NL} \tag{2.30}$$

Where $\nabla_{\perp}^{2}$ is the transverse Laplacian operator and $z$ is the direction of propagation axis. Factors $S_L$ and $S_{NL}$ denote the linear and nonlinear source terms in the laser electric field [20]. The E (r,t), $S_L$ (r,t) and $S_{NL}$ (r,t) can be written in terms of complex amplitudes A(r,t), $S_L(\mathbf{r},t)$, $S_{NL}(\mathbf{r},t)$ and rapidly varying phase $\Psi$(z,t)=$k_0$z - $\omega_0$t ($k_0$ is the carrier wave number, $\omega_0$ is the carrier frequency, $\hat{e}_x$ is a transverse unit vector in the direction of polarization and c.c. denotes the complex conjugate ) as:

$$\mathbf{E}(\mathbf{r},t) = A(\mathbf{r},t)exp[i\Psi(z,t)]\hat{e}_x/2 + c.c., \tag{2.31}$$

$$\mathbf{S}_L(\mathbf{r},t) = S_L(\mathbf{r},t)exp[i\Psi(z,t)]\hat{e}_x/2 + c.c., \tag{2.32}$$

$$\mathbf{S}_{NL}(\mathbf{r},t) = S_{NL}(\mathbf{r},t)exp[i\Psi(z,t)]\hat{e}_x/2 + c.c.. \tag{2.33}$$

By substituting the electric field, the linear and nonlinear source terms in Eq. 2.30 yields and canceling the rapidly varying phase factor from both sides:

$$\left(\nabla_\perp^2 - k_0^2 + \frac{\omega_0^2}{c^2} + 2ik_0\frac{\partial}{\partial z} + 2i\frac{\omega_0}{c}\frac{\partial}{\partial t} + \frac{\partial^2}{\partial z^2} - \frac{1}{c^2}\frac{\partial^2}{\partial t^2}\right) A(\mathbf{r},t) = S_L(\mathbf{r},t) + S_{NL}(\mathbf{r},t) \tag{2.34}$$

The linear source amplitude $\mathbf{S}_L$ contains the conventional dispersion parameters, the linear susceptibility of bound electrons and the refractive index n($\lambda$). The nonlinear source $\mathbf{S}_{NL}$ is a sum of multiple effects such as: bound electrons, Raman, plasma, relativistic electrons and ionization (see Eq. 6-12 from [20]). The most important aspects with respect to these equations are: the $n_2$ is part of the source term "bound electrons" responsible for the Kerr effect, self-focusing; the plasma column from source term "plasma" involves a decrease of the refractive index $n$, thus defocusing effect; source term "wakefield" leads to modulation of the plasma density at the plasma frequency; the term "relativistic electron" yields to critical self-focusing due to plasma; the source term "ionization" causes the depletion of the laser energy due to ionization.

The complete equation which describes the 3D evolution of the complex laser field amplitude A(r,t) can be found in Eq. 15 from Ref. [20]. In its comprehensive formulation, the equation tends to become intricated. Therefore, for the sake of simplicity, only the second-order dispersion (of significance primarily for extremely short pulses) and linear losses (a parasitic effect necessitating minimization) are kept while the Raman and plasma nonlinearities are disregarded. These nonlinear influences, including the instantaneous Kerr nonlinearity, can be harnessed for pulse compression. To facilitate presentation, the equation is cast in normalized terms, wherein the coordinates z and r, the time t, and the amplitude E of the electric field are all scaled relative to the corresponding radiation parameters at z = 0, and relative to the length L of the nonlinear medium. Under this initial assumptions the Eq. 2.34 have been shortened and well-described in 2 review papers [18, 21].

The equations used in the following chapters, particularly in Chapter 4 (ELFIE experiment), and in conjunction with the PyNLO module in subsequent sub-chapters, are presented in the following sections.

### 2.3.2 SPM equations -with assumptions

In the context of the slowly varying amplitude approximation, the propagation of laser pulses through a medium characterized by Kerr nonlinearity is elaborated by means of the generalized nonlinear Schrödinger equation (NLSE) in the following form [18].

$$\frac{\partial A}{\partial z} + \frac{1}{u}\frac{\partial A}{\partial t} + \frac{i}{2k_0}\nabla_\perp A - i\frac{k_2}{2}\frac{\partial^2 A}{\partial t^2} + \frac{3\pi\chi^{(3)}}{2n_0 c} \times \left(i\omega_0 |A|^2 A + 2A\frac{\partial |A|^2}{\partial t} + 2|A|^2\frac{\partial A}{\partial t}\right) = 0 \tag{2.35}$$

where the intensity is related to A(z,t) through $I = cn_0|A|^2/(8\pi)$, $u$ is the group velocity (first order derivative of $n_0(\omega)$ with respect to (w.r.t) $\omega$) and $k_2$ is the group velocity dispersion, $\omega_0 = 2\pi c/\lambda_0$, $\chi^{(3)}$ is the cubic susceptibility tensor related to the nonlinear refractive index $n_2$ via the formula:

$$n_2 = (2\pi/n_0)^2\chi^{(3)} \tag{2.36}$$

In Eq. 2.35 it was assumed that there is no plasma production due to the low intensity case and the pulse duration is longer than the field cycle. Thus, this equation involves the explanation of diffraction effects, wherein the term transverse Laplace operator, with the dispersion of the pulse included in the term containing the second time derivative, and the influence of Kerr nonlinearity, depicted by the terms featuring $\chi^{(3)}$. The operator $\nabla_{\perp}$ holds significance in the context of the development of small scale self-focusing (depicted in detail in Chapter 4 ELFIE experiment) as well as laser beam diffraction.

Group velocity dispersion plays a pivotal role in reshaping the pulse envelope. Its overall impact is contingent upon the initial spectral phase modulation and the relation between the signs of the medium's parameters, namely $k_2$ and $n_2$. Generally, for solid transparent dielectrics, $k_2$ and $n_2$ tend to be positive within the visible and near-infrared spectral ranges. The theory related to $n_2$ will be detailed and experimental results will be presented in the following chapter. When these signs are inversely oriented, the potential for temporal self-compression during propagation through the medium arises.

Moreover, Eq. 2.35 does not include higher-order dispersion terms, which would manifest as terms involving third, fourth, etc., time derivatives of A, and the inertialess nonlinearity (typical values for electron orbiting period 0.11 fs lower than the pulse duration). Also, the equation excludes a term characterized by an operator that rectifies the slowly varying amplitude approximation and is responsible for the spatio-temporal focusing [19].

The three terms in the round parenthesis denote: $1^{st}$-quasistatic response while $2^{nd}$ and $3^{rd}$-the wave nonstationarity [15]. The overall contribution describes the nonlinear dispersion.

When the intensity is increased, the group velocity term $u$ implies that the higher-intensity part of a pulse propagates more slowly than the wings in media with positive $n_2$, resulting in a self-steepening of the pulse front and in the formation of an envelope shock wave.

Considering the propagation of a laser pulse with $\tau > 25$ fs in a medium with weak diffraction effects and ignoring the last 2 terms of Eq. 2.35, this equation can be re-written as:

$$\frac{\partial A_n}{\partial Z} - i\frac{D}{2}\frac{\partial^2 A_n}{\partial \tau^2} + iB\left|A_n\right|^2 A_n = 0 \tag{2.37}$$

where Z=z/L, $\tau$= (t-z/u)/$\tau_{in}$, the $A_n$ normalized amplitude at the input of the medium, B is the B-integral and D-dispersion term given by:

$$D = L\frac{k_2}{\tau_{in}^2} \tag{2.38}$$

$$B_{int} = \frac{2\pi}{\lambda_0} L n_2 I(t) \tag{2.39}$$

On one hand, dispersion has the effect of altering the pulse shape and phase while leaving the amplitude of the spectral components unchanged. On the other hand, nonlinearity, such as Self-Phase Modulation, modifies the spectrum while leaving the pulse shape unaffected. When considering the Nonlinear Schrödinger Equation (NLSE), it can also be employed to describe self-focusing and self-trapping phenomena, where the transverse diffraction term replaces the dispersion term.

In summary, the most crucial terms in Eq. 2.37 are the second term related to dispersion and the third term associated with nonlinearities originating from a material with a thickness of $L$. The solution to this equation can be expressed as:

$$A_n(\tau, z) = A_n(\tau, 0)e^{i\Phi_{NL}(\tau,z)} \tag{2.40}$$

Thus, it can define the nonlinear phase:

$$\Phi_{NL}(\tau, z) = k_0 z \frac{n_2}{n_0} |A_n(\tau, 0)|^2 \tag{2.41}$$

The nonlinear frequency shift :

$$\Omega(\tau, z) = -\frac{\partial \Phi_{NL}}{\partial \tau} = -k_0 z \frac{n_2}{n_0} \frac{\partial |A_n(\tau)|^2}{\partial \tau} \tag{2.42}$$

The spectral broadening:

$$\Delta\Omega(z) = max\left(2k_0 z \frac{n_2}{n_0} \frac{\partial |A_n(\tau)|^2}{\partial \tau}\right) \approx 2k_0 z \frac{\delta n_{max}}{n_0 \tau} \tag{2.43}$$

where $\delta n_{max}$ is the maximum change in the refractive index. Frequency spectrum extent increases with the increase of the field amplitude and distance and with the laser pulse duration decrease.

The chirp (THz/ps):

$$C(\tau, z) = \frac{\partial \Omega(\tau, z)}{\partial \tau} = -k_0 z \frac{n_2}{n_0} \frac{\partial^2 |A_n(\tau, 0)|^2}{\partial \tau^2} \tag{2.44}$$

The nonlinearity-induced frequency modulation around the pulse peak is characterized by a positive chirp, signifying a transition from a negative to a positive frequency shift. This favorable chirp polarity is governed by the positive nature of $n_2$.

In media with normal dispersion, lower frequencies experience advancement, leading to temporal expansion of the nonlinearly chirped pulses. Conversely, in media with anomalous dispersion, lower frequencies are delayed, resulting in the temporal compression of nonlinearly chirped pulses.

The spectral broadening and the pulse shortening factor can be defined, on short as:

$$F_\omega = \frac{\Delta\Omega_{out}}{\Delta\Omega_{in}} \tag{2.45}$$

$$F_\tau = \frac{\tau_{in}}{\tau_{out}} \tag{2.46}$$

The same two parameters can be described by a linear dependence on the B-integral in a wide value range of parameters B and D as follows [18](Eq. 11):

$$F_\omega = 1 + g_\omega B(1 - h_\omega \sqrt{D}) \tag{2.47}$$

$$F_\tau = 1 + g_\tau B(1 - h_\tau \sqrt{D}) \tag{2.48}$$

The coefficients g and h for $\omega$ ($\approx$ 0.88 and 0.59) and $\tau$ ($\approx$ 1.5 and 1.36 ) are highly dependent on B-integral values. Complete range of values can be found in [18] (Table 1).

The last two equations will be further extended by me, in Chapter 4 ELI-NP 100 TW experiment while introducing 4 new coefficients; namely Temporal Strehl Ratio (TSR), Spatial Strehl Ratio (SSR), DM compensation factor and the energy losses.

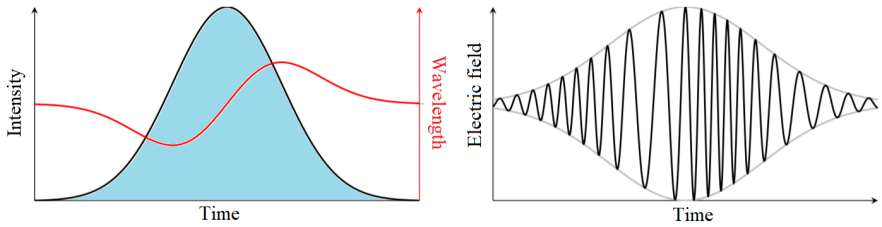


Figure 2.7: Left: the spectral intensity and spectral phase; Right: the envelope of the electric field while the spectral broadening occurs

### 2.3.3 SPM - the simplest description

Other references [22] reduce even more the previous Eq. 2.42, keeping just the nonlinear term while adding the contribution of absorption in the material in a distance $z$. The solution becomes:

$$A(z) = A(0)e^{-\frac{\alpha z}{2}}e^{-in_2|A(0)|^2 L_{eff}} \tag{2.49}$$

where $L_{eff}$ is the effective length of the material given by the next equation and $\alpha$ is the absorption (usually found as attenuation) factor. The last 2 parameters namely $L_{eff}$ and $\alpha$ will be used in Chapter 3, Measurements of $n_2$.

$$L_{eff} = \frac{1 - e^{-\alpha z}}{\alpha} \tag{2.50}$$

The variation of the linear refractive index produces the shift of the pulse phase while a laser pulse with intensity $I$ acts on the nonlinear part of the global refractive index ($n(I)=n_0+n_2I+...$)). The phase shift is:

$$\Phi(t) = \omega_0 t - k_0 z = \omega_0 t - k_0 n(I) L \tag{2.51}$$

The frequency shift is given by:

$$\Delta\Omega(t) = \frac{\partial\Phi(t)}{\partial t} = \omega_0 - k_0 L \frac{\partial n(I))}{\partial t} \tag{2.52}$$

The evolution of the frequency shift and spectral broadening which acts on the real part of the electric field is illustrated in Figure 2.7.

The electric field is a vector quantity that varies with time and space. The real part of the electric field represents the actual oscillatory behavior of the electromagnetic wave. In other words, it gives the information about how the electric field varies with time as the pulse moves through space.

The evolution of the frequency shift and spectral broadening in the real part of the electric field is a crucial consideration in the design and analysis of optical systems. It impacts a range of applications, including the generation of ultrashort laser pulses.

Several factors can cause frequency shifts, with one of the most common being the phenomenon of dispersion. Dispersion is the dependence of the speed of light on its frequency. Dispersion can cause these different frequencies to travel at different speeds, which leads to a change in the shape and duration of the pulse.

Therefore, I will summarize in Figure 2.8 the influence of the pulse duration (a, b), nonlinear refractive index amplitude $*10^{-20}$ $m^2/W$ (c) and the material thickness (tk (mm)) (d) on the central wavelength shift. For this illustration I have changed the frequency shift (Hz) in wavelength shift (nm) which will follow the figures axes in the following chapters.

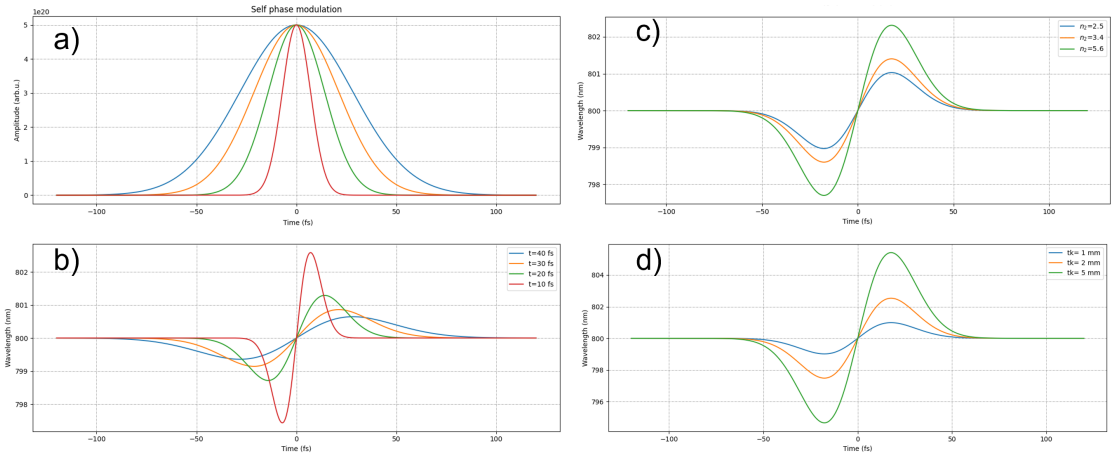


Figure 2.8: Influence on the SPM (simple description case) of the pulse duration (HWHM) (where **a** illustrates the temporal profile used for **b**), nonlinear refractive index ($*10^{-20}$ $m^2/W$) (**c**) and thickness of the material (**d**). The case of no chirp is considered.

For a) and b) I analyzed the change in the laser pulse intensity through the variation of pulse duration. For c) and d) the initial pulse duration was fixed at 25 fs. The material chosen for b) and c) was 1 mm of FS and it has been varied up to 3 mm in d).

In Figure 2.8 b), both the amplitude and efficiency of Self-Phase Modulation can be observed as the pulse duration decreases. Notably, the broadening effect becomes significantly more pronounced as either the amplitude of $n_2$ or the thickness of the material increases.

The limitations of material thickness are related to self-focusing and small scale self-focusing. Actual solutions implies multiple material plates with smaller thickness and a specific distance between them [23, 24].

## 2.4 SPM-high energy

During the interaction with high energy laser pulses, alongside the effects presented in Chapter 2.3.1, SPM can have effects on both temporal and spatial parts of the laser pulse. In this complex interplay, the phenomena of SPM in time and SPM in space intertwine intricately, exerting substantial mutual influence upon each other. This aspect is further discussed in Chapter 4 ELI-NP (2) experiment. The most important effects are summarized as follows:

### 2.4.1 Self-steepening

One of the first effects is the self-steepening. The high intensity part of the laser pulse is tilted towards larger $\tau$, or in other words the peak of the pulse is traveling at a velocity lower than the group velocity. Also the self-steepening effects leads to shock creation assuming some conditions such as the *critical distance* -the peak is displaced at a specific distance of the order of the pulse width from the center of the pulse [25].

### 2.4.2 Beam nonuniformity

The spatial nonuniformity of the laser beam, coupled with the nonuniformity of the optical material, can lead to several effects, including asymmetrical broadening and reduced efficiency. Additionally, these factors can contribute to self-focusing phenomena known as

Large Scale Self Focusing (LSSF) and Small Scale Self Focusing (SSSF), nonlinear phase aberrations, nonlinear broadening (terms like $n_4 I^2$), and nonuniform pulse compression.

As the laser beam propagates further within the medium, these effects have the potential to amplify and reach critical levels. This progression can result in two significant outcomes: self-steepening, leading to the creation of a shock front, and self-focusing, which confines the beam to a spot primarily defined by higher-order nonlinear effects and diffraction.

Aberrations arising from these phenomena can be categorized into two distinct components: parabolic and nonparabolic. Parabolic aberrations are defined by the focal length $f$ of a "nonlinear lens", with positive behavior ($f > 0$) when $n_2 > 0$. These parabolic aberrations can be effectively counteracted by using a conventional negative lens with a focal length of -$f$. In such cases (where a lens with -$f$ is needed), it is sufficient to consider that the "nonlinear lens" reduces the distance between the beam waist and the focal point of the focusing parabola. Nonlinear beam aberrations can be quantified using parameters like the $M^2$ factor (as described in the theory of Gaussian beam propagation) and the Strehl ratio.

In the case of a Gaussian intensity distribution, the central part of the beam has a more significant impact compared to the edges. To address these issues, flat-top beams are often used. However, even flat-top beams exhibit uniformity issues in the envelope. The effects of these nonuniformities and the Small Scale Self-Focusing effect (SSSF) are described in detail in Chapter 4 of the ELFIE experiment.

### 2.4.3 Pulse Duration and Intensity

In the context of employing high-power peak laser pulses, distinct variations arise in the duration and intensity of the compressed pulse across different regions of the cross-section. In other words, when moving from the beam periphery towards the central axis, the degree of spectral broadening and the corresponding intensity augmentation display noteworthy differences. Specifically, at the beam periphery, these effects are notably less pronounced compared to the pronounced alterations experienced along the beam axis, wherein the B-integral reaches its maximum value. This issue is identified as the primary constraint when it comes to self-phase modulation in the context of unguided propagation through a nonlinear medium [18].

## 2.5 B-integral

The B-integral holds paramount significance in the realm of ultrashort and ultra-intense laser pulses. As laser technology has evolved to produce increasingly shorter and more intense pulses, the precise control of these pulses' temporal and spectral characteristics has become crucial for numerous applications, ranging from scientific research to medical diagnostics and industrial processes.

In essence, the B-integral quantifies the extent to which different spectral components of a pulse experience varying propagation velocities. This phenomenon, often referred to as dispersion, arises due to the wavelength-dependent refractive index of the medium through which the pulse travels. The dispersion, in turn, affects the pulse's intensity profile and can even lead to the formation of unwanted satellite pulses if not properly managed.

The B-integral (denoted as $B_{int}$) can be calculated as follows:

$$B_{int} = \frac{2\pi}{\lambda} \int n_2 I(z) dz \approx \frac{2\pi}{\lambda} n_2 I L \tag{2.53}$$

When surpassing values of approximately 3–5, a potential hazard arises in the form of self-focusing. This phenomenon involves the intensification of the nonlinear lensing effect to such an extent that the laser beam contracts to an exceedingly minute radius.

For ultrashort laser pulses, particularly those with broad spectral bandwidths, the B-integral acts as a key metric to predict and control the amount of dispersion-induced distortion. It provides insight into how much the pulse will broaden or compress during propagation. A high B-integral value indicates significant dispersion and the potential for detrimental effects, while a low value indicates minimal distortion.

Furthermore, in the realm of ultra-intense laser pulses, where peak powers can reach extreme levels, the B-integral becomes even more crucial. The intricate interplay between nonlinear effects, dispersion, and self-focusing can profoundly impact the propagation dynamics of such pulses. Excessive B-integral values can lead to dramatic changes in the pulse's spatial and temporal characteristics, resulting in self-focusing, filamentation, and even the generation of complex plasma structures.These phenomena not only affect the pulse's quality and stability but also impact the efficiency and safety of the laser-matter interactions.

The precise control of the B-integral is pivotal for achieving the desired outcomes in fields like high-energy physics, precision material processing, and medical procedures that rely on ultrashort and ultra-intense laser technology. Hence the need to calculate the B-integral within a laser system by accurately computing the laser intensity when dealing with materials with nonlinear index characteristics. However, accomplishing this task is challenging because it requires comprehensive understanding of the involved material and laser parameters, even without considering the potential changes in these factors over time.

Within this thesis, I used the equations for dispersion of the materials to calculate the refractive index, GDD, TOD and the measurements of $n_2$ for each material to retrieve the B-integral, simulate the broadening and the perfect dispersion compensation.

## 2.6 Theory and measurements of Kerr effects

### 2.6.1 Nonlinear refractive index

The refractive index of many optical materials is a parameter which depends on the irradiance of the light. Materials exposed to sufficiently high fields, easily accessible with CW or pulsed lasers, can become nonlinear. They can exhibit either nonlinear absorption (NLA) or/and non-negligible nonlinear refraction (NLR). These nonlinearities are described through two coefficients namely nonlinear absorption coefficient (NAC) and nonlinear refractive index (NRI). The knowledge of the NRI and NAC of materials is of great interest for their potential application in optical devices, B-integral and Kerr effects control.

The change of the refractive index with the irradiance leads to Kerr effects: filamentation, auto-focusing and defocusing, SPM, etc. [26, 27]. For example knowing the value of $n_2$ it can be estimated how self focusing (SF) may occur. Thus, SF may cause spatial collapse of the laser beam when it propagates through transparent optical materials, often leading to optical damage.

The Kerr effect is a third order electro-optic effect, in which the refractive index of a material is changed by a specific amount, equivalent to the square of the electric field intensity (E). At high irradiance the global refractive index can be described by the expansion of *n(I)* in a Taylor series:

$$n(I) = n_0 + n_2 \cdot I + n_4 \cdot I^2 + \cdots \tag{2.54}$$

Where the irradiance can be expressed as:

$$I = 2 \cdot n_0 \cdot \epsilon_0 \cdot c \cdot |E^2| \tag{2.55}$$

And $\epsilon_0$ is the vacuum permittivity and $c$ is the speed of light, $n_0$ is the linear refractive index, $n_2$ is the nonlinear refractive index (third order) and $n_4$ is the fifth order nonlinear refractive index etc.. This relation is responsible for self-focusing effect ($n_2 > 0$) due to the transverse intensity profile causing an induced gradient-index lens. The intensity of the pulse varies with time, which, according to equation 2.6.1, leads to a time dependent-change of the refractive index:

$$n(I(t)) = n_0 + n_2 \cdot I(t) \tag{2.56}$$

After propagation in the z direction through the material with thickness $L$, the optical field accumulates a nonlinear phase for each frequency component $\omega_0$:

$$\Phi_{NL}(z,t) = \omega_0 \cdot n_2 \cdot I(z,t) \cdot L \tag{2.57}$$

In general, the NRI can be retrieved from nonlinear phase measurement. The NRI is responsible for applications based on optical switching, optical logical gates, communications, active elements, high power lasers etc. [26].

### 2.6.2 Nonlinear absorption

One of the mechanisms responsible for nonlinear absorption is the two-photon absorption. This effect can be inferred from the Lambert-Beer law of absorption. For higher light irradiance the probability for two photons to influence a material at the same time is significantly increased. Nonlinear absorption is a third-order nonlinear process that can be quantified by the parameter $\beta$ -the nonlinear absorption coefficient (NAC). The NAC is constant with respect to intensity, concentration and sample thickness. However it will change with respect to the excitation wavelength. The total absorption is thus given by:

$$\alpha = \alpha_0 + \beta \cdot I \tag{2.58}$$

In the above equation, $\alpha$ represents the total absorption coefficient, while $\alpha_0$ represents the linear absorption coefficient. Measuring and determining the value of $\beta$ allows for the differentiation of both effects: nonlinear refraction and absorption. This separation is essential for extracting the NRI value without the influence of absorption effects [28, 29]. S. Bahae is recognized as one of the pioneering researchers in the field of NRI.

## 2.7 Methods to measure the nonlinear refractive index and absorption

A wide range of techniques have been proposed, described and used to measure optical nonlinearities such as: Z- scan [28], I- scan [30], degenerate four-wave mixing [31] (DFWM), nonlinear interferometry [32], ellipse rotation [33], etc.. Extensions of these basic techniques to allow the use of Gaussian or non-Gaussian-beam profiles, thick samples and large phase nonlinearities have been proposed [34].

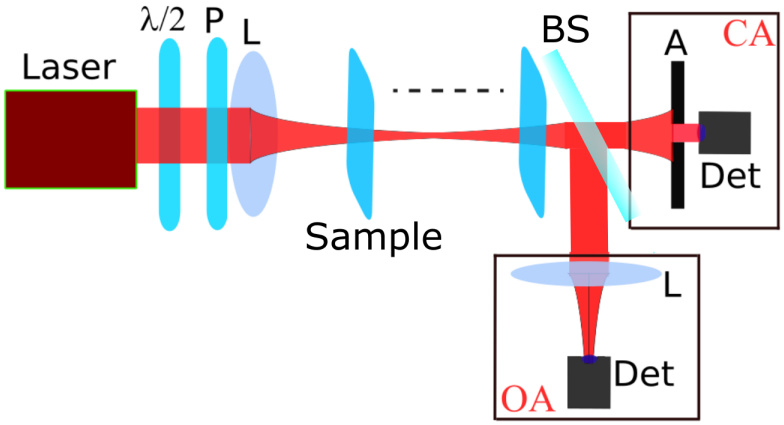


Figure 2.9: Illustrative scheme of Z-scan method with Open and Closed Aperture configurations. A-Aperture, BS-Beam Splitter, Det-Detector, L-lens, P-Polariser and $\lambda/2$-waveplate

### 2.7.1 Z-scan method

The most extensively used method for measuring NRI and NAC of thin samples is the Z-scan method. This method is based on the self-focusing effect of a probe beam and the power/energy/voltage measurement behind an aperture while varying the sample position. Due to the changes in spot size along the Z-axis (thus, the name Z-scan), the sample experiences different values of light irradiance while moving. The resulting transmitted signal is detected in the far field as a function of the sample position with respect to the focal plane (usually, z = 0 is defined at the focus). The Z-scan method has two specific configurations namely a closed aperture (CA) for NRI retrieval where just a part of the light, the one that pass through an aperture, placed in front of the detector is recorded, and an open aperture (OA) for NAC retrieval where all the light is collected into the detector by using a focusing lens (See Figure 2.9). As detectors for the transmitted light are used photodiodes (PDs) or other kind of sensors coupled to power/energy meters.

A positive value for the nonlinear refractive index ($n_2$) results in a focusing effect, whereas a negative value leads to a defocusing effect (as illustrated in Figure 2.10). Through the experimental setup utilizing Z-scan, I obtained experimental data points, which are well fitted by the theoretical curves.

### 2.7.2 Peak-Valley transmittance (PVT)

One of the simplest methods for estimating the NRI is to calculate the Peak to Valley Transmittance (PVT), which is the difference between the maximum and minimum values observed in a Z-scan transmittance curve. This straightforward approach provides a quick estimate of the NRI based on experimental data.

The NRI can be written as:

$$n_2 = \frac{\Delta PV}{0.406 \cdot k \cdot I \cdot L_{eff}} \tag{2.59}$$

where $\Delta PV$ is the difference between the maximum and the minimum normalized transmission, $k$ is the wave vector, $I$- input intensity and $L_{eff}$ is the effective length given by:

$$l_{eff} = \frac{1 - e^{-\alpha L}}{\alpha} \tag{2.60}$$

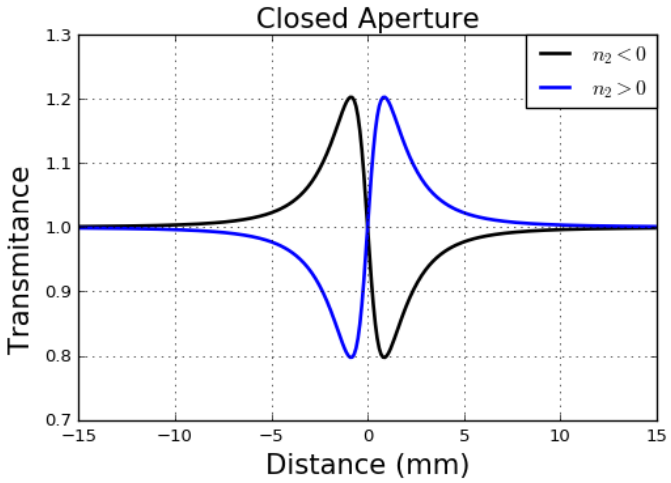


Figure 2.10: The form of the measured signal in relation to the sign of the Nonlinear Refractive Index of materials.

where $\alpha$ is the linear absorption coefficient and $L$ is the length of the sample. The peak-valley transmittance change is related to the small phase variation ($|\Delta\Phi| < 1$) through Eq. 2.61 and this change can be seen in Figure 2.11:

$$\Delta T_{PV} \simeq 0.406 \cdot \Delta\Phi \simeq 0.406 \cdot k \cdot n_2 \cdot I \cdot l_{eff} \tag{2.61}$$

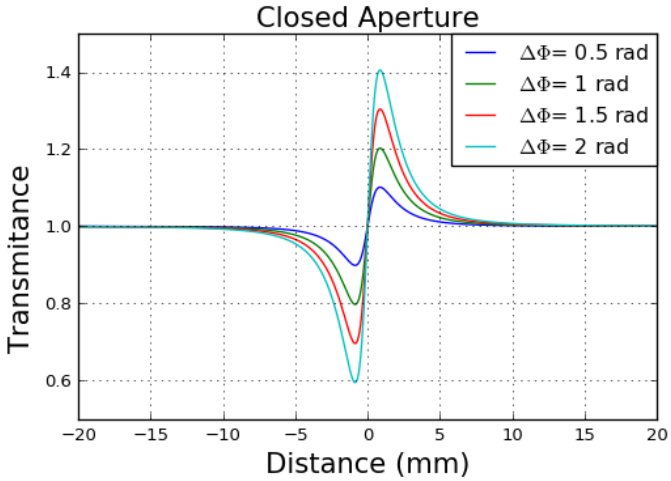


Figure 2.11: Peak-valley variation as a function of the $\Delta\Phi$ for a pure third-order nonlinearity

The authors of Ref. [28] propose a simple fitting equation for the determination of the NRI:

$$T(z, \Delta\Phi) \simeq 1 - \frac{4 \cdot \Delta\Phi \cdot x}{(x^2 + 9) \cdot (x^2 + 1)} \tag{2.62}$$

where $x = z/z_R$.

The Z-scan technique can provide accurate results under a few limitations as: condition for far-field ($d >> z_R$), small phase variation ($|\Delta\Phi| < 1$), $|\Delta T_{PV}| \simeq 1.7 \cdot z_R$, Gaussian beams and thin samples [28].

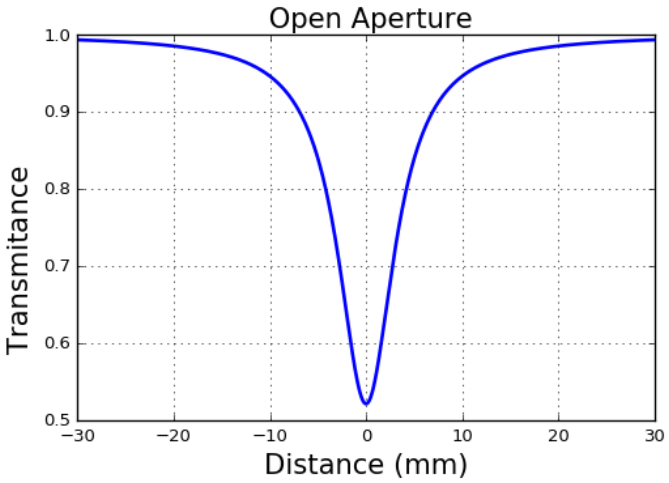


Figure 2.12: Open aperture curve used to fit the NAC

The open aperture Z-scan technique is a method used to measure the nonlinear absorption coefficient (NAC) of a material. In this technique, a beam splitter and a focusing lens are typically employed after the sample. The lens is used to collect all the transmitted light, hence the name "open aperture". The resulting curve provides information about the focal point, which can be determined by translating the sample before and behind the focal point. At the focal point, the absorption is at its highest, as indicated in Figure 2.12. This technique allows for the characterization of nonlinear absorption properties in materials.

The Eclipse Z-scan (EZ-scan) is a derivative technique based on the Z-scan method, with a significant improvement. In EZ-scan, a disk is placed in front of the detector instead of an aperture. A lens is used to collect the eclipsed beam into a detector, allowing for the measurement of the specific $n_2$ curve. This method offers higher sensitivity and the capability to measure both thermal and non-thermal nonlinearities in materials [35]. It provides a more comprehensive understanding of the nonlinear optical properties of the material under investigation.

### 2.7.3 I-scan method

In addition to the Z-scan techniques, there are I-scan measurements, wherein the same region of the sample is illuminated, the sample being stationary in the setup. Typically, the sample is placed at $\pm$ 0.85 times the Rayleigh range ($Z_R$) (measured from the focal plane of the focusing lens) during the measurement. This setup is suitable for investigating both small and large areas. By keeping the sample away from the focal plane of the focusing lens, potential material damage is avoided, and the overall sample surface exposure is minimized (See Figure 2.13). The open and closed aperture configurations are similarly employed in recording transmitted light, facilitating the determination of NAC and NRI. Both methods yield insights into the magnitude and sign of NRI and NAC [30].

### 2.7.4 Other methods

Since the first proof of concept proposed by S. Bahae, many other techniques have been widely used and developed. These techniques include:

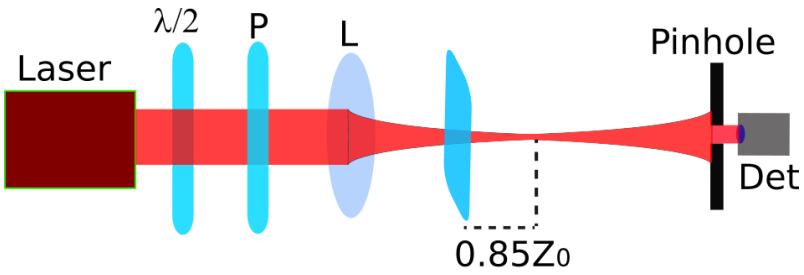


Figure 2.13: Illustrative setup for I-scan configuration

#### 2.7.4.1 Wave-mixing

Three-wave or four-wave mixing methods were used to measure nonlinear refractive index and other ultrafast material responses with a higher accuracy and sensitivity. As a result of wave-mixing is an improved signal-noise ratio. The Three-Wave Mixing process involves the interaction in the sample of two laser beams of frequencies $\omega_1$ and $\omega_2$ resulting generation of new frequencies from their difference or sum. The main disadvantage is their complicated setup [31]. For the case where four waves are required (degenerate four-wave mixing DFWM), a single laser source can be used. Two different types of measurement can be distinguished: resonant and non-resonant DFWM.

The resonant DFWM takes into account the optical absorption at the frequency of the interacting light beams. The absorption will induce a spatial modulation of the population causing a spatial grating. Thus, both absorption and phase grating can be found in a resonant DFWM.

In the case of the non-resonant DFWM, the used frequency is far from the absorption spectrum leading to an optical phase conjugation.

The nonlinear interaction of two pump beams with a signal beam inside of a $\chi^3$ nonlinear medium generates a fourth beam, which is phase conjugated to the signal beam. Other methods based on different polarization are used to separate the effect of nonlinear absorption and refraction.

#### 2.7.4.2 Pump-Probe

Pump-probe method is using two light beams to shine a sample. The pump beam will induce a change in the refractive index along the propagation path through the sample. The sample should have low absorption for the pumping wavelength. A probe beam monitors the response, usually with a lower optical intensity that does not significantly affect the sample. By varying the time separation of the two laser pulses, the probe beam, by passing through the sample, will monitor the phase change induced by the pump [36]. Slow and fast nonlinear responses can be identified using this technique. A derivative method is the degenerate pump-probe where identical frequencies are used. The probe beam is separated from the pump beam by orienting the probe with polarization changed or in a non-collinear geometry.

#### 2.7.4.3 Interferometry

The variation of phase in a sample can be measured using a Mach-Zehnder or Michelson interferometer configuration, which relies on the interference pattern of light. When the input irradiance is low, straight-line interference fringes are observed, but for high irradiance, curved fringes appear. Methods based on Fourier analysis are commonly employed to retrieve the phase information from these fringe patterns [36, 37].

To achieve time resolution in phase measurements, a streak camera can be used. This allows for the observation of how the phase changes over time. However, this setup requires precise alignment and stability to obtain accurate results.

## 2.8 Case study: Large phase shift problem

When the phase shift $\Delta\phi$ becomes larger than 1, the equations proposed by S. Bahae can not longer describe with sufficient accuracy the Z-scan results. Different fitting equations have been proposed to account for materials that exhibit larger phase shifts [38, 39, 40]. For small phase shifts, all these fitting equations should reduce to the basic Eq. 3.5. To address higher-order phase shifts, new fitting equations have been proposed, which consider both the nonlinear refractive index (NRI) and the nonlinear absorption coefficient (NAC) [41].

Ramirez et al. introduced a method based on Z-scan and Self-Phase Modulation (SPM) in thin media using Gaussian beams [42]. They employed numerical calculations of the Fraunhofer integral to obtain the on-axis intensity in Z-scan or SPM experiments. This model can describe samples with various magnitudes of maximum nonlinear photo-induced phase shifts in purely refractive nonlinear thin media. They investigated two cases: when the phase shift is smaller than $\pi$ and when it is larger than $\pi$. The normalized transmission for phases less than $\pi$ is given by:

$$T(z) = 1 + \frac{2m\Phi_0 x}{x^2 + (m+1)^2 (x^2+1)^{m/2}} + \frac{m^2 \left(3x^2 - (2m+1)\right) \Phi_0^2}{(x^2+1)^m \left(x^2 + (m+1)^2\right) \left(x^2 + (2m+1)^2\right)} \tag{2.63}$$

where $m$ can be any real positive number related to the degree of nonlinear response non-locality. This equation and the one proposed by S. Bahae were used in the following Chapter- Nonlinearities measurements to fit the experimental results. Despite using Eq. 2.63, where the parameter $m$ can be adjusted, the fitting curves still do not entirely coincide with the raw data. As a result, I explored alternative cases and equations in an attempt to provide a more accurate description, particularly when considering a substantial phase shift alongside absorption effects. Below, I'll briefly outline a few of these alternatives in terms of their fitting equations and the conditions under which they are applicable.

Lee et. al. proposed the following equation based on an analytical theory for large phase shift [43]. The method can be applied for both small and large phase shifts, as well as for thin and thick materials. The theory is built on Gaussian beam formalism, and the normalized transmission is given by:

$$T(z) = \frac{1 + \frac{2\sigma x + \sigma^2}{1+x^2} - \frac{2\sigma}{(1+x^2)^2}\Phi_0}{1 + \frac{2\sigma x + \sigma^2}{1+x^2} - \frac{4(x+\sigma)}{(1+x^2)^2}\Phi_0 + \frac{4}{(1+x^2)^3}\Phi_0^2} \tag{2.64}$$

where $\sigma = \frac{l_{eff}}{z}$

Yin et al. proposed a simplified method to determine both nonlinear coefficients. The main advantage of this work is that $\beta$ can be deduced from the $T_\Psi$ $(x = \pm 0.85)$ [40]:

$$T(x) = -\frac{4\left(3x^4 + 10x^2 - 9\right)x}{\left(x^2+9\right)^2 \left(x^2+1\right)^2}\Phi_0 - \frac{2\left(x^2+3\right)}{\left(x^2+9\right)\left(x^2+1\right)}\Psi_0 \tag{2.65}$$

Kwak et al. deduced a fitting equation using aberration free approximation of a Gaussian Beam through a nonlinear medium including both nonlinear coefficients which can be applied to samples with large phase shift [44].

$$T(z) = \frac{1}{1 - \frac{4x}{(1+x^2)^2}\Delta\Phi_0 + \frac{4}{(1+x^2)^3}\Delta\Phi_0^2} \tag{2.66}$$

$$T(z)\,(phase + absorption) = \frac{1}{1 - \frac{4x-n}{(1+x^2)^2(1+q)}\Delta\Phi_0 + \frac{4}{(1+x^2)^3(1+q)^2}\Delta\Phi_0^2} \tag{2.67}$$

where $n = \beta/2kn_2$ and $q = \beta I_0 l_{eff}$. Thus the nonlinear refraction and absorption are coupled in the $n$ factor.

Bing Gu et al. have used the Gaussian decomposition method (GD) to get the Z-scan curves for an optically thin material with both refractive and absorptive part of the third order nonlinearities. From the fitting of the experimental curve both indices can be extracted [45].

$$\begin{aligned} T(x) = 1 + \frac{1}{\sqrt{2}}\frac{4x\phi_0 - \left(x^2+3\right)q_0}{\left(x^2+1\right)\left(x^2+9\right)} + \\ + \frac{1}{\sqrt{3}}\frac{4\Delta\phi_0^2\left(3x^2+5\right) + q_0^2\left(x^4+17x^2+40\right) - 8\Delta\phi_0 q_0 x\left(x^2+9\right)}{\left(x^2+1\right)^2\left(x^2+9\right)\left(x^2+25\right)} \end{aligned} \tag{2.68}$$

where $q_0 = \beta I_0 (1-R) l_{eff}$ and R is the Fresnel reflectivity coefficient.

In order to achieve a close alignment with the actual value of $n_2$ through a perfect fit, the equations introduced by Bahae and Ramirez were employed for phase fitting. The Bahae model demonstrated remarkable accuracy for phases below 1 radian, while the Ramirez model proved effective for phases below $\pi$. The notable advantage of the Ramirez model lies in its ability to adjust the parameter $m$, offering a feasible means to numerically fine-tune experimental outcomes—particularly beneficial for accommodating substantial phase shifts and a significant nonlocal nonlinear response.

This model emerged as exceptionally valuable and adeptly matched experimental outcomes for materials like plastics that exhibit a nonlocal response, as detailed in Adair's work [46].

As for the other equations, they were utilized to attain improved fits for asymmetric Z-scan curves derived from measurements. These curves often involve complexities such as energy fluctuations or higher-order nonlinearities, requiring alternative equation models for more accurate descriptions.

### 2.8.1 Discussion

A comprehensive exploration of self-phase modulation involves an examination of the multifaceted optical phenomena that come into play. To proceed, certain assumptions are introduced to simplify the scenario, thereby arriving at the fundamental circumstances where spectral broadening through self-phase modulation (SPM) becomes evident. The simplified models can estimate the frequency of the outlying peaks.

The Kerr nonlinearity induces a modulation in the temporal phase of a propagating pulse within the material. This phase modulation engenders a chirp, characterized by the parameter $k_2$. As illustrated in Figure 2.8, a notable observation emerges: a single instantaneous frequency $\omega_0$ occurs at two distinct time instances (namely, $t_1$ and $t_2$). The cumulative phase alteration over time encompasses both a linear contribution ($\omega_0\Delta t$) and a nonlinear phase shift (NPS). The NPS escalates with $\omega_0$, ranging from -$k_2$ to 0. The interplay of constructive and destructive interference between these two moments engenders the sinusoidal modulation discernible in the pulse's spectral profile.

The electric field of a pulse, that is subjected to SPM, shows a phase delay which is greater at higher intensity regions than at lower intensity regions (See Figure 2.7).

Upon accounting for the chirp, the spectral shape undergoes pronounced transformation. Notably, the central spectrum experiences a lack of spectral interference manifesting as multiple peaks and troughs within the oscillations. The amplitude and frequency of the sinusoidal modulations are intrinsically linked to the maximum chirp's magnitude and location [47].

The dispersion, the SPM, B-integral and nonlinear refractive index are core attributes for the topic of this work. They are related to the materials (i) and to the laser parameters (ii).

**(i)** It has been shown that the index of refraction $n$, thickness of the material ($L$), quality of the material, sample size (for high power laser i.e. 10 PW @ELI-NP has 55 cm [48]) and when the irradiance is high enough, the contributions of higher orders of the nonlinear refractive index ($n_4$...) to $n$, linear and nonlinear absorption, losses (i.e. Fresnel reflections) affect the overall effect of the SPM and B-integral and need to be carefully understood and investigated prior to the experiments.

**(ii)** The spot size, the input energy, pulse duration (in short, irradiance), the beam uniformity, laser pulse contrast, Strehl ratio, different irradiances and pulse durations across the large beams (>10 mm), Dazzler and Deformable Mirrors, play as major determinants on the post compression efficiency.

This Chapter covers a comprehensive understanding of the nonlinear effects related to SPM (from the complex towards the simplified theory). Three key terms: B-integral, NRI $n_2$ and NAC $\beta$ were investigated from the theoretical point of view.

The Z-scan method is the most used technique employed to measure the Nonlinear Refractive Index (NRI) and Nonlinear Absorption Coefficient (NAC) in samples, regardless of their thickness. This method capitalizes on the phenomenon of self-focusing observed in a probe beam. It involves altering the sample's position while measuring power, energy, or voltage behind an aperture.

The Z-scan method comprises two distinctive configurations: the closed aperture (CA) configuration, used for extracting NRI, where only the light passing through an aperture placed in front of a detector is recorded; and the open aperture (OA) configuration, utilized for determining NAC. The OA setup involves the use of a focusing lens to capture all light transmitted by the investigated sample. In both cases, power meters or energy meters are used to capture the transmitted light.

To effectively apply these concepts, I implemented the equations for dispersion, nonlinear refraction and absorption and B-integral in dedicated programming codes, which were extensively utilized in the subsequent chapters of my work. A concise review of various methods for measuring NRI was also presented. This review played a crucial role in aiding me to implement and further refine Z-scan and I-scan techniques to characterize a variety of materials.

Considering the critical requirement for high optical quality materials, optimal laser parameters, and efficient chirped mirrors, the forthcoming chapter deals these aspects. It will explore manufacturing and measurement challenges, propose solutions, and showcase the novelty of the results achieved in this context.

## 2.9 Published results of this chapter

**P.-G. Bleotu** et al., "PRISM COMPRESSOR ENABLING PULSE DURATION MEASUREMENTS AT ELI-NP EXPERIMENTAL AREAS"-in ELI-NP reports 2019

[13]. V.Aleksandrov, **P.-G. Bleotu** et al., "Upgrading design of a multi-TW femtosecond laser", Romanian Reports in Physics, 2020.

[49]. V.Aleksandrov, **P.-G. Bleotu**, D Ursescu, "Femtosecond Pulse Shortening Using Cascaded Quadratic Nonlinearities for High Temporal Contrast", CLEO, 2019.

# Bibliography


[1] D Geskus. "Design and construction of regenerative amplifier and compressor for chirped pulse amplification". en. In: (2006), p. 66.

[2] Zhaoyang Li, Cheng Wang, et al. "Fourth-order dispersion compensation for ultra-high power femtosecond lasers". In: *Optics Communications* 357 (Dec. 2015), pp. 71–77. URL: https://www.sciencedirect.com/science/article/pii/S0030401815300407 (visited on 08/19/2023).

[3] Robert Szipöcs, Kárpát Ferencz, et al. "Chirped multilayer coatings for broadband dispersion control in femtosecond lasers". EN. In: *Optics Letters* 19.3 (Feb. 1994). Publisher: Optica Publishing Group, pp. 201–203. URL: https://opg.optica.org/ol/abstract.cfm?uri=ol-19-3-201 (visited on 08/19/2023).

[4] E. Treacy. "Optical pulse compression with diffraction gratings". In: *IEEE Journal of Quantum Electronics* 5.9 (Sept. 1969). Conference Name: IEEE Journal of Quantum Electronics, pp. 454–458.

[5] Donna Strickland and Gerard Mourou. "Compression of amplified chirped optical pulses". In: *Opt. Commun* (1985), pp. 219–221.

[6] Alexander V. Tikhonravov, Michael K. Trubetskov, et al. "To the design and theory of chirped mirrors". en. In: *Optical Interference Coatings*. Tucson, Arizona: Optica Publishing Group, 1997, WE.2. URL: https://opg.optica.org/abstract.cfm?URI=OIC-1998-WE.2 (visited on 08/19/2023).

[7] Ivan B. Angelov, Aaron Von Conta, et al. "Investigation of the laser-induced damage of dispersive coatings". en. In: ed. by Gregory J. Exarhos, Vitaly E. Gruzdev, et al. Boulder, Colorado, Oct. 2011, 81900B. URL: http://proceedings.spiedigitallibrary.org/proceeding.aspx?doi=10.1117/12.899116 (visited on 08/20/2023).

[8] Ji in Kim, Jin Woo Yoon, et al. "Post-compression of a 100-TW Ti:sapphire laser (Conference Presentation)". In: *High-power, High-energy Lasers and Ultrafast Optical Technologies*. Vol. PC12577. SPIE, June 2023, PC125770G. URL: https://www.spiedigitallibrary.org/conference-proceedings-of-spie/PC12577/PC125770G/Post-compression-of-a-100-TW-Ti-sapphire-laser-Conference/10.1117/12.2669875.full (visited on 06/13/2023).

[9] Volodymyr Pervak. "Recent development and new ideas in the field of dispersive multilayer optics". EN. In: *Applied Optics* 50.9 (Mar. 2011). Publisher: Optica Publishing Group, pp. C55–C61. URL: https://opg.optica.org/ao/abstract.cfm?uri=ao-50-9-C55 (visited on 09/19/2023).

[10] Gilles Chériaux. "Influences des distorsions de phase sur le profil d'impulsions femtosecondes dans l'amplification a de rude frequence. Applicationa la generation d'impulsions de 30 tw a 10 hz dans le saphir dore au titane". These de doctorat. Paris 11, Jan. 1997. URL: https://www.theses.fr/1997PA112145 (visited on 08/18/2023).

[11] Jeff Squier, Chris P. J. Barty, et al. "Use of mismatched grating pairs in chirped-pulse amplification systems". EN. In: *Applied Optics* 37.9 (Mar. 1998). Publisher: Optica Publishing Group, pp. 1638–1641. URL: https://opg.optica.org/ao/abstract.cfm?uri=ao-37-9-1638 (visited on 06/06/2023).

[12] Selcuk Akturk, Xun Gu, et al. "Extremely simple single-prism ultrashort-pulse compressor". EN. In: *Optics Express* 14.21 (Oct. 2006), pp. 10101–10108. URL: https://www.osapublishing.org/oe/abstract.cfm?uri=oe-14-21-10101 (visited on 01/14/2019).

[13] V Aleksandrov, G Bleotu, et al. "Upgrading design of a multi-TW femtosecond laser". In: *Romanian Reports in Physics* 72 (June 2020).

[14] Y. R. Shen and Guo-Zhen Yang. "Theory of Self-Phase Modulation and Spectral Broadening". en. In: *The Supercontinuum Laser Source*. Ed. by Robert R. Alfano. New York, NY: Springer New York, 1989, pp. 1–32. URL: https://doi.org/10.1007/978-1-4757-2070-9_1 (visited on 08/10/2019).

[15] Akhmanov, V. A. Vysloukh, et al. *Optics of Femtosecond Laser Pulses*. English. 1992 edition. New York: American Institute of Physics, Oct. 1991.

[16] Fujio Shimizu. "Frequency Broadening in Liquids by a Short Light Pulse". In: *Physical Review Letters* 19.19 (Nov. 1967). Publisher: American Physical Society, pp. 1097–1100. URL: https://link.aps.org/doi/10.1103/PhysRevLett.19.1097 (visited on 08/20/2023).

[17] R. R. Alfano and S. L. Shapiro. "Observation of Self-Phase Modulation and Small-Scale Filaments in Crystals and Glasses". In: *Physical Review Letters* 24.11 (Mar. 1970), pp. 592–594. URL: https://link.aps.org/doi/10.1103/PhysRevLett.24.592 (visited on 08/10/2019).

[18] E. A. Khazanov, S. Yu Mironov, et al. "Nonlinear compression of high-power laser pulses: compression after compressor approach". en. In: *Physics-Uspekhi* 62.11 (Nov. 2019). Publisher: IOP Publishing, p. 1096. URL: https://iopscience.iop.org/article/10.3367/UFNe.2019.05.038564/meta (visited on 11/09/2020).

[19] V. Kandidov, S. Shlenov, et al. "Filamentation of high-power femtosecond laser radiation". In: *Quantum Electronics* 39 (June 2009), p. 205.

[20] P. Sprangle, J. R. Peñano, et al. "Propagation of intense short laser pulses in the atmosphere". In: *Physical Review E* 66.4 (Oct. 2002). Publisher: American Physical Society, p. 046418. URL: https://link.aps.org/doi/10.1103/PhysRevE.66.046418 (visited on 08/21/2023).

[21] E. A. Khazanov. "Post-compression of femtosecond laser pulses using self-phase modulation: from kilowatts to petawatts in 40 years". en. In: *Quantum Electronics* 52.3 (Mar. 2022). Publisher: IOP Publishing, p. 208. URL: https://iopscience.iop.org/article/10.1070/QEL18001/meta (visited on 07/13/2022).

[22] Govind P. Agrawal. *Nonlinear Fiber Optics*. en. Academic Press, Oct. 2012.

[23] V. N. Ginzburg, A. A. Kochetkov, et al. "Suppression of small-scale self-focusing of high-power laser beams due to their self-filtration during propagation in free space". en. In: *Quantum Electronics* 48.4 (Apr. 2018). Publisher: IOP Publishing, p. 325. URL: https://iopscience.iop.org/article/10.1070/QEL16637/meta (visited on 03/07/2022).

[24] Vladislav Ginzburg, Mikhail Martyanov, et al. “Small-scale fluctuations of laser beam fluence at the large B-integral in ultra-high intensity lasers”. EN. In: *Optics Express* 31.3 (Jan. 2023). Publisher: Optica Publishing Group, pp. 4667–4674. URL: https://opg.optica.org/oe/abstract.cfm?uri=oe-31-3-4667 (visited on 02/08/2023).

[25] D. Anderson and M. Lisak. “Nonlinear asymmetric self-phase modulation and self-steepening of pulses in long optical waveguides”. In: *Physical Review A* 27.3 (Mar. 1983). Publisher: American Physical Society, pp. 1393–1398. URL: https://link.aps.org/doi/10.1103/PhysRevA.27.1393 (visited on 08/21/2023).

[26] Robert W. Boyd. *Nonlinear Optics,Third Edition,9780123694706,2008*. URL: https://www.academia.edu/18337240/Boyd_Nonlinear_Optics_Third_Edition (visited on 09/27/2019).

[27] Richard Lee Sutherland, Daniel Garth McLean, et al. *Handbook of nonlinear optics*. en. 2nd ed., rev. and expanded. Optical engineering 82. New York: Marcel Dekker, 2003.

[28] M. Sheik-Bahae, A.A. Said, et al. “Sensitive measurement of optical nonlinearities using a single beam”. en. In: *IEEE Journal of Quantum Electronics* 26.4 (Apr. 1990), pp. 760–769. URL: http://ieeexplore.ieee.org/document/53394/ (visited on 02/19/2019).

[29] A. Ajami, W. Husinsky, et al. “Two-photon absorption cross section measurements of various two-photon initiators for ultrashort laser radiation applying the Z-scan technique”. EN. In: *JOSA B* 27.11 (Nov. 2010), pp. 2290–2297. URL: https://www.osapublishing.org/josab/abstract.cfm?uri=josab-27-11-2290 (visited on 07/22/2019).

[30] I Dancus, V I Vlad, et al. “Z-SCAN AND I-SCAN METHODS FOR CHARACTERIZATION OF DNA OPTICAL NONLINEARITIES”. en. In: *Romanian Reports in Physics* 65.3 (2013), pp. 966–978.

[31] Robert Adair, L. L. Chase, et al. “Nonlinear refractive-index measurements of glasses using three-wave frequency mixing”. en. In: *Journal of the Optical Society of America B* 4.6 (June 1987), p. 875. URL: https://www.osapublishing.org/abstract.cfm?URI=josab-4-6-875 (visited on 07/19/2019).

[32] M. J. Moran, C.-Y. She, et al. “Interferometric measurements of the nonlinear refractive-index coefficient relative to CS2 in laser-system-related materials”. In: *IEEE Journal of Quantum Electronics* 11 (June 1975), pp. 259–263. URL: http://adsabs.harvard.edu/abs/1975IJQE...11..259M (visited on 11/05/2020).

[33] A. Owyoung. “Ellipse rotation studies in laser host materials”. In: *IEEE Journal of Quantum Electronics* 9.11 (Nov. 1973). Conference Name: IEEE Journal of Quantum Electronics, pp. 1064–1069.

[34] R. de Nalda, R. del Coso, et al. “Limits to the determination of the nonlinear refractive index by the Z-scan method”. en. In: *Journal of the Optical Society of America B* 19.2 (Feb. 2002), p. 289. URL: https://www.osapublishing.org/abstract.cfm?URI=josab-19-2-289 (visited on 07/19/2019).

[35] A. S. L. Gomes, E. L. Filho, et al. “Thermally managed eclipse Z-scan”. en. In: *Optics Express* 15.4 (Feb. 2007), p. 1712. URL: https://www.osapublishing.org/oe/abstract.cfm?uri=oe-15-4-1712 (visited on 07/19/2019).

[36] Ioan Dancus, Silviu T. Popescu, et al. “Single shot interferometric method for measuring the nonlinear refractive index”. EN. In: *Optics Express* 21.25 (Dec. 2013). Publisher: Optical Society of America, pp. 31303–31308. URL: https://www.osapublishing.org/oe/abstract.cfm?uri=oe-21-25-31303 (visited on 12/01/2020).

[37] R. Quintero-Torres and M. Thakur. “Measurement of the nonlinear refractive index of polydiacetylene using Michelson interferometry and $z$ -scan”. en. In: *Journal of Applied Physics* 85.1 (Jan. 1999), pp. 401–403. URL: http://aip.scitation.org/doi/10.1063/1.369397 (visited on 07/19/2019).

[38] Shu-Qi Chen, Zhi-Bo Liu, et al. “Study on Z-scan characteristics for a large nonlinear phase shift”. en. In: *Journal of the Optical Society of America B* 22.9 (Sept. 2005), p. 1911. URL: https://www.osapublishing.org/abstract.cfm?URI=josab-22-9-1911 (visited on 09/12/2019).

[39] Mohammad Reza Rashidian Vaziri. “Z-scan theory for nonlocal nonlinear media with simultaneous nonlinear refraction and nonlinear absorption”. EN. In: *Applied Optics* 52.20 (July 2013), pp. 4843–4848. URL: https://www.osapublishing.org/ao/abstract.cfm?uri=ao-52-20-4843 (visited on 07/22/2019).

[40] M. Yin, H.P. Li, et al. “Determination of nonlinear absorption and refraction by single Z-scan method”. en. In: *Applied Physics B: Lasers and Optics* 70.4 (Apr. 2000), pp. 587–591. URL: http://link.springer.com/10.1007/s003400050866 (visited on 05/06/2019).

[41] P. Chen, D. A. Oulianov, et al. “Two-dimensional $Z$ scan for arbitrary beam shape and sample thickness”. en. In: *Journal of Applied Physics* 85.10 (May 1999), pp. 7043–7050. URL: http://aip.scitation.org/doi/10.1063/1.370510 (visited on 05/08/2019).

[42] E. V. Garcia Ramirez, M. L. Arroyo Carrasco, et al. “Z-scan and spatial self-phase modulation of a Gaussian beam in a thin nonlocal nonlinear media”. en. In: *Journal of Optics* 13.8 (Aug. 2011). Publisher: IOP Publishing, p. 085203. URL: https://doi.org/10.1088%2F2040-8978%2F13%2F8%2F085203 (visited on 11/30/2020).

[43] Sang Jo Lee, Geun-Hyeong Kim, et al. “Z-scan analysis for photorefractive LiNbO3:Fe crystals of arbitrary thickness”. en. In: *Journal of the Korean Physical Society* 67.3 (Aug. 2015), pp. 413–417. URL: http://link.springer.com/10.3938/jkps.67.413 (visited on 04/10/2019).

[44] Chong Hoon Kwak, Yeung Lak Lee, et al. “Analysis of asymmetric Z-scan measurement for large optical nonlinearities in an amorphous As2S3 thin film”. en. In: *Journal of the Optical Society of America B* 16.4 (Apr. 1999), p. 600. URL: https://www.osapublishing.org/abstract.cfm?URI=josab-16-4-600 (visited on 04/10/2019).

[45] Bing Gu, Wei Ji, et al. “Analytical expression for femtosecond-pulsed z scans on instantaneous nonlinearity”. en. In: (), p. 6.

[46] Robert Adair, L. L. Chase, et al. “Nonlinear refractive index of optical crystals”. en. In: *Physical Review B* 39.5 (Feb. 1989), pp. 3337–3350. URL: https://link.aps.org/doi/10.1103/PhysRevB.39.3337 (visited on 03/27/2019).

[47] Christophe Finot, F. Chaussard, et al. “Simple guidelines to predict self-phase modulation patterns”. EN. In: *JOSA B* 35.12 (Dec. 2018). Publisher: Optica Publishing Group, pp. 3143–3152. URL: https://opg.optica.org/josab/abstract.cfm?uri=josab-35-12-3143 (visited on 08/24/2023).

[48] S. Gales, K. A. Tanaka, et al. "The extreme light infrastructure—nuclear physics (ELI-NP) facility: new horizons in physics with 10 PW ultra-intense lasers and 20 MeV brilliant gamma beams". en. In: *Reports on Progress in Physics* 81.9 (Aug. 2018). Publisher: IOP Publishing, p. 094301. URL: https://doi.org/10.1088/1361-6633/aacfe8 (visited on 02/11/2021).

[49] Veselin Aleksandrov, Gabriel Bleotu, et al. "Femtosecond Pulse Shortening using Cascaded Quadratic Nonlinearities for High Temporal Contrast". en. In: *2019 Conference on Lasers and Electro-Optics Europe & European Quantum Electronics Conference (CLEO/Europe-EQEC)*. Munich, Germany: IEEE, June 2019, pp. 1–1. URL: https://ieeexplore.ieee.org/document/8872446/ (visited on 08/19/2023).

CHAPTER 3

# Chapter 3 Optical components for post-compression

*A road map of expertise, challenges and improvements*
— Gabriel P. Bleotu

In the previous chapter, several theoretical tools for describing nonlinear light-matter interactions were presented. Using those theoretical tools, in this chapter, I will provide a comprehensive overview of the preliminary results on the full characterization of optical components for spectral broadening.
As detailed in Section 2.3, the non-linear refractive index is a key parameter for self-phase modulation (SPM). Thus, the selection of appropriate materials is paramount for high-energy laser systems, with a particular emphasis on preserving their optical qualities.
This chapter highlights the specification in fabrication of glass and plastic plates while underscoring the essential material properties necessary for successful spectral broadening. The complete characterization of the optical properties of materials was conducted around the central wavelength ($\lambda_{central}$ = 800 nm), specific to Ti:sapphire lasers, including the laser systems utilized in the subsequent chapter.
I will describe the results obtained with consecrated techniques and I will introduce novel techniques that have been developed to measure and to characterize the nonlinear refractive index and the laser-induced damage threshold. Furthermore, I will demonstrate the practicality and effectiveness of a dedicated experimental setup that has been employed to conduct these measurements.
This chapter presents original results (measurements and simulations) and contributions to the field of materials characterization. Despite the ongoing developments in material science and post-compression research, there is a notable absence of published results that match the comprehensive characterization undertaken in this chapter. The data presented here represent a developmental roadmap, showcasing progress, problem-solving, and the expertise gained along the way. In essence, it outlines the journey from fundamental techniques to addressing challenges and discovering solutions.

## 3.1 Optical materials for spectral broadening

This section discusses the importance of finding suitable materials for high-energy laser systems and the preservation of the laser pulses optical quality. It mentions the fabrication of glass plates and the properties required for materials used in spectral broadening.

The most suitable materials for Petawatt- class laser should have a high ratio between the diameter and the thickness of the optical materials. The optical quality of the material is related to the wavefront distortion which can alter the quality of the focused beam on target. Fabrication of 20 cm diameter and 1 mm thickness, glass plates, with high optical quality has been developed [1] and used to compress from 63 fs to 20.5 fs. The largest optical glass material presented in this work, a 30 cm Schott AF32eco, 0.3 mm thickness, was used here to generate SPM that can support 11 fs (0.5 PW beam at Apollon (see Chapter IV))[2]. Still, the difficulties for fabrication of large (m size) and thin (sub mm) glass plates remain unsolved.

One of the main requirements, in the high energy lasers systems, is the preservation of the optical quality of the initial compressed pulse. This quality can be altered after propagation through free space, other optics or materials. Thin Film Compression (TFC) method, described in Chapter I, is based on the insertion of a new material into the pulse path. Depending on the quality and the nonlinear response of the material, the pulse parameters may be slightly changed. The materials used to generate the SPM effect must have, first of all, the necessary optical characteristics and properties. These include:

1) Good moldability, high flowablity- allow a good fit in size and shape;

2) Adequate chemical composition: Depending on the chemical elements used, the coefficients of linear and non-linear absorption differ;

3) Low optical birefringence;

4) Extremely low water absorption and moisture permeation;

5) High heat resistance (very important for high repetition rate lasers);

6) Low auto-fluorescence;

7) High transparency;

8) Surface quality: low roughness;

9) Minimal wavefront distortions;

10) Low dispersion (GDD);

11) High damage threshold (LIDT);

12) Different sizes and thicknesses;

13) Vacuum compatibility;

The chemical properties, including the mechanical ones, can be found in the data sheets provided by the manufacturers and are not the subject of this thesis. The mentioned optical properties are essential for HPLS proposed upgrade and they need to be measured in detail. All the plastic materials used in this thesis are procured from commercial manufacturers (i.e. Microfluidic Chip Shop, Osaka Gas Chemicals OKP-F1, MGM).

The majority of the plastic materials which are studied further covers the mentioned conditions. So far, there is still no material that provides the best values for each property. A series of materials such as cellulose acetate, Poly(methyl methacrylate) (PMMA) have been and are being used to expand the spectral bandwidth [3]. A series of new plastics such as Zeonor [4, 5], Zeonex, Apel films, OKP [6] and Schott and Corning Glasses offer future perspectives, and these are the ones we investigate here. Also, they are coming with the main advantage of reduced cost compared with nonlinear crystals such as LBO, BBO, KDP [7] etc.

For PW class, the possibility to have large manufacturing size (higher than 30 cm) and to preserve the laser pulse properties after passing through material are both essential for scaling the process from prototype testing on small beams to full aperture laser facilities. In this respect, plastics offer obvious advantages such as large size, high optical quality (low roughness, high transmission), a refractive index close to the glass one (i.e. Zeonex has n=1.52 ) etc. However, they also have drawbacks: the LIDT damage threshold is lower compared with glass (1), the plastic film thickness may introduce a positive dispersion that can alter the pulse duration (2) and the surface poor quality leads to deformation of the wavefront and appearance of hotspots and a larger focus (3). As a consequence, the quality of interaction between the laser pulse and the target can be affected.

At the moment, plenty of optical bulk materials are available on the market for various purposes and can be potentially used. As a first step, a complete characterization (see Figure 3.1) of their optical properties is needed to select the most suitable among them. In this chapter, I will discuss the work done to measure the dispersion, the roughness, the transmission, the vacuum compatibility, the nonlinear refractive index, the nonlinear absorption coefficient and the transmitted wavefront of various plastic and glass materials. As a second step, I will provide a detailed discussion of three key characteristics: nonlinearities, the laser-induced damage threshold (LIDT), and spectral broadening characterization. These aspects are key parameters for the selection of materials in the context of SPM and post-compression processes.

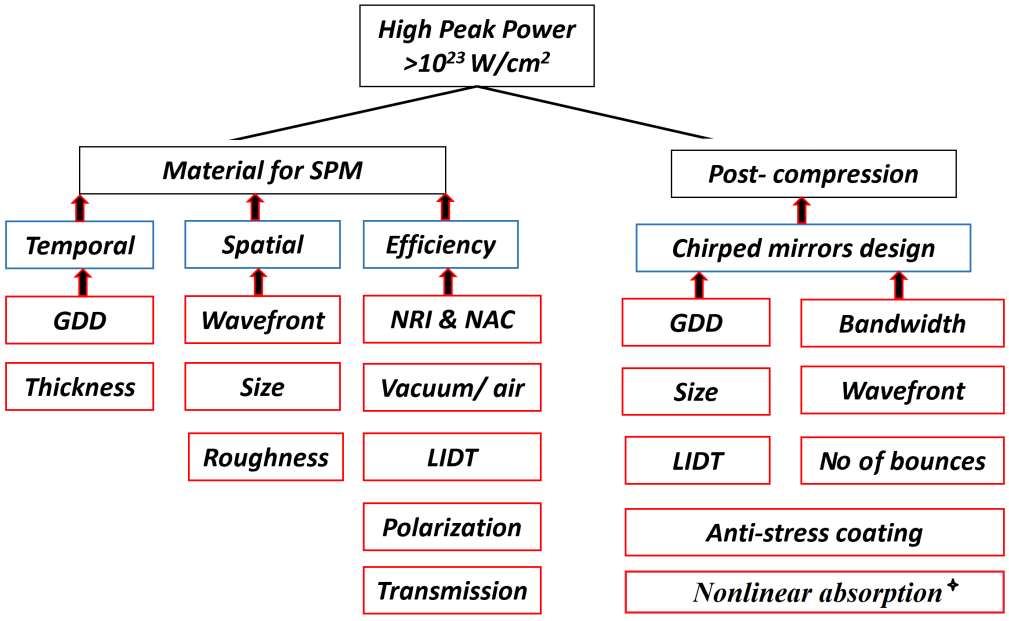


Figure 3.1: The key parameters towards an efficient post-compression experiment for peak power enhancement

Each element from Figure 3.1 plays an important role for an efficient peak power enhancement. They can be related to two main groups: the right material for SPM and Chirped mirrors (CM) choice. The CM parameters were established after multiple discussions with the manufacturers such as Ultrafast-Innovation, Optosigma, LaserOptik, Laser2000 and after previous experience gained from experiments [8, 9, 10]. The star alongside the nonlinear absorption in CM is a novel parameter observed recently in experiments and which is not deeply understood till present.

## 3.2 Optical materials characterization

This section focuses on various characterization methods for optical materials. It presents the measurements of the group delay dispersion (GDD) and of the third-order dispersion (TOD), as well as the measurement of roughness measurements. The impact of these parameters on transmitted wavefront is analyzed and discussed.

The materials chosen to be characterized were: glasses-FS (2 types), BK7, SF5, Zeonor, Zeonex, Topas, Apel, PMMA, PolyCarbonate (PC) and they were commercially available.

### 3.2.1 Dispersion

When a short pulse propagates through a material it will accumulate dispersion. The dispersion is proportional with the length of the material. This effect induces pulse duration stretching in time. A shorter pulse duration (with larger bandwidth) is more sensitive to even small levels of dispersion. For instance, after passing through 1 mm of FS glass, a laser pulse ($\lambda_{central}$ = 800 nm) with 5 fs pulse duration will be stretched in time to 25.27 fs while a 50 fs pulse duration to 50.06 fs. Thus, the GDD of each material contributes to the choice of the right chirped mirrors which are used to compensate the positive dispersion introduced by the material. The dispersion for several materials was measured using a Chromatis device (KMLabs) for both S and P polarizations. The results were similar and they can be seen in Figure 3.2 where the S-polarization results were used as example.

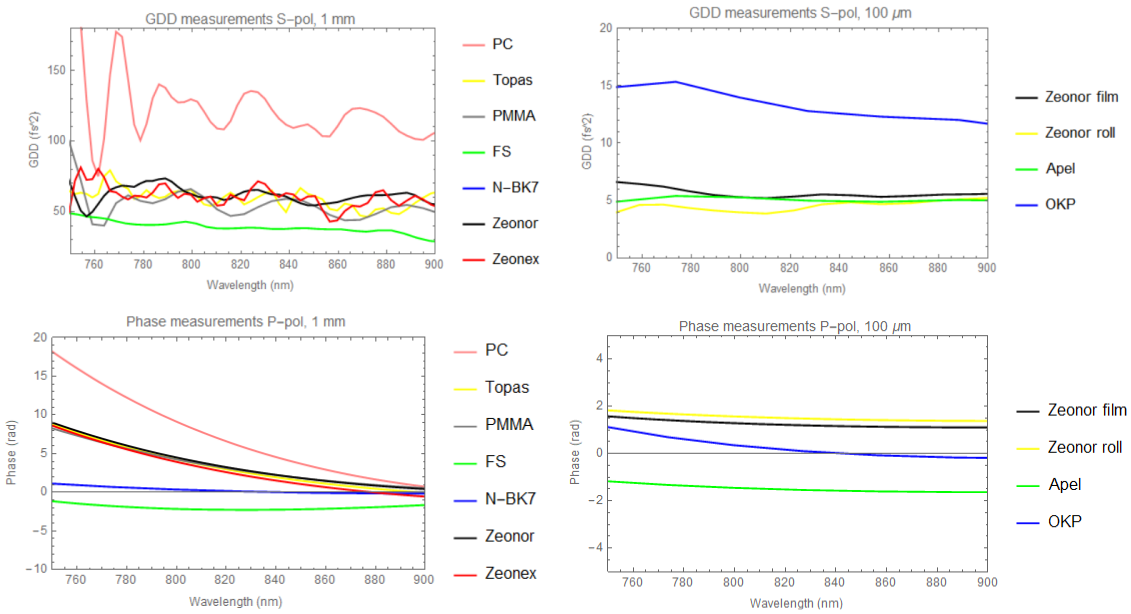


Figure 3.2: Group delay dispersion (top) and Phase measurements (bottom) for thick (1 mm) and thin (100 $\mu m$) transparent materials

The device uses time-domain white light interferometry (WLI) to offer information about the GDD ($fs^2$), the TOD ($fs^3$), and phase (rad) which are general properties of reflective and transmissive optical components that need to be known when femtosecond pulsed lasers are used.

The main results are presented in Table 3.2, at the end of this sub-section. The ideal material should have the lowest GDD value to not alter the pulse duration and to be easily compensated by the CMs. It was observed that the NRI is also smaller for materials with low GDD as for instance 1 mm of FS compared with 1 mm of Zeonor. According to Eq.2.57

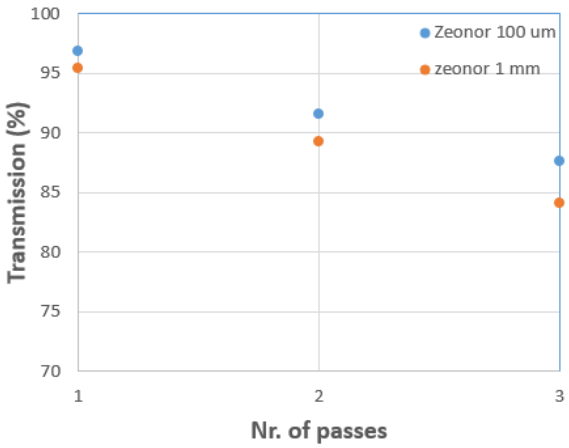


Figure 3.3: Transmission measurements dependence of the no. of passes for Zeonor plastic with 2 different thicknesses, 1 mm and 0.1 mm

the nonlinear phase will be smaller thus the broadening effect will be smaller too. As an early conclusion, I can mention the possibility of using multiple thin (hundreds of microns) plastic materials to enhance the SPM process. This method was proposed also to minimize the effect of small-scale self-focusing in ultrahigh-power lasers [10].

Besides the GDD measurements, TOD was measured too with values ranging from 170 $fs^3$ (FS) to 775 $fs^3$ (Zeonex, PC). For the thin films, the TOD was below 12 $fs^3$. Within Chromatis measurements, the phase was acquired too and presented in Figure 3.2 bottom. This preliminary measurements (before experiments) are useful for the design of the CMs. The data of GDD and phase for 1 mm FS were used in the design of the CM (See Chapter 3.6). I observed that, for the chosen materials, the results were very similar for both S and P polarizations and therefore this materials can be used at different laser facilities.

### 3.2.2 Transmission

The transmission was measured using the Avesta laser system, P-polarized, presented in Figure 3.7 and an energy meter. The energy was measured before and after each sample positioned at Brewster angle. The results are presented in Table 3.2. Similar measurements were performed for 2, 3 and 4 passes through the material. All of them offer a good transmission (more than 96%) thus reducing the energy losses through transmission, absorption, or secondary reflections (Fresnel reflections). An example of transmission data is shown in Figure 3.3 where the same material but with 2 different thicknesses was compared. In the literature, both single pass [9] or several [4] have been used to post-compress the laser pulses. These information were used in all the experiments presented in the following Chapter.

From the transmission measurement, it was concluded that the thin (100 $\mu$m) plastic materials have better transmission due to the optical quality. This advantage will be further elucidated through roughness and transmitted wavefront measurements. To compensate for the thickness parameter in SPM, multiple films can be used in series.

### 3.2.3 Roughness

The material quality and roughness can influence the transmitted wavefront of a short laser pulse. A profilometer (Sensofar, S Neox) based on white light interferometry was used to measure the roughness of each material (see Figure 3.4a). The light interference occurs

when there is a difference in distance traveled by the light (light path) from the surface of a target object to a certain point. The sample surface irregularities make these path lengths to be unequal thus creating an interference pattern on the CCD. The interference pattern is translated into peaks and valleys on the sample surface. The results were obtained using a 50X microscope objective. It was observed that the thin materials have a lower roughness (see Table 3.2) and thus, qualitatively speaking, their contribution to wavefront distortions is minimum.

### 3.2.4 Vacuum compatibility

To minimize the interaction with air and to avoid ionization, high power laser pulses are propagated through vacuum. Taking into account that the SPM process is achieved in vacuum and that no vacuum tests are provided by the plastic materials manufacturers, a series of measurements was performed to test the out gassing effects of each material. A vacuum chamber (down to $10^{-9}$ mbar) pumped by a turbo-molecular pump was used to see if the vacuum is maintained while those materials are used (See Figure 3.4b). Two pieces of Zeonor with 1.5 mm thickness and 125 mm diameter were placed also in vacuum to observe if a larger quantity of material influences the final vacuum pressure. It can be seen that after 15 minutes of pumping the chamber reached the nominal pressure. All the materials can be used in vacuum and they do not present any vacuum contamination risk.

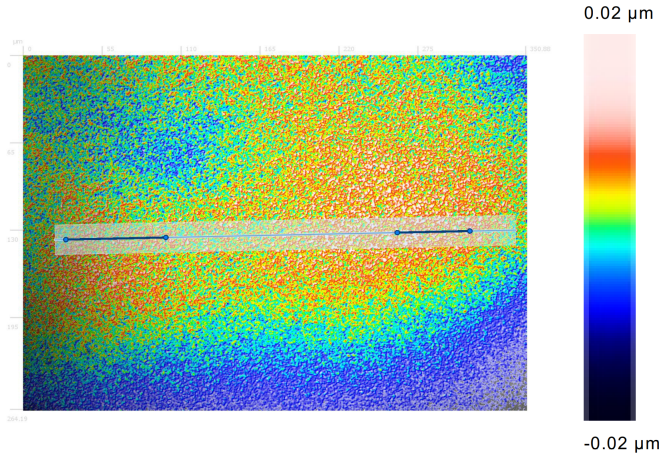


(a)

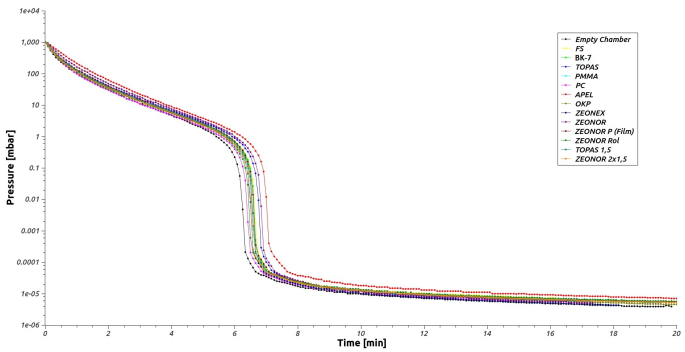


(b)

Figure 3.4: Example: Zeonor film surface roughness for 350 x 264 $\mu m$ sample (top) and vacuum measurements (bottom)

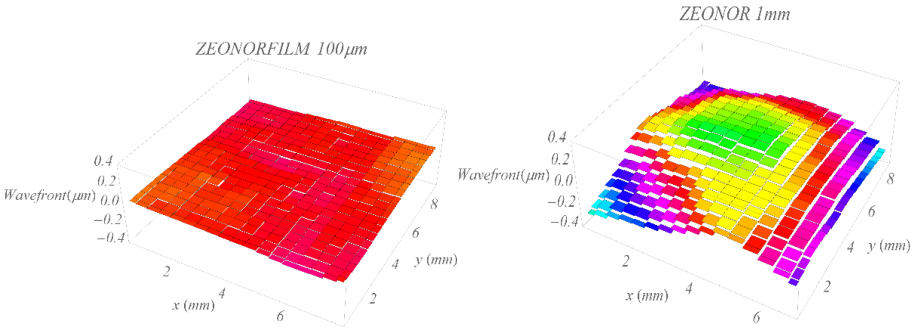


(a) (b)

Figure 3.5: Example: Wavefront distortions comparison between a) Zeonor thin film and b) Zeonor thick film

### 3.2.5 Wavefront distortions

Experiments based on particle acceleration or laser-matter interaction require a high quality focused beam [11]. This criterion is related to the wavefront distortion. The insertion of a transparent material in the laser pulse optical path may lead to spectral broadening but also to a distorted focused beam. The results shown in the next section will detail these effects by comparing different materials with respect to SPM and Far-Field (FF) images. The wavefront aberrations introduced by the materials have been mentioned, investigated and solutions were implemented to correct them [12].

An adaptive optics kit (THORLABS- Adaptive optics Kit) and a reconstruction software were used to determine the variation of the peak-to-valley and RMS for each material. The role of the deformable mirror (DM) is to compensate (correct) the wavefront aberrations within the optical arrangement, as part of the closed-loop system alongside the wavefront sensor and real-time control software. The DM was used to create a flat reference wavefront of a He-Ne laser beam expanded to a 1 inch diameter. The laser beam wavefront after passing through the material is shown in Figure 3.5 where same materials with different thicknesses and optical quality were compared. As a reference, the measured beam (in the absence of the sample) had a wavefront with RMS of $\lambda/13$ $\mu m$ and a Peak to Valley (P-to-V) of $\lambda/3$ $\mu m$. Thin plastic materials proved to be more suitable for experiments where the FF is important. Taking into account that SPM is related to the material thickness, multiple thin samples can be used in series at the Brewster angle.

The quality of thin film plastics as Zeonor was observed also in the Profilometer measurements. For the thin material, a deviation of 0.18 nm was measured across 100 $\mu$m while for the thick one, a deviation of 3.20 nm was measured across 243 $\mu$m. The comparative results of 1 mm and 0.1 mm Zeonor are illustrated in Figure 3.6

## 3.3 Experimental Setup

To be able to measure as much as possible material properties, I designed and built an experimental setup which can measure transmission, nonlinearities and damage threshold.

The experimental setup I used, is depicted in Figure 3.7. It consists of three main subensembles (I, II and III). The first one is based on a Z-scan (open and closed aperture) or I-scan configuration [13, 14] aimed to measure and to double validate the sign and the magnitude of the NRI and NAC. Secondly, a long working distance imaging system (LWDIS) is used to measure and qualify the laser induced damage threshold through different image

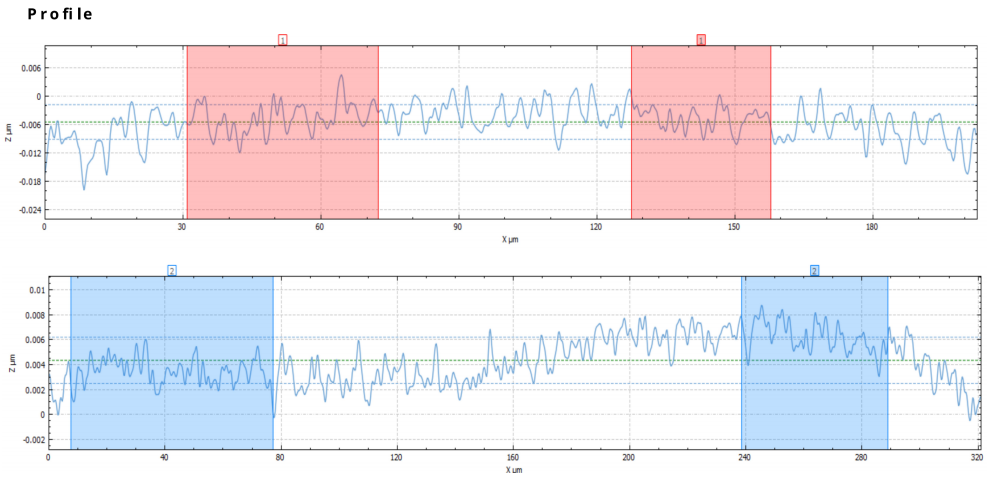


Figure 3.6: Profilometry results of Zeonor plastic across the surface.

processing methods (discussed in Chapter III). Thirdly, a Fiber Spectrometer (FS) was used to monitor the spectral broadening during the shots.

An AVESTA Ti:sapphire laser system was used to provide compressed laser pulses (40 fs, 800 nm, 10 Hz, 1 mJ) to the experimental setup. The pulse energy was reduced by using a wedge with a 4% transmission and the combination between a $\lambda/2$ waveplate (WP) and a polarizer cube (POL). The WP was mounted on a motorized rotation stage allowing the polarization to change by up to 90° for 45° of WP rotation. The transmitted energy ($36\ \mu J \pm 1.5\ \mu J$) was focused by a plano-convex lens (L1) with a 40 cm focal length. The pulse duration ($40 \pm 3$ fs ) was measured using a SHG Autocorrelator and confirmed with SHG FROG [15].

### 3.3.1 Assembly no. I - nonlinearities measurements

The reflected energy was measured using a energy meter (EM) and used for energy monitoring when Z-scan or I-scan measurements were performed (see Figure 3.7 I). The energy on the sample was estimated using 1% of the transmitted energy through the mirror M2 on PD1 calibrated using Malus' law. The data recorded from the ensemble of the photodiodes PD1-3 (type DET10A2 Si detector, 1 ns rise time) and the oscilloscope (4 channels Tektronix, 1 GHz) were used to estimate the nonlinear refractive index and the nonlinear absorption coefficient of the sample. Using the reflection from a high quality thin FS plate (TP) the light was split by the 50-50 beamsplitter to the PD2 for the closed-aperture Z-scan measurements (NRI retrieval) and to PD3 for the open-aperture Z-scan measurements (NAC retrieval). PD3 collects all the light focused by a plano-concave lens (L2) with a 10 cm focal length and the light which arrives on PD2 is limited by the detector aperture- 0.8 $mm^2$. For the Z-scan measurements, the sample was mounted on a motorized translation stage with a 50 mm travel range.

### 3.3.2 Assembly no. II - LIDT measurements

A long working distance imaging system (LWDIS) (see Figure 3.7 II) was designed and manufactured to efficiently monitor and diagnose, in real time, the intensity pattern in the interaction area of a laser beam with the sample. This kind of imaging system was proposed also to qualify the focal spot of the high power laser systems [16]. The LWDIS is realized using an 8 inch aperture spherical mirror to gather the light and a microscope objective to further magnify the image on the CCD detector plane. A 6-inch diameter

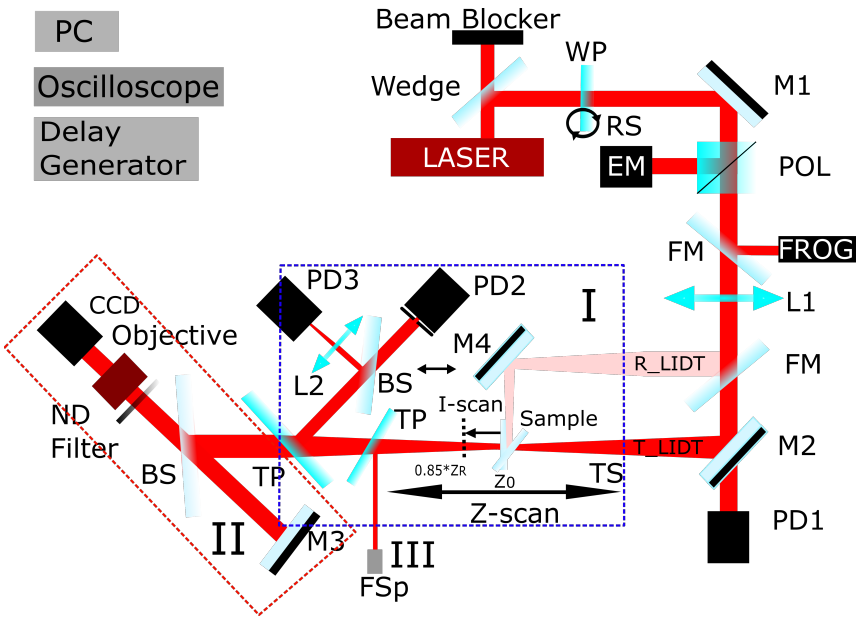


Figure 3.7: Experimental Setup in air: I) **I and Z-scan** for Nonlinear Absorption Coefficient and Nonlinear refractive index (NRI) measurements [3], II) **Long Working Distance Imaging System (LWDIS)** for LIDT measurements and III) **Fiber Spectrometer (FSp)** for Self Phase Modulations (SPM) measurements. The setup has the following optical elements: BS-beamsplitter, EM -energy meter, FS- fiber spectrometer, FM- flip mirror, LASER - Ti: Sapphire, L1 and L2 -focusing lenses, M1, M4-high reflective mirror, M2- 99% reflective mirror, M3- spherical mirror, ND- neutral density filter, POL- polarizer, PD1, PD2 and PD3 - photodiodes, TP- thin FS plate, TS- translation stage, RS -rotation stage, WP - $\lambda/2$ waveplate.

beamsplitter with distortions of the transmitted wavefront $< \lambda/20$ is used to redirect the light reflected from the spherical mirror to the microscope objective and to attenuate the incoming light amplitude. This assembly (II) was designed to estimate in real time the LIDT in both reflection and transmission, and thus I extended the capabilities of this setup for numerous types of samples.

Online monitoring of the image in the object plane of the LWDIS objective was the quickest method to estimate, in real time when the damage occurs. It also provided an alternative method to qualify the nonlinearities from the images analysis.

### 3.3.3 Assembly no. III - SPM measurements

A fiber spectrometer (see Figure 3.7 III) (Ocean View, 700 - 900 nm range) was used to record the spectral broadening when incrementing the laser pulse energy (0 - 46 $\mu J$). To avoid SPM generation in the other optical components (i.e. TP, BS2), the beam size was large enough to maintain a fluence ($J/cm^2$) which does not change the spectral characteristics of the laser pulse.

Automation of the entire experiment requires a specific synchronization time control for all the devices. The delay generator triggered by a signal from the laser control unit is used to generate on-demand pulses by gating the opening of the Pockels cell, and also to send synchronization signals to the camera, PDs, AC and the oscilloscope used for data acquisition. We designed, using the Python programming code, an user interface which allows to select the measurement type (I-scan, Z-scan or both for the damage tests), the translation and rotation stages steps, number of shots, CCD camera level saturation, online CCD image monitoring with and without laser illumination, the spectrum and online

averaging of the PD2 and PD3 signals during measurements.

I contributed in the automation through the implementation of the translation stages, PDs signal acquisitions, absorption and refractive index points plot and with multiple ideas related to size of the beam monitoring, variable ND filter, LIDT tests algorithms and with the calibrations factors for energy and spot size. The development of this automatized experimental setup, provides rapidity and control over the acquired data and makes it a complete characterization system which can be used to characterize a large variety of transparent materials.

### 3.3.4 Experimental setup calibration

In the following sub-chapters dedicated to nonlinearities and LIDT measurements, the major laser parameters are the input spot size, focus, $M^2$ -quality factor for a Gaussian beam, the pulse duration and the laser pulse energy. Any deviation from their mean value will lead to other effects like large phase shift, high nonlinear effects, damage, large standard deviation of the measured parameters (i.e. $n_2$, fluence).

My preliminary observations, when the setup was not automatized, were: i) photodiodes signal vary rapidly, ii) photodiodes were not able to measure low signal due to their threshold even if the nonlinearities were present, iii) variation of the input energy due to Oscillator/ Regenerative amplifier/ Pockels cells, temperature and humidity led to noisy curves, iv) the spot size variation led to different irradiances while the sample was in the focus and thus higher nonlinearities arised. In my case, when the input energy had a Root Mean Square (RMS) value higher than 6% the experiment was repeated. In other words, to avoid plenty of problems that are not mentioned in the reference papers, it is important to pay a careful attention to the following laser parameters:

#### 3.3.4.1 Spot size and $M^2$

The beam spot size after the polarizer was 8 ±0.3 mm and focused by L1 in the object plane of the LWDIS. The CCD camera captured the image of the beam on the sample. The distance between the LWDIS objective and the sample was set to 25 mm, aligning the object plane and the focal plane of the lens at the origin. This specific position of the translation stage (TS) was crucial for Z-scan measurements. Lens L1 was mounted on another translation stage with an adjustable range of 13 mm, allowing us to change the beam spot size on the sample.

The spot size calibration coefficient was obtained using a calibrated 1951 USAF resolution test chart placed in the object plane of the LWDIS (See Figure 3.8). The distance between two lines (88.4 $\mu$m) was equivalent to 80 pixels on the CCD camera resulting in a calibration coefficient of 1.10 $\mu$m/pixel.

By varying the lens position and recording the images on CCD camera, it was possible to estimate the $M^2$ parameter (<2.2 for both axes). The measured beam spot sizes on X and Y directions, are showed in Figure 3.9.

The minimum measured waist was 41.25 $\mu m$ at $1/e^2$ on X axis and 32.45 $\mu$m on Y axis. The residual astigmatism may come from the laser chain. The astigmatism was reduced to minimum with the orientation of the lens L1. The experimental results were measured by keeping the lens at a distance of 10 mm far away from the LWDIS object plane.

The effective beam area on surface ($S_{\text{eff}}$), considering a Gaussian shape beam with respect to the ISO standards [17], has been computed using the equation (3.1) [18], where the $A_{\text{pixel}}$ and $A_{\text{max}}$ indicate the amplitudes of each pixel in the CCD matrix and the maximum amplitude of the matrix, respectively. The pixel area $S_{\text{pixel}}$ in the object plane of the IS is determined by calibration using the USAF 1951 target.

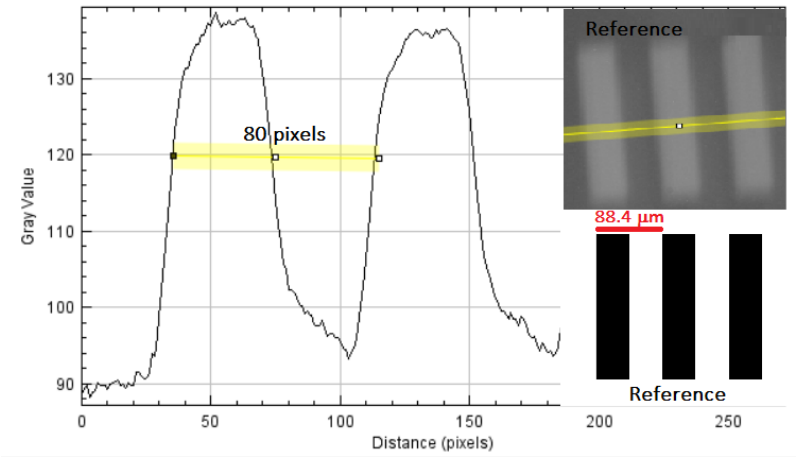


Figure 3.8: Spot size calibration using a resolution test chart

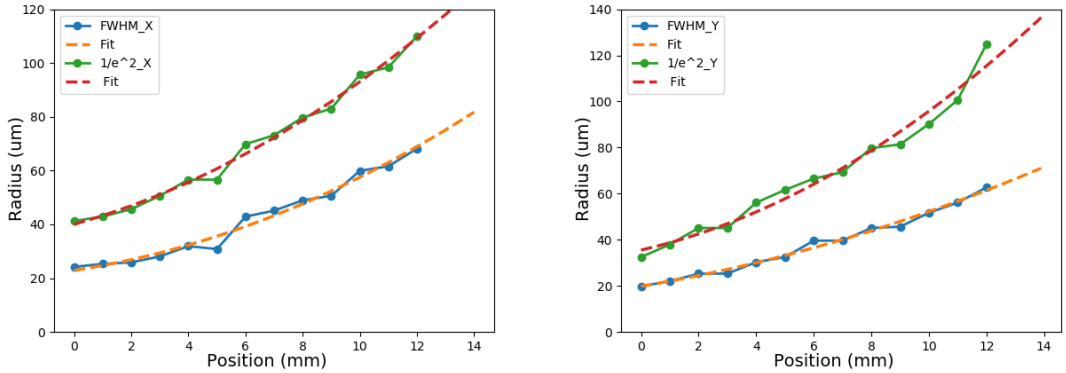


(a) Beam radius at FWHM and at $1/e^2$ on X axis (b) Beam radius at FWHM and at $1/e^2$ on Y axis

Figure 3.9: The beam diameter variations with the lens displacement

$$S_{\text{eff}} = \frac{S_{\text{pixel}} \sum_{\text{pixel}} A_{\text{pixel}}}{A_{\text{max}}} \tag{3.1}$$

The effective area will be further used for LIDT measurements in the fluence estimation or plotting the color map.

#### 3.3.4.2 Laser pulse energy

While working with fs laser pulses, the fluctuations in energy can appear from shot to shot. To know the value of energy at each shot, I used the Malus Law calibrated with the signal from the reference photodiode (PD1). The energy calibration was done by rotating the WP from 0 to 90°, 1° step and recording 20 PDs amplitude values at each step. The mean of these 20 values is presented below with orange dots. A cosine function was used to fit the normalized averaged PD1 data and to estimate the transmitted energy on the sample (Fig. 3.10).

$$Transmission = (1 + (cos(4 * \theta * \pi/180))) * 0.5 \tag{3.2}$$

$$Energy_{sample} = Transmission * Energy_{input} \tag{3.3}$$

where $\theta$ is the angle of the WP, in degrees and Energy$_{input}$ was the measured energy after the polarizer.

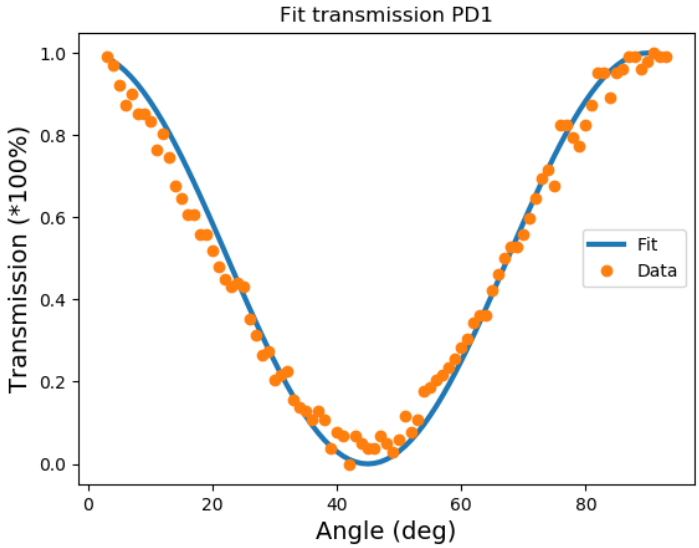


Figure 3.10: Transmission percent as a function of the waveplate angle

The energy at minimum transmission was not 0 due to the residual polarization from POL and the limitation of the PDs noise. As a short conclusion, this calibration was very useful to know, shot to shot, the energy of the laser pulse and to implement it in the nonlinearities algorithm fit.

#### 3.3.4.3 Pulse duration

The LIDT and Z-scan measurements require the pulse duration at the sample front face. For the Z-scan measurements, the pulse duration on the sample was estimated by taking into account the propagation through 16 mm of BK7 glass (WP -3 mm, POL- 10 mm and L1- 3 mm). Considering the group velocity dispersion (GVD) of BK7 glass as 44.68 fs$^2$/mm and an initial pulse duration of 42 fs, 24 nm bandwidth, the pulse duration was equivalent to 60 fs at FWHM. An example of the temporal measurements can be seen in Figure 3.11.

To retrieve the shortest laser pulse duration of 40 fs, I detuned the optical compressor introducing negative dispersion through the displacement of the gratings and incidence angle in compressor tuning. For the radius Z-scan and Image Z/I scan methods, the polarizer was changed with a thinner one (3 mm). The pulse duration measurements were performed before the lens (L1) with a 5 mm spot size out of 8 mm.

## 3.4 Nonlinearities Measurements

In this section, various techniques will be explored to measure and characterize these nonlinear effects with precision. Moreover, I will uncover the potential of novel techniques that are used to qualify the NRI providing faster or combined alternatives.

The most important experimental parameters regarding a Z-scan measurement are the precise knowledge of the values for energy, waist, pulse duration and size of the aperture.

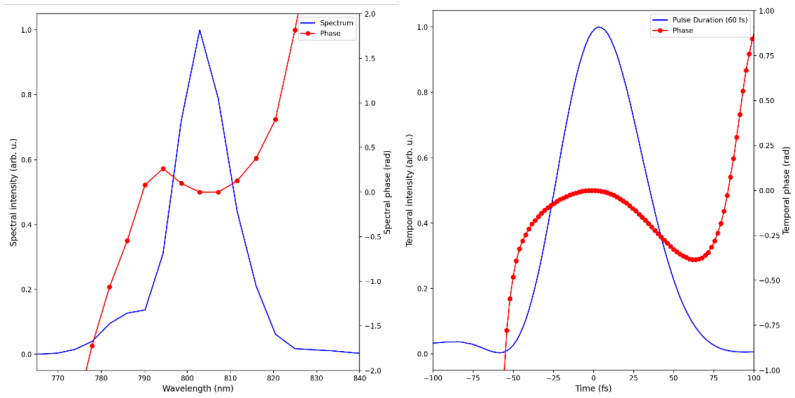


Figure 3.11: Pulse spectrum and spectral phase (left) and pulse duration and temporal phase measurements

By averaging 10 incident images, the waist was estimated to 33 $\mu m$ on X axis and 42 $\mu m$ on Y axis with an uncertainty of 5%. For this measurement, $z_R$ was calculated to be 4 mm at the central wavelength of 800 nm.

From a Z-scan measurement, the normalized transmittance (named Transmittance in the following figures) is obtained by dividing the data from CA and OA (PD2 and PD3) to the reference values obtained when the sample is far from the focus, and no nonlinearities occurred. By dividing the data from CA to OA, a pure nonlinear refraction coefficient can be determined. Consequently, by fitting the Z-scan curves, the sign and magnitude of $n_2$ or $\beta$ are extracted. The nonlinear characterization of these plastics was done for the first time, to the best of my knowledge. The preliminary results measured for glasses were compared with the values from the literature. These values were used for the validation of the plastics nonlinear coefficients and the reliability of the setup.

The NRI and NAC were measured for different values of the energy and the results were fitted with the following equations extracted from [13].

$$T_{OA} \simeq 1 - \frac{\beta \cdot I \cdot l_{eff}}{(1+x) \cdot 2\sqrt{2}} \tag{3.4}$$

$$T_{CA} \simeq 1 - \frac{4 \cdot \Delta\Phi \cdot x}{(x^2+9) \cdot (x^2+1)} \tag{3.5}$$

### 3.4.1 Nonlinear refractive index, nonlinear absorption

Figure 3.12 presents examples of Z-scan and I-scan measurements for a well known material: Fused Silica (FS, $SiO_2$). Using the classical Z-scan method proposed by S. Bahae [13], the NRI and NAC (see Figure 3.12a) were measured and shown to be in agreement with what other research teams found [19]. The classical I-scan method was used to crosscheck the results. This method can also be used to identify and distinguish between the four regions (I- linear regime, II- the nonlinear regime where the contribution of the NRI is significant, III- high-order nonlinearities, multiphoton ionization, self-focusing, and non-permanent damage (the material return to its ground state after molecular relaxation), IV- permanent damage) (see Figure 3.12b). In the following section, I will consider the third and forth regions as one, namely "Damage", see Figure 3.48) .

The last 3 regions should be further studied for a better understanding, in the fs regime, where the actual NRI and LIDT database is quite low. These material phases provide information about the irradiance level and where a repetitive measurement should

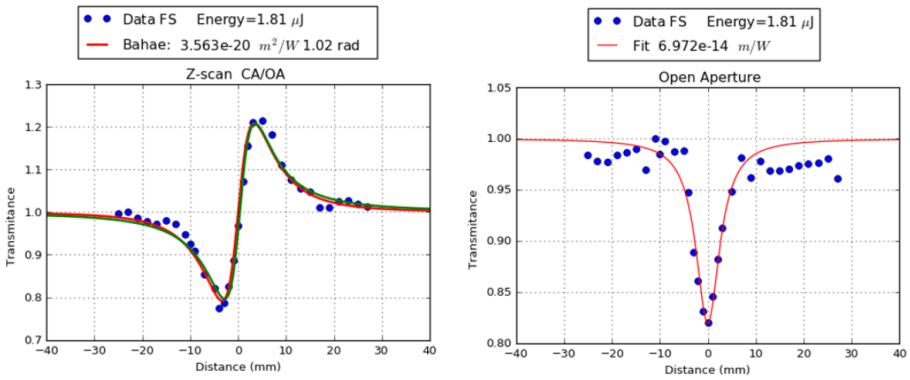


(a)

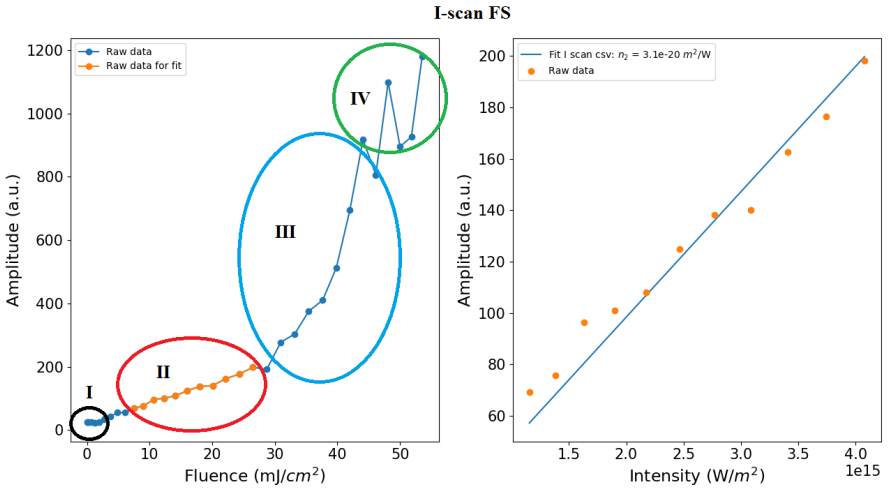


(b)

Figure 3.12: a) Example of NRI and NAC results from a Z-scan measurement and b) the material phases from linear regime to the permanent damage and NRI result from an I-scan measurement

stop, thus avoiding the permanent material damage. Using the fitting equation from [14], the NRI was retrieved (see Figure 3.12b right graph).

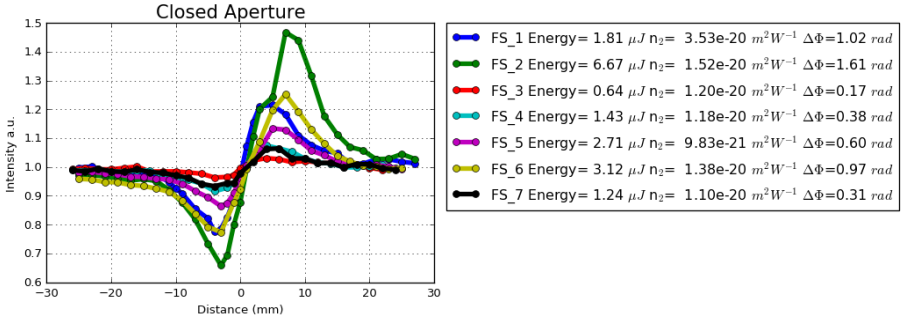


Figure 3.13: Experimental results of NRI measurement for FS at different input energies

### 3.4.2 Presence of high-order nonlinearities and large phase shift

This section presents my personal observations concerning the distinctive characteristics of asymmetric Z-scan curves arising from the interplay of high-order nonlinearities and

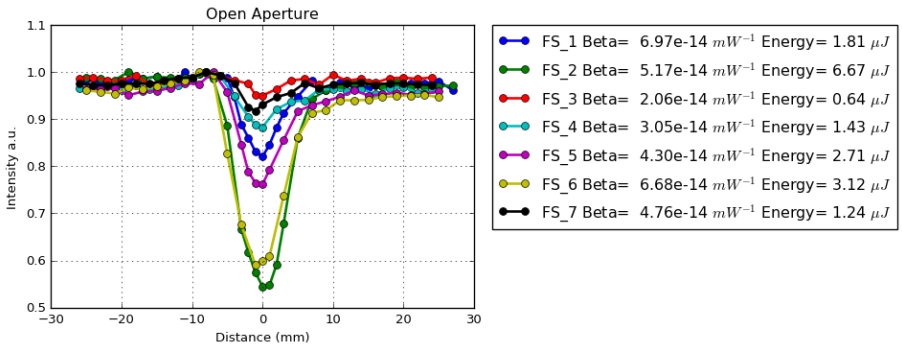


Figure 3.14: Experimental results of NAC measurement for FS at different input energies

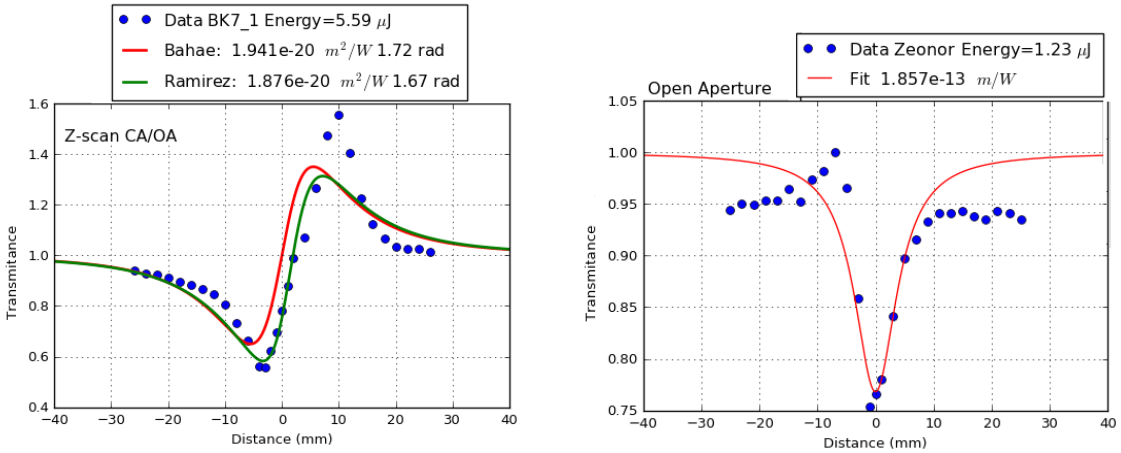


Figure 3.15: Examples of large shift and high-order nonlinearities observed in the normalized transmittance curves while measuring NRI and NAC for glass BK7 and Zeonor

substantial phase shifts.

Based on the findings presented earlier (refer to Figure 3.12a), it has become evident that obtaining an accurate measurement of nonlinearities in the femtosecond regime is a rather fortuitous endeavor. As a response to this challenge, I directed my focus towards examining the relationship between variations in input energy and the parameters $n_2$ and $\beta$.

While performing Z-scan measurements with energies between 0.64 $\mu$J and 6.67 $\mu$J, I observed that the right energy to set is a matter of guess (signal too low or too high). For instance, 1.81 $\mu$J was the most suitable for FS and the asymmetry. Even if I paid attention to the other research papers observations such as phase lower than 1 radian, the difference between 0 and the peak or the valley to be less than 20% the value of NRI, was not a constant. This statement is certified in Figure 3.13.

From the NAC measurements (see Figure 3.14), I have observed the appearance of the damage when the change of transmittance decreases to 50% or even more and clear damage when it decreases to 10% or even more.

These observations were implemented in the experimental software and thus the OA and CA data were plotted after each shot. Whenever a clear overpass of the ratio was recorded the software stopped the measurement.

During the measurements, I observed different other behaviors of the normalized transmittance curve as illustrated in Figure 3.15. Therefore, I extracted some of the prominent parameters that influence the NRI and NAC measurements in the femtoseconds regime

which include:

**Intensity of the Laser Pulse**: the nonlinear refractive index is often proportional to the square of the laser pulse intensity. In the femtosecond regime, where high peak intensities can be achieved, the nonlinear response becomes more pronounced.

**Wavelength of the Laser**: the wavelength of the laser pulse plays a role in determining the electronic and vibrational resonances within the material. These resonances can enhance or reduce the nonlinear response.

**Electronic Band Structure**: the electronic band structure of the material affects the interaction between the laser photons and the electrons in the material. Materials with specific electronic properties, such as semiconductors or materials with delocalized electrons, may exhibit stronger nonlinear effects.

**Electronic Relaxation Times**: the time it takes for excited electrons to relax back to their ground states can influence the nonlinear response. In the femtosecond regime, where the laser pulse duration is on the order of femtoseconds, materials with shorter electronic relaxation times can exhibit different nonlinear behaviors.

**Saturation Effects**: as the laser intensity increases, the nonlinear response can saturate. This means that at very high intensities, the increase in nonlinear refractive index becomes less pronounced due to the depletion of available energy levels.

**Material Composition and Structure**: various optical materials exhibit different nonlinear responses due to their composition and structure. Crystalline, amorphous, or composite materials can have distinct nonlinear properties.

**Third-Order Nonlinear Susceptibility**: the third-order nonlinear susceptibility ($\chi^{(3)}$) is a material-specific parameter that quantifies the third-order nonlinear response. It depends on the electronic and vibrational properties of the material and it is present in all optical materials independent on their symmetry properties.

**Temporal Characteristics of the Laser Pulse**: the pulse duration, the shape of the laser pulse and its temporal profile can affect the nonlinear response. Ultrafast laser pulses in the femtosecond regime can induce complex interactions between different energy levels in the material.

It is important to note that the nonlinear refractive index is often influenced by a combination of these factors, and understanding their interplay is essential for tailoring and predicting the nonlinear behavior of materials in the femtosecond regime, therefore it is essential to implement other techniques.

In my pursuit of a more profound comprehension of the NRI, I used the equations outlined in Section 2.8. The objective was to attempt to extract NRI values for a specific material at two distinct energy levels. The outcomes of this endeavor are displayed in Figure 3.16.

In addition to addressing challenges posed by significant phase shifts, thick samples, and higher irradiances, some researchers have extended their equations to incorporate the influence of the Nonlinear Absorption Coefficient (NAC), denoted as "+abs". While these equations have demonstrated favorable outcomes for widely studied materials such as $CS_2$ (a reference material), it appears that the inclusion of other coefficients might be warranted.

Notably, when dealing with plastic materials, a noteworthy constraint manifested when employing the Z-scan method on thin 100 $\mu$m plastic films. In these cases, the Z-scan signal was masked by noise, considerably complicating the process of data fitting. This challenge was particularly evident in instances involving materials like OKP and Apel film.The possible appearance of multiple reflections inside the film could be the reason of this optical noise. The source of this noise will be further investigated.

After performing multiple sets of measurements, a strategic decision, to explore innovative methodologies that could potentially minimize the dependence on the inherent

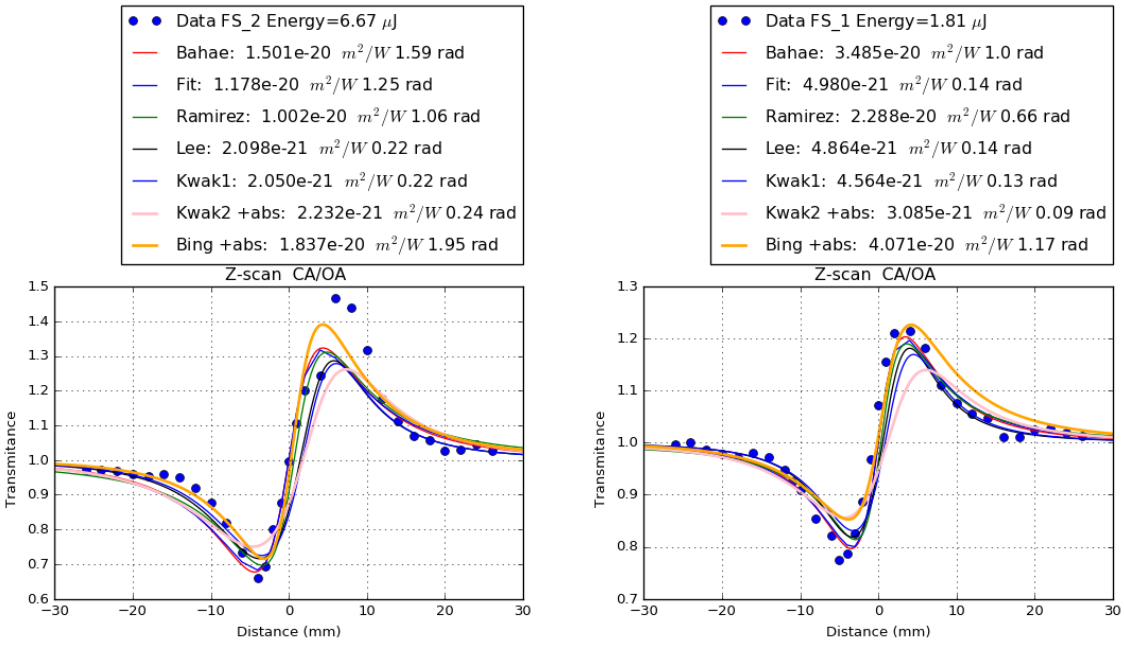


Figure 3.16: Different fitting equations for asymmetric Z-scan measured data

characteristics of the materials was adopted. Despite these advancements, a persistent obstacle remained in the form of laser stability. This challenge prompted my active involvement in the development of novel techniques aimed at addressing these concerns.

In this context, I took on the responsibility of executing measurements and meticulously analyzing the resulting data for the further enumerated methods.

### 3.4.3 Radius Z-scan

Another setup advantage is the NRI extraction from the images recorded during the LIDT measurements. Recording the CCD object plane images using the LWDIS, I was able to detect the damage occurrence, size and location and to extract the NRI analyzing the radius beam profile at FWHM or at $1/e^2$ from the images. While the sample is moving along the Z direction, it will act as a lens, changing the image spot size on the CCD. Being a different type of measurement (image processing compared with light amplitude measurements), the data were fitted with the classical equation demonstrated by M. Bahae [20] and also with an equation based on ABCD matrix formalism [21]. The fitting results were similar.

The main advantages of the Radius Z-scan method are the stability and repeatability compared with classical Z-scan as it can be observed in Figure 3.17. For instance, for classical Z-scan measurement when a pulsed laser is used at low energy (i.e. to avoid damage, few $\mu J$ level, 40 fs) the detectors can reach their noise level resulting in an incapability of distinguishing the good signal. The images recorded for the radius Z-scan method are less sensitive to the laser beam pointing instability. Using the same setup, both Z-scan with photodiodes or CCD can offer comparative results in the same measurement. Taking into account this drawback of classical Z-scan at low energies, I successfully applied and used this method to measure the NRI. The results presented in Table 3.2 are in good agreement with the classical Z-scan and I-scan measurements.

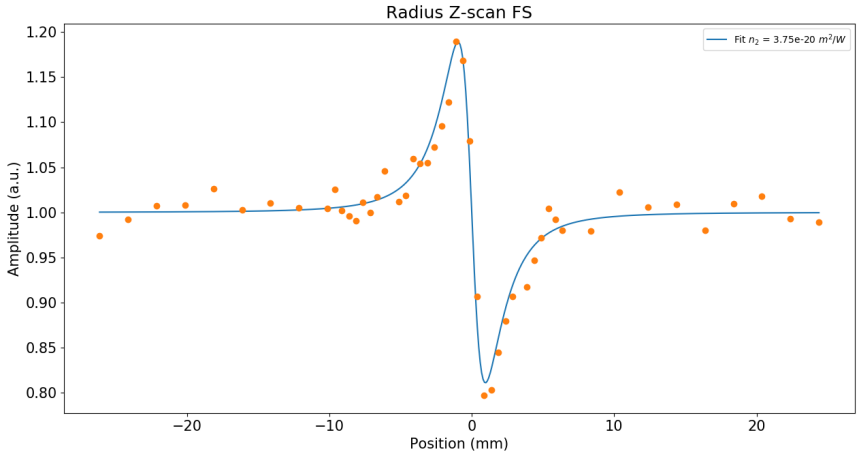


Figure 3.17: Example of Radius Z-scan measurement in 1 mm FS glass

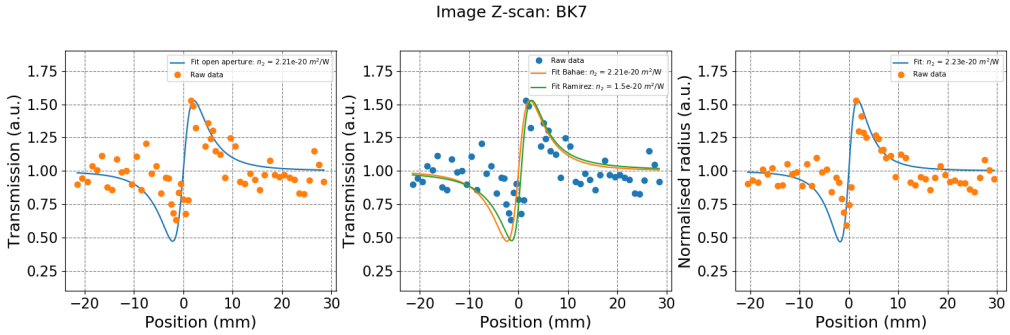


Figure 3.18: Image Z-scan technique for NRI measurements

### 3.4.4 LIDT-Aperture

The experimental setup, assembly no. II, used for damage monitoring, was further used to qualify the NRI. While the first assembly recorded optical signal by PDs, the CCD camera recorded the images of the laser spot size. We observed on the camera that the beam size is also modified during Z-scan measurement in a similar way to the one seen on PDs. Hence, I developed an algorithm that can extract from each image the radius of the beam and plot it as a function of the distance in 3 ways (See Figure 3.18). For the first one (open aperture), I took into consideration all the incoming light, for the second (closed aperture) I defined a software generated aperture with a specific width to simulate the closed aperture conditions and in the third case I chose to normalize the measured radius as in the previous method (Radius Z-scan).

### 3.4.5 The perspectives of the negative $n_2$

Another interesting topic that I have started to develop is linked to the negative nonlinear refractive index of $TiO_2$, topic presented in Ref. [22] and extended by me, in the frame of the high power lasers. This study had the main following advantages:

- B integral compensation: to counteract the accumulation of substantial phase nonlinearities throughout the laser chain—largely attributable to components such as Ti:sapphire crystals and Pockels cells, each possessing positive $n_2$ values—a strategic

approach was devised. By routing the laser pulse through a medium with properties characterized by negative $n_2$, the pronounced large phase effects can be mitigated.

- Debris shield: within numerous research facilities, the implementation of a debris shield has become a standard practice to safeguard the focusing parabolic mirror against debris generated by laser-matter interactions. However, this seemingly straightforward protective measure introduces temporal and nonlinear challenges. Specifically, the ultra-short laser pulse accumulates Group Delay Dispersion (GDD) and B-integral effects. To tackle these intricacies, a groundbreaking solution was conceptualized: the deposition of a thin layer of material with inherent negative nonlinearities. This innovation is under active development, and I have been deeply involved in its realization.

- Self-Defocusing: as elaborated in Chapter II, materials characterized by negative nonlinearities induce a self-defocusing effect upon their integration into the laser chain or interaction zone. This phenomenon presents a valuable avenue for manipulating laser beam characteristics (divergence) in the laser chain.

For this work $TiO_2$ coating have been deposited on FS, BK7 and on fused quartz. It has been shown that the $n_2$ for anatase energetic phase of this material has a negative value [22]. I have tried 2 techniques Magneto-sputtering (MS) and Pulsed Laser Deposition (PLD) to deposit 100, 200, and 400 nm of $TiO_2$. The data retrieved from X-ray Diffraction (XRD) reveal that the anatase state was not obtained with MS but there was a small peak while using PLD. For the $n_2$ measurements, the substrate used had a thickness of 1 mm for each of the three deposition layers.

The Z-scan curves showed a predominant positive NRI compared with the reference. The $n_2$ was close to the noise region and it could not be estimated with Z-scan technique. Further studies involve I-scan or pump-probe measurements. The main reasons are related to the color of the deposition (grey-black) which dimmed the amplitude of the signal, the amplitude of the anatase state (A004) peak which was not high enough and the deposition thickness which may not be sufficient to overpass the positive nonlinearities of the substrate. Even if the actual results did not showed a clear effect of the negative $n_2$, this topic remains a subject of interest for the further research.

## 3.5 Laser Induced Damage Threshold LIDT

In this Section, I will describe the main steps I performed to develop experimental setups and algorithms to estimate the LIDT.

### 3.5.1 General introduction

The LIDT is an important criterion for high power laser system components, providing information about the irradiance limits that can be used. Following the ISO 21254-1-4:2011 standards [17], multiple groups were developing methods and laboratories (i.e. Spica Technologies, Laser Zentrum Hannover, LIDARIS, ISOTEST) to measure the LIDT [23]. The LIDT is proportional to the peak power of the laser, but also scales with wavelength, beam diameter, and, most importantly, the pulse duration [18, 24, 25].

Beside those characteristics, different testing methods as 1-on-1 (one shot and one spot), N-on-1 (N shots on the same spot), N-on-M (multiple shots on multiple spots), R-on-1 (Ramping fluence on the same spot) or *pass or fail* tests are used to qualify statistically the damage. The increase in optical scattering of the test site is interpreted as

a direct consequence of the bulk or surface properties altered by the contributing damage mechanism.

The pivotal aspect of the measurement process revolves around identifying instances of damage, a task that can be accomplished either while the sample is being irradiated (online) or subsequent to irradiation (offline). The selection of methods to determine LIDT frequently hinges on the utilization of online scattered light detection, online imaging, or offline microscopy.

In a majority of cases when employing online detection, the scattered light is an indicator of the damage onset. The increase in optical scattering from the designated test area is interpreted as a direct consequence of the alteration/destruction in bulk or surface properties induced by the damage mechanisms. Other online LIDT methods include acoustic detection through piezoelectric sensors, the detection of ablated plasma, measurements of low-loss absorption, wavefront sensing, and thermovision of the irradiated region [17].

The materials under test, which could be used in the future with the setup described in Section 3.3, may include glasses, plastics, nano wires, single layers, multi layers, or dielectric coatings on a specific substrate.

The defining intrinsic characteristic that governs the optical resilience of materials and coatings against ultrafast pulses is the materials' bandgap. Consequently, the selection of materials featuring the widest feasible bandgap is imperative when designing coatings for high-power laser systems. The comprehensive optical threshold of a multilayer coating is subject to various factors, capable of either amplifying or diminishing it. Defects that originate during the deposition process or propagate from the substrate can significantly diminish the LIDT values. Remarkably, such defects can cause reductions in LIDT values by multiple factors. Conversely, adjustments to the optical design offer an alternative means to impact the LIDT. For instance, modifying the design can lead to a reduction in the electric field intensity within layers characterized by lower bandgap values. This alteration in turn contributes to an augmentation of the total LIDT.

The case of materials coating was further investigated by me with respect to the high damage threshold coatings and chirped mirrors damage threshold which will be further detailed. I performed data analysis for samples in both reflection or transmission, respectively proving the capabilities of the experimental setup.

Within this thesis, the chosen LIDT detection methods were based on online microscopy and transmittance. These combined methods alongside the data analysis software I realized, provide multiple advantages such as: high sensitivity and clear correlation to functional damage, automatic sequences, direct image generation, high reliability and are suitable for both surface and bulk damages.I will present several ways to analyze the LIDT in the order of their implementation and complexity. The work I initialized within LIDT was further extended towards 3 methods: spatial frequencies analysis (first time introduced by me in the field of LIDT), large beam area LIDT and sub-threshold LIDT detection.

### 3.5.2 Online monitoring method

For the following results, the AVESTA laser pulses I used (800 nm, 60 fs, 10 Hz, or single shot) were measured with the SHG FROG. The pulse duration measurements had a standard deviation of 3 fs. The beam area, considered a Gaussian shape beam at $1/e^2$ (40*42 $\mu m^2$ in focus and 180*176 $\mu m^2$ at 12 mm far away from focus) was estimated using the LWDIS calibrated with 1951 USAF slit targets (1 pixel = 1.13 $\mu m$). The energy was calibrated using PD1 and the polarization cosine equation [26].

A series of LWDIS object plane images were recorded to monitor at each energy step the appearance of damage as shown in Figures 3.19, 3.20. After laser irradiation, the

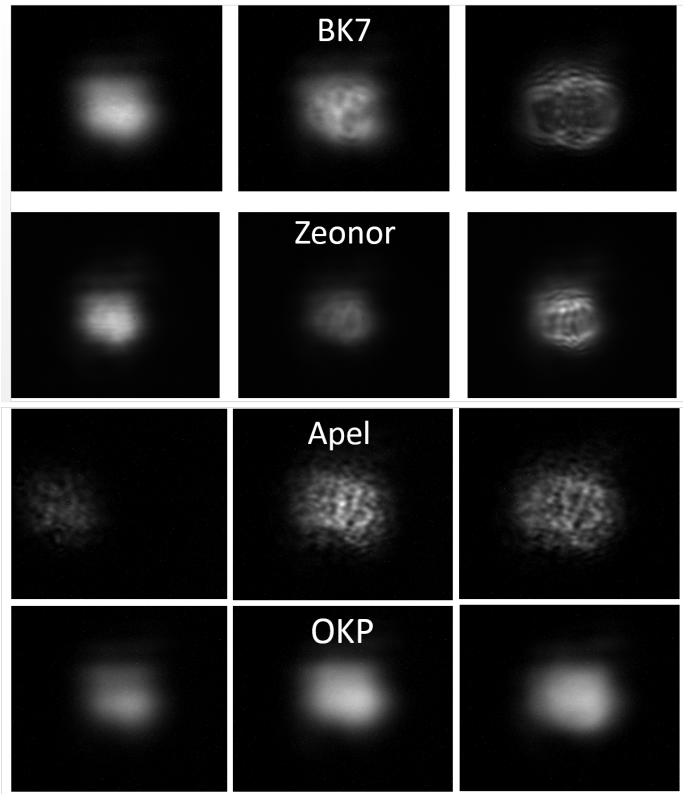


Figure 3.19: Example of online monitoring under direct irradiation during LIDT test for 1 mm (BK7 and Zeonor) and for 0.1 mm (Apel and OKP) thicknesses in an R-on-1 damage test

samples were analyzed by microscopy and profilometry to establish at which energy level the damage starts. This cross-check with offline microscopy was used to qualify and to understand the effects seen in the images. To qualify the damage at this stage, two methods were used. The first was based on the **direct irradiation** where all the transmitted light was collected by the LWDIS objective. For the second one, called **eclipsed irradiation**, the central part of the transmitted beam light was blocked so that only the scattered light was collected.

After processing the images (subtract the background, center the beam in the image, fit the surface), I introduced the image size in $\mu$m and the fluence for 3 intermediate irradiation stages considering the images acquired at the begging, in the middle and at the end of the irradiation. The dark spots from figure 3.21 correspond to filamentation channels observed with offline microscopy. For thick materials the damage appears within the bulk but while the damage for the thin samples appears at their surface. The damage was more prominent in the thick material due to the filamentation process and the absorption law, which both depend on the material thickness.

The filamentation was mostly observed in the 1 mm thickness materials. The first correlation with the damage seen in the online detection was observed at the profilometer analysis. Hence the dark spots from Figure 3.22 are equivalent to the less intense pixels from Figure 3.21.

The images recorded with the CCD camera had multiple uses. Firstly, from each saved image was extracted the mean value of the gray levels of the pixels. This value was plotted in Figure 3.23 to estimate the damage fluence starting point for both methods (direct and eclipsed). The preliminary results are presented in Figure 3.23 where the two methods were compared. It can be seen that when the damage starts to occur, the intensity has a

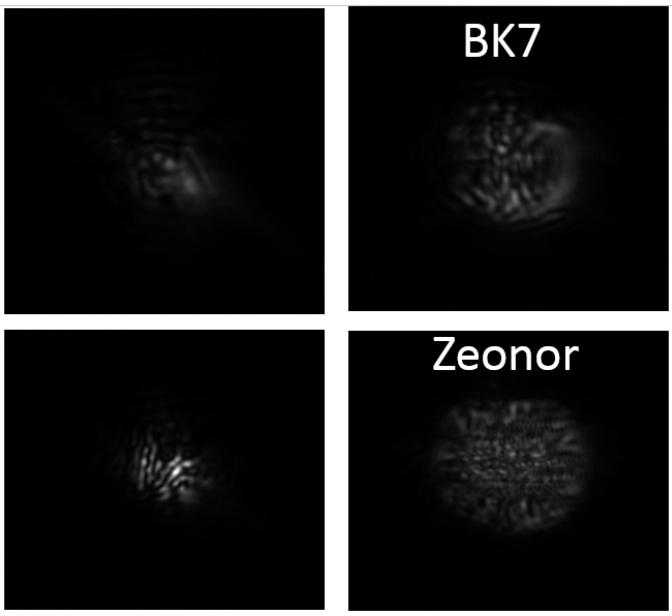


Figure 3.20: Example of eclipsed irradiation for BK7 and Zeonor with 1 mm thickness in an R-on-1 damage test

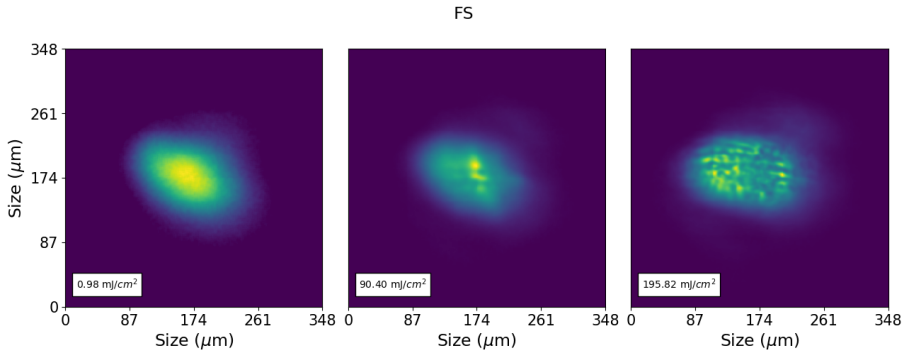


Figure 3.21: Post processed data from online microscopy results measured with setup from Assembly II - Section 3.3.2

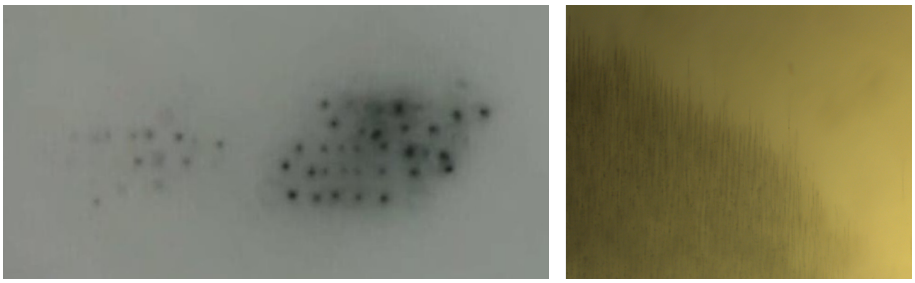

Figure 3.22: Example of self focusing observed with Profilometer (at 2 different fluences) and with the microscope

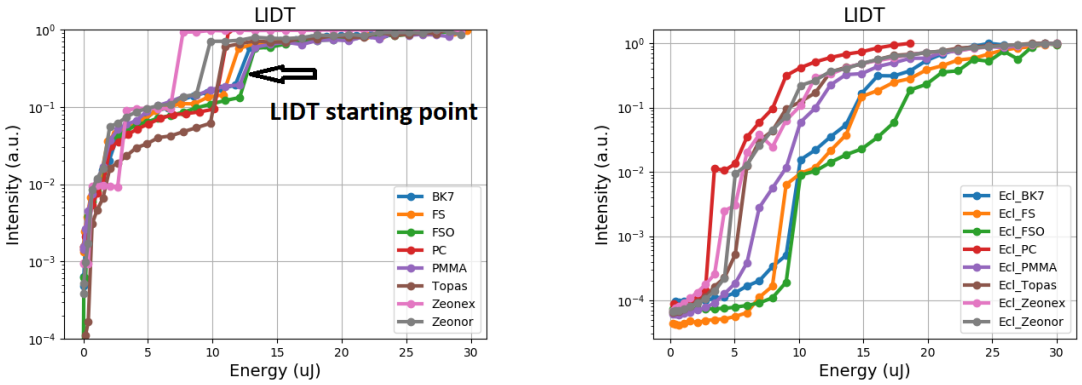


Figure 3.23: Log scale LIDT results for direct and eclipsed irradiation

jump (see inside arrow) due to a larger amount of scattered light. The eclipsed method showed that the damage can be put in evidence earlier (at lower energy- see the starting point, in energy, where the vertical jump in the intensity amplitude occurs). The image data analyses have also shown that this second method can offer better information about the scattering level of each material. The scattering level was estimated from the recorded image beam size. According to the ISO damage standards, the scattering level of each material helps in the preliminary estimation of the LIDT and can be also used to choose the right size (1"/2") of the scattered light collimation lens.

As far as the irradiance increased I was able to see micro and macro damage structures. Firstly, three images were chosen to illustrate the appearance of the damage structures in the full beam configuration (see Figure 3.21). Left image shows the sample without damage, at lower irradiance, middle image with micro damage structures and right side, image with macro damage structures. Micro damages are non-permanent modifications in the material structure which are related to the surface quality of the material, beam shape and profile, and the energy distribution in the beam. All the materials, with 1 mm thickness, followed the same rule of damage process.

Thinner ones, 0.1 mm thickness, had a constant variation and the damage could not be estimated from this type of images. A solution for this is a discrete input energy increment or a thicker material.

Secondly, from the beam image size was extracted the beam profile diameter at $1/e^2$ and at FWHM, mediated (the first 4 images, where the linear regime occurs, were used) and normalized. In this way, all the possible errors, such as: sample position or input beam size fluctuations were reduced. This data analysis method was used to estimate the beam diameter for the Radius Z-scan values plotted on the Y axis of Figure 3.17.

Thirdly, similar with the techniques used in the Z-scan configuration, the NRI and NAC can be obtained using the magnitude of the gray levels of the pixels from the full image (like an Open Aperture) or from a defined aperture into the image beam area (like a Closed Aperture). The extracted results were in a good agreement with the results from the Z-scan or I-scan (see "LIDT-aperture" method from Table 3.2).

With online microscopy and direct irradiation, it was straightforward to determine when clear damage occurred compared to eclipsed irradiation. However, I faced challenges distinguishing between two closely spaced fluence values to ascertain whether damage had occurred or not.

I have understood that the amplitude of the image may have been affected by the filter in front of the CCD camera due to manual filter interchange. In both cases, post-irradiation data analysis and cross-checking with offline microscopy were necessary.

Looking ahead, there are some potential improvements to consider. For instance, we could reduce the size of the beam blocking element from its current 20 mm diameter metal piece. Shifting the blocker position closer to the smaller spots obtained in spot size, near the TP, is another option. Additionally, implementing a calibration factor retrieved from other types of tests is worth considering.

### 3.5.3 Spatial frequency method

Spatial frequencies are a fundamental concept in both the field of lasers and image processing. They play a fundamental role in understanding the behavior of electromagnetic waves in lasers and the representation and analysis of images in image processing.

An irradiance distribution in either the object or image plane exhibits a composition of "spatial frequencies" akin to how a time-domain electrical signal comprises various frequencies, using Fourier analysis. Any given profile traversing an irradiance distribution, whether it is in the object or image plane, consists of inherent spatial frequencies. When we extract a one-dimensional profile from a two-dimensional irradiance distribution, we acquire an irradiance-versus-position waveform. Remarkably, this waveform can be decomposed using Fourier analysis just as we would decompose a more familiar electrical signal in volts versus time.

The Fourier decomposition provides insights into the frequencies inherent in the waveform, expressed in terms of spatial frequencies, measured in cycles (cy) per unit distance. This measurement is analogous to temporal frequencies measured in cycles per second (cy/s) for a time-domain waveform. Typically, in optical systems, spatial frequencies are quantified in cycles per millimeter (cy/mm).

Spatial frequency ($\nu$), often denoted as $q$ in other references, is typically measured in cycles per unit length, commonly expressed as cycles per millimeter.

In image processing, spatial frequencies are often represented as two-dimensional quantities ($\nu_x$, $\nu_y$). The formulas for calculating the spatial frequencies in the x and y directions are:

$$\nu_x = m/N \tag{3.6}$$

$$\nu_y = n/M \tag{3.7}$$

Where m and n are the numbers of cycles in the x and y directions within a given image region. N and M are the dimensions (number of pixels) of the image in the x and y directions, respectively.

The idea of spatial frequencies has been used for image processing [27], for face perception [28], adopted in the theory of Small Scale Self-Focusing [10, 29, 30, 31, 32] and it has also been implemented and studied to reach subexawatt few-cycle pulses generation [33]. While performing data analysis for ELFIE experiment (See Chapter 4.1), where I studied the influence of the beam features in the SPM process using spatial frequencies, I had the original idea to use this type of frequencies, in LIDT estimation.

#### 3.5.3.1 Spatial frequencies algorithm

The spatial frequencies algorithm comprises a series of steps in image analysis that are employed to extract the amplitude of the power spectrum. Here is an overview of the four implementation steps of the algorithm:

**Image Recording**: initially, images are recorded using the Long Working Distance Imaging System (LWDIS) or any other imaging system. The resolution of the camera used is a key parameter. In this case, the estimated resolution with the LWDIS was 11 $\mu$m.

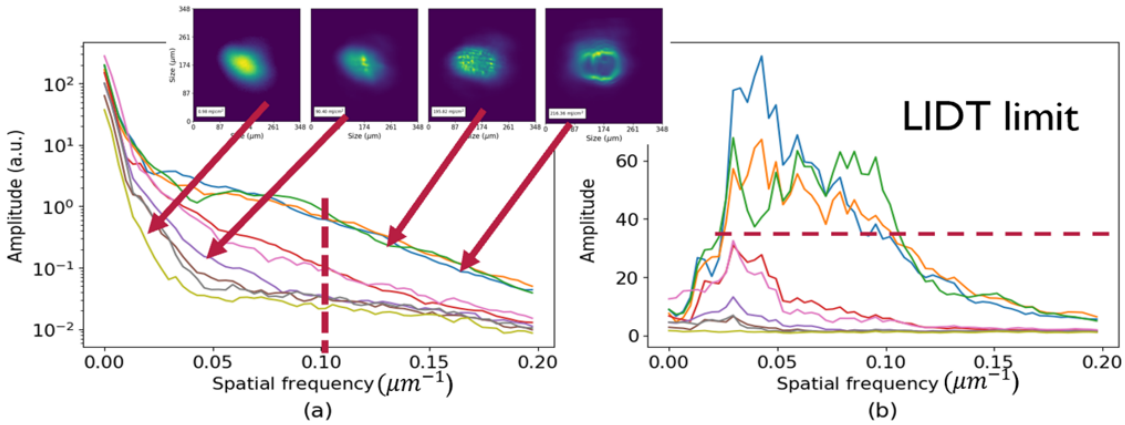


Figure 3.24: Spatial frequencies method applied on Fused Silica glass, where a) represents the amplitude curve for each modulation frequency of the beam profile. Inset: the corresponding pulse profiles, and b) the ratio between each measured image and the reference.

**Image Treatment**: this step involves various image processing tasks such as resizing, centering, background subtraction, and fluence estimation. All of these processes are carried out within a Python interface, where different functions for data analysis were designed.

**Fourier Analysis**: in this step, I computed the 2-dimensional Discrete Fourier Transform (DFT) of the images. The DFT samples frequencies along both the X and Y axes. To encompass the entire image, *Histogram integration* of the complete Fourier Transform data was performed. The histogram function provided by Python, computes the histogram of a flattened array based on the number of bins and their upper and lower range.

**LIDT Estimation**: LIDT estimation takes into account the amplitude of Spatial Frequencies (Power spectrum) and the Ratio magnitude (See Figure 3.24). The Ratio magnitude is computed by dividing each n-th DFT image (where n=2, 3, and so on) by the DFT of first image recorded at a specific fluence.

Additionally, I have cross-checked the results obtained from this method with a microscopic approach (using a microscope or profilometer) to validate the LIDT limit.

#### 3.5.3.2 Applications of spatial frequencies analysis

I will present a few examples where I implemented this method.

**Spatial frequencies method applied for the LIDT of glass**. Using this method, a FS glass has been chosen as example (See Figure 3.24). This method was presented in Ref. [34] and it has received numerous appreciations from the LIDT community. It can be observed that when the fluence is increasing, the amplitude of the power spectrum for each spatial frequency starts to increase. Multiple power spectra amplitude are plotted in Figure 3.24 a) to show the damage evolution.

**Spatial frequencies method applied for the LIDT of perovskite oxides**

Perovskite oxides belong to a class of materials characterized by a distinctive crystal structure known as the perovskite structure. These materials have attracted substantial interest within the realms of materials science, chemistry, and physics, thanks to their versatile properties and promising applications.

The laser input parameters were: pulse duration of 60 fs at FWHM, 800 nm, 10 Hz, linear polarization, beam diameter 260 ± 12 $\mu$m, 1000 shots per site and AOI 45°. The input energy was adjusted by manipulating the half waveplate and the polarizer, and the tests were conducted in ambient air using the reflective part of the experimental setup

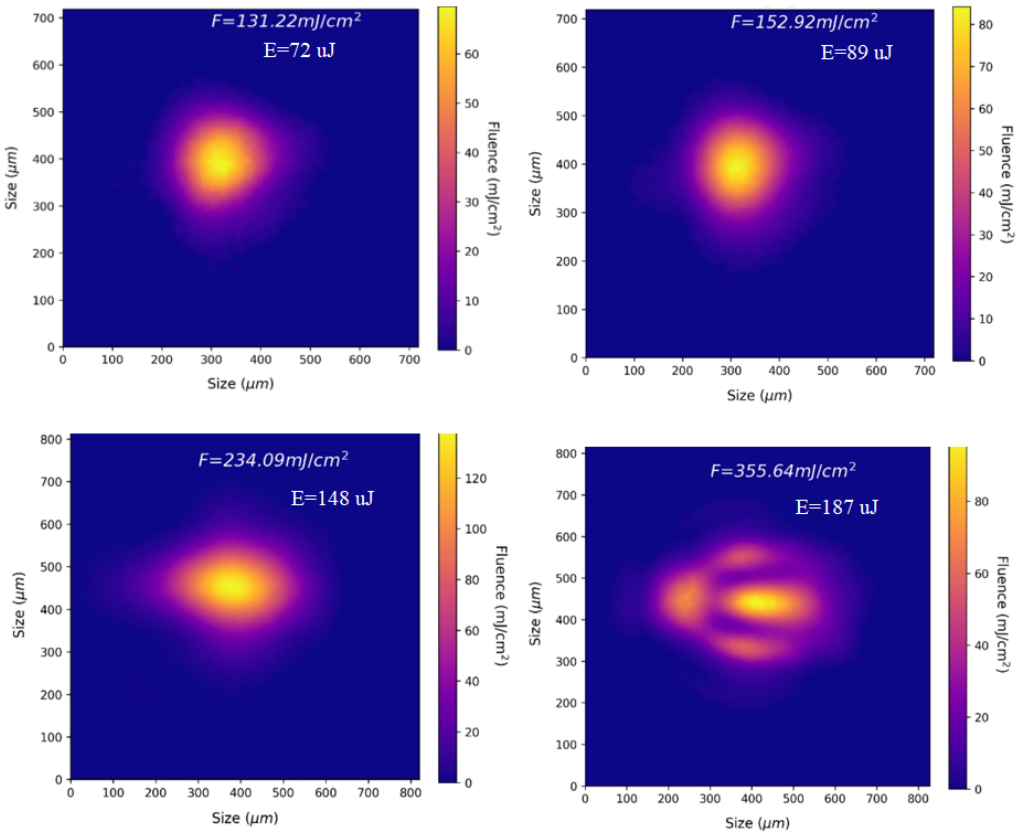


Figure 3.25: LIDT using the imaging system for two types of perovskite oxides. Typical damage morphology before (left) and after damage (right)

shown in Figure 3.7.

The Laser-Induced Damage Threshold analysis of these materials has not only highlighted the sensitivity of the measurement (refer to Figure 3.25), but it has also demonstrated the potential for real-time online analysis of damage evolution as observed through spot size changes (as illustrated in Figure 3.26).

The analysis of axis diameter provided a rapid means to determine if damage had occurred. However, it relies on the specific line across the laser beam that is selected for measurement. Additionally, in cases where a coating contains residual clusters, this factor may impact the decision regarding whether damage has occurred at a particular site.

A highly significant observation made in Figure 3.25 (top) is that damage is not readily observable in real-time (online) but becomes evident only during offline examination. However, when the same images were subjected to analysis using the spatial frequency method, a distinct alteration in the power spectrum emerged (as depicted in Figure 3.27-left).

This result highlights the method's sensitivity when data analysis is performed in real-time. Real-time analysis significantly reduces the time required for cross-checking with the offline microscope to determine whether damage has occurred or not. Based on this observation, I have established a threshold, represented by the black horizontal and vertical lines, which can be applied to both axes of the figure. This threshold serves as an indicator, providing users with warnings when the threshold has been reached.

The analysis of each irradiated site has been assessed within the context of the damage probability curve. Figure 3.28 presents the damage probability graph derived from a statistical evaluation involving five irradiated sites per fluence.

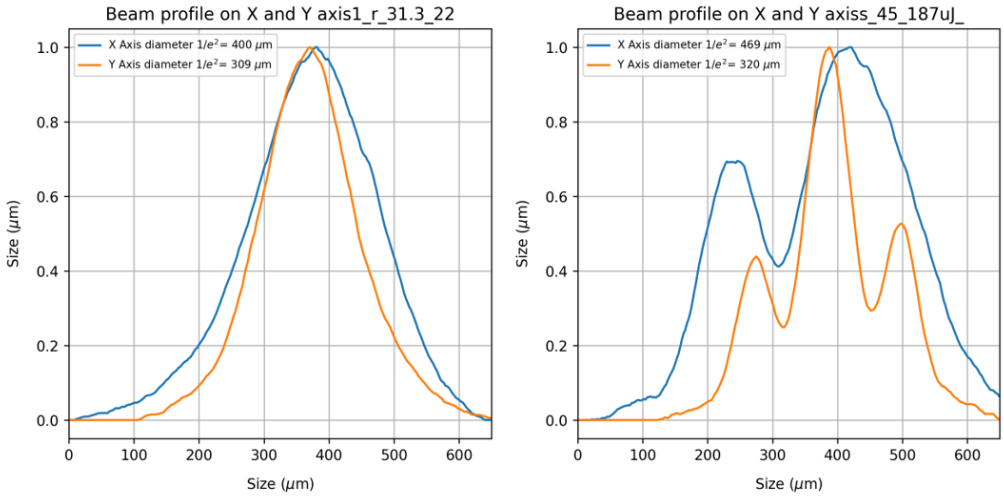


Figure 3.26: Beam profile on X and Y axis, AOI 45°

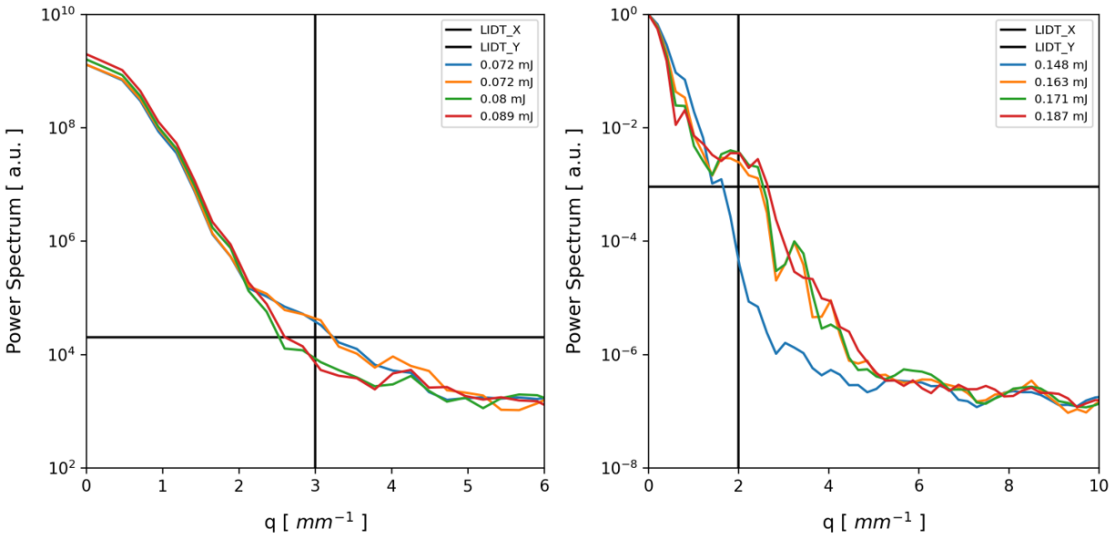


Figure 3.27: Spatial frequencies analysis results for 2 types of perovskite oxides. LIDT_ $X/Y$ denotes the threshold that can be used for each axis and $q$ denotes spatial frequencies axis

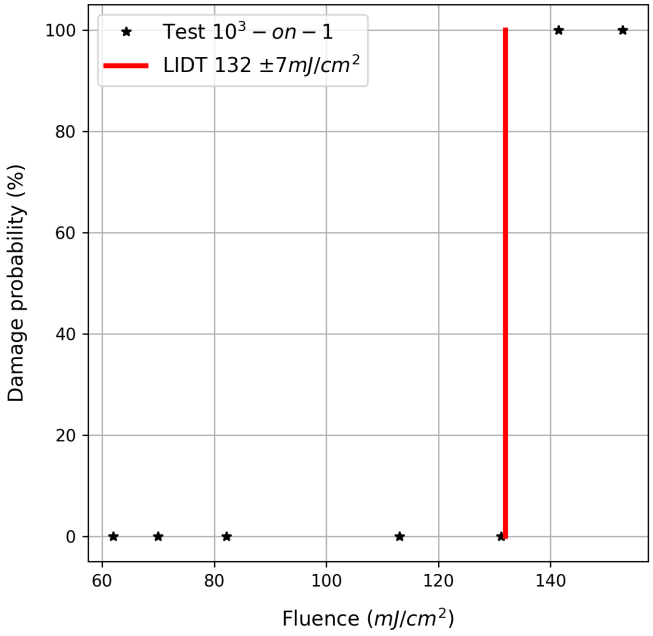


Figure 3.28: Example of perovskite oxide damage probability graph for 1000-on-1 shots where 5 sites were irradiated.

Section 3.5.3 has found extensive application in various experiments, including the assessment of Laser-Induced Damage Threshold for glasses and plastic materials, perovskite oxides, the ELFIE experiment, and large-beam LIDT experiments that will be detailed in the upcoming section.

This method's versatility and sensitivity have been demonstrated through its successful application in multiple experiments, all of which involve the analysis of images.

### 3.5.4 Large beam LIDT. Damage mask method

The Large Beam LIDT method represents a more versatile approach for analyzing numerous irradiated sites from a single image. Building upon the concept initially presented in Ref. [35], we employed a single laser pulse with varying fluence levels across its surface. This irregular fluence distribution, as illustrated in Figure 3.30a, image number **1**, allowed us to generate a significantly higher number of irradiated sites from a single, larger site.

In this setup, each pixel of the CCD camera corresponds to an irradiated site with a specific gray level intensity, which corresponds to a particular fluence. By utilizing the color map provided by the LIDT mask, we achieved the highest level of statistical data for irradiated sites presented so far. The results obtained through this approach have been documented and published in Ref. [34].

#### 3.5.4.1 Large beam LIDT algorithm

The algorithm operates with a minimum of two images: one representing the Near Field profile of the input laser, and the other showing the damaged site. The algorithm involves the following key steps:

**Image Processing**: initially, this step involves various image adjustments, such as image rotation and the conversion of damage images from normal to 16-bit binary format (distinguishing damaged vs. undamaged pixels as 255 vs. 0).

**LIDT Calculation**: in this phase, the image containing damage information is converted into true binary format (sequences of bits 0 and 1). This binary representation is overlaid on the laser intensity image, allowing the algorithm to calculate the percentage of damaged pixels at each intensity level.

**Optimal Translation Parameters**: the next critical step is to find the optimal parameters for shifting one of the images to maximize the number of "accurate" pixels. Accurate pixels are identified based on predefined intensity thresholds, and the program efficiently determines the most suitable translation parameters.

**LIDT Mask**: subsequently, the algorithm further resizes the image around the origin point (0,0) based on specified scaling parameters (scale X, Y). Depending on the scaling parameters, pixels are either cropped or filled with 0s to achieve the desired image size.

**Binarization**: the program also includes functionality to convert damage matrices into binary format (sequences of bits 0 and 1). This can be also done defining damage based on a specific threshold. The flexibility of this feature allows for adaptation to various damage definitions.

This comprehensive approach enables the algorithm to effectively process and analyze input images, ultimately contributing to the determination of Laser-Induced Damage Threshold.

#### 3.5.4.2 Experimental setup

The estimation of LIDT was conducted using 100 TW laser pulses from ELI-NP, focusing the 65 mm beam down to millimeter size with a spherical mirror labeled as SM. The experimental setup, as depicted in Figure 3.29, allowed for precise control of various parameters.

The samples were positioned on a 3D stage, enabling shots on two different mirrors without the need to break the vacuum. The Z-axis motorized translation stage was employed to vary the spot size, ranging from 3 mm to 7 mm. The maximum energy on the target was 409 mJ. Energy variation on the target was achieved through a 50 mm waveplate installed in the laser bay, with the 100 TW compressor serving as a polarizer.

The setup presented in Figure 3.29 can be divided into three main parts:

**On-site Detection LIDT**: this part involved reflecting the sample's image onto a CCD camera using an objective lens. It was essential in quickly determining whether a site had been damaged immediately after the shots. This allowed for adjustments to the input energy based on pass/fail test results. However, this assembly was not suitable for detecting small blurs or filamentation due to the resolution limitations of the CCD camera and objective.

**Scattered Detection LIDT**: in this part, images were recorded after each shot or after every 10 shots. The spatial frequency method could be applied to this data.

**Spectral Broadening Setup**: this section was designed to simultaneously measure both the LIDT and the spectral broadening of transparent materials. A wedge and the reflection from the beam dump (made of FS glass) were used to attenuate the laser pulses and prevent them from becoming external sources of broadening. Various materials, including FS, SF5, and Zeonor, were investigated in this setup.

#### 3.5.4.3 Experimental results of large beam LIDT

Once the samples were irradiated, each site was imaged using a microscope which can image mm scale objects. The Near Field of the laser from Figure 3.30a denoted as **1** was overlapped with the microscope images presented in Figure 3.30a as **2**, after the cleaning and masking algorithm presented above, resulting in the LIDT mask labeled as **3**.

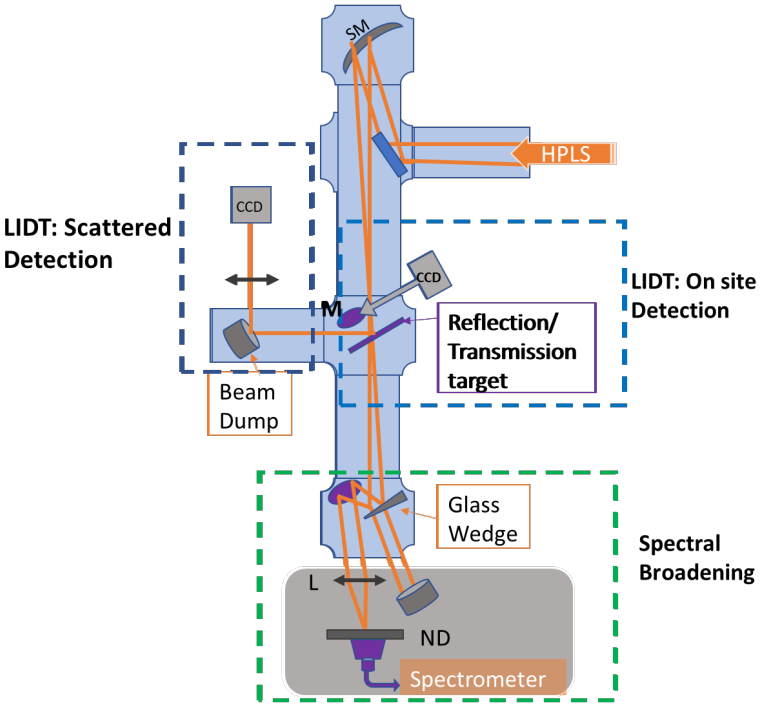


Figure 3.29: Experimental setup used for LIDT detection (on site and scattered light) and spectral broadening in vacuum. Where L-lens, M-Mirror, ND- Neutral Density filter SM-spherical mirror [34]

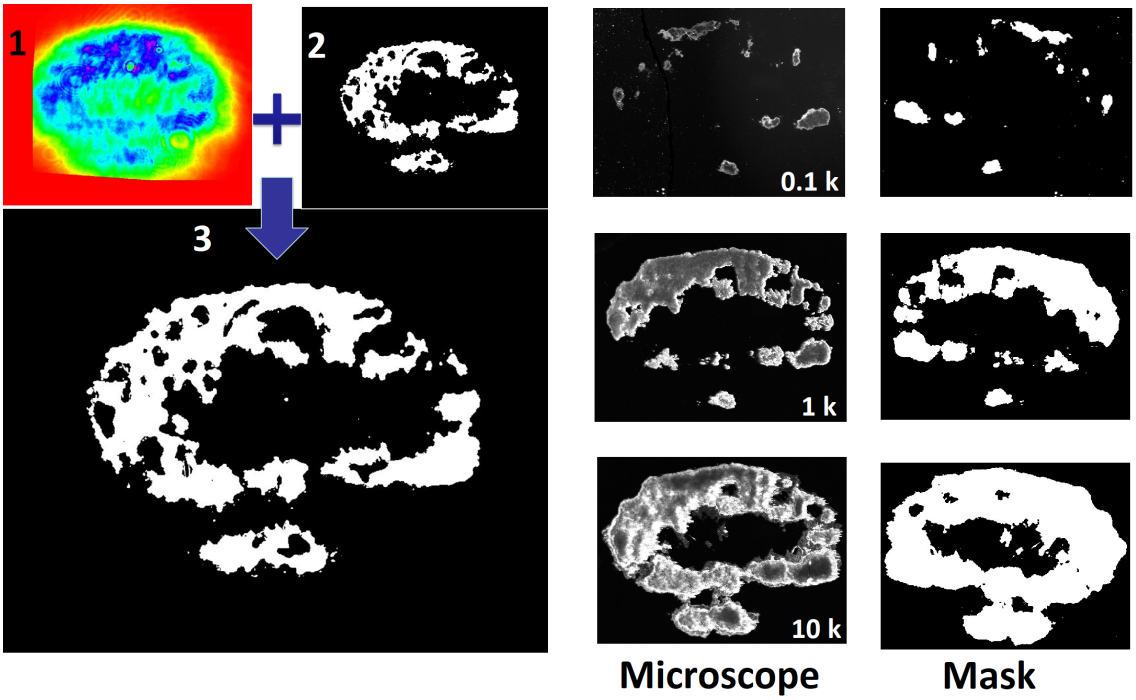


(a) (b)

Figure 3.30: Large beam LIDT-Mask method (left) and examples of the LIDT masks of Silver mirror after 10 (top), 100 and 1000 (bottom) shots [34]

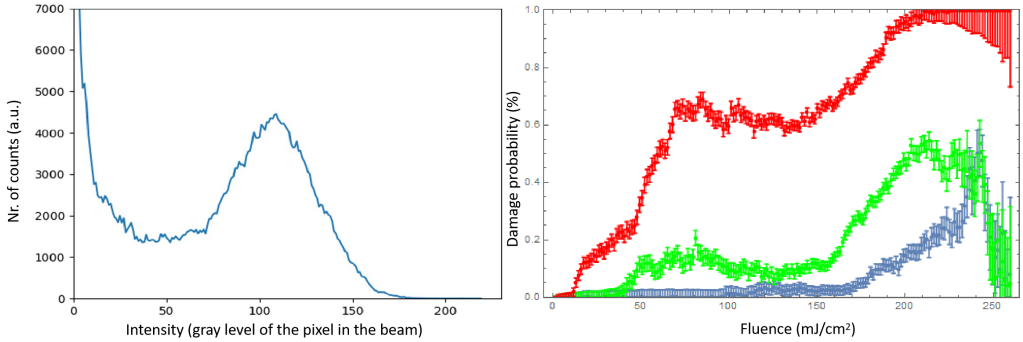


Figure 3.31: Large beam LIDT method applied for $TiO_2$:Silver mirrors, where the number of counts statistics for the 100 shots per site (left) and the damage probability obtained for 10 (blue), 100 (green), and 1000 (red) shots per site were used. [34]

The same principle was used in Figure 3.30b where 3 different no. of shots have been used to irradiate Ti:Silver mirrors. For instance (See Figure 3.31-left ), when the value of the gray level reached 100 (a.u.), more than 4000 pixels had the same amplitude. Hence, the damage probability was extracted from each image as a function of the fluence. The fluence has been calculated as follows:

$$Energy_{pixel} = E_{shot}/Sum_{pixels} \tag{3.8}$$

where $E_{shot}$ is the overall shot energy (J) and $Sum_{pixels}$ includes all the image pixels magnitude (counts). Thus, the fluence is given by:

$$F = Intensity_{amp} * Energy_{pixel}/Area \tag{3.9}$$

In the above equation, $Intensity_{\text{amp}}$ represents the value of the gay level for each pixel, measured in counts, and "Area" corresponds to the area of each pixel in square centimeters ($cm^2$).

Here's a preliminary summary of the observed damage profiles for different numbers of laser shots with more detail:

**10 Shots:** with only 10 laser shots, the damage isn't very well defined. However, it is notable that the damage spots closely follow the highest intensity areas of the laser. Consequently, our graph aligns with our expectations, showing damage incubation at an fluence of approximately 60 $mJ/cm^2$ and a clear rise in damage at an intensity of about 120 $mJ/cm^2$. It is essential to note that both of these areas have damage levels significantly below 10%, as most areas remain undamaged.

**100 Shots:** when we increase the number of shots to 100, we observe a significantly improved damage image. It now closely resembles the laser profile, indicating a more accurate representation of the damage distribution. Our graph illustrates the initiation of incubation at an intensity of around 40 $mJ/cm^2$, with proper damage emerging at an intensity of approximately 100 $mJ/cm^2$.

**1000 Shots:** with 1000 laser shots, we obtain a remarkably accurate damage image. It closely mirrors the laser profile, reflecting a high level of precision in capturing the damage distribution. The graph highlights incubation occurring at intensities between 10 and 30 $mJ/cm^2$, with proper damage emerging beyond this range.

In summary, the number of laser shots has a substantial impact on the clarity and accuracy of the damage profile. With more shots, the damage image becomes more defined and aligns better with the laser profile, enabling us to observe incubation and proper damage more clearly and accurately.

These results have been presented at SPIE Laser Damage 2022 and reported in Ref. [34].

### 3.5.5 Langmuir Probe - Target Current (LPTC) method

In the case of ultrafast laser systems with peak powers increased to 10 PW, the ensuring of the long-term and trouble-free performance of optical components exposed to lasers becomes a paramount concern. Our research is dedicated to understanding how optical materials behave when subjected to fluences below the standardized Laser-Induced Damage Threshold value [17]. To accomplish this, an innovative approach that concurrently examines surface-emitted particles using Langmuir Probe (LP) and target (compensation) current (TC) measurements [36, 37] has been proposed. Our results have been rigorously validated through spatial modulation analysis and offline microscopy [34].

Our groundbreaking *in-situ* LIDT monitoring system enabled us to detect measurable signals of ionization, even at fluences significantly lower than the LIDT values estimated by conventional methods. This discovery effectively unveils the endurance limits of optical surfaces when subjected to a single-shot energy scanning mode. By integrating LP and TC as on-shot diagnostic tools for optical components, our research has the potential to profoundly enhance the reliability of the next generation of ultrafast laser systems.

In this part of work, are presented the results obtained for $ZrO_2$ deposited films on fused silica (FS) substrates using the Pulse Laser Deposition technique. The results have been reported in Ref. [38] and submitted to HPLSE journal.

#### 3.5.5.1 Experimental setup used for LPTC

The setup depicted in Figure 3.7 has been expanded with a novel component that utilizes the input laser pulse within a vacuum environment.

LPTC experiments were conducted within a vacuum chamber at a residual pressure of $10^{-3}$ Pa, using a single-shot mode, on pristine surfaces. The oxide thin films were electrically connected to an oscilloscope for target current measurements. A tungsten wire with a diameter of 0.5 mm and a length of 2 mm served as the active region for the Langmuir Probe (LP), positioned at a distance of 1 cm from the irradiated surface. To prevent any interaction with the femtosecond pulse and additional contributions to the recorded current traces, the LP was placed off-axis relative to the irradiation plane. Both LP floating current and target current were recorded using a Tektronix oscilloscope with a 50 Ohms input impedance.

In this work, I will present the setup, the method, and the results obtained for a $ZrO_2$ single-layer thin film. A comprehensive analysis, including detailed results and a thorough comparison between the microscopy and LPTC methods, has been documented in a paper for two distinct types of samples manufactured under three different oxygen pressure conditions.

#### 3.5.5.2 Description of LPTC method

Material removal from the target mirror involves a complex interplay of electrostatic and thermal mechanisms, which are separated both temporally and spatially. The initial stages of laser ablation are characterized by rapid electrostatic interactions, while the subsequent stages are predominantly driven by thermal processes. Previous research [37] has demonstrated that the Langmuir Probe (LP) serves as a suitable tool for estimating the nanosecond ablation threshold limit. This suitability arises from the LP's sensitivity to contributions from each stage of ablation[36].

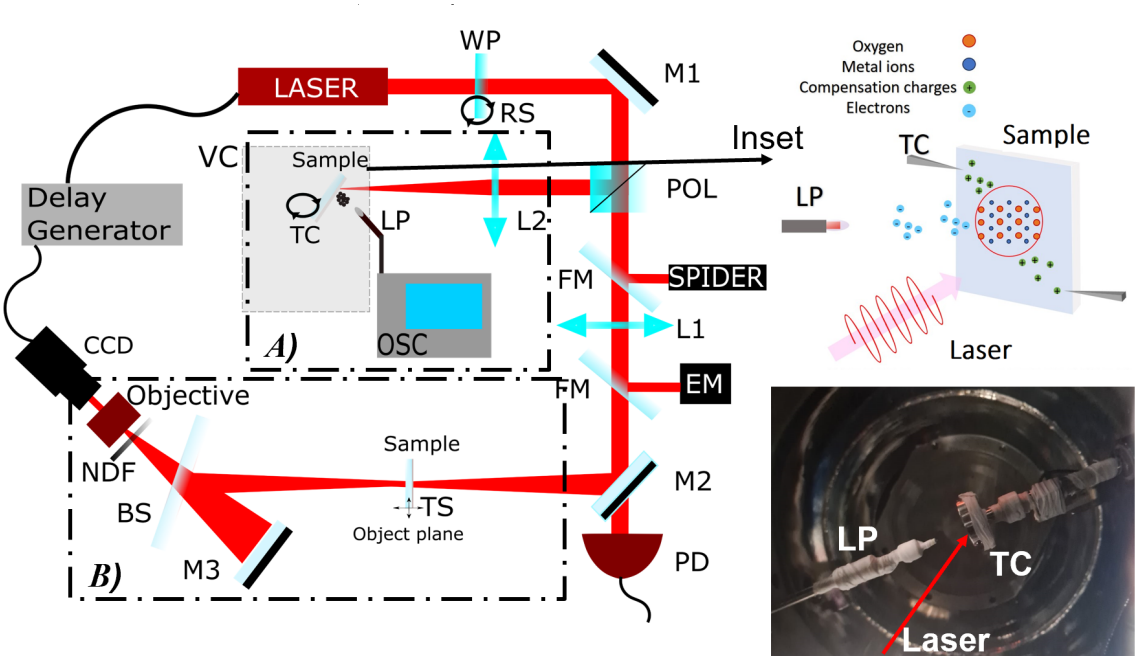


Figure 3.32: Experimental setup where: BS – beamsplitter, EM – energy meter, FM- flip mirror, LASER – Ti: sapphire, L1 and L2– focusing lenses, LP- Langmuir Probe, M1– high reflective mirrors, M2-99% reflective mirror, M3- spherical mirror, NDF- neutral density filter, OSC- Oscilloscope, POL- polarizer, PD – photodiode, TC- Target current, TS- translation stage, RT -rotation stage, VC- Vacuum chamber, WP – half-waveplate. Inset theoretical and experimental view.

In general, LP implementation focuses on characterizing the dynamics of ionized species at fluences significantly higher than the ablation threshold, often measured at distances exceeding 2-3 cm from the irradiated target [39]. However, given that the LP technique relies on charge collection, it holds promise for sub-threshold measurements as well. Concerning Laser-Induced Damage Threshold studies, there remains significant interest in the behavior of optical components below the threshold, where understanding electron emission and target compensation current across a wide range of irradiation conditions becomes imperative.

Certain key properties of dielectric mirrors, such as defects and oxygen vacancies, can influence the local electrical properties of the film, and consequently, the local value of the LIDT. In accordance with the femtosecond-ablation theory [40], the initial particles to undergo excitation are electrons. These electrons are ejected from the target material, leaving the surface with a positive charge. This charge separation establishes an electric field that accelerates the target's ions, ultimately resulting in the material's breakdown.

Since the process of electron ejection is gradual, it implies that even below the conventionally defined LIDT limit, charges are emitted and can be collected using electric diagnostic tools. Any charge imbalance induced in the sample due to laser irradiation can be characterized by two responses: a transient electronic current, which can be detected by the Langmuir Probe (LP), and a target compensation current within the dielectric film (target) that has an opposite sign, maintaining charge neutrality.

The Target Current (TC) is responsible for collecting charges with relatively low kinetic energy, which is determined by the signal's lifetime. As the fluence increases and exceeds the Laser-Induced Damage Threshold, plasma formation occurs. The total charge recorded over time as a function of fluence is depicted in Figure 3.33. When this total current is plotted against fluence and fitted using the femtosecond-ablation theory [40], the initiation

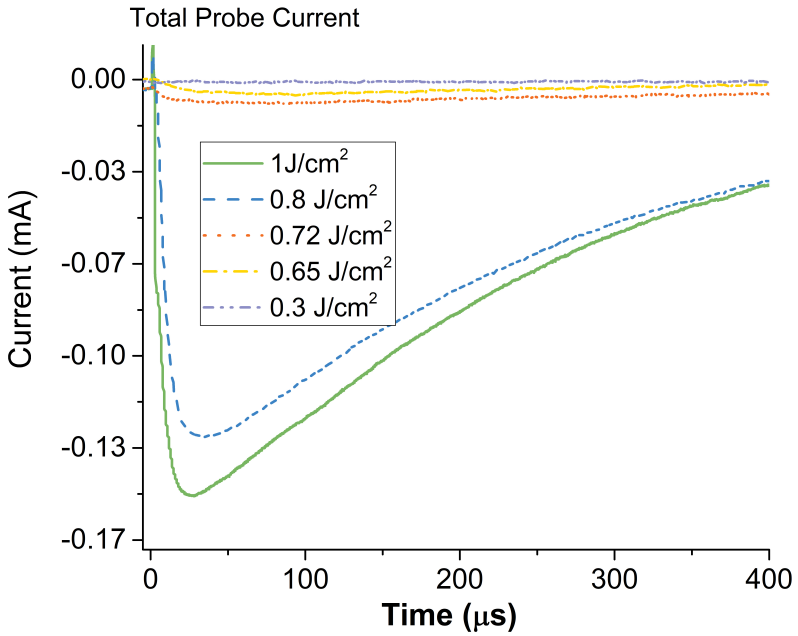


Figure 3.33: Examples of the recorded currents time-evolution with the increase of the fluence

point of LIDT damage formation is determined.

In this context, the LIDT value is defined as the point where the slope of the charge increase intersects with the baseline established during low irradiation. Taking the example illustrated in Figure 3.34, for the $ZrO_2$ thin film deposited in 0.8 Pa of $O_2$, the LIDT value determined from the TC current (0.81 J/cm$^2$) is lower than the one obtained from the LP current (1.04 J/cm$^2$) with 0.23 J/cm$^2$. This difference is attributed to the higher sensitivity of TC measurements, which capture all charges generated at the surface level, while the LP signal is significantly affected by measurement geometry and charge scattering during expansion. The combined use of the LP and TC serves the purpose of comprehending the removal mechanisms. LP provides quantitative data regarding the ejected particles, which can be subsequently correlated with the temporal trace of the target compensation current. This correlation helps in gaining insights into the processes involved.

#### 3.5.5.3 Experimental LIDT results using LPTC

The LIDT values determined using the *ex situ* microscopy technique and the LP-TC approach proposed here exhibit an overall trend. Notably, the single-pulse LP-TC values tend to be lower than those inferred from the multi-pulse *ex-situ* microscopy determination (see Figure 3.35). This difference signifies an increase in detection sensitivity by a factor of 2.5 for $ZrO_2$ samples. The single-pulse LP-TC method bypasses the statistical analyses often required by optical methods, which take into account changes in the irradiated areas. This outcome marks a significant advancement toward real-time and in-operation monitoring of optical devices in high-power laser facilities. The heightened sensitivity of the electrical method is expected since it relies on the electrical charge imbalance induced by the interaction between the fs laser and the thin film.

The *ex situ* optical microscopy method serves to confirm the threshold, but its effectiveness becomes apparent only after evident film damage, which may manifest as discoloration [41], surface alteration [42], filamentation [43], or crater formation [44].

To verify the relevance of the LP-TC method in the context of high-power infrastructures, the obtained values were compared with the theoretical extrapolation fitting equation

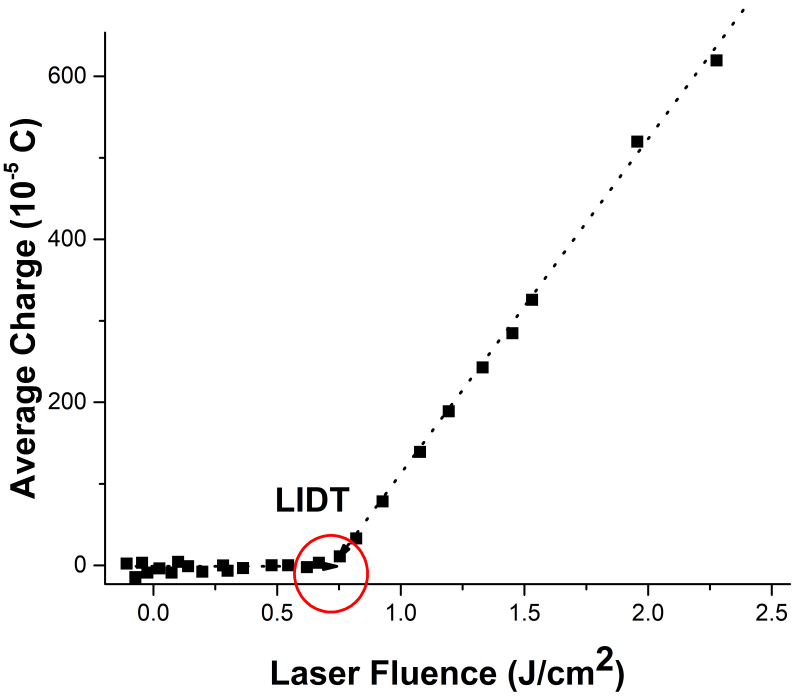


Figure 3.34: Total collected charge as function of the laser fluence calculated for $ZrO_2$ films

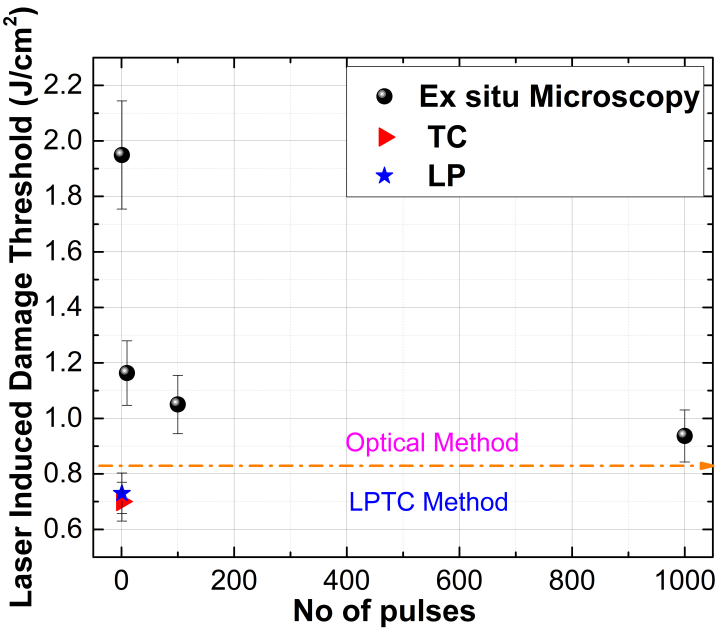


Figure 3.35: Comparison of measured LIDT values between ex-situ microscopy (following ISO) and LP-TC method.

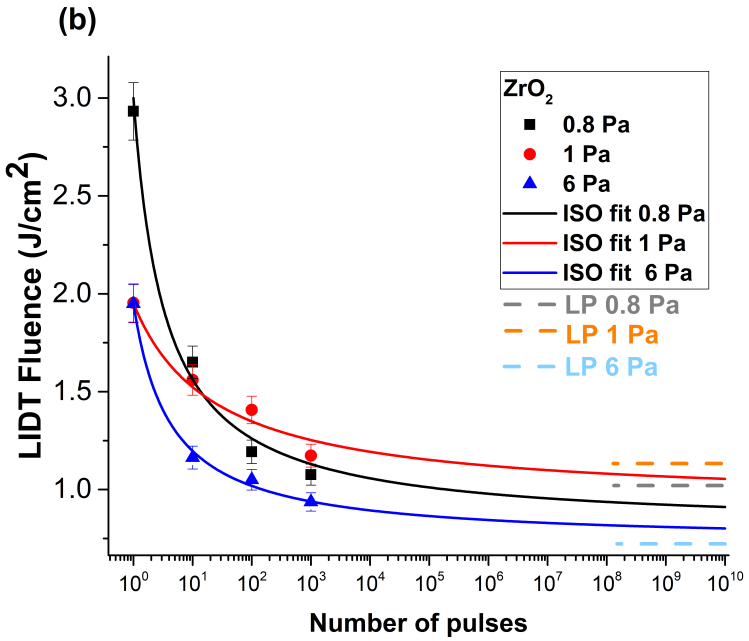


Figure 3.36: The LIDT fluence predicted for a very large number of shots and the values obtained through electrical measurements for films of $ZrO_2$, which were produced under varying oxygen background pressures.

outlined in ISO 21254-2:2011(E) [17]. According to the standard, the LIDT fluence ($H_{Th}$) concerning S-on-1 test damage as a function of the number of pulses ($N$) is defined as:

$$H_{Th}(N) = H_{Th,\infty(LPTC)} + \frac{H_{Th,1} - H_{Th,\infty(LPTC)}}{1 + \delta^{-1} \cdot \log_{10}(N)} \tag{3.10}$$

The extrapolation curve is related to three fitting parameters namely: $H_{Th,1}$ -the 1-on-1 damage threshold, $H_{Th,\infty}$- the endurance limit of the optical surface and $\delta$ a parameter which describes the characteristics damage curve with the number of pulses.

The LPTC determined LIDT values were utilized with the Eq. (3.10) to calculate $H_{Th,\infty}$. By adopting the endurance limit as estimated by LPTC, we successfully reconstructed the $H_{Th}(N)$ function for all the samples in our study. These results are visually represented in Figure 3.36 (solid lines). Each curve in the figure represents a set of simulated values that gradually converge towards the LIDT value determined by LPTC after $10^3$ shots. When the *ex-situ* microscopy data were integrated into this analysis, it becomes evident that the data points align closely with the trends defined by the simulated curves. This outcome substantially deepens our appreciation of the benefits offered by the LP-TC method for LIDT estimation.

The capacity to measure both the charges ejected and subsequently compensated in the irradiated film using a single pulse naturally relates to the long-term irradiation stability of thin films. Furthermore, the consistency observed between *ex-situ* microscopy and the LPTC approach underscores the dependability of these methods for real-time operational monitoring of optical components.

### 3.5.6 Offline microscopy

The offline microscopy was used to validate the occurrence of the damage for all the online methods. An example of the retrieved results from a Leica microscope can be seen

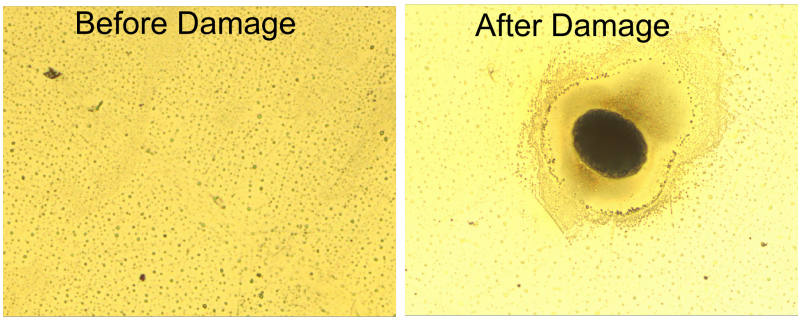


Figure 3.37: Examples of Leika microscope images before and after damage occurs

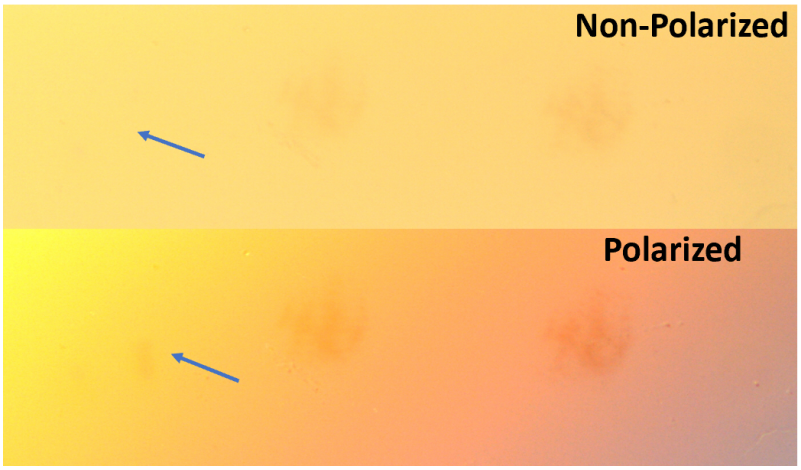


Figure 3.38: Leica microscope images with 2 different polarizations for an R-on 1 damage test.

in Figure 3.22 and 3.37.

Furthermore, using different polarization, I was able to detect permanent damages which initially were considered un-damaged sites. This result is illustrated in Figure 3.38.

#### 3.5.6.1 LIDT of contaminated samples

In the latter part of the LIDT studies, the focus shifted to the issue of mirror contamination. I contributed to the development of a new experimental setup and conducted studies under various plasma and oxygen pressures to investigate the elimination of laser-induced carbonization. For this study, I was involved in performing nanosecond LIDT irradiation measurements at the ISOTEST laboratory (INFLPR), as well as spectral and dispersion measurements.

Understanding laser-induced contamination on optics and developing countermeasures against it is important for maintaining the performance of optical elements in high-power or high-intensity laser facilities.

Two types of mirrors, realized with different coating methods (ion-assisted deposition and electron beam evaporation), were tested. They were irradiated with a Ti:Sapphire short-pulse laser operating at 810 nm, with a typical focal spot radius of 30 $\mu$m. The laser had a pulse duration of approximately 30 fs and operated at a repetition rate of 10 Hz. A systematic investigation was conducted to study the effects of coating type, incident laser fluence, and vacuum pressure during air injection. The effectiveness of mitigating laser-induced contamination was observed in the data obtained at 5 mbar for an average

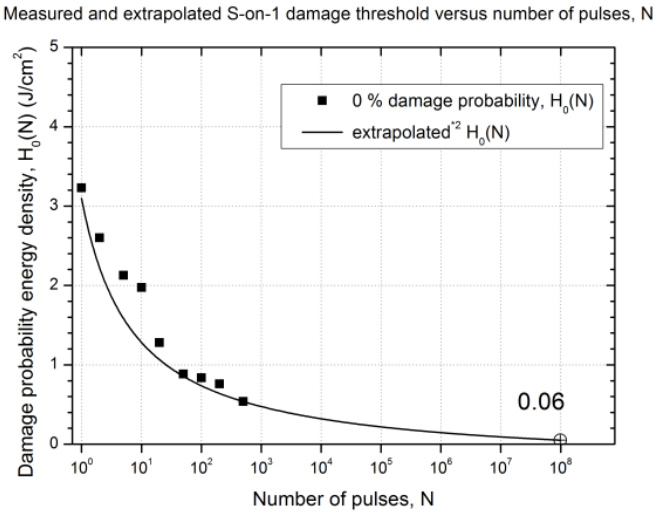


Figure 3.39: Damage probability curve for contaminated dielectric mirror.

laser fluence of 29.2mJ/cm$^2$ (168.7 mJ/cm$^2$ at peak fluence).

Analysis of the beam patterns resulting from 10,000 laser shots suggested the presence of carbonization due to laser-induced contamination. Notably, a carbonization-like pattern was observed only on the dielectric sample with ion-assisted deposition.

In the nanoseconds regime, LIDT (6 ns, 220 $\mu$m, 10 Hz) results were employed to calculate the percentage reduction in LIDT$_\infty$ for the contaminated mirror in comparison to the results obtained after cleaning. This analysis revealed a decrease in LIDT$\infty$ from 0.17 to 0.06 (see Figure 3.39).

Recent studies have demonstrated various cleaning methods to recover the optical performance of these elements. Notably, laser-oxygen interaction, particularly with high-pressure gas injection, shows promise for cleaning and *in-situ* mitigation of laser-induced contamination, even at low-pressure injection levels.

Therefore, I was involved in the mitigation of different types of oxygen plasma, which can be used to "clean" contaminated mirrors. To do this, carbon coating was deposited on a dielectric mirror. The sample was divided into 3 regions: a) no contaminant deposition, b) carbon deposition, and c) surface after plasma cleaning.

I will present 2 methods to investigate the samples.

**Spectral Measurements** Using a broadband source, a sample mirror placed at a 45°angle, and a spectrometer, I recorded the transmission spectra from each of the three regions. The measurements results and the ratio between the regions are presented in Figure 3.40. Worth noting, the only observed modification is related to an attenuation of the spectra. Furthermore, it is important to highlight that the spectra after cleaning were identical to the reference one, demonstrating that mirrors can be effectively cleaned and reintegrated into the high-power laser chain.

On the other hand, the ratio results revealed a sensitivity of approximately 7%. To enhance this sensitivity, I conducted dispersion measurements using the Chromatis device.

Figure 3.41 illustrates the GDD characteristic curves for all three regions. An unexpected result arose from the GDD ratio, which exhibited a difference of about 70 fs$^2$. Given that the device's resolution is $\pm$ 2 fs$^2$, these findings demonstrate considerably higher sensitivity in comparison to spectral measurements. The GDD result implies that this

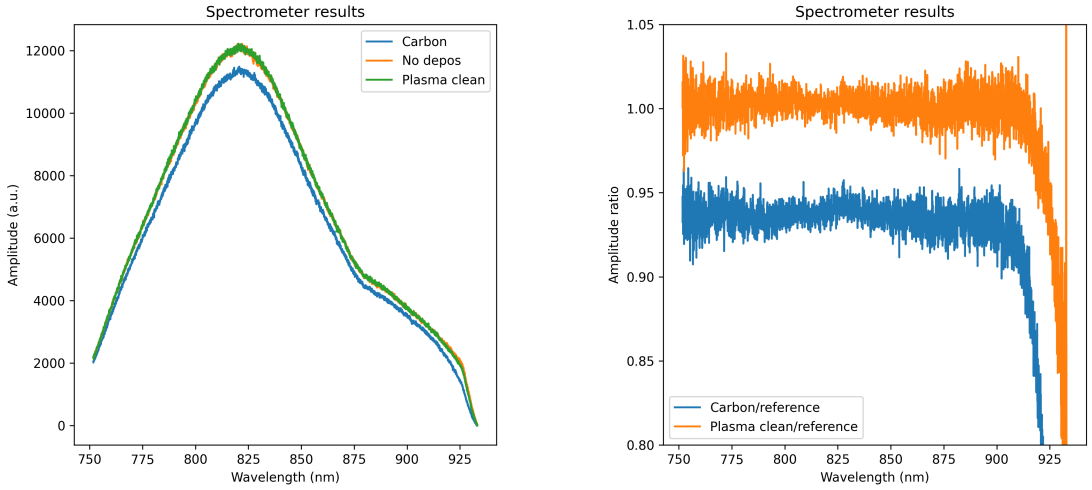


(a) (b)

Figure 3.40: Spectral measurements of the white light reflected from the surface of interest and their spectra ratio

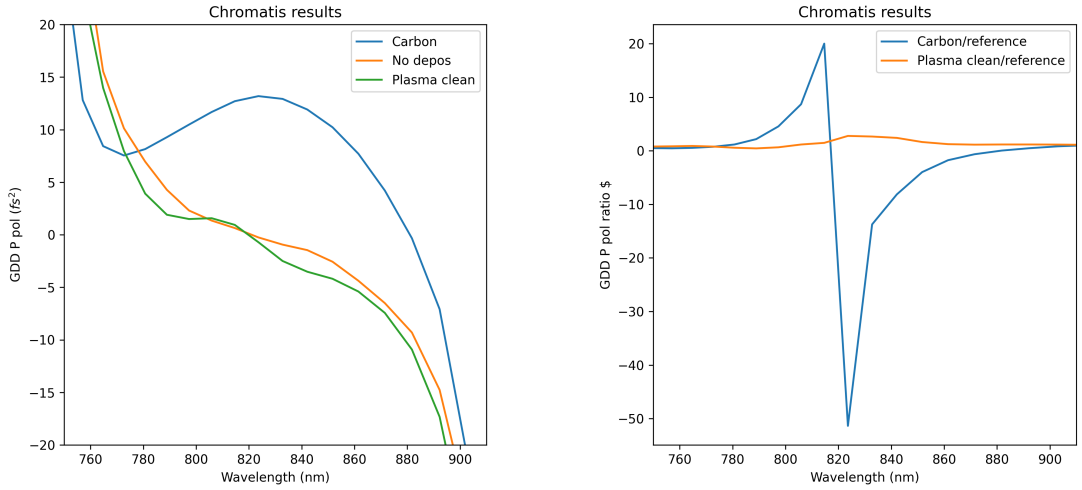


(a) (b)

Figure 3.41: Group Delay Dispersion measurements using Chromatis device and their ratio

measurement method holds promise as a candidate for effectively mitigating laser-induced contamination.

### 3.5.7 Discussion

The Laser-Induced Damage Threshold (LIDT) is an important parameter for high-power laser optics, and for the materials that could be used for spectral broadening and post-compression. Hence, this study required a dedicated *in-house* setup to measure it.

I proposed and built one experimental setup while being involved in the development of two others.

The first, operating in air (as shown in Figure 3.3), is capable of determining in real-time optical properties, such as (I) nonlinear coefficients (including nonlinear refractive index and nonlinear absorption coefficient), (II) LIDT using a long working distance imaging system, an d (III) spectral broadening.

The advantages of this proposed experimental setup are the following:

1. It uses a laser system based on Ti:sapphire amplification at 800 nm, similar to High-Power Laser systems based on Ti:Sapphire.
2. It employs femtosecond pulse durations.
3. It measures LIDT for both transmission and reflection (specifically designed for coated surfaces).
4. It accommodates horizontal or vertical polarization.
5. It offers a resolution of 11 $\mu$m.
6. It features a user-friendly interface and is fully automated.
7. It operates at 10 Hz or single-shot modes.
8. It supports 1-on-1, S-on-1, or R-on-1 LIDT test protocols.

Data analysis is performed using the gray level of the pixels from direct and eclipsed irradiation, the spatial frequency method, and Langmuir probe-target current (LPTC), which can be used in both air and vacuum environments. The qualification of the initial parameters (energy, duration, surface) and the testing method align with ISO 21254 standards 1-4 [17].

The second experimental setup, designed for use in a vacuum environment (as shown in the Figure 3.29), is intended for large beams with varying intensity distributions. It offers the advantage of analyzing multiple fluences per pixel and provides increased statistical data on damaged points.

The third setup, abbreviated as LPTC, utilizes the second assembly from the first setup to complement the results obtained in vacuum for the same samples. This final configuration offers higher sensitivity and the possibility to estimate the $\mathrm{LIDT}_{infty}$ in a single shot.

In summary, the key experimental parameters for both LIDT setups are detailed in Table 3.1. With these two configurations, I was able to adapt various types of samples, including glasses, plastics, nano depositions, nano wires, silver, dielectric, and plasma mirrors. Investigating the LIDT of nano wires and plasma mirrors contributed to a better understanding of laser pulse contrast and pre-pulse intensity.

| Input parameters: | Range | Tuning | Diagnostics |
|---|---|---|---|
| Pulse duration | 40 -200 fs | Compressor | Autocorrelator & FROG |
| Pulse energy | 0.1 $\mu$J- 6 mJ | Malus law (POL+WP) | Energy meter |
| Spot size | 80 $\mu$m – 8 mm | Lenses + beam reducers | LWDIS, USAF test target |

Table 3.1: Laser pulses metrology used in the LIDT setups

My research on LIDT has contributed to a deeper understanding of filamentation, the incubation process, light scattering, contamination and permanent damage.

## 3.6 Chirped mirrors design

The final component of the post-compression setup is the Dispersion Management System (DMS), which involves the design and implementation of chirped mirrors (CMs). In addition to the specifications outlined in Figure 3.1, I have emphasized certain characteristics that were discussed in detail with various manufacturers (LaserOptik, Laser2000, Altechna, UltrafastInovations, Optosigma).

Two types of CM configurations were investigated. The first configuration involves the use of 2 CMs as a pair, where the dispersion introduced by the first CM is compensated for by the second one (the peak position of CM1 corresponds to the minimum of CM2 at a specific wavelength). Figure 3.42 provides a preliminary example of a CM pair, illustrating the overall Group Delay Dispersion (GDD) as a function of the incidence angle (9°and 15°). This figure also highlights the limitations at the bandwidth edges where the mean value of GDD is not reached.

The second configuration consists of a single CM capable of compensating for the GDD. This configuration offers benefits such as space optimization and the compensation of lower values of dispersion (i.e., 40 $fs^2$).

### 3.6.1 Chirped mirrors specifications

The following specifications were taken into consideration to compensate for up to 3 mm of fused silica (FS) or 2 mm of BK7 glass, which may be used in 1 or 2 stages of post-compression:

Spectral bandwidth: 650-950 nm; Central wavelength 807 nm; Polarization: P; Diameter: 75 mm, **150 mm**; Incidence angle (AOI): between 9-30 or **45**°; GDD: -90 or **-70** $fs^2$ ± 10 $fs^2$ over the spectrum; Reflectivity > 99.5% over the spectrum; Optical surface roughness <2 nm; Coating P-V wavefront error: $<\lambda/10$; Substrate P-V wavefront error: $<\lambda/10$; LIDT > 260 $mJ/cm^2$; Scratch-dig (optical surface quality): 20:10 or better; Clear aperture >90%;

The bold numbers denote the CMs characteristics used in the last experiment of Chapter IV.

In the following, the results regarding overall dispersion, transmission, angle of incidence (AOI), LIDT, reflected bandwidth, and wavefront are discussed.

### 3.6.2 Chirped mirrors characterization

I investigated the dispersion after a pair of CMs, the damage threshold, the peak-to-valley (P-V) wavefront, and the reflected spectrum as functions of the incidence angle on the mirrors (AOI). The AOI plays an important role when dealing with large beams (> 6 cm) due to space constraints in the interaction chamber and clear aperture limitations. I analyzed the overall GDD obtained at AOIs of 9, 10, 15, 30, and 45 degrees. As the beam size increases, the cost and the challenges associated with manufacturing and maintaining the GDD and P-V wavefront within specifications become critical. Currently, the largest reported CM has a diameter of 10 inches.

The most conclusive results regarding GDD were obtained for 30-degree, 4-inch mirrors, which can handle the 100 TW beam at ELI-NP. Figure 3.43 illustrates that the precision in manufacturing and layer thickness was reflected in the GDD measurements, with an RMS value of ± 6 $fs^2$, as determined using a Chromatis device.

For all the investigated cases of AOI, the transmittance or reflectance met the required specifications.

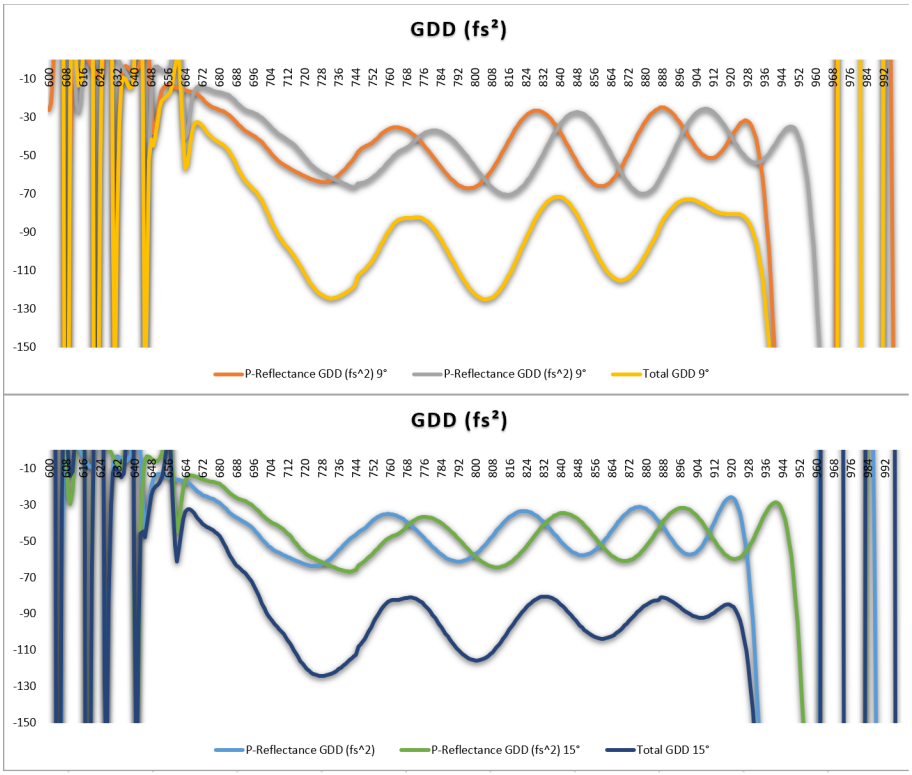


Figure 3.42: GDD as a function of the incidence angle of 9°and 15°for a CM pair

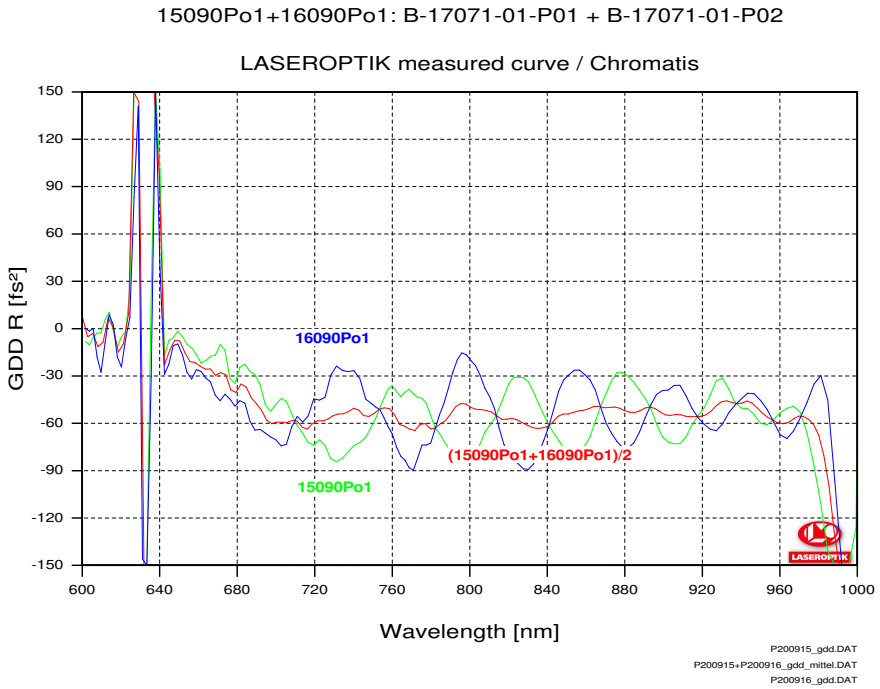


Figure 3.43: Simulated GDD for an input AOI of 30°where P01 and P02 denote the mirrors deposition order. Courtesy of LaserOptik.

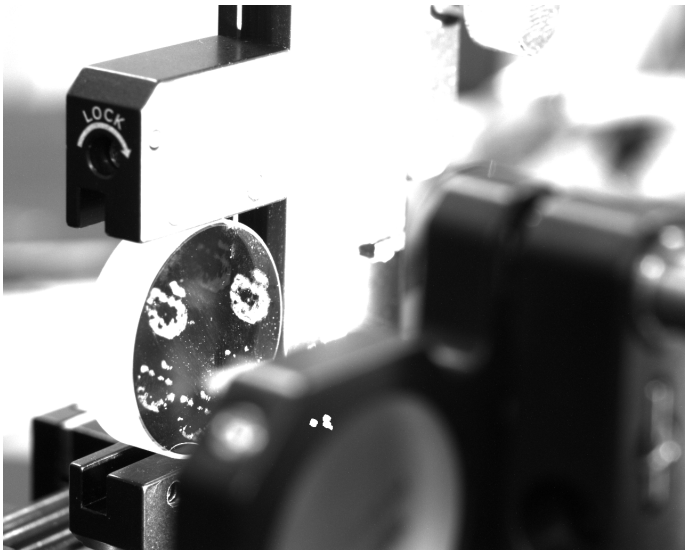


Figure 3.44: Offline analysis of Large beam LIDT on HT chirped mirror

### 3.6.3 Chirped mirrors LIDT

The LIDT of the chirped mirrors was assessed through the large beam LIDT method, in conjunction with online imaging, and these findings were cross-referenced with the offline microscopy results.

#### 3.6.3.1 Large beam LIDT on chirped mirrors

The chirped mirrors in high-power laser systems need to withstand a substantial number of shots, often exceeding 1000 (1k).

For the laser input parameters, we have the following specifications: Wavelength: 800 nm; Repetition Rate: 10 Hz; Energy per Shot: 90.65 mJ (with a 15-degree waveplate rotation); Input Spot Size: 3.6 mm; Input beam fluence: 250.77 mJ/cm$^2$, P-Polarization.

The chirped mirror utilized in this setup had high transmittance (HT), a diameter of 25 mm and the distance between two sites on the mirror surface was 5 mm (see Figure 3.44).

Three different LIDT configurations were examined with respect to the number of laser pulses applied, which are presented in Figure 3.45 and described below.

The large beam LIDT makes it possible to obtain a large number of measurement points and cover a wide range of fluences from a single measurement.

**500 Shots:** when considering 100 laser shots consecutively up to 500 shots, we observed a two-stage incubation process. In the initial stage, which spans from approximately 25 to 50 gray level intensity (GLI), we notice slight damage. Although this damage appears in a low number of points (few percent), it is still higher than zero when accounting for errors. The second incubation stage, encompassing 60 to 100 GLI, shows the emergence of more noticeable damage. Beyond the 100 GLI, we encounter full damage. It is worth noting that a relatively low damage threshold, around 40 GLI, was utilized in this assessment. Consequently, a significant portion of the surrounding areas also exhibited damage. This suggests that much of the observed damage is either incubated or quite small in this stage.

**1000 Shots:** in the case of 1000 laser shots, a similar incubation pattern is observed, albeit with some variations. Again, a low damage threshold, roughly 50 intensity gray level, was employed, leading to considerable noise in the results. This time, only one incubation

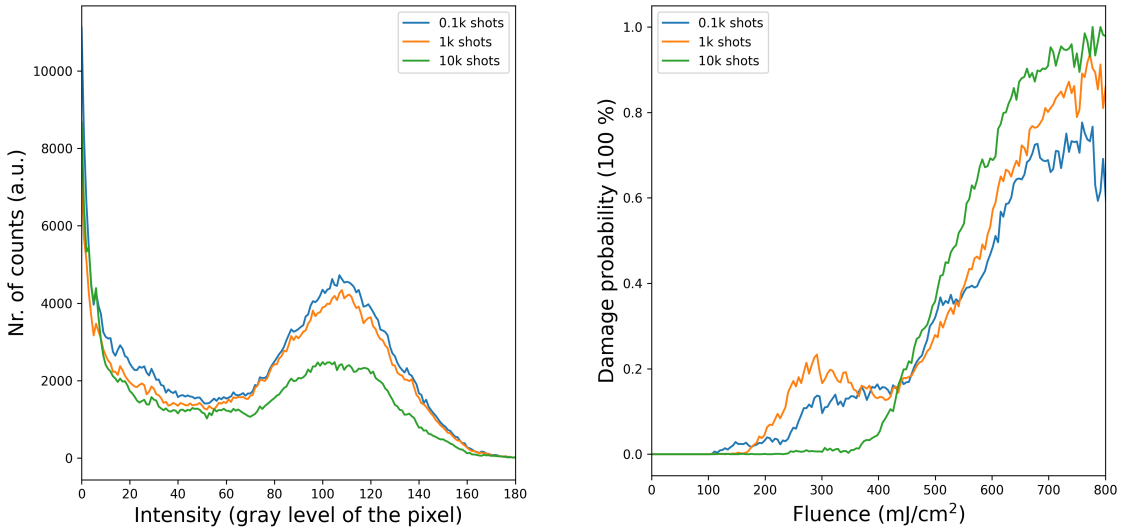


(a) (b)

Figure 3.45: Pixels damage probability for 100 *5 (R-on-1 test, with 100 shots per energy), 1000 and 10 000 shots

stage is evident, spanning from around 40 to 90 GLI. Beyond the 90 GLI, we observe full damage.

**10,000 Shots:** when the number of pulses was increased to 10,000, the damage profile becomes more distinct. It closely resembles the laser profile itself. Remarkably, there is no observable incubation in this scenario. Instead, the damage curve exhibits a sharp and well-defined rise. Damage initiation begins after 90 shots, and full damage is observed beyond this point.

In summary, the number of laser shots plays a significant role in shaping the damage profile, the presence of incubation stages, and the threshold for detecting damage. The use of a large beam with a gradient of fluences offers the highest statistic ever reported in such configuration.

### 3.6.3.2 ISO standard LIDT on chirped mirrors

The large beam LIDT method was validated through standard ISO measurements using fs laser pulses (70 fs pulse duration, 300 $\mu$m spot size). The results are presented in Figure 3.46, where a high transmission (HT) chirped mirror (CM) was compared with a high reflective (HR) CM. It can be observed that the most relevant LIDT value was obtained for 1,000 pulses. Comparing these measured values with the large beam LIDT method, they appeared to be quite similar. A threshold value with an error of $\pm$ 30 mJ/cm$^2$ is attributed to the ISO measurement due to the residual material expelled from the sample during the previous large beam LIDT test.

From my LIDT measurements, these 2 types of CM can be safely used at a fluence ($LIDT_{inf}$) of 100 mJ/cm$^2$ $\pm$ 15 mJ/cm$^2$.

In conclusion the actual limitations of the CMs are related to the size, LIDT, bandwidth and nonlinear absorption.

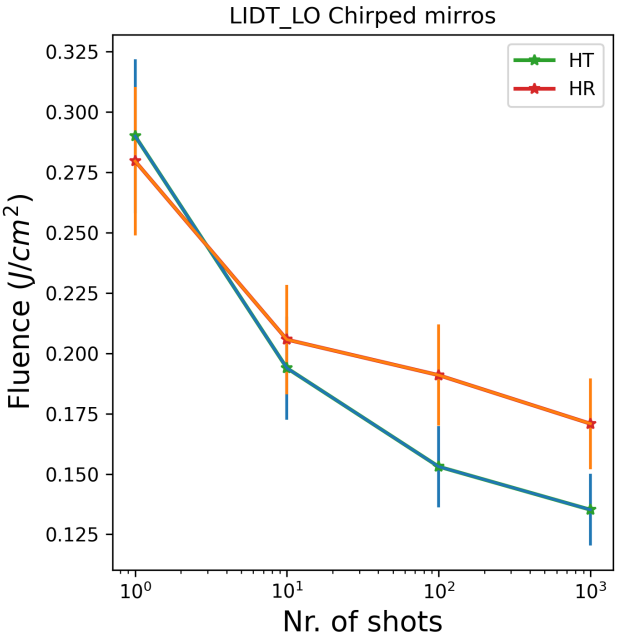


Figure 3.46: LIDT results on 2 types of Chirped mirrors produced by LaserOptik using the experimental setup detailed in Figure 3.7 in air.

## 3.7 Discussion

This chapter provides a detailed understanding of the main optical materials properties namely: dispersion, roughness, transmission, vacuum compatibility, wavefront distortions, nonlinearities (refraction and absorption), self-phase modulation, and laser induced damage threshold. All these parameters have been measured using dedicated devices. For the last 3 properties, I designed an experimental setup, completely automatized, which is able to measure and to provide real time feedback and diagnostics results.

I contributed to the development of new techniques to measure the nonlinearities such as Radius Z-scan and LIDT aperture or to measure the LIDT through spatial frequencies, large beam LIDT or Langmuir Probe-Target Current methods. On both sides, nonlinearities or LIDT respectively, the techniques are novel developed, complementary providing quantitative and qualitative results.

I performed a case study of negative $n_2$ analyzing samples of $TiO_2$ anatase, deposit on quarts, FS, BK7 and Sapphire through Magneto-Sputtering and Pulse Laser Deposition technique. Different thicknesses of $TiO_2$ from 200-600 nm have been deposited and qualified with the ellipsometer. From the NRI measurements, I observed that the thickness was too low to compensate the positive $n_2$ of the substrate even if the preliminary calculations based on Ref. [45] results indicate that the effect of the negative part is predominant.

A complete characterization of optical materials used for post-compression has been performed for the first time, to the best of my knowledge. The experimental results of these sections 3.2 and 3.4 are summarized in the following Table 3.2.

The nonlinear studies were summarized and illustrated in Figure 3.47.The nonlinear phase variation as a function of the input energy is illustrated in Figure 3.47. The NRI value is retrieved from $\Delta\Phi \approx n_2 I$, hence the phase is strictly correlated with $I$. Considering that the pulse duration and the input spot size fluctuation are below 4%, I observed that the phase has a different dependence (slope) for each material while the energy is increased.

| **Material** | **GDD** ($fs^2$) | **T** (%) | **R** ($\mu m$) | **WF RMS** ($\mu m$) | **WF** ($\mu m$) | **NRI - $n_2$** | | | | **NAC -** $\beta$ |
|---|---|---|---|---|---|---|---|---|---|---|
| | | | | | | **Z-scan** | **I-scan** | **Radius Z-scan** | **LIDT-Aperture** | |
| **FS** | 36 | 97 | 5.94 | 0.08 ($\sim\lambda/7$) | 0.18($\sim\lambda/2$) | 3.56 | 3.15 | 3.75 | 3.23 | 5.16 |
| **BK7** | 45 | 96.1 | 6.46 | 0.09 ($\sim\lambda/6$) | 0.18($\sim\lambda/2$) | 1.59 | 2.75 | 2.21 | 2.85 | 18.8 |
| **Zeonor** | 75 | 95.4 | 6.92 | 0.1 ($\sim\lambda/6$) | 0.46($\sim\lambda/2$) | 3.71 | 2.48 | 4.71 | 2.55 | 12.3 |
| **Zeonex** | 67 | 96.5 | 7.29 | 0.06 ($\sim\lambda/10$) | 0.34($\sim\lambda/2$) | 4.49 | 2.67 | 4.37 | 2.75 | 14.4 |
| **Topas** | 70 | 96.2 | 6.52 | 0.07 ($\sim\lambda/9$) | 0.33($\sim\lambda/2$) | 4.96 | 3.8 | 4.69 | 4.45 | 7.06 |
| **PC** | 136 | 95.6 | 6.23 | 0.09 ($\sim\lambda/6$) | 0.42($\sim\lambda/2$) | 3.34 | 2.53 | 4.34 | 2.72 | 16.4 |
| **PMMA** | 58 | 96.4 | 5.64 | 0.09 ($\sim\lambda/6$) | 0.45($\sim\lambda/2$) | 2.33 | 2.53 | 3.02 | 2.58 | 4.38 |
| **OKP*** | 7 | 96.7 | 6.21 | 0.03 ($\sim\lambda/18$) | 0.21($\sim\lambda/3$) | - | 5.37 | 2.81 | 4.71 | 2.02 |
| **Apel*** | 8 | 96.3 | 5.37 | 0.04 ($\sim\lambda/13$) | 0.22($\sim\lambda/3$) | 5.57 | 4.5 | 5.17 | 4.08 | 9.4 |
| **Zeonor*** | 7.5 | 96.8 | 4.74 | 0.01 ($\sim\lambda/45$) | 0.09($\sim\lambda/8$) | - | 5.88 | 4.69 | 5.13 | 10.3 |

Table 3.2: Preliminary results for materials characterization where T- Transmission, R- the Roughness and WF- the Wavefront Root Mean Square (RMS) and Peak-to-Valley (P-V), '-'- not measured. The materials with * had a thickness of 0.1 mm while the other 1 mm. NRI is in units of $*10^{-20}m^2/W$ and NAC is in units of $*10^{-14}m/W$. The NRI values have a standard deviation of $\sim$ 15% due to the variation of the input laser parameters and they are in agreement with the values from the literature.

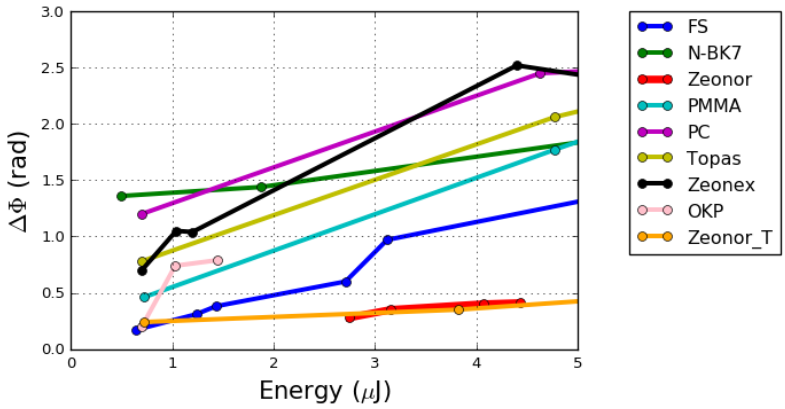


Figure 3.47: Nonlinear phase as a function of the input energy for the chosen optical materials

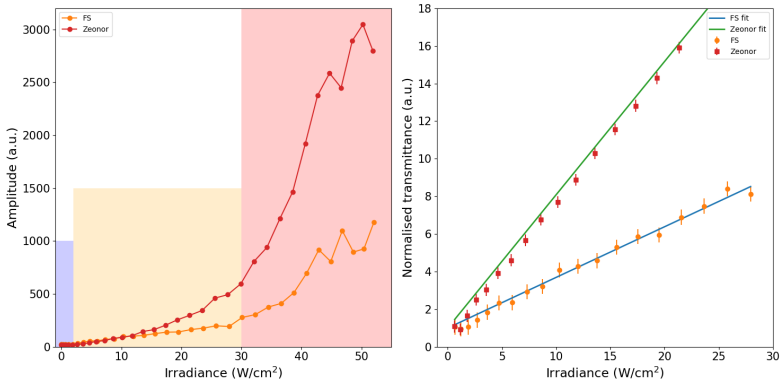


Figure 3.48: I-scan measurements. Raw data plotted in the 3 regions of interest (Left) and the raw data and fit for FS and Zeonor (Right).

This graph helped me to know where to stop the variation of the energy to not overpass 1 rad. There were also higher nonlinear materials as PolyCarbonate (PC) for which I always measured a higher phase.

Another perspective to obtain the NRI was from the I-scan type measurements where I summarized the interaction of light with matter in the 3 regions (linear, nonlinear and damage). Beside the fitting curve, a rough estimation can be done by dividing the slope of each curve to the reference (i.e. FS where the NRI has been measured in multiple references [4]).

**LIDT** Within this work, I was involved in building three experimental setups (one in air and two in vacuum), and I contributed to the development of four methods to investigate LIDT. These methods include original ones, such as spatial frequency analysis, and in collaboration with other teams, we developed the Large Beam LIDT and the Langmuir Probe - Target Current methods. The fourth method, offline microscopy, was further extended with real-time viewing, which can image the entire surface to be damaged. Furthermore, I introduced Profilometer analysis, which can provide information about the damage depth and filamentation length.

The issue of laser system mirror contamination and carbonization is essential in high-power facilities. In my research, I focused on the removal of laser-induced carbonization and contamination using oxygen-based plasma, and I demonstrated an increase in the sensitivity of differentiation methods by conducting GDD (Group Delay Dispersion) mea-

surements.

Furthermore, I conducted measurements and compared the LIDT of two chirped mirrors, considering the most important parameters. The high-reflectivity mirrors exhibited the highest LIDT value.

The spectral broadening is related to the nonlinear refractive index and also to the laser intensity. The latter term is strictly dependent on the fluence that reaches the material and, thus, the LIDT. Therefore, with the measured data of NRI, I implemented SPM simulations which, with the data of LIDT for each material, were closer to the experimental measurements.

The damage threshold fluences for glasses (following the ISO standards) were >1 J/cm$^2$, whereas for 1 mm thick plastic, they did not surpass 100 mJ/cm$^2$. The 100 $\mu$m thick plastic samples exhibited a doubled LIDT compared to the 1 mm thickness ones, attributed to the low impact of self-focusing.

The LIDT results were presented at 7 conferences (see List of Publications), reported in 2 proceedings (SPIE), and the LPTC results were submitted as a paper.

The work performed, including setup, method, analysis, and reporting, was summarized as a standard LIDT procedure of ELI-NP Optics Laboratory. Therefore, within this work, the ELI-NP facility has the capability to perform standardized LIDT measurements, utilize complementary methods to fully characterize different types of samples, and prioritize sensitivity, statistical analysis, sub-threshold measurements, and automation as key aspects.

This sub-chapter is concluded with the main results, as a table, from the materials characterization (Table 3.2). Different glass and plastic materials were compared to fulfill the criteria mentioned in Figure 3.1. It can be observed that the perfect material (no dispersion, low wavefront distortions, high NRI and LIDT) does not exist but that novel thin materials such as Zeonor and OKP (100 $\mu m$) lead to a better response than BK7 or FS for the SPM process. With their low wavefront distortions, high NRI, large size and higher LIDT compared to other plastics, these thin materials can be used in series and separated in space to minimize the potential small scale self-focusing effect.

The glass materials can be used if the roughness is improved ($\lambda/10$) or the wavefront distortions are corrected with a deformable mirror. For both cases (plastic or glass) a deformable mirror loop is recommended to improve the focal spot quality. Their importance is presented within experimental measurements in the next Chapter.

## 3.8 Publications of this chapter

The activity related to LIDT has been published in Ref. [34, 38] and the work related to LPTC "Exploring fs-laser irradiation damage subthreshold behavior of dielectric mirrors via electrical measurements" was submitted in High Power Laser Science and Engineering journal.

[38]. **P.-G. Bleotu**, S. Irimiciuc, A. Dumitru, D.G. Matei, R. Udrea, D. Craciun, I. Dancus, V. Craciun, D. Ursescu, Target current and spatial modulations analysis for LIDT measurements using fs laser irradiation, in: Laser-Induced Damage in Optical Materials 2023, SPIE, Dublin/Livermore, United States, 2023: p. 81. https://doi.org/10.1117/12.2685157.

[34]. **P.-G. Bleotu**, A. Naziru, A.H. Okukura, S. Popa, D. Matei, A. Dumitru, C. Alexe, V.P. Iancu, A.-M. Talposi, V.C. Musat, I. Dancus, L.P. Caratas, B. Boisdeffre, T. Samoskoi, J. Takahisa, J. Wheeler, G. Mourou, D. Ursescu, LIDT station development with femtosecond pulses at ELI-NP, in: Laser-Induced Damage in Optical Materials 2022, SPIE, 2022. https://doi.org/10.1117/12.2641616.

# Bibliography


[1] V N Ginzburg, I V Yakovlev, et al. "Compression after compressor: threefold shortening of 200-TW laser pulses". en. In: *Quantum Electronics* 49.4 (Apr. 2019), pp. 299–301. URL: http://stacks.iop.org/1063-7818/49/i=4/a=299?key=crossref.7ad3e5ee4900d83cf1e95515a378bd43 (visited on 05/06/2019).

[2] P.-G. Bleotu, J. Wheeler, et al. "Spectral broadening for multi-Joule pulse compression in the APOLLON Long Focal Area facility". en. In: *High Power Laser Science and Engineering* 10 (2022). Publisher: Cambridge University Press. URL: https://www.cambridge.org/core/journals/high-power-laser-science-and-engineering/article/spectral-broadening-for-multijoule-pulse-compression-in-the-apollon-long-focal-area-facility/62E91CE89219A83DCAC94BEE27CD4F6F (visited on 03/07/2022).

[3] S Yu Mironov, V N Ginzburg, et al. "Using self-phase modulation for temporal compression of intense femtosecond laser pulses". en. In: *Quantum Electronics* 47.7 (July 2017), pp. 614–619. URL: http://stacks.iop.org/1063-7818/47/i=7/a=614?key=crossref.05447f7085d35235d951af5ca02eabd4 (visited on 02/06/2019).

[4] Jonathan Wheeler, Gabriel Petrişor Bleotu, et al. "Compressing High Energy Lasers through Optical Polymer Films". en. In: *Photonics* 9.10 (Oct. 2022). Number: 10 Publisher: Multidisciplinary Digital Publishing Institute, p. 715. URL: https://www.mdpi.com/2304-6732/9/10/715 (visited on 10/04/2022).

[5] M. Masruri, J. Wheeler, et al. "Optical Thin Film Compression for Laser Induced Plasma Diagnostics". en. In: *Conference on Lasers and Electro-Optics*. San Jose, California: OSA, 2019, SW4E.3. URL: https://opg.optica.org/abstract.cfm?URI=CLEO_SI-2019-SW4E.3 (visited on 06/20/2023).

[6] Daniel Ursescu, Dan Matei, et al. "First HPLS Experiments at ELI-NP: Spectral Broadening in Thin Films". en. In: *Frontiers in Optics* (2020), p. 2.

[7] Vladislav Ginzburg, Ivan Yakovlev, et al. "10 fs, 1.5 PW Laser with Nonlinear Pulse Compression in KDP Crystal". en. In: (2022), p. 2.

[8] S. Yu. Mironov, S. Fourmaux, et al. "Thin plate compression of a sub-petawatt Ti:Sa laser pulses". en. In: *Applied Physics Letters* 116.24 (June 2020), p. 241101. URL: http://aip.scitation.org/doi/10.1063/5.0008544 (visited on 06/22/2020).

[9] S Yu Mironov, J Wheeler, et al. "100 J-level pulse compression for peak power enhancement". en. In: *Quantum Electronics* 47.3 (Mar. 2017), pp. 173–178. URL: http://stacks.iop.org/1063-7818/47/i=3/a=173?key=crossref.bc537e9b520e19d80018dbb8797b98f9 (visited on 02/06/2019).

[10] E. A. Khazanov, S. Yu Mironov, et al. "Nonlinear compression of high-power laser pulses: compression after compressor approach". en. In: *Physics-Uspekhi* 62.11 (Nov. 2019). Publisher: IOP Publishing, p. 1096. URL: https://iopscience.iop.org/article/10.3367/UFNe.2019.05.038564/meta (visited on 11/09/2020).

[11] G. Wormser, C. Barty, et al. *The White Book of ELI Nuclear Physics Bucharest-Magurele, Romania*. Vol. 68. Romanian Report in Physics, Dec. 2010. URL: http://www.eli-np.ro/whitebook.php.

[12] Ji In Kim, Ji In Kim, et al. "Wavefront-corrected post-compression of a 100-TW Ti:sapphire laser". EN. In: *Optics Express* 30.15 (July 2022). Publisher: Optica Publishing Group, pp. 26212–26219. URL: https://opg.optica.org/oe/abstract.cfm?uri=oe-30-15-26212 (visited on 10/18/2022).

[13] M. Sheik-Bahae, A.A. Said, et al. "Sensitive measurement of optical nonlinearities using a single beam". en. In: *IEEE Journal of Quantum Electronics* 26.4 (Apr. 1990), pp. 760–769. URL: http://ieeexplore.ieee.org/document/53394/ (visited on 02/19/2019).

[14] I Dancus, V I Vlad, et al. "Z-SCAN AND I-SCAN METHODS FOR CHARACTERIZATION OF DNA OPTICAL NONLINEARITIES". en. In: *Romanian Reports in Physics* 65.3 (2013), pp. 966–978.

[15] Rick Trebino, Kenneth W. DeLong, et al. "Measuring ultrashort laser pulses in the time-frequency domain using frequency-resolved optical gating". en. In: *Review of Scientific Instruments* 68.9 (Sept. 1997), pp. 3277–3295. URL: http://aip.scitation.org/doi/10.1063/1.1148286 (visited on 11/12/2020).

[16] B. Dromey, C. Bellei, et al. "Third harmonic order imaging as a focal spot diagnostic for high intensity laser-solid interactions". en. In: *Laser and Particle Beams* 27.2 (June 2009). Num Pages: 5 Number: 2, pp. 243–248. URL: http://dx.doi.org/10.1017/S0263034609000329 (visited on 07/26/2021).

[17] ISO. *ISO 21254-2:2011*. en. URL: https://www.iso.org/standard/43002.html (visited on 07/11/2023).

[18] Laurent Gallais and Jean-Yves Natoli. "Optimized metrology for laser-damage measurement: application to multiparameter study". en. In: *Applied Optics* 42.6 (Feb. 2003), p. 960. URL: https://www.osapublishing.org/abstract.cfm?URI=ao-42-6-960 (visited on 09/09/2020).

[19] David Milam. "Review and assessment of measured values of the nonlinear refractive-index coefficient of fused silica". en. In: *Applied Optics* 37.3 (Jan. 1998), p. 546. URL: https://www.osapublishing.org/abstract.cfm?URI=ao-37-3-546 (visited on 02/01/2021).

[20] Mansoor Sheik-Bahae. "Nonlinear refraction and optical limiting in [quotation mark]thick[quotation mark] media". en. In: *Optical Engineering* 30.8 (1991), p. 1228. URL: http://opticalengineering.spiedigitallibrary.org/article.aspx?doi=10.1117/12.55902 (visited on 05/08/2019).

[21] Radoslaw Kolkowski and Marek Samoc. "Modified Z-scan technique using focus-tunable lens". en. In: *Journal of Optics* 16.12 (Oct. 2014). Publisher: IOP Publishing, p. 125202. URL: https://doi.org/10.1088%2F2040-8978%2F16%2F12%2F125202 (visited on 11/09/2020).

[22] Hua Long, Guang Yang, et al. “Femtosecond Z-scan measurement of third-order optical nonlinearities in anatase TiO2 thin films”. en. In: *Optics Communications* 282.9 (May 2009), pp. 1815–1818. URL: https://linkinghub.elsevier.com/retrieve/pii/S0030401809001059 (visited on 02/07/2019).

[23] Aurel Stratan, Alexandru Zorila, et al. “Automated test station for laser-induced damage threshold measurements according to ISO 21254-1,2,3,4 standards”. In: *Proc SPIE* (Nov. 2012).

[24] L. Gallais, J. Natoli, et al. “Statistical study of single and multiple pulse laser-induced damage in glasses”. en. In: *Optics Express* 10.25 (Dec. 2002), p. 1465. URL: https://www.osapublishing.org/oe/abstract.cfm?uri=oe-10-25-1465 (visited on 09/04/2020).

[25] Stavros G. Demos, Mike Staggs, et al. “Investigation of processes leading to damage growth in optical materials for large-aperture lasers”. en. In: *Applied Optics* 41.18 (June 2002), p. 3628. URL: https://www.osapublishing.org/abstract.cfm?URI=ao-41-18-3628 (visited on 09/28/2020).

[26] Robert W. Boyd. *Nonlinear Optics,Third Edition,9780123694706,2008*. URL: https://www.academia.edu/18337240/Boyd_Nonlinear_Optics_Third_Edition (visited on 09/27/2019).

[27] Shutao Li, James T. Kwok, et al. “Combination of images with diverse focuses using the spatial frequency”. In: *Information Fusion* 2.3 (Sept. 2001), pp. 169–176. URL: https://www.sciencedirect.com/science/article/pii/S1566253501000380 (visited on 09/01/2023).

[28] Adriana Fiorentini, Lamberto Maffei, et al. “The Role of High Spatial Frequencies in Face Perception”. en. In: *Perception* 12.2 (Apr. 1983). Publisher: SAGE Publications Ltd STM, pp. 195–201. URL: https://doi.org/10.1068/p120195 (visited on 09/01/2023).

[29] Sergey Mironov, Vladimir Lozhkarev, et al. “Suppression of small-scale self-focusing of high-intensity femtosecond radiation”. en. In: *Applied Physics B* 113.1 (Oct. 2013), pp. 147–151. URL: https://doi.org/10.1007/s00340-013-5450-1 (visited on 11/01/2022).

[30] Vladislav Ginzburg, Mikhail Martyanov, et al. “Small-scale fluctuations of laser beam fluence at the large B-integral in ultra-high intensity lasers”. EN. In: *Optics Express* 31.3 (Jan. 2023). Publisher: Optica Publishing Group, pp. 4667–4674. URL: https://opg.optica.org/oe/abstract.cfm?uri=oe-31-3-4667 (visited on 02/08/2023).

[31] V. N. Ginzburg, A. A. Kochetkov, et al. “Suppression of small-scale self-focusing of high-power laser beams due to their self-filtration during propagation in free space”. en. In: *Quantum Electronics* 48.4 (Apr. 2018). Publisher: IOP Publishing, p. 325. URL: https://iopscience.iop.org/article/10.1070/QEL16637/meta (visited on 03/07/2022).

[32] Alexander M. Rubenchik, Sergey K. Turitsyn, et al. “Modulation instability in high power laser amplifiers”. en. In: *Optics Express* 18.2 (Jan. 2010), p. 1380. URL: https://www.osapublishing.org/oe/abstract.cfm?uri=oe-18-2-1380 (visited on 01/09/2022).

[33] Aleksandr A. Voronin, Aleksei M. Zheltikov, et al. “Subexawatt few-cycle lightwave generation via multipetawatt pulse compression”. en. In: *Optics Communications* 291 (Mar. 2013), pp. 299–303. URL: https://linkinghub.elsevier.com/retrieve/pii/S0030401812012230 (visited on 03/07/2022).

[34] Gabriel Petrisor Bleotu, Andrei Naziru, et al. "LIDT station development with femtosecond pulses at ELI-NP". In: *Laser-Induced Damage in Optical Materials 2022*. Vol. PC12300. SPIE, Dec. 2022. URL: https://www.spiedigitallibrary.org/conference-proceedings-of-spie/PC12300/0000/LIDT-station-development-with-femtosecond-pulses-at-ELI-NP/10.1117/12.2641616.full (visited on 12/09/2022).

[35] Shenjiang Wu, Junhong Su, et al. "The effect of the applied electric field on laser-induced damage of dielectric thin films". In: *Materials Research Express* 4.1 (Jan. 2017), p. 016403. URL: https://doi.org/10.1088/2053-1591/4/1/016403 (visited on 02/03/2022).

[36] S. A. Irimiciuc, S. Gurlui, et al. "Langmuir probe investigation of transient plasmas generated by femtosecond laser ablation of several metals: Influence of the target physical properties on the plume dynamics". en. In: *Applied Surface Science*. 10th International Conference on Photoexcited Processes and Applications 417 (Sept. 2017), pp. 108–118. URL: https://www.sciencedirect.com/science/article/pii/S0169433217307158 (visited on 07/17/2023).

[37] Radu Udrea, Stefan Andrei Irimiciuc, et al. "Subthreshold Laser Ablation Measurements by Langmuir Probe Method for ns Irradiation of HfO2 and ZrO2". In: *Materials* 16.2 (Jan. 2023), p. 536. URL: https://www.mdpi.com/1996-1944/16/2/536 (visited on 07/10/2023).

[38] Gabriel Petrisor Bleotu, Stefan Irimiciuc, et al. "Target current and spatial modulations analysis for LIDT measurements using fs laser irradiation". en. In: *Laser-Induced Damage in Optical Materials 2023*. Ed. by Christopher W. Carr, Detlev Ristau, et al. Dublin/Livermore, United States: SPIE, Nov. 2023, p. 81. URL: https://www.spiedigitallibrary.org/conference-proceedings-of-spie/12726/2685157/Target-current-and-spatial-modulations-analysis-for-LIDT-measurements-using/10.1117/12.2685157.full (visited on 09/22/2023).

[39] Jikun Chen, James G. Lunney, et al. "Langmuir probe measurements and mass spectrometry of plasma plumes generated by laser ablation of La0.4Ca0.6MnO3". In: *Journal of Applied Physics* 116.7 (Aug. 2014), p. 073303. URL: https://doi.org/10.1063/1.4893479 (visited on 07/10/2023).

[40] Nadezhda M. Bulgakova, Alexei N. Panchenko, et al. "Impacts of Ambient and Ablation Plasmas on Short- and Ultrashort-Pulse Laser Processing of Surfaces". In: *Micromachines* 5.4 (Dec. 2014), pp. 1344–1372. URL: https://www.mdpi.com/2072-666X/5/4/1344 (visited on 07/10/2023).

[41] Praveen Kumar Velpula, Daniel Kramer, et al. "Femtosecond Laser-Induced Damage Characterization of Multilayer Dielectric Coatings". en. In: *Coatings* 10.6 (June 2020). Number: 6 Publisher: Multidisciplinary Digital Publishing Institute, p. 603. URL: https://www.mdpi.com/2079-6412/10/6/603 (visited on 02/24/2021).

[42] Laurent Gallais, Benoit Mangote, et al. "An exhaustive study of laser damage in ion beam sputtered pure and mixture oxide thin films at 1030 nm with 500 fs pulse durations". In: *Laser-Induced Damage in Optical Materials: 2012*. Ed. by Gregory J. Exarhos, Vitaly E. Gruzdev, et al. Vol. 8530. Backup Publisher: International Society for Optics and Photonics. SPIE, 2012, 85300K. URL: https://doi.org/10.1117/12.977553.

[43] JiaHui Wen, Meiping Zhu, et al. “Optical and femtosecond laser-induced damage-related properties of Ta2O5-based oxide mixtures”. en. In: *Journal of Alloys and Compounds* (Apr. 2023), p. 170352. URL: https://www.sciencedirect.com/science/article/pii/S0925838823016559 (visited on 05/03/2023).

[44] Shunli Chen, Yuan’an Zhao, et al. “Femtosecond laser-induced damage of HfO2/SiO2 mirror with different stack structure”. In: *Appl Opt* 51.25 (Sept. 2012), pp. 6188–6195.

[45] Hua Long, Aiping Chen, et al. “Third-order optical nonlinearities in anatase and rutile TiO2 thin films”. en. In: *Thin Solid Films* 517.19 (Aug. 2009), pp. 5601–5604. URL: https://linkinghub.elsevier.com/retrieve/pii/S0040609009002181 (visited on 08/31/2023).

CHAPTER 4

# Chapter 4 Experiments

The results from the previous chapter played an essential role in guiding the experimental work detailed in this chapter. Key parameters such as dispersion, the nonlinear refractive index, B-integral, and self-phase modulation simulations were harnessed in the execution of four post-compression experiments.

This chapter delves into four distinct experimental campaigns where we focused on the post-compression of ultra-short laser pulses, ranging from an initial pulse duration of 350 fs down to 27 fs. These experiments entailed high-energy laser systems, spanning from 0.3 J to 7 J in energy. The post-compression was achieved using the thin film compression method [1]. These experiments were conducted at facilities in France, including ELFIE, LASERIX, and Apollon, as well as at the ELI-NP facility in Romania. Various optical materials, including FS, BK7, SF5, Zeonor, and OKP, were employed.

Key output parameters that were closely examined in these experiments include spectral broadening, pulse duration, wavefront distortions, energy losses, and spatio-temporal couplings. The insights gained from this experimental work are discussed in detail throughout this chapter.

## 4.1 ELFIE campaign

The post-compression technique was employed on the ELFIE laser system at the LULI facility, where a laser pulse with an energy of 7 joules and an initially measured duration of 350 femtoseconds was utilized. For this experiment, optical nonlinear materials consisting of a 5 mm thick FS window and a 2 mm Zeonor (or COP) polymer were employed. The initial pulse, which had a diameter of 9 cm, underwent spectral broadening, resulting in a bandwidth equivalent to a Fourier-limited pulse duration of 124 fs. Subsequently, a partial post-compression process reduced the pulse duration to 200 fs.

Upon analyzing the spatial spectra of the beam fluence, it was observed that fluctuations increased uniformly by a factor of 4 across the entire range of studied frequencies. This increase was attributed to small-scale self-focusing phenomena.

In this work, I was involved in the implementation of the experimental setup, measurements, data analysis and in the manuscript writing. I investigated the pulse duration measurements from the SHG FROG device, the spatial frequency method applied on the spectral broadening dependence of the input beam features and the small scale self focusing (SSSF) effect.

The results of this section were published in Ref. [2].

### 4.1.1 Experimental Setup

The ELFIE laser facility operates on a Chirped Pulse Amplification (CPA) laser architecture, which begins with a Ti:Sapphire front-end and subsequently employs mixed silicate/phosphate glass amplifiers. The laser beam is subjected to compression under vacuum conditions, resulting in a duration of approximately 350 femtoseconds at a wavelength of $\lambda = 1.057$ micrometers. During the experimental campaign, the laser system operates at a repetition rate of one shot every 20 minutes, with each shot delivering the full energy of 7 J.

The experimental configuration for this campaign is depicted in Figure 4.1. The experiment was conducted under the following conditions:

To enhance the uniformity of the effective beam profile, a 7.0 cm diameter apodizer was strategically positioned upstream of the final amplifier, resulting in an input energy on the sample of 4.8 ± 0.8 J. The pulse duration, measured using both an Autocorrelator (AC) and an SHG FROG, exhibited slight variations due to shot-to-shot energy fluctuations, with a mean value of 350 fs ± 20 fs.

For measurements outside of the interaction chamber, the beam size was reduced using a telescope comprising a focusing parabola and a lens. Additionally, the energy was attenuated using a wedge. The low-energy pulse traversed a 7-mm-thick $MgF_2$ window, emerging with an approximate 1 cm diameter. It then proceeded to the optical diagnostic table, which employed 25 mm aperture optics.

A series of six mirrors with negative dispersion (UFI HD65; designed for a bandwidth of 1010 nm to 1070 nm) was installed. Each mirror could provide a phase correction of $-1000$ fs$^2$, resulting in a total GDD contribution of $-6000$ fs$^2$. While this value was insufficient to significantly affect a 350 fs pulse, it was expected to partially recompress the pulse, especially considering its broader spectrum. Although spectrogram images from the SHG-FROG offered valuable real-time feedback during the experimental campaign, the low signal at the device's input port led to a reconstructed error that exceeded acceptable limits for reporting in this context.

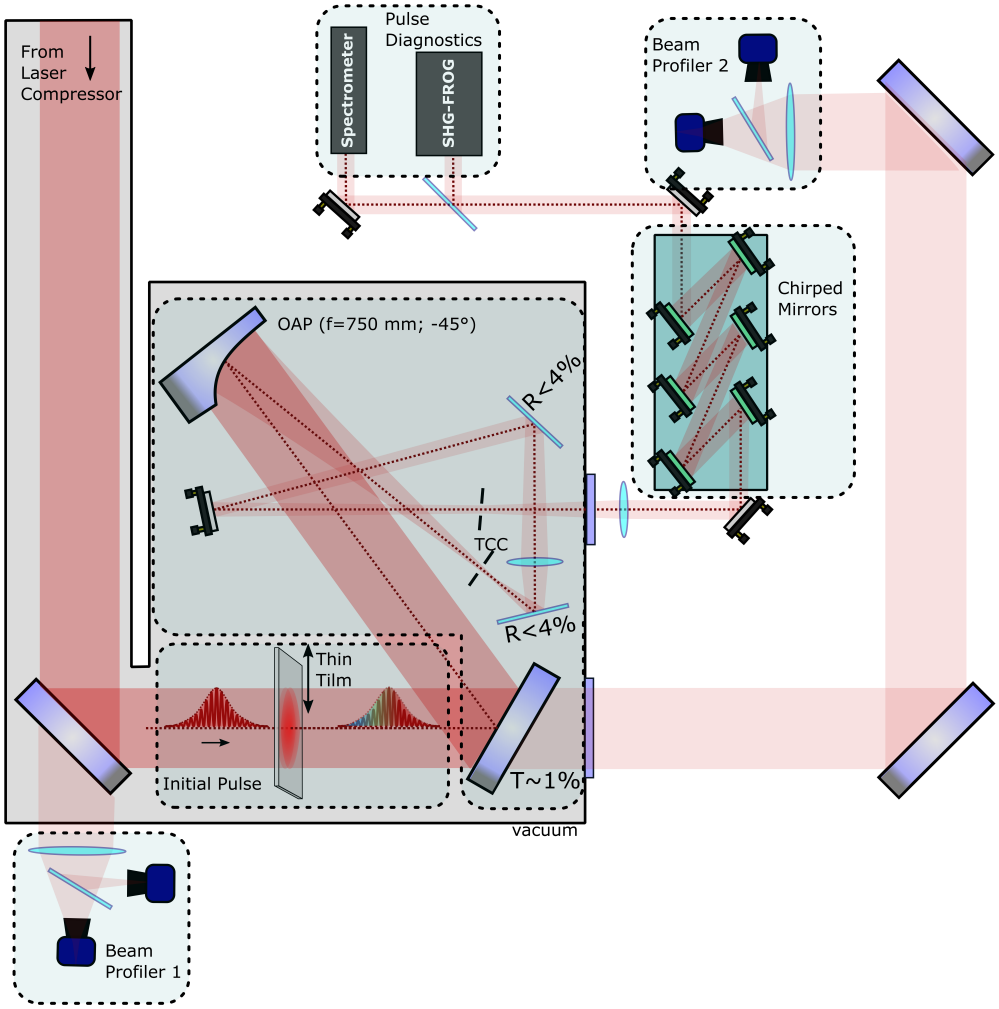


Figure 4.1: Experimental setup used in ELFIE campaign, where OAP denotes off-axis parabola and TCC the focus. Figure extracted from Ref. [2]

### 4.1.2 Spectral and temporal measurements

The spectral amplitudes obtained during the experimental campaign via the imaging spectrometer are depicted in Fig. 4.2. This figure illustrates the comparison between the original laser spectrum, recorded after the final amplifier (blue), and the spectra obtained in different scenarios: No Material (Fig. 4.2a), Fused Silica (Fig. 4.2b), or COP (Fig. 4.2c), all during the same shot.

Throughout Fig. 4.2, the central wavelength of the laser system remains constant at $\lambda = 1057.5$ nm, and the reference spectrum maintains a Full Width at Half Maximum (FWHM) bandwidth of $\Delta\lambda_{ref} = 5.4 \pm 0.3$ nm. This bandwidth is sufficient to support a Fourier-limited pulse duration of approximately 300 fs.

In Fig. 4.2a, where there is no material interaction, the absence of broadening indicates that no significant Self-Phase Modulation (SPM) occurs during beam transport and measurement. A specific shot from this scenario, shown in Figure 4.2d, reveals an autocorrelation measurement corresponding to a pulse duration of 340 ± 10 fs.

For the specific Fused Silica (FS) case highlighted in Fig. 4.2b, the measured energy is slightly higher at $E \sim 4.8$ J, compared to $E \sim 4.2$ J for the reference shot. Additionally, the central wavelength experiences a slight shift to $\lambda L = 1056.5$ nm, and the bandwidth expands to $\Delta\lambda_{FS} = 13.3$ nm. This increased bandwidth is capable of supporting a shorter pulse duration of 124 fs.

For the laser shot interacting with the COP film in Fig. 4.2c, the pulse energy measures lower at $E \sim 3.9$ J. When examining the spectrum associated with COP, the central wavelength undergoes a shift to $\lambda = 1055.0$ nm, and the Full Width at Half Maximum (FWHM) bandwidth broadens to $\Delta\lambda_{COP} = 12.4$ nm. This expanded bandwidth can support a shorter pulse duration of 132 fs.

From this dataset, the measured spectral increase ratio for FS is denoted as $F_{\omega}^{FS} = 2.66$. This value can be compared to the models presented in Section 2.3.2 and Ref. [3] for the expected broadening, given that $B_{int} \sim 1.78$ and $D \sim 0.00078$. These parameters predict an expected factor of $F_{\omega}^{FS} = 2.6$.

Figures 4.2d and 4.2e display the autocorrelator (AC) measurements, first without any material interaction and then after interaction with the FS window and the set of chirped mirrors. By assuming a Gaussian temporal profile of the pulse, the AC fit reveals an initial reference pulse duration of 340 fs. After the introduction of the FS, this duration reduces to 200 fs, indicating a chirp corresponding to approximately GDD $\sim 3000$ fs$^2$. The optical components within the beam transport path, including telescope lenses, vacuum window, and beamsplitters, collectively contribute to an additional chirp of 1000 fs$^2$.

An interesting aspect is depicted in Figure 4.2f, which illustrates the relationship between the spectral FWHM bandwidth and the presence of FS material compared to the absence of any material. This relationship is examined as a function of the chirp introduced into the input pulse by adjusting the separation of the gratings within the laser compressor. When FS is installed, the optimal compressor position is achieved when the bandwidth reaches its maximum value of 13.3 nm. Subsequently, as the grating separation is modified in either direction, the bandwidth decreases.

### 4.1.3 Influence of the beam features in the SPM process

#### 4.1.3.1 Beam Profile

In addition to pulse duration and spectral measurements, I conducted an analysis of the beam profile and the quality of a post-compressed beam in both the near-field (NF) and far-field (FF).

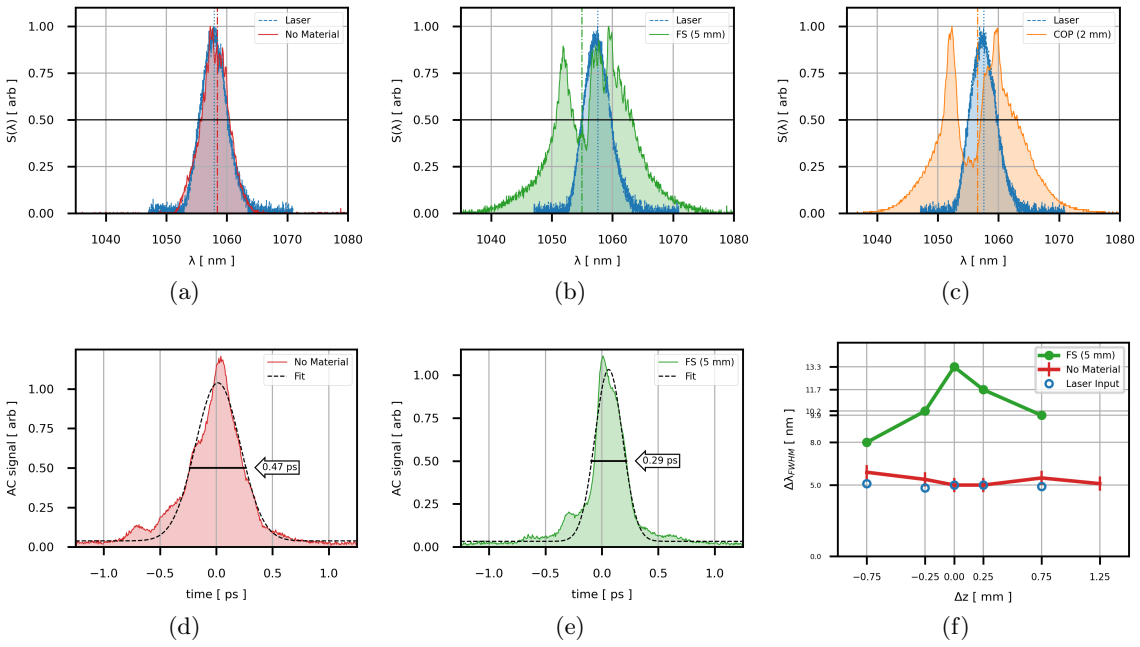


Figure 4.2: The spectral broadening due to self-phase modulation (SPM) is compared to the laser spectrum measured before interaction in panels (a)-(c) for different scenarios: no material (red), FS (green), and COP (orange). Panel (a) represents the initial pulse spectrum measured without any material interaction, showing minimal changes in the spectra. In panel (b), a 4.8 J pulse interacts with 5 mm of FS, while panel (c) illustrates the outcome of a 3.9 J pulse passing through 2 mm of COP. AC measurements, presented in panels (d) and (e), yield FWHM fit results for the cases of no material (0.50 ± 0.05 ps) and fused silica (0.41 ± 0.9 ps), corresponding to pulse durations of 0.34 ps and 0.2 ps, respectively. Panel (f) shows the resulting spectral FWHM bandwidth in nanometers, relative to the input pulse chirp, defined by the variation in the laser compressor grating separation ($\Delta z$ [mm]). In the absence of material (red), the initial FWHM bandwidth remains relatively constant at 5.1 nm despite changes in the laser compressor gratings' separation. With fused silica, the compressor position is optimized when the broadened bandwidth (green bullets) aligns with the measured laser bandwidth (blue). Figures extracted from Ref. [2]

While the ELFIE laser system is designed to provide a flat-top beam under optimal conditions, amplification and beam propagation through the laser chain can introduce modifications to the beam profile. I monitored variations in beam size and modulations over the course of several days, as shown, as example, in Figure 4.3. A slight shift in beam size of 10-15 pixels (74-111 $\mu m$) was observed but did not significantly impact the overall results. This shift could be attributed to factors such as changes in the laser chain, adjustments to grating positions, sample positioning within the beam, and so on.

The shots are categorized by date, time, location (SAC - before the interaction chamber (IC) without material, and SATE - with material, inside the IC before the post-compressor), and name (NS - No Sample, FS - Fused Silica, and COP - Zeonor plastic).

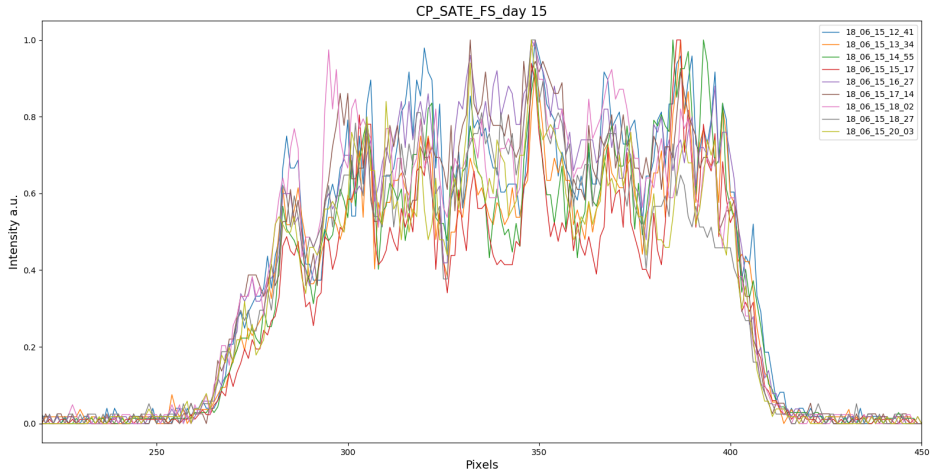


Figure 4.3: Beam profile variations after the insertion of the laser pulses with FS material as a function of the grating position during a day.

The evolution of the beam profile after passing through the material has a notable impact on the beam's characteristics. Since most post-compression methods rely on the self-phase modulation effect, future research will delve into the specific contributions of different materials to SPM during laser shots. A comparative analysis will be conducted between the two best shots from different days to gain further insights into this phenomenon.

#### 4.1.3.2 Spatial frequencies on Near-Field images

A series of image processing modifications were introduced to analyze the effects of self-phase modulation. The first step of the processing involved background subtraction. Each image was treated as a matrix. The background was determined as the mean value of all the gray lavel of the pixels from the first row of the beam matrix. Pixels with gray level lower or equal to the background were considered to have the same value as the background. To obtain the final image with the background removed, the background value was subtracted from all the pixels, effectively setting the overall background to 0. This process also helped to eliminate any potential effects of logarithms on negative values.

The second step was to retrieve the power spectrum from the Fast Fourier Transform of Near-Field images using the spatial frequencies analysis. A common set of operations was applied to all images: the 2D Fast Fourier Transform (FFT) function was applied, followed by a frequency shift to center all the low frequencies (the DC components). Then,

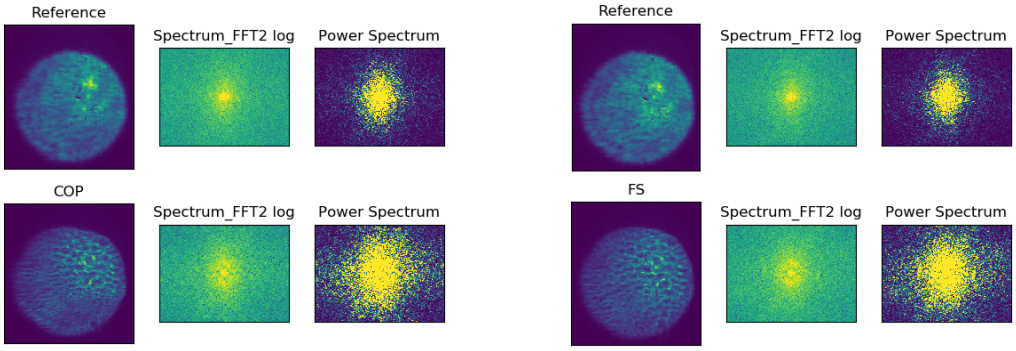


(a) (b)

Figure 4.4: Beam profile, FFT spectrum and Power Spectrum for COP (a) and FS (b). The same scale is used in upper and lower images.

all values were converted to their absolute values, and finally, the result was squared to obtain the Power Spectrum (as shown in Figure 4.4).

The image in Figure 4.4 clearly shows the spreading of energy from low frequencies to high frequencies. However, this data analysis approach provides only a qualitative perspective on how the Far-Field should appear, and it does not offer quantitative information about the influence of self-phase modulation on each frequency or the evolution of features with and without the material.

To investigate these characteristics more thoroughly, four types of data analysis approaches were employed (See Figure 4.5). Two of these approaches are related to the linear profiles along the X and Y axes, which I determined from the Power Spectrum. These approaches provide information about how the features evolve along the X and Y axes (see Figure 4.5, top). One limitation of these approaches is that they consider only a subset of the data. As seen in Figure 4.4, pixel's gray levels differ at different lines and columns, so these approaches may provide limited information about the overall beam.

The other two approaches involve circular and histogram integration and are based on the analysis of the overall beam size (see Figure 4.5, bottom).

**Circular integration** involves counting the pixel's gray levels within a circle, starting from the center of the image and increasing the radius with a bin value of 1, step by step. At each step, the sums of all values within the radius bins are counted, and the radial profile is obtained through normalization by dividing each sum by the total number of bins. This method provides a complete spectrum of the entire image.

**Histogram integration**, on the other hand, counts all the flattened pixel's gray levels from a specific radius, starting from (0,0). The histogram integration will encompass the counts of values that fall within each bin. By adjusting the "bins" parameter, the granularity of the histogram can be modified (see for instance the inset of Figure 4.6). Histograms serve as valuable tools for visualizing data distributions, offering insights into the arrangement of values within various intervals.

Compared to circular integration, the non-normalized spectrum from histogram integration shows a clear curve that drops for spatial frequencies higher than 0.86 $mm^{-1}$ (see Figure 4.5, bottom).

Similar results to circular integration were obtained when histogram integration was normalized. For further analysis, data from histogram integration were used.

Another aspect of data analysis related to the resolution of the Power Spectrum con-

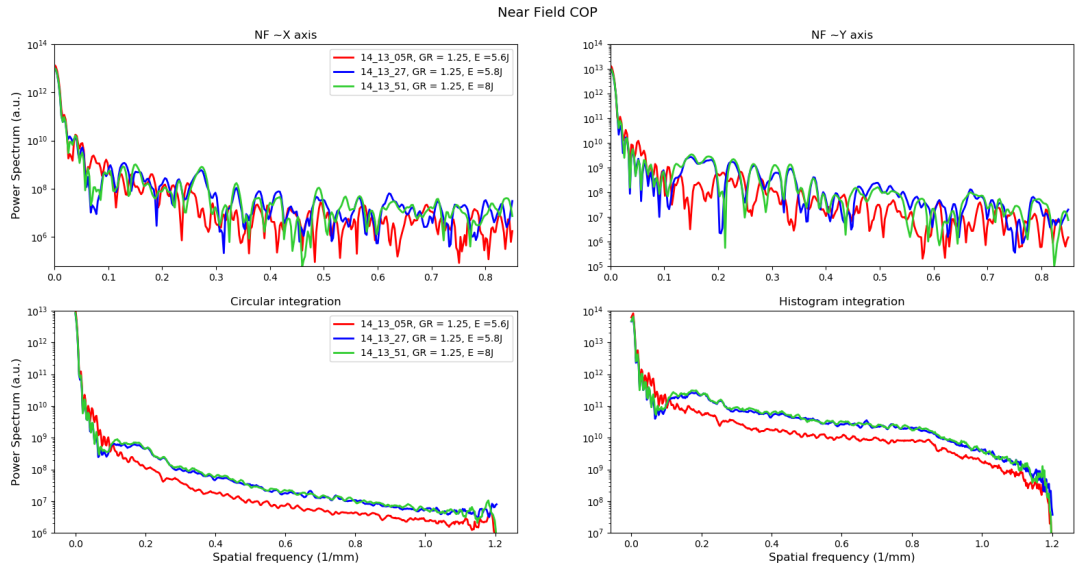


Figure 4.5: Spatial modulations on X and Y (top) and integrated (circular and histogram) beam modulation (bottom) as a function of the Power Spectrum.

cerns the number of bins and the image size, as shown in Figure 4.6. The radial integration resulted in a resolution of 409 bins, equivalent to the number of pixels along the original image's diagonal. To achieve a better resolution, three cases were analyzed: a) a cropped and squared image with 496 pixels, b) the original rectangular image, and c) a squared padded image with 656 pixels.

In case (a), the resolution was too low, and some of the feature peaks may be lost (see inset). In case (b), due to the fact that circular integration starts from the image center, and the image is not squared, some information may be lost. In case (c), with a squared image, both circular and histogram radial integration provide the same information.

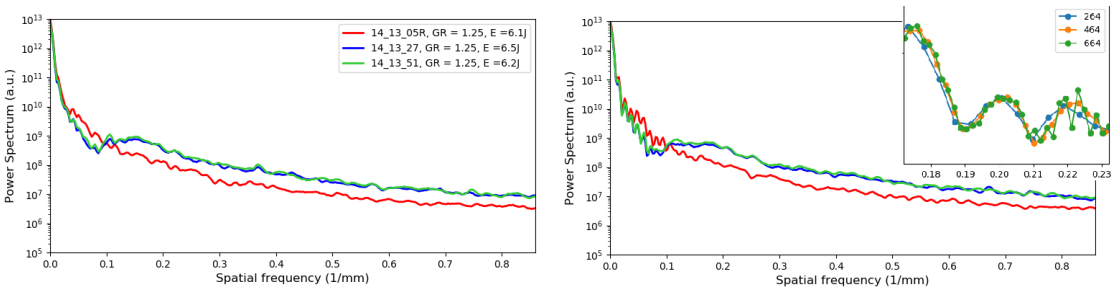


Figure 4.6: Spatial modulations for histogram integration as a function of the bins number (409 left and 462 right). Inset: the curves shapes differences as a function of the bins number.

The image was transformed from pixels to spatial frequency equivalents to the real beam using the following method. Due to the symmetry, the spatial frequencies were shifted to 0 by subtracting the middle pixel from each pixel number. From the pixel size of 7.4 $\mu m$ and the calibration factor (cf) of 0.0126, a calibration constant ($const$) was calculated as follows:

$$const = size_{pixel}/cf$$

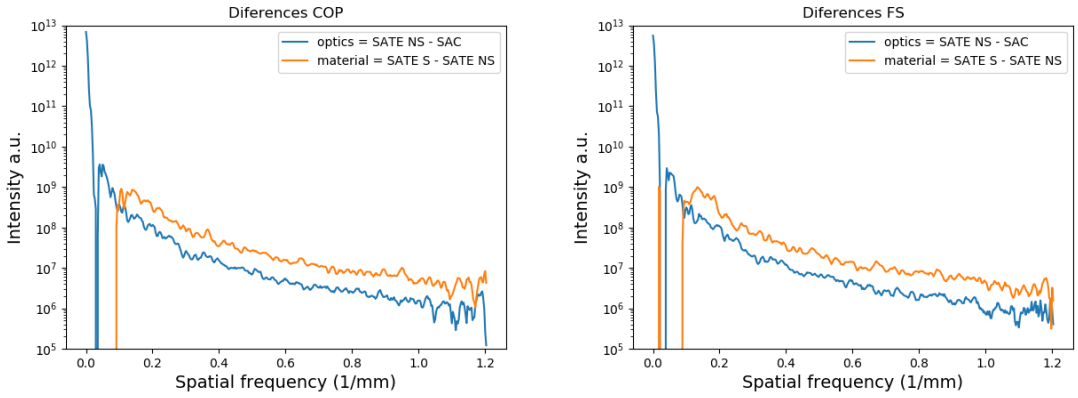


(a) (b)

Figure 4.7: Influence of optics and materials for COP (a) and FS (b)

The scale on each axis becomes:

$$scale = pixel_{no} * const$$

and the equivalent spatial frequency (SF (1/mm)):

$$SF = pixel_{nr}/(scale_{max} - scale_{min}) \tag{4.1}$$

To discern the origin of certain peaks, figure 4.7 showcases the influence of the material and imaging optics. The data were subtracted from the beam profile at different locations in the laser chain (SAC - no sample (NS), SATE - NS, SATE-material). The curves were generated using histogram integration around the image center by summing all contributions of each pixel's magnitude.

I summarized the overall analysis for each material in a dedicated figure and for a better visualization of this analysis, I split Figures 4.8 in 4 parts, as follows: (left side) The reference beam denoted with the acronym (these acronyms refer to the position where the profile in the Near-Field (NF) was measured.) "SATE" (**A**) (in the interaction chamber without material) and the beam after passing through the material (**B**) (COP or FS) and the shot number "i". Beside this, the images offer information regarding the beam size and beam features fluence.

Figure 4.8 **C** treats the beam features evolution in the spatial frequency domain. The energy is distributed along the beam profile allowing the beam features amplification through the SPM process. These effects are seen in the power spectrum evolution for a grating position of 1.25 equivalent with the best compression condition (350 fs). The power spectrum graph shows the spatial frequencies evolution along the propagation through SAC (before the interaction chamber), SATE (in the interaction chamber with material) and on the diagnostic bench at the output of the interaction chamber (Two different shots denoted through orange and green colors). The introduced SPM can be observed in the differences arising between the SAC and SATE measurements (i.e. red curve with green curve) after accounting for influences of the imaging optics (all the optics from SAC to SATE position where the beam is measured after passing through or after it has been reflected). After passing through the material, each spatial frequency lower than 1 ($mm^{-1}$) is amplified.

Two different shots were used to show the amplification curve characteristic for each type of material and to observe the repeatability of the results.

On the Figure 4.8 **D**, it can be seen that the main gain is obtained for the spatial frequencies between 0.1 and 0.4 ($mm^{-1}$). The ratio graphs show how each frequency gains amplitude with respect to the mean reference (without material) of the day (blue). A specific characteristic of this analysis type is the damage size detection, if they occur, because each spatial frequency peak offers information about a specific feature size inside of the image. A higher peak was observed in the spatial frequency during the data analysis when, at a specific shot, the sample was damaged.

The color bar indicates the laser fluence ($J/cm^2$) in the beam, calculated as follows:

$$Energy_{pixel} = E_{shot}/sum$$

where $E_{shot}$ is the overall shot energy (J) and $sum$ includes all the image pixels magnitude (counts). Thus, the fluence is given by:

$$F = max_{amp} * Energy_{pixel}/Area \tag{4.2}$$

Where $max_{amp}$ is the maximum amplitude of each pixel (counts) and Area is the pixel size area ($mm^2$). The X and Y axis of each beam profile image is equivalent with the real size of the beam.

Figure 4.9 illustrates the magnitude evolution of the ratios when the optimal compression position is reached. The magnitude of these differences suggests that beam modulation across the axes can vary from shot to shot and does not consistently exhibit the expected features due to the material's influence. In contrast, the radial differences consistently displayed the main features shot by shot, with variations stemming from differences in beam profile, energy, and irradiance between shots.

Not all spatial frequencies were amplified due to SPM generated in the material. Both figures reveal regions of spatial frequencies where their amplification is lower compared to others. For COP, these frequencies are around 0.28-0.31, 0.46, and 0.54 $mm^{-1}$, corresponding to regions in the beam of 3.57-3.22, 2.15, and 1.83 mm.

For FS, these frequencies are around 0.29 and 0.41 $mm^{-1}$, corresponding to 3.44 and 2.41 mm. These frequencies may be harmonics of the fundamental wavelengths of the beam.

Another aspect related to the ratios is the point at which spatial frequencies start to be amplified. The dark blue region in Figure 4.10 represents frequencies that begin to spread their energy at a starting point of 0.11 for COP and 0.10 for FS. The laser shots may have higher fluence compared to the reference shot due to energy variations. This energy is distributed along the beam profile, allowing for the amplification of beam features through the SPM process.

The maximum amplification of beam features was observed at a relative grating position (denoted as $GR$) of 1.25, which provides the best compression. The magnitude of lower-frequency components spreads towards higher frequencies, favoring their amplification. Depending on the material type, specific spatial frequencies are amplified to a greater extent (see Figure 4.10, for spatial frequencies between 0.2-04 $mm^{-1}$). The primary gain occurs in the spatial frequencies between 0.1 and 0.4 ($mm^{-1}$). The Power Spectrum ratio graphs depict how each frequency gains amplitude relative to the mean reference of the day (blue).

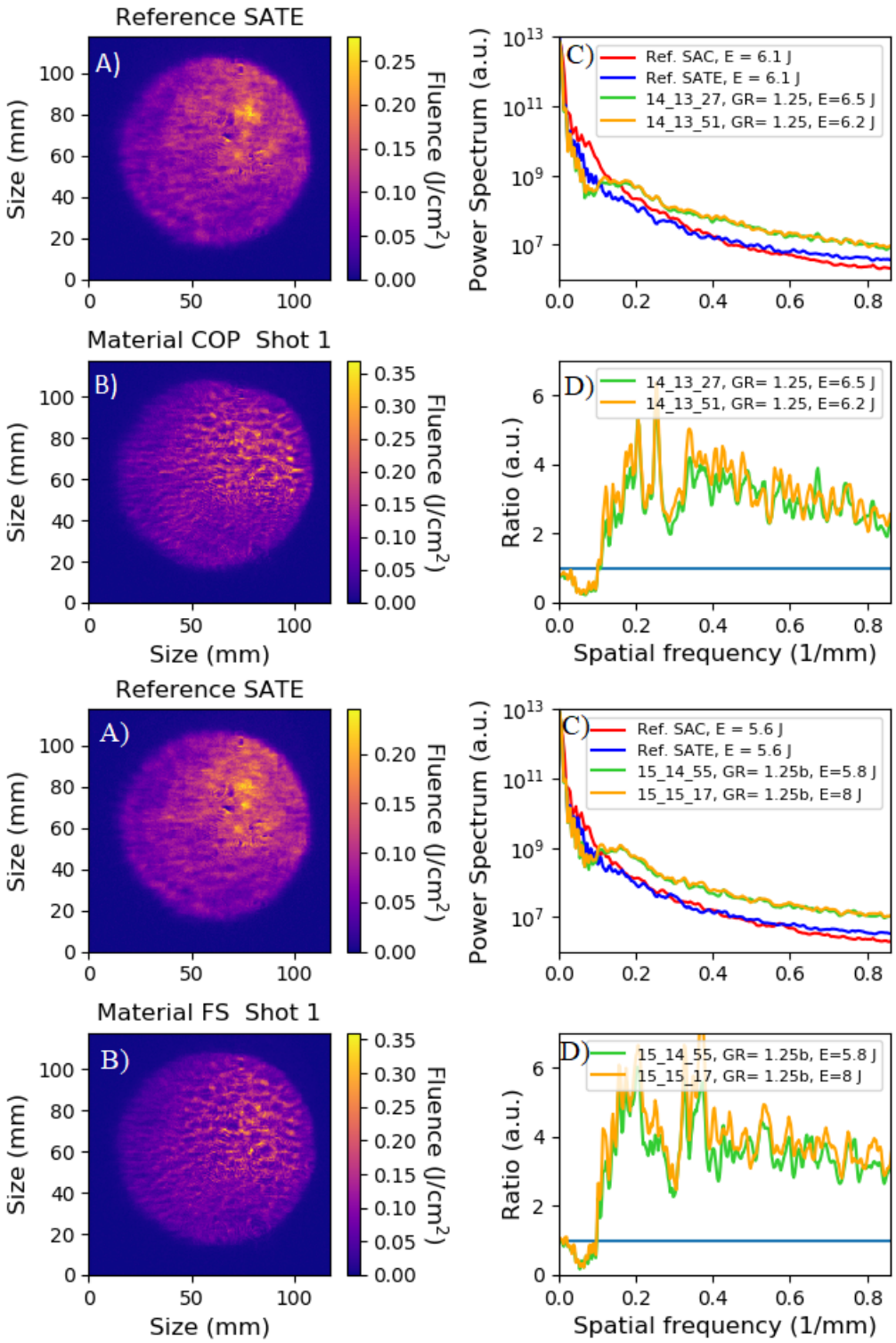


Figure 4.8: Comparison between COP (top) and FS (bottom): Reference and shot beam profile (C), the power spectrum and the ratio (D) (the ratio between the amplitude of the shot no. "i" power spectrum and the mean reference SATE of the day without material power spectrum) at different energies, where GR is the grating position.

The ratio magnitude evolution can be observed when the best compression position is reached. Not all the spatial frequencies were amplified due to SPM generated in the

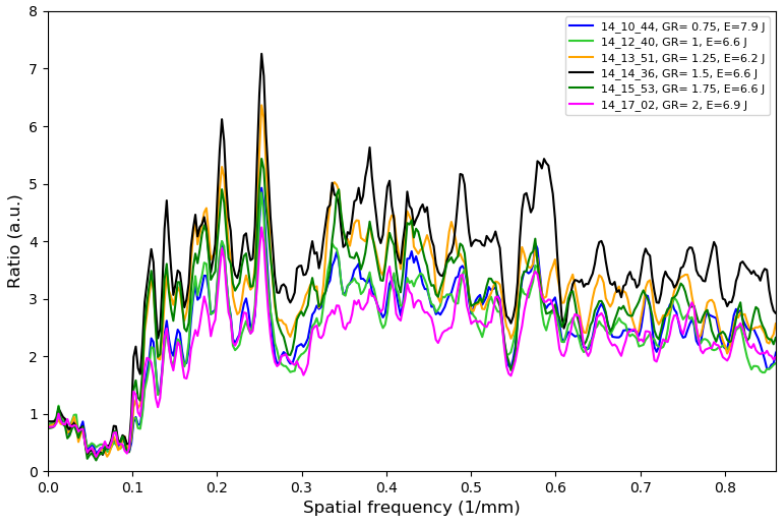


Figure 4.9: 2D Power spectrum ratio as a function of the gratings position/GDD variation, for COP material. The highest amplification was observed at the best compression or when the energy was increased.

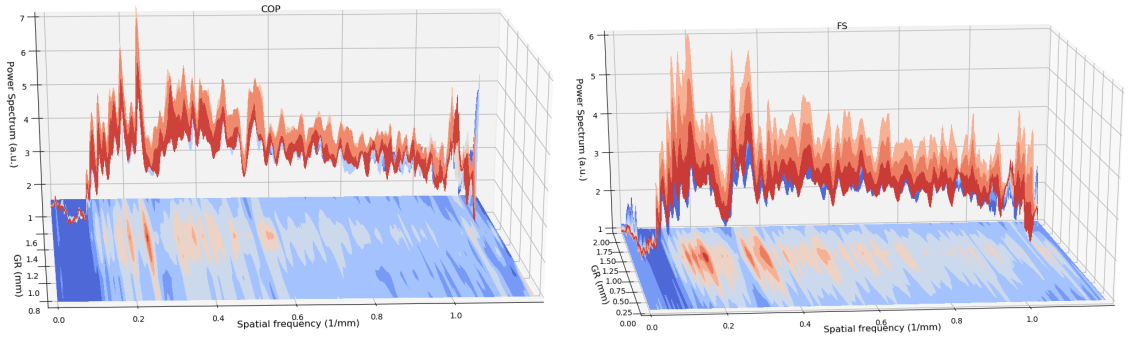


(a) (b)

Figure 4.10: 3D evolution of the power spectrum ratio for gratings position displacement (GR) for COP (a) and FS (b).

material. From both Figure 4.10 a) and b) it can be spotted regions of spatial frequencies where their amplification is low compared with the others. For COP, those frequencies were around 0.28-0.31, 0.46, 0.54 $mm^{-1}$ corresponding to regions in the beam around 3.57-3.22, 2.15 and 1.83 mm. For FS frequencies around 0.29 and 0.41 $mm^{-1}$ corresponding to regions around 3.44 and 2.41 mm. Those frequencies may be harmonics of the fundamental spatial periods.

In the next section, I investigated the theory of small-scale self-focusing applied to the beam profiles of ELFIE laser.

#### 4.1.3.3 Small Scale Self-Focusing (SSSF)

In Figure 4.11, the full aperture images of the beam captured by the Beam Profile 2 diagnostics can be observed, both before (Fig. 4.11 **a**) and after (Fig. 4.11 **b**) inserting the material (FS), illustrating the changes in spatial modulation.

To analyze the spatial frequency modulations in the beam, **two circular regions** were selected. Region I in Fig. 4.11 **a** corresponds to a high average fluence, while region II has approximately 1.7 times lower fluence, leading to a reduced B-integral.

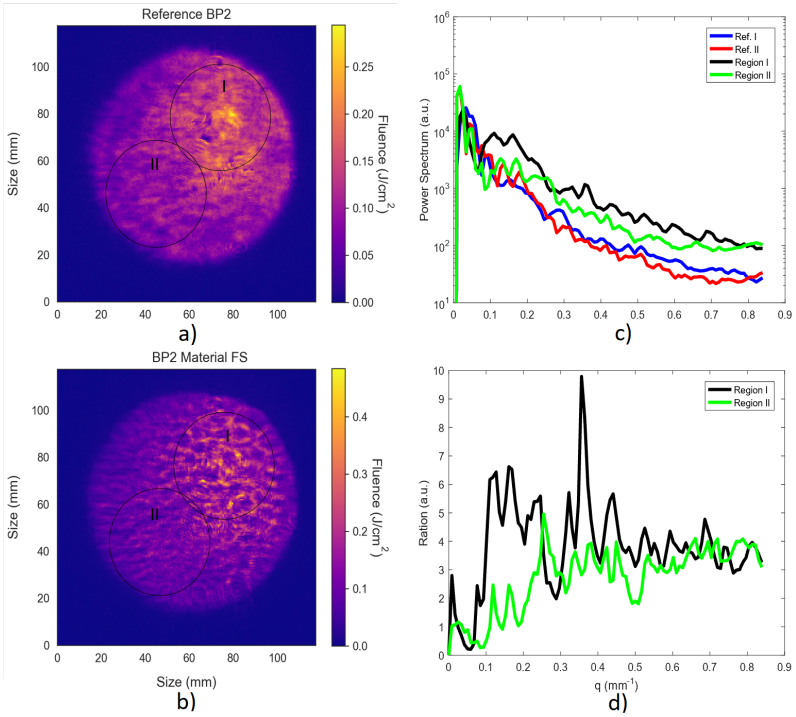


Figure 4.11: Comparison of the Beam Profile between the Reference (a) and FS (b). In (c), the power spectrum of two distinct laser regions (Region I, denoted in black, and Region II, denoted in green) is shown before and after the nonlinear interaction. The ratio of the power spectra, relative to the initial corresponding reference, provides insight into the relative gain in Spatial Modulation Instabilities (SMI) in (d). Figure extracted from Ref. [2]

In Figure 4.11 **c**, one can see the results of circular integration of the 2D Fast Fourier Transform (FFT) of the two beam profile regions, both before and after introducing the materials. This quantifies the small-scale spatial features that emerge within the beam profile due to self-phase modulation. The near-field system has the capability to resolve images with the smallest feature size in the beam, approximately 0.59 mm (corresponding to a spatial frequency of about 1.7 $mm^{-1}$), limited by the pixel size relative to the beam image.

Figure 4.11 **d** shows the ratio of the power spectra before and after introducing the nonlinear material for each of the two regions. Several observations can be made: The relative gain at high frequencies remains roughly constant in the spatial modulation instabilities across the accessible frequencies for both curves, even though there is a 1.7 factor difference in B-integral. At low spatial frequencies, the behavior differs. The low-intensity region II exhibits reduced gain in modulations below 0.3 $mm^{-1}$, while the high-intensity region shows an increase in modulation within the region of approximately 0.1 $mm^{-1}$ to 0.3 $mm^{-1}$.

This phenomenon reveals the existence of two distinct types of self-focusing: large-scale and small-scale self-focusing. Large-scale self-focusing is primarily determined by the critical power ($P_{cr}$) [3], and it becomes noticeable when the length of the medium approaches the self-focusing length.

The growth in the amplitude of spatial harmonics becomes evident when the B-integral surpasses unity, and these harmonics belong to an amplification band. The boundaries of this band depend on the beam intensity and the cubic nonlinearity coefficient ($n_2$) and are independent of the length of the nonlinear medium (as demonstrated in Ref. [4]).

A similar pattern of spatial noise amplification was observed in [5] (Figure 4, where

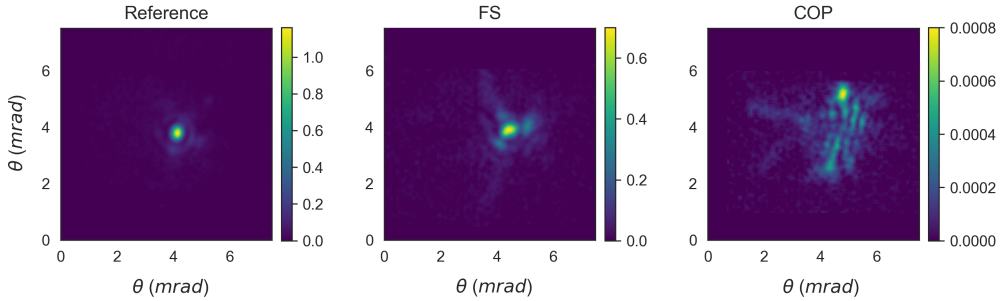


Figure 4.12: Far Field images of both FS and COP material. Figure extracted from Ref. [2]

L=200 mm exhibits a similar pattern to our beam profile). Here, the gain factor of spatial noise depends on the spatial frequency and B-integral. This theoretical model presented in Ref. [4] indicates that the positions of maxima and dips in the gain factor versus spatial frequency dependence are determined by the B-integral value and the distance between the source of spatial noise and the nonlinear sample.

In practical laser setups, sources of spatial noise are distributed along the beam path, and the behavior of the gain factor concerning spatial frequencies observed in experiments deviates from the model, requiring additional investigation. Furthermore, there are at least two factors that need to be considered in the theoretical model: spatial [6] and temporal filtering of spatial harmonics originating from regions of strong field within a nonlinear sample. Both of these factors contribute to an additional suppression of small-scale self-focusing development.

Analyzing the amplification of spatial harmonic amplitudes is a valuable approach to estimate the B-integral and prevent excessive SSSF, which can negatively impact beam quality.

#### 4.1.3.4 Far-Field Analysis

Far-Field data were obtained using the experimental setup presented in figure 4.1. Two types of materials (COP and FS) were compared with the reference image.

In the case of FS material the Far-Field quality increased (see Figure 4.12). At the best compression (GR=1.25), the beam profile is similar to the reference making it a suitable candidate material for applications which require a best focus. The further the gratings position was shifted, the FF quality started to deteriorate. The energy was spread between the beam lobs creating multiple hot spots.

In the case of COP material, the FF data did not show an Airy pattern as it was expected in the theoretical case. Compared with the reference, the beam energy is spread along other lobs of the profile. As a conclusion, this type of material is not suitable for applications which require a best focus. The main reason behind this spread lies with the quality and thickness of the material.

The spread of energy in focus due to gratings position/ GDD was subject of a separate experimental campaign and will be further analyzed and discussed in Section 4.4.

### 4.1.4 Discussion

The proof-of-principle demonstration successfully showcased post-compression for long pulses, specifically those exceeding 100 fs, while dealing with multi-Joule input energies. Beyond the limits of existing laser installations, there is considerable potential to apply post-compression techniques to novel laser designs. A critical requirement for laser-plasma

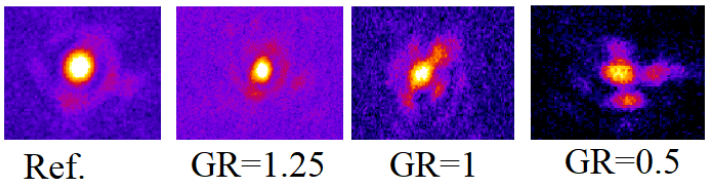


Figure 4.13: Far-Field beam profile of FS: Reference and the FF measured at different positions of the gratings (GR=1.25 ≈ 350 fs)

processes to move beyond the realm of discovery science and into practical applications is the development of efficient high-peak-power and average-power laser drivers.

One proposed solution for an industrial-scale, high-energy laser capable of operating at frequencies exceeding 100 kHz involves a fiber chirped pulse amplification (FCPA) system (subject discussed in Section 1.2.2.3). While FCPA systems can efficiently produce pulses at high repetition rates, the inherent bandwidth limitations of fiber-based amplifiers tend to limit the minimum achievable pulse duration to around 300 femtoseconds. To reach the coveted few-cycle pulse regime, a post-compressor is essential. Consequently, FCPA laser systems are likely to benefit significantly from the integration of highly efficient post-compression stages to achieve substantial compression factors.

The development of an efficient and scalable CAN laser [7, 8] system based on fiber laser technology holds the potential to provide an economical and versatile tool capable of meeting the requirements of a broad range of applications. This includes the ability to drive multiple stages of acceleration within a laser accelerator facility, highlighting the growing importance of such laser technologies in advancing scientific research and practical applications.

In the case of Fused Silica, the spectral broadening of a 350 fs pulse was measured to expand from 5.0 nm to 13.3 nm, enabling the support of pulse durations as short as 124 fs. After undergoing energy attenuation and passing through a set of chirped mirrors, significant phase correction led to a measured reduction in pulse duration down to 200 fs. For situations where large aperture chirped mirrors are employed, no energy attenuation would be required, allowing for an increase in peak intensity from 0.23 TW/cm$^2$ to 0.37 TW/cm$^2$ within the partially compensated pulse duration. With further optimization, this could potentially reach a peak intensity of 0.6 TW/cm$^2$, especially for the shortest 124 fs pulses. Additionally, the implementation of a second TFC stage could offer further compression possibilities in the future.

Within this experiment, I learned the importance of material quality, particularly concerning wavefront distortions and the quality of the focal point (Chapter 3 studies were performed after this experiment). Optimizing this process might benefit from the use of a deformable mirror, although the ELFIE facility currently lacks this capability. Nonetheless, spectral broadening emerged as a viable method for preliminary optimization of the grating compressors. Additionally, spatial frequency analysis proved valuable for delving into the mechanisms at play, including self-phase modulation, small-scale self-focusing, B-integral, and the laser-induced damage threshold.

The Power Spectrum ratio graph illustrated the evolution of spatial frequencies along the propagation path through SAC, SATE, and the material. From SAC to SATE, one can observe the influence of imaging optics, which can also introduce SPM. After passing through the material, each spatial frequency below 1 ($mm^{-1}$) experiences amplification. Two different shots with the same amount of energy follow the characteristic amplification curve for each type of material. The shape of the curve can be used to distinguish between two unknown materials.

The experimental results (ratio of the power spectrum and B-integral as a function of the spatial frequencies) obtained at ELFIE are in qualitative and quantitative agreement with the theoretical predictions presented in previous research [5]. Therefore, the ELFIE experiment serves as valuable confirmation and complements the existing theoretical work.

## 4.2 LASERIX campaign

The second significant experiment took place at the LASERIX facility in France. In this experiment, we showcased that Zeonor, a plastic material, exhibits enhanced spectral broadening and shorter pulse durations compared to fused silica (FS). This plastic material can be operated near its damage threshold by utilizing a specialized roller mechanism for periodic refreshing. By varying the total amount of material through multiple film foldings, we demonstrated the scalability of this approach to reach power levels in the tens of petawatts. By employing the plastic material within a vacuum environment, we achieved a two-fold post-compression of the pulse.

My contributions to this experiment included data analysis (nonlinearities, pulse duration, spectral broadening) and writing of the manuscript.

### 4.2.1 Experimental Setup

The initial laser parameters included a 45 fs pulse duration and variable energy levels up to 500 mJ, all delivered through an 18 mm diameter beam.

To control and adjust the input energy reaching the sample, a variable attenuator (VA) was strategically positioned before the compressor. Additionally, partial reflectors (PR1) were employed to attenuate the energy of the laser pulses. This precaution was taken to prevent excessive self-phase modulation (SPM) generation, especially in areas such as the vacuum window (W), and to safeguard against potential damage to subsequent optical components.

A fraction of the beam energy (2%) is directed by a beam-splitter (PR2) towards a lens with a focal length (f) of 300 mm. This lens is employed for imaging diagnostics (IM box) to examine the near and far fields (NF and FF, respectively), enabling qualitative monitoring of the collimated and focused beam mode profiles.

The majority of the energy (98%) reflected by PR2 is directed towards the dispersion management (DM box), which comprises chirped mirrors (CM) from Ultrafast Innovations (HD58). These CMs provide a Group Delay Dispersion of -250 $fs^2$ per bounce. By slightly adjusting the angle of incidence on the first mirror, the option is provided to pass through a pair of chirped mirrors, allowing for combinations of 2, 4, or 6 bounces (typically 4 bounces). As the CMs tend to overcompensate the initial pulse chirp, glass windows (W, 0.5 mm, 50 mm diameter) are introduced into the beam path to enable control of the pulse duration.

A compact prototype of a Film Roller Mechanism (FRM) has been constructed and tested in a small-scale experimental setup. The FRM was utilized in conjunction with the Thin Film Compression technique within a vacuum environment to obtain experimental results. This roller mechanism was also used for the transmission measurement presented in Section 3.2.2.

For accurate pulse duration measurements, two temporal diagnostics are employed in parallel: the Light Conversion TIPA Single-shot Autocorrelator (AC) and the FastLite WIZZLER (WZ). The WIZZLER has the additional capability to retrieve the spectral phase of the pulse, facilitating final pulse compression optimization.

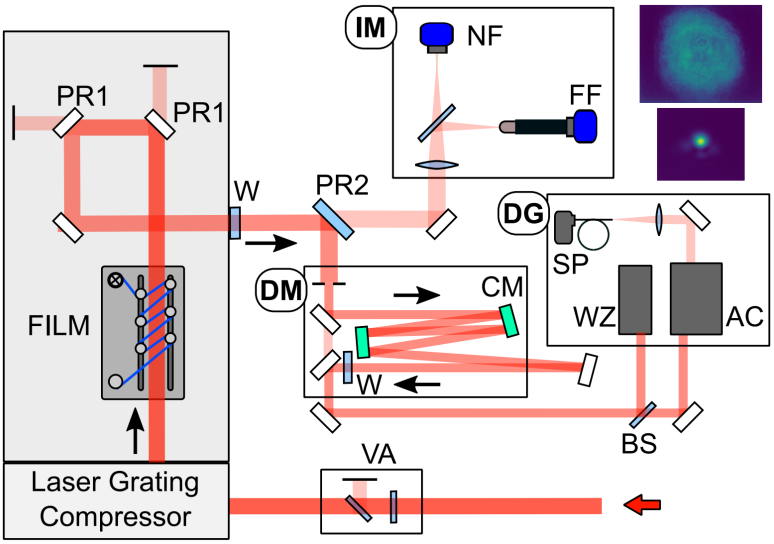


Figure 4.14: Experimental setup used in the LASERIX campaign. Figure extracted from Ref. [9]

To complement these diagnostics, a fiber spectrometer (SP) from Ocean Optics (USB 2000) records the spectrum of the pulse, allowing for comparison with the spectra obtained from the other diagnostic tools. The COP films are positioned at Brewster's angle in relation to the incoming beam. This arrangement effectively creates an optical path length equivalent to 0.71 mm when considering a 6-pass configuration.

### 4.2.2 Experimental Results

The investigation of the COP response involves maintaining a constant amount of film for all tests, utilizing a six-pass configuration. The pulse energy is systematically varied to observe how the COP film reacts to changes in laser intensity. Multiple shots, ranging from five to ten, are conducted for each energy level.

#### 4.2.2.1 Spectral and temporal measurements

Fig. 4.15 presents the pulse spectral amplitude and phase measurements obtained with the WIZZLER, as a function of input energy. The upper panel displays the amplitude, while the lower panel shows the phase. Each spectrum measurement is overlaid with its corresponding phase information in green. Additionally, when applicable, the reference spectrum is superimposed in gray. The reference spectra were acquired with the roller mechanism removed from the beam line, and only two energy points ($E_p$ = 78.7 mJ and $E_p$ = 157.9 mJ) are available, with pulse energy values similar to those used with COP films. The reference spectrum's phases remain flat since the compressor was adjusted during the experiment to deliver an optimized pulse duration.

The pulse bandwidth and duration values are tabulated in Table 4.1 with respect to the input energy $E_p$. Additionally, these pulse parameters are displayed as a function of the scaling variable $\xi$, where $\xi$ is defined as $E_p \cdot \Delta z$, with $\Delta z$ representing the material thickness in millimeters.

The trend is evident in the data, showing an increase in bandwidth and a decrease in pulse duration as the input pulse energy increases while keeping the amount of COP material constant (in a 6-pass configuration).

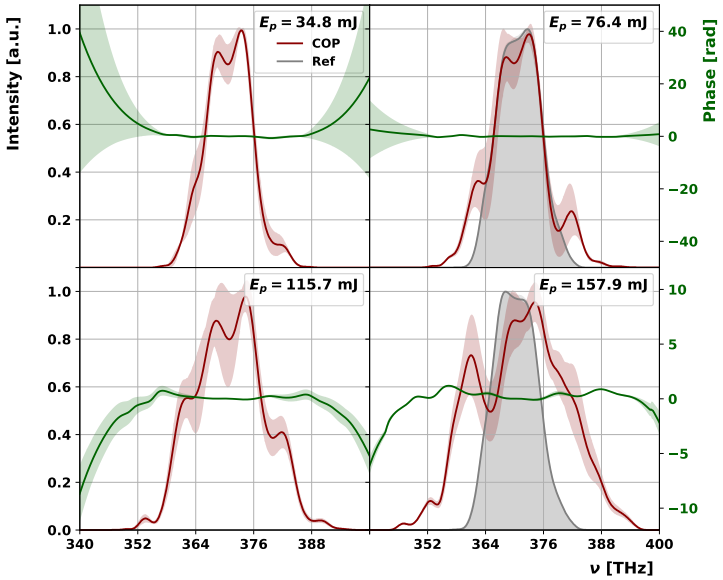


Figure 4.15: Spectral broadening as a function of the input energy was measured using 6 layers of COP film positioned at Brewster angle. Figure extracted from Ref. [9]

| $E_p$ $[mJ]$ | $\xi$ $[J \cdot mm]$ | $\Delta\lambda_{FWHM}$ $[\pm 2nm]$ | $\tau_p$ $[fs]$ |
|---|---|---|---|
| – | – | 21. | 45.5 |
| 35 | 0.025 | 24. | 43.3 |
| 76 | 0.054 | 30. | 32.6 |
| 116 | 0.081 | 37. | 29.4 |
| 158 | 0.112 | 47. | 23.4 |

Table 4.1: Measured pulse parameters for 6× COP (0.71 mm thickness) configuration. "–" denotes the reference

#### 4.2.2.2 Nonlinear refractive index estimation

As mentioned in Chapter 2, the extent of self-phase modulation and spectral broadening hinges on the nonlinear refractive index (NRI). In this study, we conducted spectral measurements to determine the magnitude of the NRI for COP, with the NRI of FS serving as the reference.

The relative maximum spectral shift due to Self-Phase Modulation (SPM), denoted as $\delta\omega_{rel}$, is estimated from the experimental data by taking the difference between the bandwidth measured after SPM ($\Delta\omega_{spm}$) and the initial reference bandwidth ($\Delta\omega_o$): $\delta\omega_{rel} \sim \Delta\omega_{spm} - \Delta\omega_o$.

In Figure 4.16, a comparison of the measured relative spectral shift for six passes of COP at a thickness of 0.1 mm (6× COP) with that of a Fused Silica plate at normal incidence is presented. It is evident that the response to the COP film is significantly larger compared to using fused silica plates.

A linear regression analysis is conducted on both datasets and is overlaid on the measurements. The ratio of the slopes obtained from the linear fits for the COP to FS data, denoted as $m_{COP}/m_{FS}$, provides access to $n_2^{COP}$ using the well-established value for fused silica, i.e., $n_2^{FS} = 2.6{\times}10^{-20}$ m$^2$/W. Consequently, the estimated value for $n_2$ for COP is approximately given by $n_2^{COP} = (2.2 \pm 0.2) \times n_2^{FS}$. Thus, the NRI of COP $n_2^{COP} = (5.8 \pm 0.6) \times 10^{-20}\ m^2/W$ . This estimation was in good agreement with what I

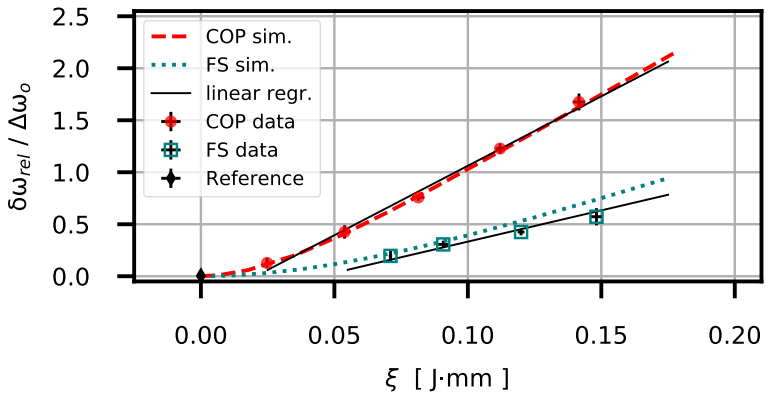


Figure 4.16: Measured response of the COP plastic film compared with FS. Figure extracted from Ref. [9]

measured in the previous chapter.

The value of $n_2^{COP}$ extracted from the experimental data is subsequently applied in simulations using the pyNLO package from Python, and the outcomes are depicted in Fig. 4.16. Initially, there was an anticipation that the relative spectral broadening would conform to a linear relationship with $\xi$. However, the empirical measurements deviate from this expectation, displaying a curved trend.

The simulation effectively reproduces this observed behavior by taking into consideration the transmission efficiency of the films. Specifically, each COP film exhibits a transmission efficiency of T = 95%, resulting in a cumulative transmission efficiency of T = 74% for six films. In the case of fused silica (FS), the transmission efficiency was T = 93%.

In scenarios without losses, the simulation output closely approximates the anticipated linear relationship with $\xi$. Nonetheless, when accounting for the losses incurred across multiple films in the simulation, the results harmonize well with the measured data, yielding a curved $\xi$-dependent function.

### 4.2.3 Discussion

Efficient spectral broadening using COP (Zeonor) plastic material has been realized showing an efficient post compression from 45.5 fs down to 23.4 fs. A set of measurements was also performed for 0.5 mm of FS where the final output pulse duration was 29 fs.

Throughout this study, we also delved into the development of multi-filamentation, examined the focal spot after broadening, and conducted simulations to analyze the spectral broadening as it relates to the thickness of COP material.

**Multi-filamentation study** The beam profile features analysis, previously proposed in the experiment, was also extended during the LASERIX campaign. When the peak power of the pulse surpasses the critical power $P_{cr}$, which is calculated as $P_{cr} = 3.79\lambda_0^2/(8\pi n_0 n_2)$ (approximately 2.6 MW for fused silica and 1.1 MW for COP at 810 nm), intense pulses exhibiting super-Gaussian modes become vulnerable to multi-filamentation. This phenomenon is triggered by the modulation instability initiated by noise in the beam profile. Such pulses, with significantly higher power than the critical power $P_{cr}$, undergo a phenomenon where they break up into multiple filaments as they propagate through a nonlinear medium of sufficient length. Each of these filaments typically carry power on the order of $P_{cr}$ [10].

The challenge lies in maximizing spectral broadening while simultaneously minimizing the risk of filamentation caused by noise in the beam profile. A way of exploration involves understanding the impact of increasing both the propagation length and pulse intensity within the material on the formation of these filaments.

The number of passes that the beam undergoes through the thin film offers an opportunity to investigate how the spatial modulation instability gain varies with increasing material thickness. The material configuration passes discretely from a reference condition with no film to a single 0.1 mm thick film, then to 4 layers of 0.1 mm thick films, and finally to 6 layers of 0.1 mm thick films. The input pulse energy used for comparing these features is approximately 160 mJ.

Notably, in the case of the 6-layer configuration, there is observable discoloration of the film in the final two passes when the film is removed from the chamber. This discoloration tends to occur around specific hotspots within the beam profile. The material damage typically becomes apparent in the later stages of the film, allowing for the possibility of partial shifts of the material to refresh the film [9].

**Focal spot study** There is a noticeable contribution from scattering within the film, which becomes evident in the far-field. Even at low energy levels with no nonlinearity introduced by the material, the 6× COP and 4× COP configurations exhibit significant degradation.

On the other hand, the single film is of higher optical quality and is mounted separately. It does not significantly degrade the ability to focus the beam. Extended studies related to the focusability of post compressed pulses of this campaign were published in Ref. [11, 12]

**Spectral broadening study** The spectral broadening as a function of input energy is depicted in Figure 4.17. In this particular case, the total COP thickness was 0.6 mm, and no damage was detected on the thin films. It is important to note that this data incorporates uncertainties in the spectral bandwidth, which can arise from variations in laser energy shot-to-shot or from the bandwidth estimation process. The latter, bandwidth estimation, will be thoroughly examined in the subsequent section 4.4.3.

The scalability of COP film up to a width of 1 m makes it a suitable material for implementation at normal incidence or even Brewster's angle, especially for large beam apertures of 10 PW-class systems, such as the 55 cm beam diameter at the HPLS 10 PW output.

Simulations were conducted to estimate the resulting increase in bandwidth for a 25 fs pulse at fluences appropriate for the 10 PW HPLS laser facility at ELI-NP, as presented in Fig. 4.18. The figure displays the induced increase in bandwidth ($\Delta\omega$) relative to the original reference bandwidth $\Delta\omega_0$ of the input pulse. This is plotted against pulse fluence, with examples provided for a single film and two films. The shaded region emphasizes the values corresponding to the relevant pulse fluences of 80 - 100 mJ/cm$^2$.

As the pulse duration is shorter, at 25 fs, in contrast to the 50 fs used in the reported LASERIX experiments, it requires a thinner material. Consequently, the simulation indicates that passing through films with thicknesses of 0.10 mm or 0.18 mm once or twice (labeled in the figure as COP 0.10 mm, COP 0.18 mm, COP 2×0.10 mm, COP 2×0.18 mm, respectively) is adequate to achieve substantial spectral broadening, even within the sub-10 fs range.

In addition to the perspectives mentioned above, thin plastic COP films can also serve as debris shields for optical components. Furthermore, an upgrade to a larger-scale roller

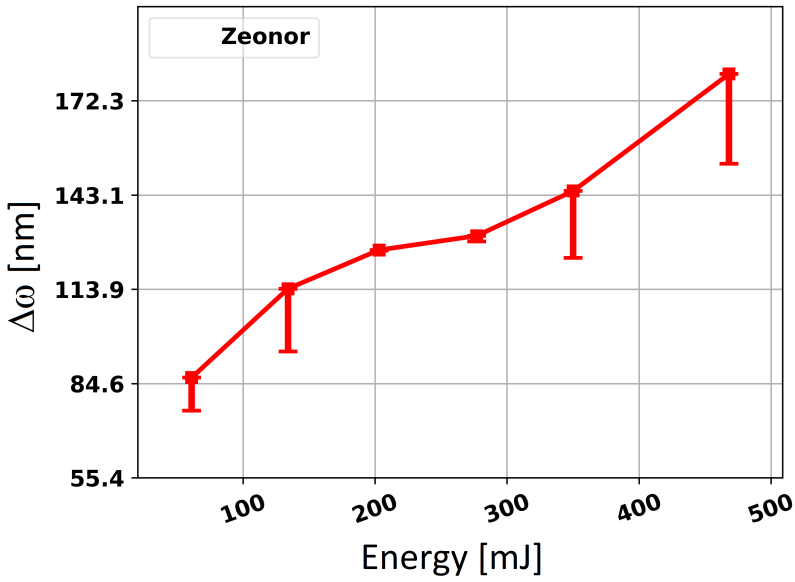


Figure 4.17: Spectral broadening as a function of input energy for Zeonor (COP) material.

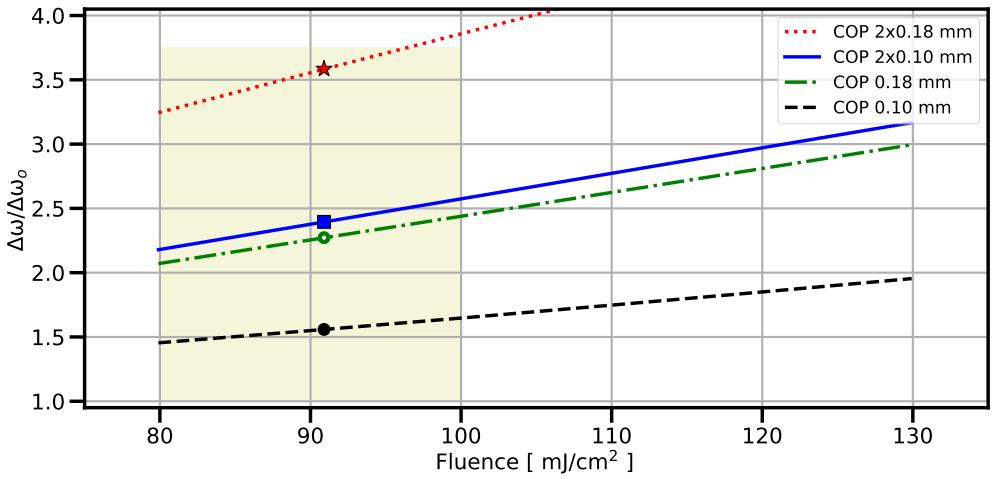


Figure 4.18: The simulated response of the COP plastic film, with an initial pulse duration of 25 fs. Figure extracted from Ref. [9].

mechanism, alongside the use of meter-scale COP films and larger chirped mirrors, could be implemented to enhance the capabilities (intensity) of the 10 PW laser system.

The complete description of the experiment can be found in the reference [9]. Other relevant studies with respect to the post-compression of these plastic materials can be found in Ref. [11, 12].

## 4.3 Apollon campaign

In this experiment, laser pulses, carrying 7 J of energy and passing through large-aperture thin glass plates (30 cm diameter), undergo spectral broadening to achieve a bandwidth suitable for generating 15-fs pulses. Furthermore, the experiment shows the potential to attain sub 10 fs pulses using 14 J of energy.

Positioning the post-compressor in close proximity to the interaction point offers an economically efficient approach to produce the shortest pulses at high energy. This strategy minimizes the requirement for high-damage, broadband optics near the final target, as opposed to needing them throughout the entire laser transport system.

One of the primary objectives of the Apollon laser system is to generate 10 PW pulses with an energy of 150 J and a duration of 15 fs at a repetition rate of 1 shot per minute. In this experiment, the 1 PW amplification line was employed to deliver 7 J of energy with a pulse duration of 25 fs at a central wavelength of 800 nm to the materials.

I was actively engaged in all aspects of this experiment, encompassing preparation, implementation, simulation, data analysis, measurements, and publication (see Ref. [13]).

### 4.3.1 Experimental Setup

The experiment operated the system at its maximum beam amplification of 14 J, but it was attenuated to 50% of the energy before reaching the compressor, resulting in 7 J within the 14 cm diameter beam, yielding a fluence of approximately 45 mJ/cm$^2$. The pulse duration, measured by both a Bonsai Autocorrelator and WIZZLER during this campaign, was 22 fs. This configuration led to a peak intensity of approximately 2.2 TW/cm$^2$, considering the entire beam diameter. The laser beam was transported under vacuum from the laser room to its exit point in the interaction chamber, adjacent to the laser diagnostic table.

To adapt the beam size of the 1 PW line, new type of glass wafers (Schott AF32eco) were placed at Brewster's angle, in vacuum. Two wavers with 0.4 and 0.4 mm, mounted in custom frames, were used in this experiment. The transmitted wavefront error for the standard wafers typically falls within the range of (1.4 ± 0.2) $\lambda$ for the 0.4 mm wafer and (1.0 ± 0.2) $\lambda$ for the 0.3 mm wafer, where the wavelength $\lambda$ was 633 nm. The achievement of this precision level required testing multiple samples before finding ones that met these specifications. Thus, here I faced the problem of polishing the samples of these large dimensions. The transmitted wavefront effects will be further characterized and discussed in Section 4.3.2.1.

The nonlinear optical properties of Schott AF32eco glass have not been officially reported. However, given that it is a borosilicate glass, it is reasonable to assume that its nonlinearity and dispersion values might similar to other glasses. We assumed $n_2 \sim 1.5 \times 10^{-16}$ cm$^2$/W and $k_2$ (800 nm) $\sim$ 44.7 fs$^2$/mm.

The spectra were measured after a second R80/T20 BS using a fiber spectrometer (SP in Figure 4.19; Ocean Optics JAZ).

The laser focal spot was fine-tuned using a closed-loop adaptive optics wavefront control system. This system utilized a deformable mirror equipped with 52 mechanical actuators

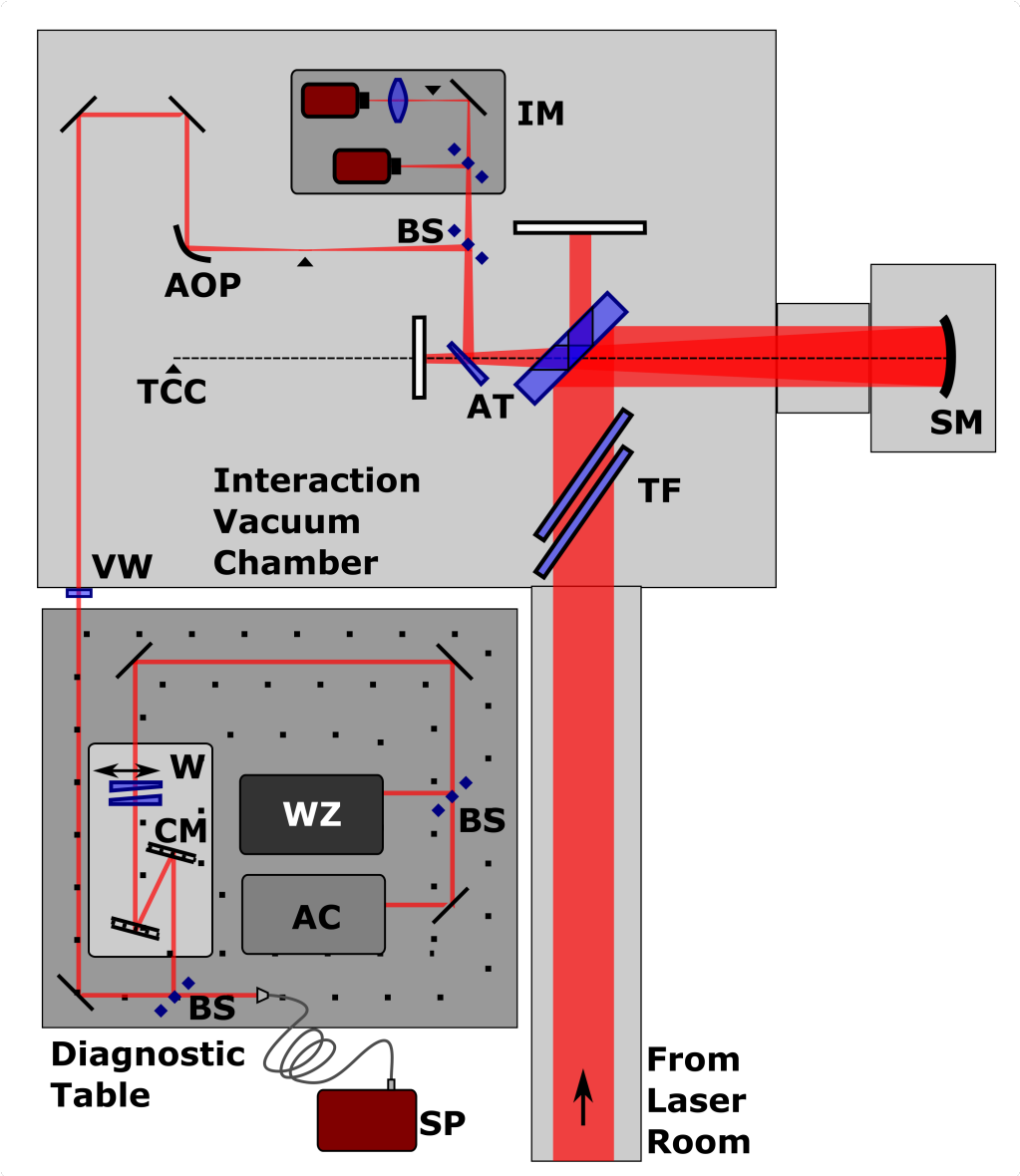


Figure 4.19: The experimental setup situated in the Long Focal Area (LFA) of the Apollon facility. In the figure, the various elements described in the text are denoted by the following acronyms: thin films (TF), spherical mirror (SM), target chamber center (TCC), attenuators (AT) consisting of uncoated fused silica substrates, beamsplitters (BS), near-field and far-field beam imaging (IM), off-axis parabola (AOP), vacuum window (VW), wedge pair (W), dispersion or chirped mirrors (CM), spectrometer (SP), WIZZLER (WZ), and autocorrelator (AC). Figure extracted from Ref. [13].

(specifically, the ILAO-star by Imagine Optic), which was positioned at the output of the amplification section.

The Apollon laser system was equipped with a DAZZLER and a Deformable mirror integrated into the laser chain. The DAZZLER played a role in both reference and pulse duration measurements, whereas the Deformable mirror was exclusively employed for reference optimization purposes. Within this experimental campaign, the optimization of the focal spot, after the broadening, was not performed.

Measurements conducted outside of a vacuum environment require additional compensation for the self-phase modulation process, which arises from factors such as the vacuum window, air propagation, and any other optical components introduced along the beam path (e.g., mirror bounces, beamsplitters, or waveplates).

In the experimental setup, the laser pulse was first reflected from a pair of negative dispersive mirrors with a diameter of 25 mm (referred to as chirped mirrors or CM in Figure 4.19). These chirped mirrors, specifically the Ultrafast Innovations HD58, are capable of providing discrete negative Group Delay Dispersion (GDD) correction at a rate of -250 $fs^2$ per bounce.

To precisely adjust the pulse duration before it reaches the Autocorrelator (AC) and the Fastlite WIZZLER, the dispersive mirrors are typically configured to overcompensate for negative chirp. This compensation is achieved using a pair of wedges (W in Figure 4.19), which provide variable positive dispersion. The specific wedges used are the Thorlabs UFBS 2550.

An estimation of the GDD introduced by various components within the beam transport and Dispersion Management System (DMS) typically falls in the range of 600 $fs^2$ to 800 $fs^2$. This value was influenced by factors such as the number of bounces on the dispersive mirror pair and the positions of the wedges.

### 4.3.2 Bandwidth analysis

Taking into account the thickness of the glass wafers and their angle with respect to the incoming beam, we can estimate a total accumulated nonlinear interaction length of $L_i \sim 0.84$ mm. Using these values, estimates for the B-integral yield $B_{int} \sim 1.4$. Along with the dispersion parameter, $D \sim 0.085$, we can calculate the expected $F_\omega$ from equation 4.3 as follows: $F_\omega$ from Eq. 4.3 to be:

$$F_\omega = 1 + 0.51\ B_{int} \sim 1.7$$

The ratio of the broadened spectrum to the spectrum of the input pulse can be represented as $F_\omega = \Delta\omega_{out}/\Delta\omega_{in}$.Predictions regarding the expected spectral broadening were obtained through simulations by fitting a linear relation to the $B_{int}$ parameter, while considering the thin film material's group velocity dispersion ( The group velocity dispersion tends to diminish the nonlinear response, especially under conditions where the pulse energy is stretched in time due to positive dispersion ($k_2 > 0$), which is typical for most materials. The parameter $D = L_i\ k_2/\tau_p^2$ accounts for the dispersion relative to the initial pulse duration. Utilizing the fit parameters derived for spectral broadening, the following relation presented in Ref. [3] is established:

$$F_\omega = 1 + 0.91\ B_{int}\left(1 - 1.5\sqrt{D}\right) \tag{4.3}$$

The following results were retrieved based on the theoretical aspects and the equations presented in Section 2.3.2 under the simulations envelope using python programming language.

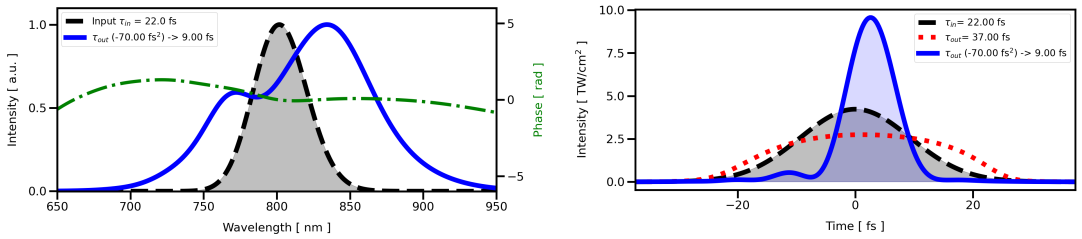


Figure 4.20: Spectral and temporal profile before and after post-compression. Figure extracted from Ref. [13].

Figure 4.20 illustrates the pulse spectra starting from an 14 J pulse initially at 22 fs duration (gray –) compared to the subsequent spectrally broadened spectrum (blue -) that supports a 9 fs pulse duration. After dispersion managements system (CMs pairs) that provides compensation to the group delay dispersion of -70 $fs^2$, the spectral phase is showed in dotted green. The pulse average intensity across the beam profile is given for the original input pulse (gray), the chirped pulse that exits the thin films (red dotted), and the compensated pulse (blue).

In this simulation, we demonstrate the potential of post-compression to achieve laser pulses with a duration of less than 10 fs at high energy. This experiment represents ***the second instance*** of achieving such results, building upon the findings presented in Ref. [14]. In the reference, the input energy was 17 J, and the input pulse duration was 74 fs, with an 18 cm beam diameter. To achieve pulse compression down to 11 fs at a power of 1.5 PW, 5 mm of FS was utilized. Several key aspects of this reference are noteworthy, including the utilization of free propagation for self-filtering, the use of 3 pairs of 20 cm CMs (Ultrafast Innovations), and a high B-integral value of 19.2.

The experimental results started with an initial 22 fs pulse, pre-chirped with -500 $fs^2$, stretch to approximately 67 fs after passing through the materials, with the peak intensity decreasing to the point where there's no significant impact on the original laser spectrum due to SPM.

When optimizing the pulse duration (with the DAZZLER) to 22 fs, the SPM process leads to spectral broadening (see Figure 4.21). The measured pulse duration, as determined by the AC, is influenced by the configuration of the DMS, and its contribution to GDD was considered in the pulse measurement. The negative chirp introduced by the DAZZLER (-500 $fs^2$) compensates for the overall positive dispersion introduced by the DMS (approximately 600 $fs^2$) following the glass film. Accounting for this, the impact of a 100 $fs^2$ chirp on a 22 fs pulse results in a pulse duration ranging between 35 and 40 fs, as measured by the AC.

As the pulse spectrum broadens through SPM, maintaining the pulse duration becomes more sensitive to the optical components. In this case, the AC measured an average pulse duration of around 150 fs, corresponding to a 15 fs pulse chirped by the 600 $fs^2$ introduced by the DMS.

Under these conditions, the pulse was too chirped to be directly measured by the WIZZLER. Time constraints during the experimental campaign prevented adjustments to the DMS system that would have allowed for a direct measurement of the shortest pulse duration with optimal spectral broadening. Despite this limitation, estimates of the pulse duration were made based on recorded laser parameters and measured spectra.

The diagnostic data for individual shots revealed an average energy per shot of 6.4 ± 0.2 J, resulting in an average fluence of 41 ± 1 mJ/$cm^2$ and an intensity of 1.97 ± 0.05 W/$cm^2$ for a 22 ± 1 fs pulse. Utilizing these parameters, it was found that $B_{int} = 1.8$ and

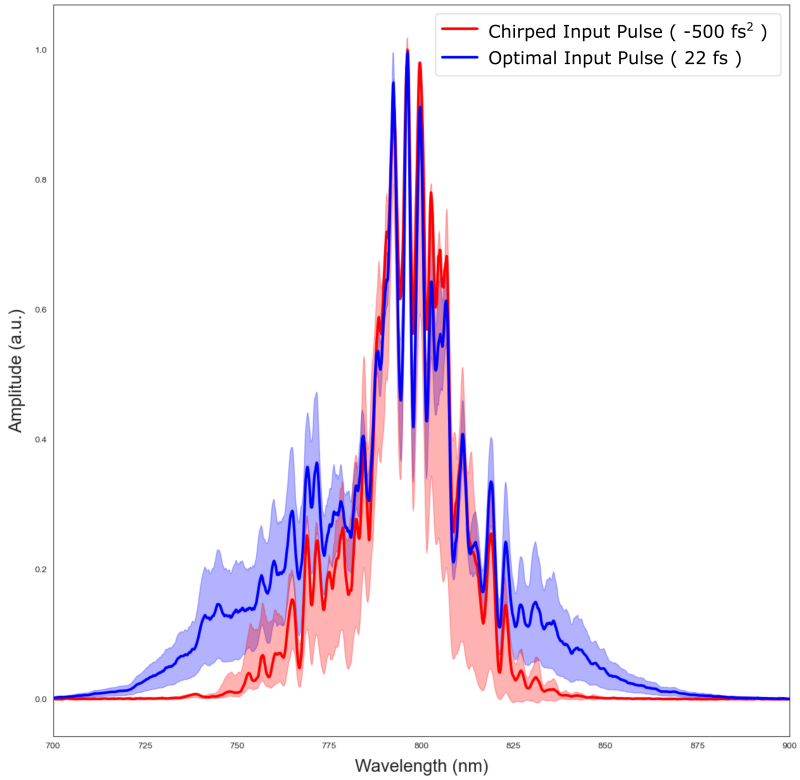


Figure 4.21: Spectral statistic for reference (red) and the output broadening (blue). Figure extracted from Ref. [13]

the spectrum to be broadened by a factor of approximately $F_\omega$=1.8.

The average measured spectral bandwidth after interacting with the thin films was determined to be 74 ± 2 nm, corresponding to a pulse duration of approximately 15 fs. This is in contrast to the original input pulse, which had an optimized pulse duration of 22 fs and a bandwidth of 41 ± 1 nm. Calculating the ratio of these measured pulse spectral bandwidths yields $F_\omega^{meas}$=1.8 ± 0.1.

The agreement between the measured value and the estimation for borosilicate glass (BK7) of these dimensions (0.7 mm), interacting with a pulse of this energy (6.4 J) and duration (22 fs) confirms that the full energy pulse can be delivered at the optimized pulse duration within the interaction chamber. It also validates the assumption made regarding the value of $n_2$ for the glass films, indicating that estimations of pulse characteristics when using the full energy in future experiments are reasonable.

#### 4.3.2.1 Far-Field Analysis

The deformable mirror exhibited the capability to correct certain aberrations introduced by the thin films. However, during this campaign, limited effort was dedicated to fully optimizing the focal spot. A comparison of the images in Fig. 4.22 reveals an increase in energy spread when the focus is observed before and after inserting the glass films. Although the focus was initially adjusted at low energy after the thin films were inserted, no final optimization was carried out at full energy before the conclusion of the available time. The color bar indicates the fluence (mJ/cm$^2$) reaching the sample.

While it is essential to suppress small-scale beam features for effective control within the nonlinear SPM interaction, with a focus on maintaining the best focus quality [11,

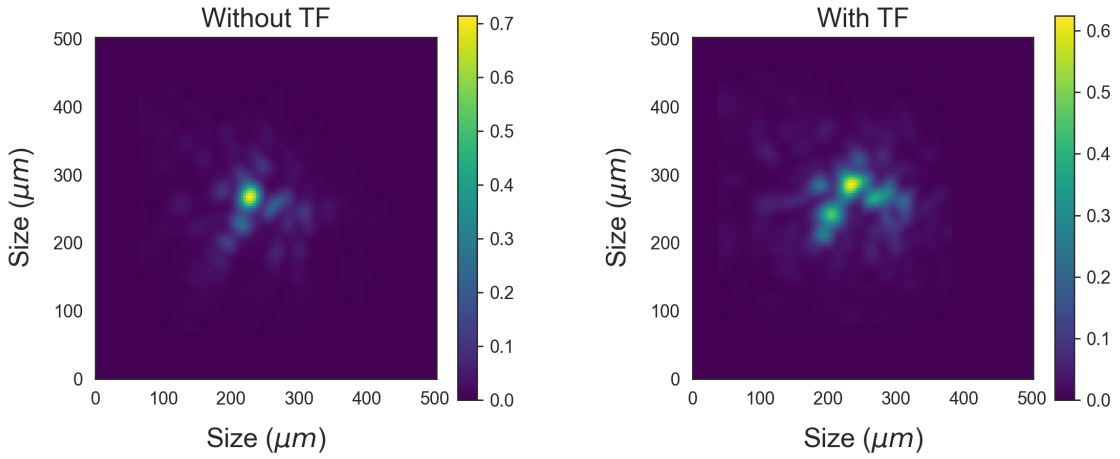


Figure 4.22: Far Field images. The image on the left displays the reference focus with no glass films in the beam path, while the image on the right depicts the focus after the thin films have been installed. Figure extracted from Ref. [13].

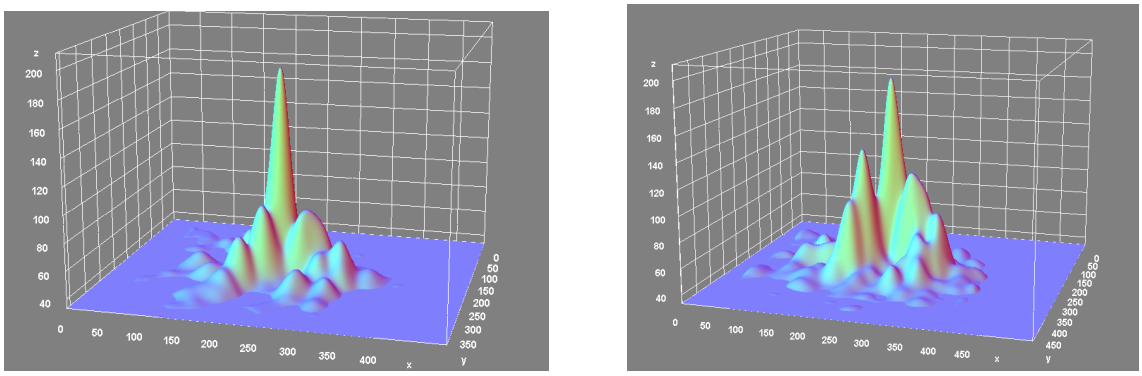

Figure 4.23: Spread of the energy in the focus before and after SPM, 3D view.

15], the primary objective in controlling the focus during this campaign was to ensure the proper functioning of laser diagnostics and to prevent any modifications to the pulse measurement. It is anticipated that the deformable mirror has the potential to rectify the observed distortion in the focus when more attention is given to its enhancement.

The energy spread in the focus is depicted in Figure 4.23. This spread primarily arises from several factors: the initial laser beam's wavefront quality, the transmitted wavefront of the material, and nonlinear interactions (specifically, self-phase modulation and nonlinear absorption). The influence of nonlinear effects on energy distribution has also been discussed in a study by another research group [16].

### 4.3.3 Spectrum and pulse duration metrology

During the Apollon campaign, I investigated the issue of estimating spectral broadening. This study aimed to answer the question: **"How large is the spectrum after spectral broadening?"** This question is straightforward when there is no temporal diagnostic present in the experiment, or when the input intensity is too high. Most temporal measurement devices work with an input energy of 50 µJ or lower (e.g., Autocorrelators, FROG), or lower energy for devices like SPIDER.

In cases where the input spectrum is Gaussian-like, the temporal envelope is also Gaussian. Therefore, the approach of measuring the spectrum and determining the pulse dura-

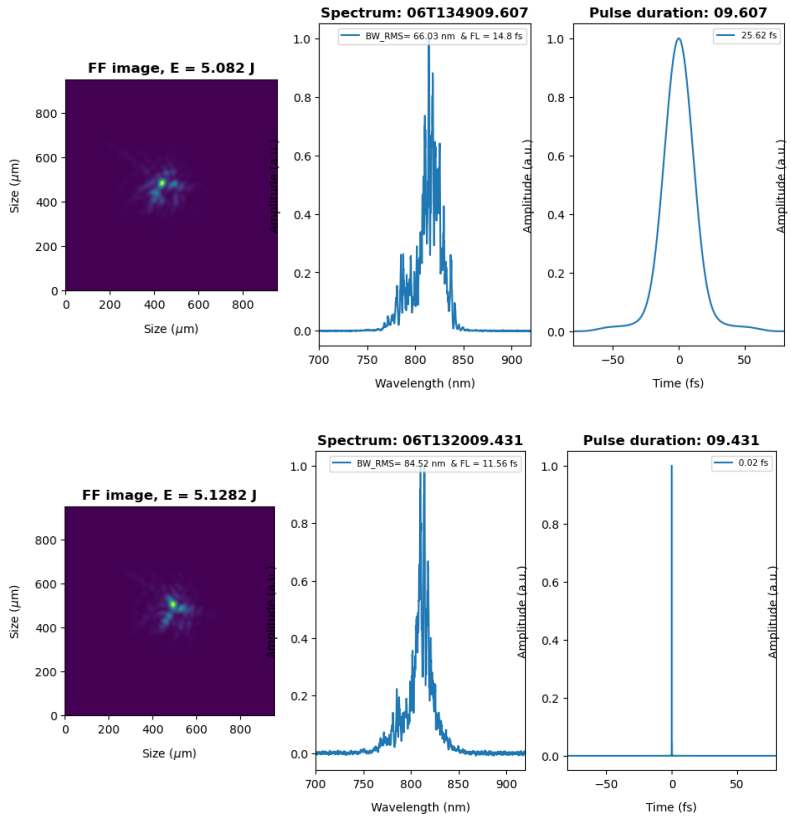


Figure 4.24: Experimental results interface where: the FF and the input energy (left), the spectrum )center) and the pulse duration (right) are illustrated in real time after each shot. This figure shows the failure (bottom) of the same algorithm to retrieve the pulse duration due to the spectrum shape

tion at the full width at half maximum (FWHM) works effectively, as suggested by theory. However, the broadening is not always uniform due to various factors such as the laser's input profile (temporal, spatial, intensity distribution) or other nonlinear effects discussed in Chapter 2. Consequently, estimating the bandwidth solely based on FWHM can be challenging. For instance, in situations where a portion of the spectrum (a few manometers) has an amplitude greater than 50%, the FWHM-based algorithm may fail.

To illustrate this problem further, see Figure 4.24, which compares two different shots (reference pulses with no self-phase modulation). The comparison involves the far-field image, energy, spectrum measured at root mean square (RMS), the Fourier-limited pulse duration, and the retrieved pulse duration from the entire spectrum. One solution that I applied for the algorithm error was to pad with 0 the frequency spectra to increase the resolution in the temporal domain.

I delved deeper into this problem and developed an algorithm to extract and compare the bandwidth at the full width at half maximum (FWHM) and at the root mean square (RMS) calculated using Eq. 4.4, as shown in Figure 4.25 (with red). The pulse duration measured at FWHM was retrieved from the Fourier transform of the entire spectrum.

$$\Delta\omega = \sqrt{\frac{\int_{-\infty}^{\infty} \omega^2 |x(\omega)|^2 d\omega}{\int_{-\infty}^{\infty} |x(\omega)|^2 d\omega}} \tag{4.4}$$

In summary, extracting the bandwidth from non-uniform spectra proved to be a challenging task. In this section, I examined the equivalent bandwidth, which was determined

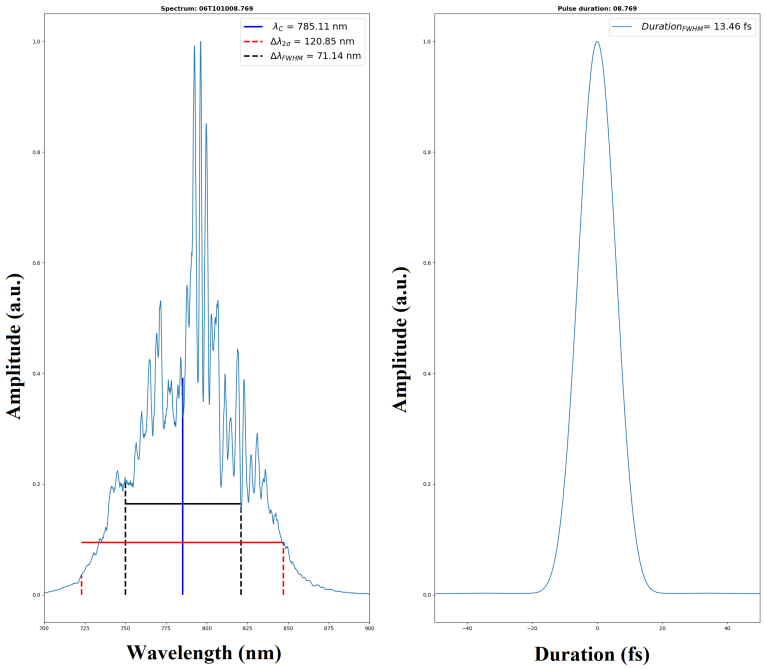


Figure 4.25: Spectral bandwidth($\Delta\lambda$) estimated at FWHM (weighted) and at RMS followed by its temporal profile with the pulse duration measured at FWHM

using the root mean square (RMS) and full width at half maximum (FWHM) methods. For the Apollon data, the RMS algorithm was found to be the most suitable due to the non-uniform nature of the measured spectra. In the next section 4.4, I will discuss the metrology of spectral broadening ($\Delta\omega$).

### 4.3.4 Discussion

During this experiment, we made significant progress in the field of post-compression techniques. We demonstrated the capability of the setup to post-compress laser pulses with 7 J energy and an ultra-short duration of 22 fs.

This experiment marked several advancements, including the use of the full beam and full energy on the sample, the utilization of a new type of glass (Schott AF32eco), larger glass size (30 cm), a mount for the glass that minimized induced stress, and the development of an algorithm for estimating spectral broadening. Furthermore, we showed the potential to achieve 9 fs pulses with the full energy of the Apollon 1 PW laser pulses.

However, we encountered challenges related to near-field images, pulse duration measurements with the WIZZLER, focal spot optimization, and a multiple times stretcher mirror damage. This campaign served as the first commissioning experiment for the 1 PW line of Apollon. Due to time constraints and the impact of the pandemic, some of these challenges could not be fully addressed in time. Nevertheless, this experience has equipped us with valuable lessons for future experiments.

The results of this experiment have been published in Ref. [13], with me as the first author.

## 4.4 ELI-NP 100 TW

The ELI-NP 100 TW campaign represents the culmination of my experience, encompassing material characterization and previous experiments.

I played an active role in all aspects of this experiment, from preparation and implementation to simulation, data analysis, measurements, and writing the manuscript (in preparation). I was responsible for implementing the experimental setup, designing and implementing mounts and motorized stages for the optical materials, all without the need to open the vacuum chamber. This aspect allowed for the insertion of three types of materials in the first compression stage. I performed measurements and data analysis for spectral and temporal data, and I also contributed to spatial and spatio-temporal analysis.

During this experiment, we examined the intensity enhancement of the non-ideal post-compressed pulses. I investigated the non-Gaussian spectra of the reference pulse and also strongly modulated spectra resulted after the spectral broadening process. Several materials configurations were tested under peak powers with an estimated B integral range from 1 $\pi$- 3 $\pi$, and larger.

This experiment offers several significant advantages, including the metrology of intensity enhancement in the focus and the comprehensive characterization (temporal, spectral, spatial, and spatio-temporal couplings) of post-compressed laser pulses. In this work, we demonstrated an average pulse duration of 11 fs using 1 J input energy over 100 shots. Simulation results, combined with spectral measurements, suggest a pulse duration of less than 6 fs when 2 J input energy is utilized. This experiment represents one of the closest approaches towards the single-cycle regime at the joule level, ever reported with measurements data. In addition to measuring the 11 fs pulse duration, this experiment also includes an extensive and detailed analysis of laser pulse metrology, surpassing any previous reports on this.

### 4.4.1 Experimental Setup

The experimental arrangement employed for post-compression and the subsequent characterization of the post-compressed pulses is illustrated in Figure 4.26.

The 100 TW beamline of ELI-NP HPLS, featuring a Ti: Sapphire laser source (2 J, 26 fs, 10 Hz, 810 nm, and a beam diameter of 55 mm), was directed towards the experimental chamber. This chamber was maintained under vacuum conditions with a pressure of $10^{-5}$ mbar. Within the chamber, samples measuring 10 cm x 10 cm (refer to Materials in Table 4.2) were positioned at a 30-degree angle relative to the incident laser beam. Motorized translation stages were utilized to enable the insertion of various material plates into the laser pulse's path. These materials were placed at two distinct locations to facilitate the use of two post-compression stages.

Four Chirped Mirrors (CMs) supplied by UltraFast Innovation were employed to recompress the laser pulses, compensating for the Group Delay Dispersion induced by Self-Phase Modulation and material dispersion. These CMs had a spectral range spanning from 650 to 950 nm, possessed a GDD of -75 $fs^2$ per bounce, had dimensions of 6 inches, and were positioned at a 45-degree angle of incidence (AOI). They exhibited a reflectivity exceeding 99%.

To minimize the potential nonlinear absorption effects that may arise [16] the fluence incident on the CMs was kept below 40 $mJ/cm^2$. Additionally, recognizing that the pulse duration would decrease by at least two times after passing through the first two CMs, a 6-inch Wedge was introduced to reduce the fluence experienced by the last two CMs. This Wedge served a dual purpose: it prevented nonlinear processes within the vacuum

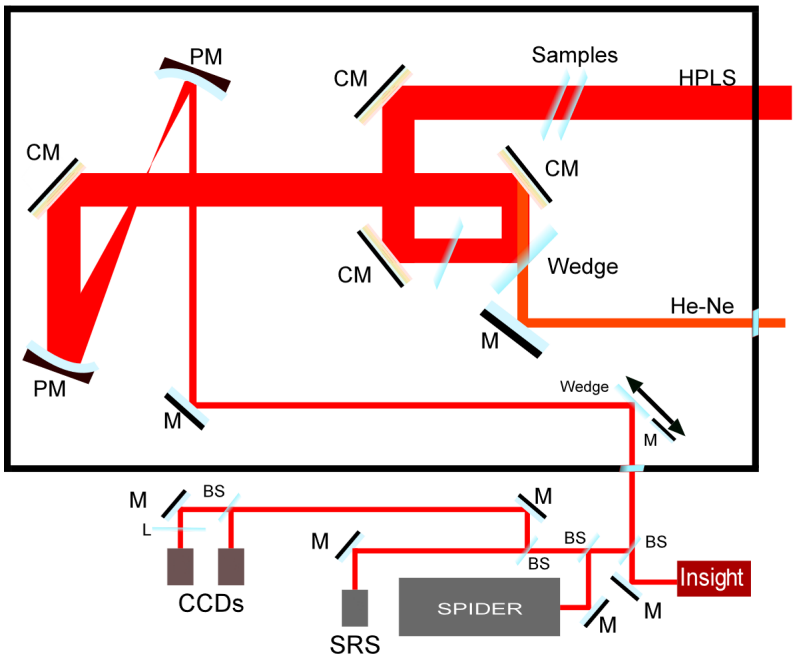


Figure 4.26: Experimental setup where: CM-Chirped Mirrors, PM-Parabolic Mirror, M-Broadband mirror, BS- Beam Splitter, SRS- Spectrally Resolved Spectrometer

window and allowed for the transmission of a He-Ne laser beam along the same pulse path as HPLS, towards the focusing parabola. Daily checks were performed to ensure the proper alignment of the He-Ne laser and HPLS.

The beam was reduced in size by a factor of 5.5 using two parabolic mirrors, PM1 (f=1.5 m, off-axis, gold coating) and PM2 (f= 0.27 m, off-axis, gold coating). The collimated beam exited the chamber through a fused silica window, with broadband antireflex coating for 650-1050 nm, with a thickness of 4 mm, was split in accordance with the specifications of the diagnostic devices.

The pulse duration before and after material insertion was measured using the FC SPIDER (Few Cycles - Spectral Phase Interferometry for Direct Electric-field Reconstruction) from A.P.E. company. This device offered a measurable range spanning from 5 fs to 180 fs, enabling accurate measurements of four cycles of laser pulses and their spectral phase.

To account for additional dispersion introduced by the vacuum window and the air in the optical path to the SPIDER, amounting to a Group Delay Dispersion (GDD) of approximately 80 $fs^2$, compensation for dispersion was achieved using the last two Chirped Mirrors (CMs) installed within the vacuum chamber.

A spatially resolved spectrometer (SRS) with a spectral range of 360 nm to 1043 nm and a spectral resolution better than 1.2 nm was utilized. The SRS device recorded each spectrum across a vertical slit positioned in front of it, facilitating the collection of information regarding the central wavelength, spectral bandwidth, and Fourier-limited duration across the beam.

Changes in the beam profile were assessed using Near-Field (NF) and Far-Field (FF) CCD cameras, while spatio-temporal couplings were evaluated using the INSIGHT device. INSIGHT employs an interferometric scanning technique to retrieve the spatio-spectral profile of the laser field [17]. Positioned near the focal region of the laser, this device combines Fourier transform spectroscopy with the Gerchberg-Saxton iterative algorithm. By incorporating spectral phase data obtained from a temporal measurement device (in this

case, SPIDER), the INSIGHT processing software can accurately calculate the complete spatio-temporal profile of the laser.

The experimental campaign involved the use of three different energy configurations. The first configuration, referred to as the low energy setting, utilized 20 $\mu$J and was primarily employed for aligning the optics and optimizing the focal spot/parabola.

The second configuration, which used 2 mJ, served a multifaceted purpose. It was used to measure various parameters, including spatio-temporal couplings (STC), focal spot deformation before and after material insertion, deformable mirror tuning, spectrum analysis, and pulse duration.

In the third configuration, a high energy setup employing 1 J was utilized to irradiate the materials, inducing Self-Phase Modulation (SPM) and spectral broadening. This configuration was subsequently used for measuring the STC, pulse duration, spectrum, as well as the Near-Field (NF) and Far-Field (FF) characteristics. Images of the FF and NF profiles were captured during the experiment using two dedicated CMOS cameras (Basler).

To facilitate diagnostic measurements without altering the beam splitters, a second wedge and a silver mirror were placed on a translation stage just before the exit of the interaction chamber. This arrangement allowed for measurements to be conducted using diagnostics while preserving the integrity of the beam splitters.

The optical materials used in this experiment were: FS (5 mm), FS (1 mm), BK7 (1 mm), SF5 (1 mm), Zeonor (0.1 mm). The following results will be **focused on BK7 material** used in a configuration of 2 glass plates providing a thickness of 2 mm. This material, for this experimental campaign, provides the best results.

### 4.4.2 Temporal Measurements

Data retrieved from SPIDER (spectrum, spectral phase, GDD, TOD, measured and Fourier Transform Limited (FTL) pulse duration) will be displayed in the following subsections. Within this section, I will show the importance of both GDD and TOD compensation while applying the theory and the experimental results developed in Section 2.1 and 3.2.1. Here, I will also introduce a new term called Temporal Strehl Ratio (TSR) which will be of help for in the future estimations of the spectral broadening.

#### 4.4.2.1 SPIDER measurements

Five configurations of nonlinear optical materials were investigated in the temporal domain using an FC SPIDER.

Spider measurements were conducted to analyze the spectral characteristics and temporal profiles of laser pulses. The results are presented in the following Figure 4.27.The spectrum, phase and pulse duration were measured for each laser shot in single shot or 10 Hz configuration.

The blue region (mean spectrum) and the shaded blue (each spectra measurement) of the figure show the normalized intensity distribution across different wavelengths compared with the reference spectrum (black). The mean spectral phase (orange) across 700 -900 nm illustrates how the phase of the pulse varies with wavelength.

The right side of the figure depicts the measured and the FTL pulse duration for the post-compressed pulse after passing through 2 mm of BK7 material. This data were further compared to the FTL pulse duration retrieved from the spectra.

These measurements provide valuable insights into the spectral and temporal characteristics of the laser pulses before and after interacting with the 2 mm BK7 material. The comparison between the measured and FTL pulse durations helps assess the efficiency of the post-compression process and the impact of the material on the pulse duration.

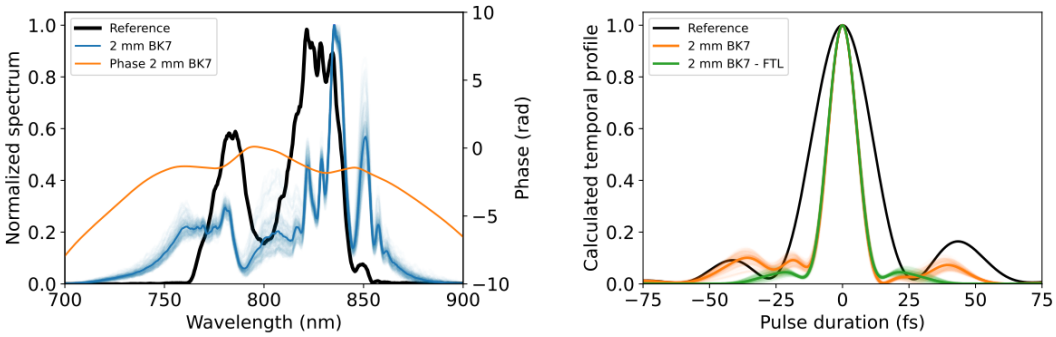


Figure 4.27: Spider measurements of: Left) spectra and the spectral phase and Right) the measured and the FTL pulse duration. These results were obtained for the reference pulse and the post-compressed pulse after passing through 2 mm of Bk7

As a further enhancement to the previously published research articles, statistical analysis was conducted on a data-set consisting of more than 100 laser shots. This analysis is illustrated in Figure 4.28.

Specifically, the orange curves representing the results for 1 mm of BK7 material indicate a variation of approximately ± 1.35 fs when only GDD is compensated. However, when utilizing 2 mm of BK7 and compensating for both GDD and TOD, the error bar decreases by nearly a factor of four, reaching approximately ± 0.4 fs. It is important to note that the compensation for GDD and TOD was achieved using the DAZZLER, which is integrated into the laser chain.

Figure 4.29 illustrates the measured and FTL pulse durations for each material, along with the best configuration of the GDD and TOD. Notably, when both GDD and TOD were optimized, the measured pulse duration closely approximated the FTL pulse duration.

It's worth noting that the higher error bars observed for the other materials may be attributed to non-optimized TOD. During this experimental campaign, the optimization was specifically applied to the configuration involving 2 mm of BK7 material.

#### 4.4.2.2 GDD and TOD influence

The minimum pulse duration was measured after GDD tuning using the Dazzler available in the laser system. Figure 4.30 illustrates the dependence of the measured and Fourier-transform limited (FTL) pulse duration as a function of the GDD for 2 mm BK7.

It is important to note that even with optimal Chirped Mirrors dispersion, only the second-order spectral phase is effectively compensated (within the error bar of GDD along the spectrum), reaching close to a zero value. In addition to GDD, compensation of third-order dispersion (TOD) is essential for reducing the concentrated energy in the side lobes. This additional optimization allowed us to achieve a pulse duration as short as 11.2 fs for the 2 mm BK7 case. The optimization of GDD and TOD is depicted in Figure 4.30, indicating a minimum pulse duration at approximately 37200 $fs^2$ Dazzler dispersion at the best compression od reference pulse.

The higher-order spectral phase of the input pulse is not zero and tends to increase during SPM. Additionally, the CMs themselves contribute to the growth of higher-order spectral phase due to nonlinear absorption (NLA). In this experiment, it is considered that NLA did not occur because, at 1 J, the fluence was only 40 $mJ/cm^2$, and the measurements did not indicate the energy reduction.

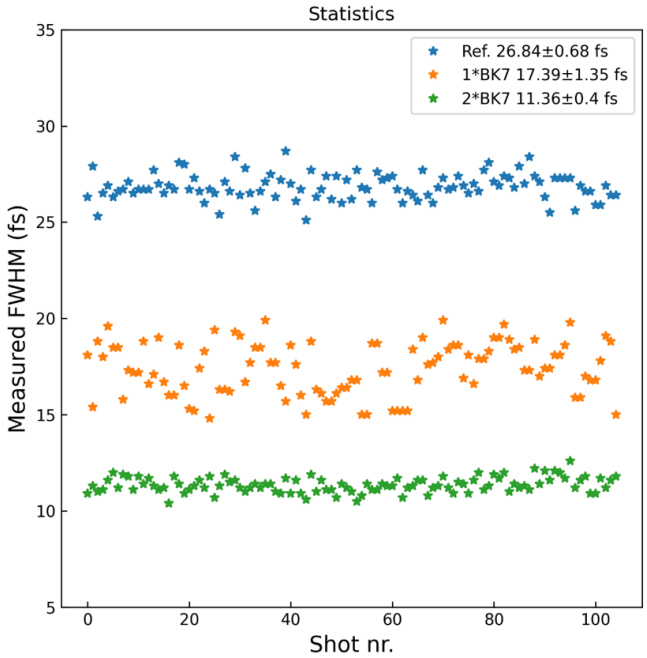


Figure 4.28: Statistics of the reference and the pot-compressed laser pulses using BK7

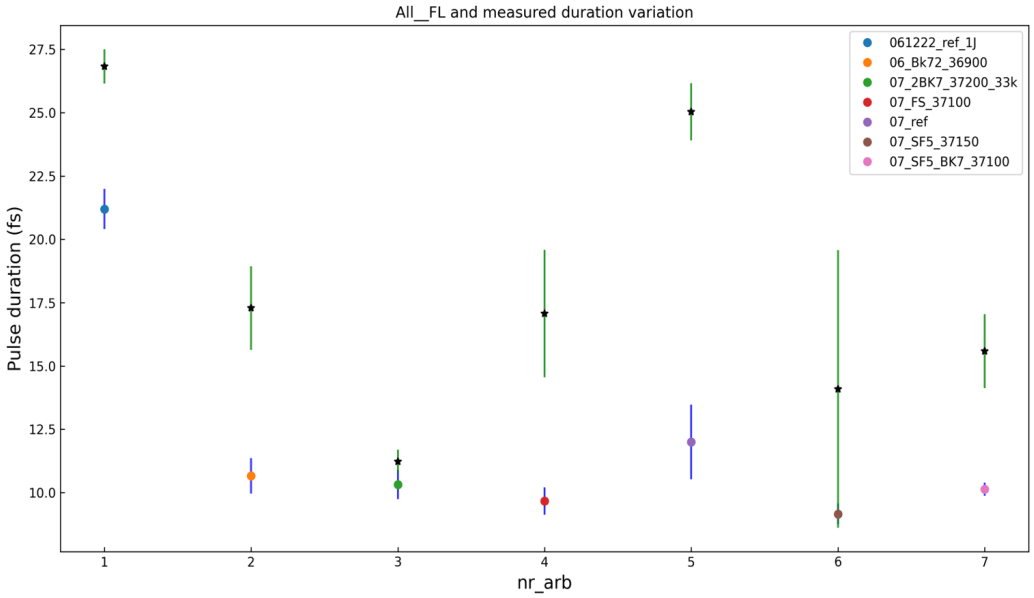


Figure 4.29: FL and measured pulse duration using SPIDER. The label denotes the Reference (ref), the day, material or materials configuration, the GDD value ($fs^2$) and the TOD ($fs^3$), when optimized

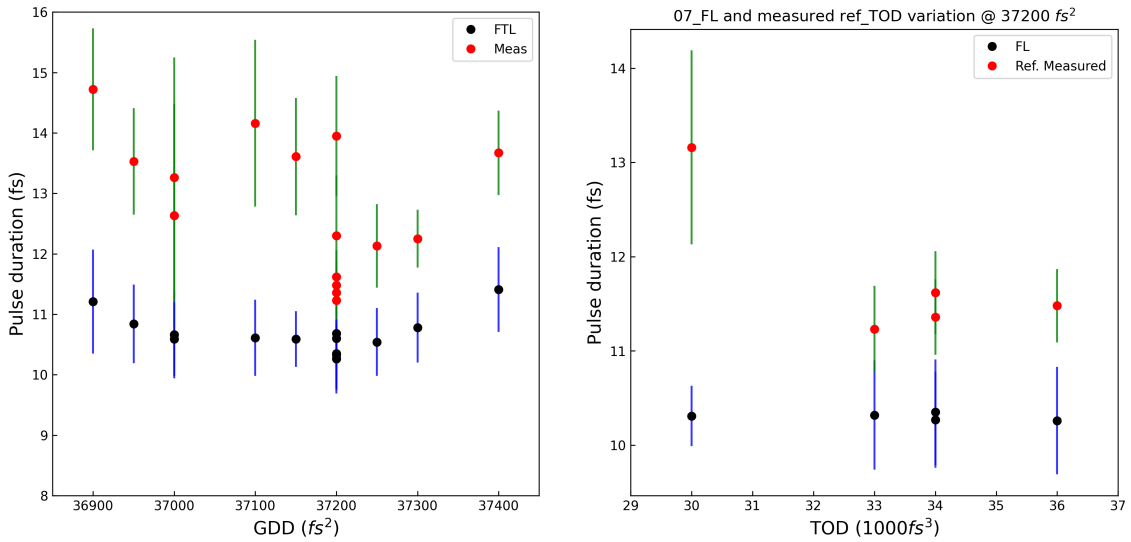


Figure 4.30: GDD and TOD influence in the pulse duration for 2 mm BK7

#### 4.4.2.3 Temporal Strehl Ratio (TSR)

To quantify the energy spread in the lobs, due to uncompensated higher order of dispersion, a new factor was introduced: Temporal Strehl Ratio, similar to the Spatial Strehl Ratio.

TSR is defined with the electric field envelope of the FTL laser pulse serving as the reference. The squared electric field envelope, obtained through FC SPIDER, undergoes normalization to match its area ($S_m$) with that of the FTL envelope ($S_{FTL}$). Consequently, TSR represents the ratio between the peak intensity of the measured curve and the peak intensity of the FTL curve.

Let's denote the areas under the respective FTL and measured temporal intensity curves as $S1$ and $S2$, respectively. Thus, the TSR can be defined as:

$$TSR = \frac{max(S_{FTL} * |\epsilon_m(t)|^2)}{max(S_m * |\epsilon_{FTL}(t)|^2)} \tag{4.5}$$

where $S_{FTL/m} = \int_{-\infty}^{\infty} |\epsilon_{FTL/m}(t)|^2 \, dt$ and $\epsilon_{FTL/m}(t)$ is the complex electric field envelope of the FTL/ measured (m) pulse.

The main results are presented in Figure 4.31. Again, the compensation of both GDD and TOD make that the spread of the energy in the side lobes of the temporal profile to be minimized. It was showed that the TSR can increase the broadening factor ($F_\omega$) and impact the intensity of the post-compressed laser pulses in subsequent compression stages.

### 4.4.3 Spectral measurements

The 2-D spectrometer (SRS) used offers several advantages. It provides spectral profiles across the entire multi-millimeter diameter of the laser beam, with a sampling resolution determined by the pixel size of a CCD camera sensor. Unlike traditional spectrometers, the 2-D spectrometer captures the laser beam within dimensions of up to tens of millimeters perpendicular to the beam's propagation axis. It does so using a slit that is tens of micrometers wide, as opposed to a traditional aperture. The resulting images are then projected onto a CCD array, which has dimensions of 12x12 mm. This setup allows us to

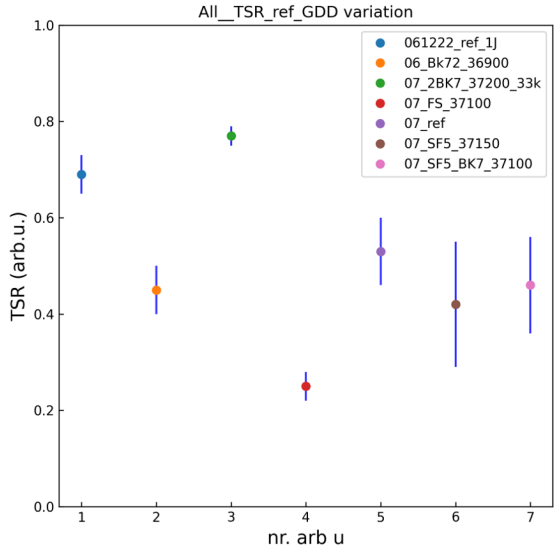


Figure 4.31: Temporal Strehl Ratio (TSR) measured for each material at the best compression configuration

obtain information about the spectral consistency, homogeneity, and spatial chirp across the entire length of the slit.

#### 4.4.3.1 Device calibration

To process the raw image data into valid spatial spectrograms, several steps were taken. First, the images were corrected using intensity attenuation data provided by the device manufacturer, as shown in the Spectral Intensity Calibration Femtoeasy graphic. Additionally, a wavelength scale calibration was applied to the horizontal pixel order, starting from left to right. The resulting wavelength scale ranged from 357.46 nm to 1040.6 nm, based on a calibration formula:

$$\lambda_{pixel} = -3.01 * 10^{-7} px^2 + 0.28 * px + 356.22 \tag{4.6}$$

The pixel order values were ranging from 4 to 2452. This calibration process ensured accurate wavelength information for the spatial spectrograms.

All spectral profiles were normalized as probability density functions by dividing each intensity value by the profile's total, thereby reducing its integral to unity. Additionally, the distribution's width was assessed using the "Standard Deviation" function in Wolfram Mathematica, which considered the wavelength sampling data and weights represented by the intensity values using "Weighted Data." In essence, the second-order moments of the distribution, specifically the variance (the standard deviation square), were computed to determine the width of the spectral profile.

Consequently, the average spectral width of the hundreds of profiles was calculated along with their standard deviation as a relative error. For instance, the spectral width of the reference laser pulse spectrogram was determined to be 61 nm with a standard deviation of 6 nm, as depicted in Figure 4.32. The color gradients seen in the Right side curves, transitioning from one mean spectrum to another, serve to illustrate the variations in the cross-sectional profile of the spectral distribution.

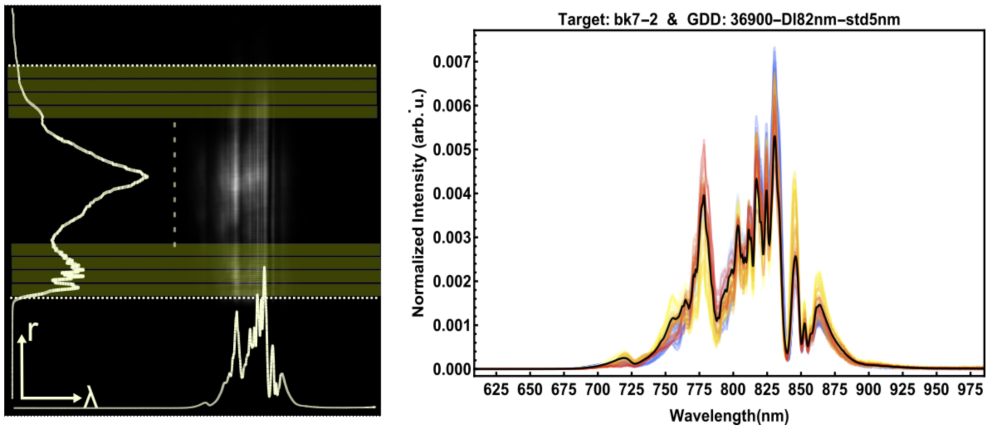


Figure 4.32: Spectrogram analysis. Left) The transverse beam spatial profile was used to identify the limiting rows for selecting the spatial interval of interest, which was then divided into 100 sub-intervals. Each of these sub-intervals was averaged, and their corresponding spatial profiles were converted into spectral profiles, and Right, all 100 spectral profiles were extracted from the spectrogram of the pulse broadened by 2 mm of BK7. The black profile represents their average.

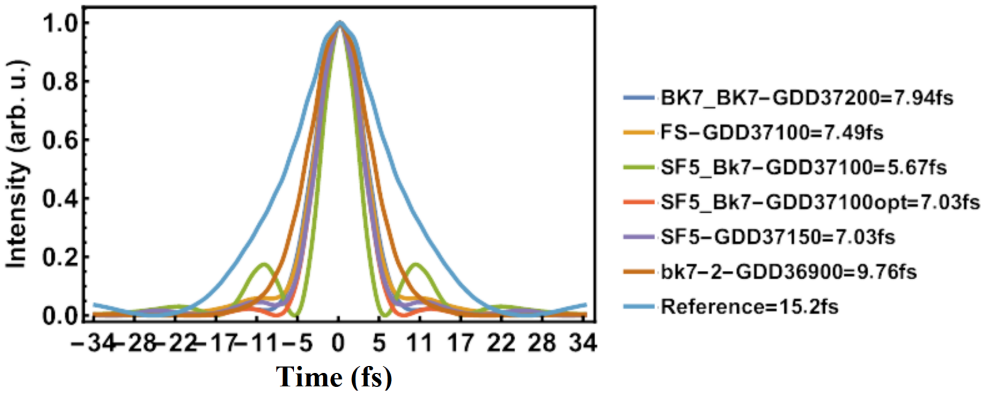


Figure 4.33: Fourier-limited pulses obtained from the spectra for each material.

#### 4.4.3.2 Spectral to temporal measurements

A temporal analysis was conducted by calculating the Fourier Time Limited (FTL) duration. This calculation involved an algorithm that utilized the Fourier inverse of the complex field derived from the average spectral profiles measured in different experimental conditions. To achieve this, the wavelengths were transformed into the frequency domain, and the spectral data were interpolated using a linear approximation, ensuring consistent resampling.

Moreover, the sampling interval was extended by zero padding to enhance resolution in the Fourier conjugate domain. To obtain the field, the real data were multiplied by a constant spectral phase profile. Applying the Inverse Fourier function to this complex field profile with the constant spectral phase yielded the Fourier-limited temporal profile. The FTL was determined, for each material or for the reference, as the full-width half maximum of this distribution, representing the minimum pulse duration achievable from a pulse with a specified spectral distribution (See Figure 4.33).

As a result of the SRS resolution, the broadening appeared slightly larger compared to the SPIDER spectrometer. For example, the FTL of the SRS spectra for 2 mm BK7 was 9.76 fs, while the FL obtained from SPIDER was 10.26 fs. In another material configu-

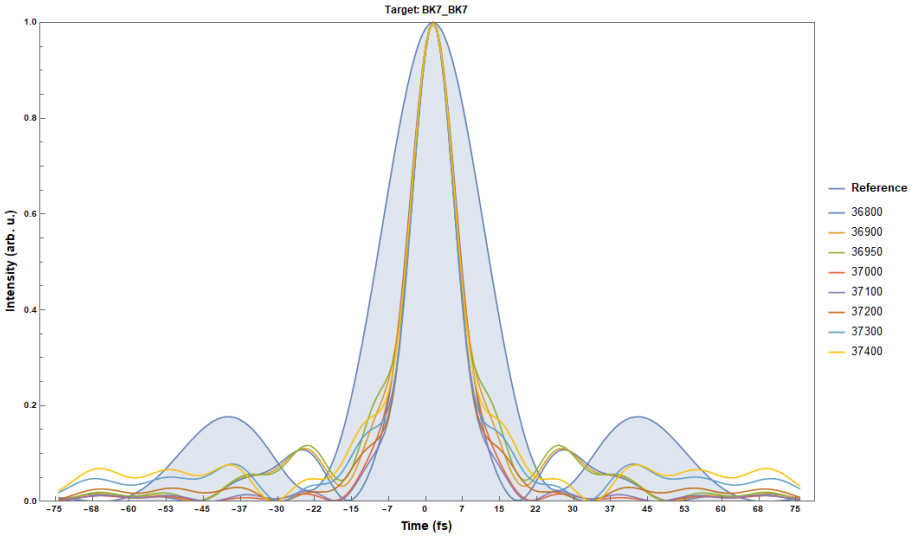


Figure 4.34: Fourier transform of the mean spectra obtained from spectral broadening in 2 mm BK7, at different GDD values.

ration, such as SF5-BK7, the FL was 5.67 fs, a value that could potentially be achieved within SPIDER measurements with further optimization of the TOD.

The influence of GDD was also observed with the SRS and is depicted in Figure 4.34. This figure illustrates the necessity of optimizing both the TOD and TSR to minimize the presence of temporal pre-pulses and post-pulses.

Another advantageous feature of the SR spectrometer is its large slit, which allows for the recording of a significant portion of the entire laser pulse. Consequently, the distribution of pulse duration across the beam was thoroughly investigated for each material configuration, as illustrated in Figure 4.35.

A summary of the mean values and their corresponding standard deviations is provided in Table 4.2. The non-uniformity in pulse duration primarily arises from variations in energy distribution across the beam, as discussed in Section 3.5.4, leading to differing B-integral values. This same trend in B-integral distribution was also identified and elaborated on in Section 4.1.3.3. Such measurements are of great significance, particularly for laser pulses that are spatially sampled from a larger input laser pulse and utilized as a *probe pulse*.

### 4.4.4 Spatial measurements

The spatial measurements pertains to the distribution profile of energy across the focal spot, which ideally should have the majority of its energy concentrated near the central peak. To assess this, three metrics were selected to quantify the degradation of the focal spot in the post-compressed laser beams:

The first metric is **the peak intensity ratio**, which involves comparing the peak intensity of the reference spot with no material to that of the post-compressed spot. This criterion holds significance in experiments where achieving the highest peak field is a primary requirement. To perform this analysis, the raw images obtained from the CCD Basler camera are initially cropped to focus on the region of interest surrounding the beam's focal profile. Subsequently, background subtraction is applied, and the images are normalized. This identical procedure is applied to both the reference and the sample images.

The second metric is **the encircled intensity ratio at $1/e^2$**. It quantifies the ratio of encircled intensity between the reference spot with no material and the post-compressed

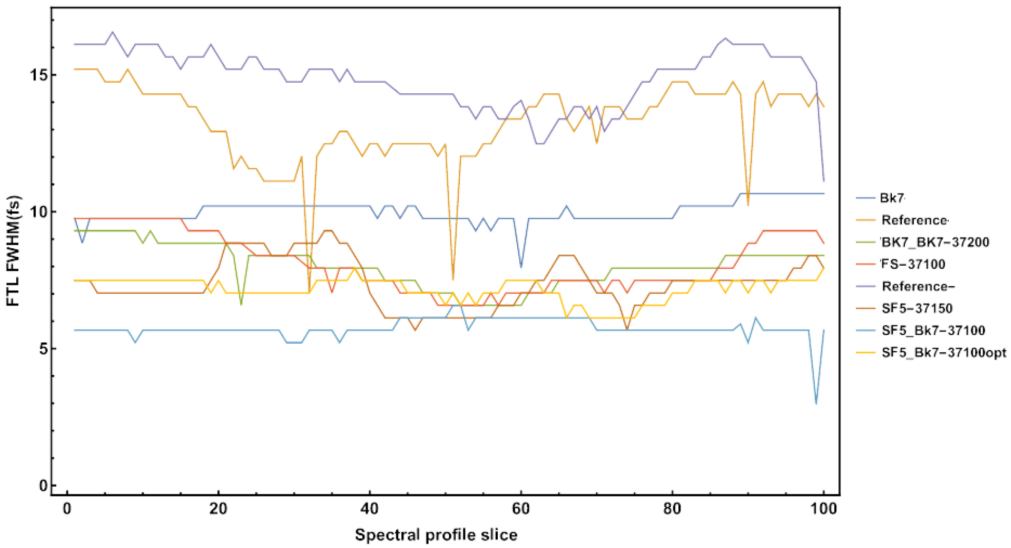


Figure 4.35: FL across the beam profile spectrum for different materials and for the reference pulses

spot. This measurement is made using a circular disk mask with a radius 'r,' where 'r' represents the distance in pixels at which the radially averaged intensity of the spot drops below $1/e^2$ of the maximum pixel value. This metric is particularly pertinent in experiments such as electron acceleration using post-compressed pulses. To achieve this, the region of interest, encompassing the majority of the profile's energy, is determined by selecting the profile's peak and plotting the radial distribution from the center to the edges. A binary circular mask with a radius 'r' is created and then multiplied with both the reference and post-compressed profiles.

The third metric is **the effective spot area**, which adheres to LIDT standards. The third metric computed is the effective area of the focal spot, calculated according to ISO 21254-1:2011 standards or Eq. 3.1.

The fourth metric is **the encircled intensity ratio at FWHM** and it followed the second metric algorithm while the threshold was increased to 50% (FWHM).

These four metrics collectively provide a comprehensive assessment of the suitability of post-compressed pulses for laser-driven experiments. The first three metrics are illustrated in Figure 4.36 while the fourth, which follows the same trend as the second metric, is presented in Table 4.2.

The introduction of thin materials as a medium for SPM can distort the beam quality through two distinct mechanisms.

For both low and high energy levels, the materials introduce geometrical aberrations, which are contingent upon the optical quality of the surfaces involved. These low-order aberrations of this nature can be readily mitigated through the use of a deformable mirror. Figure 4.37 illustrates the extent of compensation achieved for low-order Zernike coefficients.

Another factor, SPM itself, comes into play at higher energy levels. Figure 4.36 illustrates the change in focal spot quality as pulse energy increases, highlighting how nonlinear processes inside the thin materials become more pronounced.

Observations of the influence of the nonlinear effect on the focused beam were reported in a study by Kim et al. [15], focusing on collimated pulses with 2.5 J energy, corresponding to a fluence of 70 mJ/cm$^2$. The Strehl ratio decreased from 0.62 (with material, DM-corrected) to 0.37 due to SPM. However, by compensating for the SPM effect with a

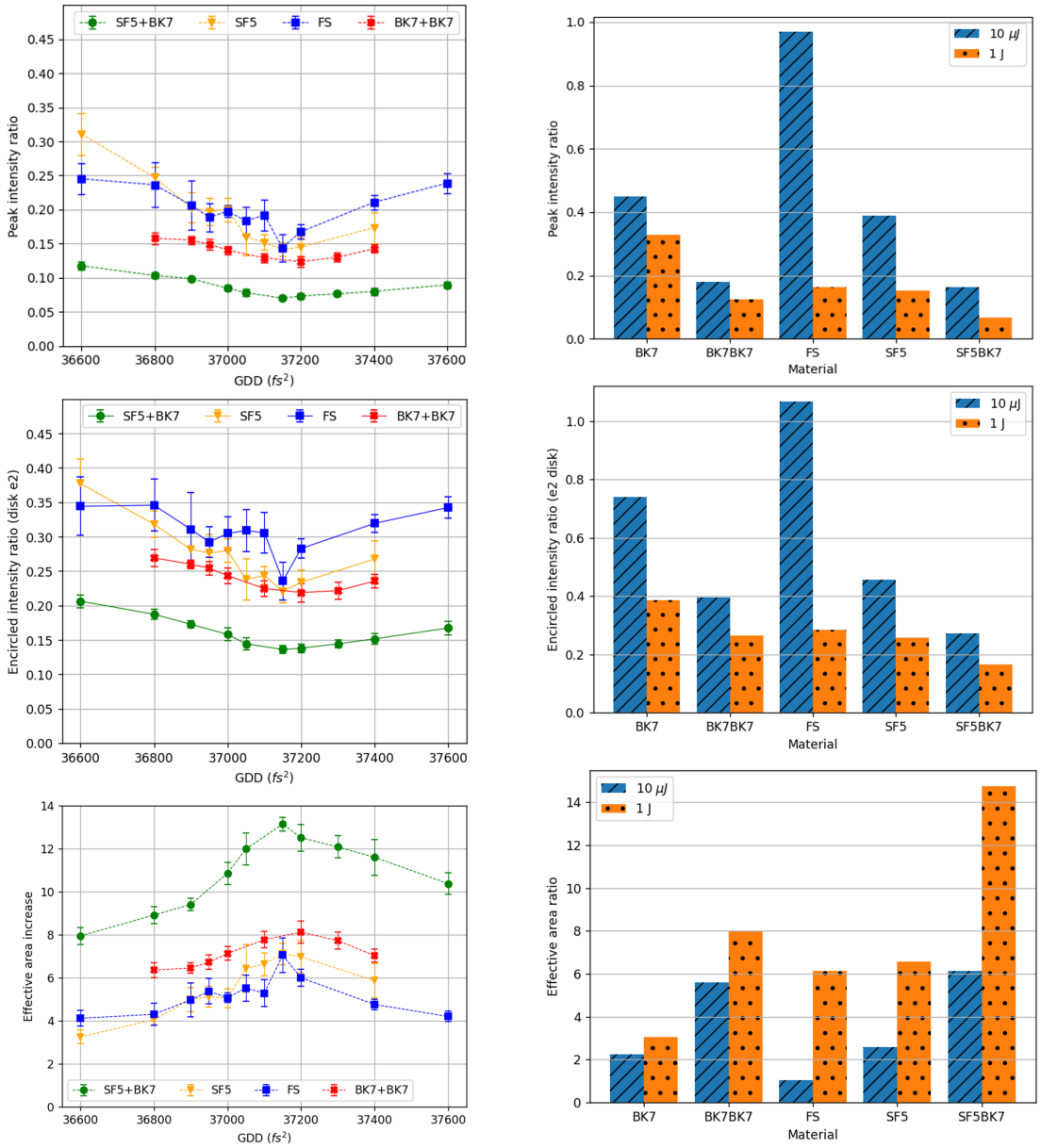


Figure 4.36: Methods (Peak intensity, Encircled intensity ratio and Effective area) to investigate the laser beam focus quality as a function of the GDD (Left) and as a function of the material type, at the best compression configuration, for Low Energy (LE- 10 $\mu$J) and high Energy (HE- 1 J ).

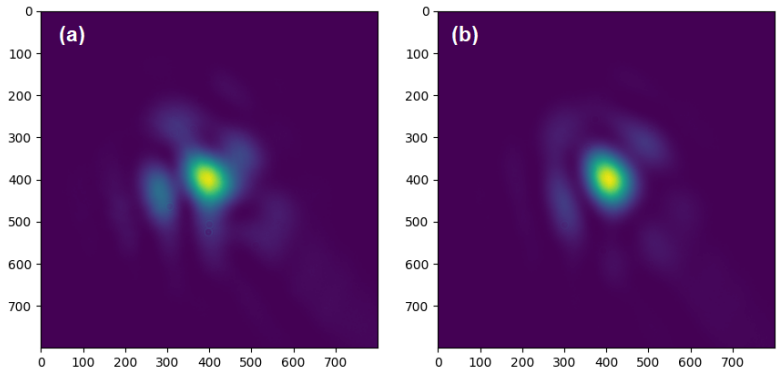


Figure 4.37: FF images without (Left) and with (Right) DM correction for BK7

deformable mirror, a Strehl ratio of 0.52 was recovered for the SPM pulses, representing a 40% relative improvement and a 20% reduction in the absolute Strehl value compared to the initial pulses.

Theoretical studies, such as those presented in Ref. [18, 19], support the observation that beam quality consistently decreases at higher energy levels. This trend is not exclusive to materials like fused silica, which may exhibit excellent spatial profiles at lower energy levels.

The above mentioned aspects demonstrate that Self-Phase Modulation, linear distortions and nonlinear processes within the material have a significant impact on beam quality. This observation is further corroborated by the relationship between spot quality and GDD depicted in Figure 4.36, left side. Near the GDD value optimal for compression, spot degradation is exacerbated across all samples, revealing a strong correlation between pulse duration and focal profile.

Despite the considerable distortions observed at high energy, the low-energy deformable mirror compensation measurements, as well as the findings from Ref. [15], highlight the potential for enhancement.

An additional improvement in spatial measurements could be achieved through double-sided polishing of the materials and with spatial filter applied to the input beam to minimize high-frequency components across the beam.

### 4.4.5 Spatio-Temporal Couplings (STC) measurements

High-power lasers possess broad spectral bandwidths and large beam diameters, rendering them highly susceptible to space-time couplings (STCs). When STCs are present in the laser field, the temporal (spectral) profile can vary across different transverse positions within the beam diameter. Conversely, the spatial profile can differ at various moments in time, corresponding to different spectral components. Consequently, performing separate temporal or spatial characterizations may yield either a localized or integrated effect, depending on the measurement approach employed. However, such separate characterizations cannot capture the full complexity of the laser field.

In our experiment, we utilized the INSIGHT technique, as described in [17], in conjunction with SPIDER. This allowed us to reconstruct the comprehensive spatio-temporal profile of the laser field at the focal point and explore the effects of spectral broadening for each spectral component. The collimated beam exiting the chamber (see Figure 4.26) was focused using an achromatic lens with a focal length of $f = 250$ mm, and the INSIGHT device was positioned in the focal region.

During this experimental campaign, we conducted measurements of the spatio-temporal contrast (STC) using the INSIGHT device at various resolutions. The STC was assessed after the interaction of ultra-short laser pulses with optical materials. At low energy, we conducted measurements both with and without the use of a deformable mirror (DM). At high energy, we measured the STC for the reference case, as well as with 1 mm BK7 and 5 mm FS samples.

Our data analysis encompassed the measurement and reconstruction of the far-field intensity, the characterization of the 3D (X, Y, $\lambda$) profile, the assessment of spatial chirp (SC), and the determination of Zernike polynomials.

The initial measurement of the high-power beam (1 J energy) without any material in the beam, which served as the reference, revealed a significant spatial chirp (SPC), indicating a variation of spatial position with respect to frequency.

It is important to note that the introduction of spectral broadening through the BK7 material did not lead to notable modifications in the spatial chirp within the focus. Specifically, for the reference beam on the $x$-axis, SPC was measured at $SPC_{ref,x} = 0.4$ $\mu$m/nm, while on the $y$-axis, it was $SPC_{ref,y} = 0.0$ $\mu$m/nm. In the case of the beam with spectral broadening in BK7, SPC values were $SPC_{BK7,x} = 0.4$ $\mu$m/nm on the $x$-axis and $SPC_{BK7,y} = 0.0$ $\mu$m/nm on the $y$-axis. The main results are presented in Table 4.2.

#### 4.4.5.1 Encircled energy in STC measurements

After inserting the BK7 plate for spectral broadening, the achromat (lens without the chromatic aberrations) was adjusted along the propagation direction to find the new best focus on the INSIGHT detector since spectral broadening significantly affected the beam's defocusing. In contrast to the far-field measurements, where the detector was not translated to locate the new best focus position, the INSIGHT measurements showed a smaller loss in spatial beam quality in the case of spectral broadening. Therefore, the role of defocus is essential in altering the focus quality of a spectrally broadened laser field. When compensating for defocus, the encircled energy ratio between the beam with and without material became comparable to the one at low energies. These calculations were performed using a similar algorithm to the one described in previous Section 4.4.4.

At low energy, the spatial chirp in the laser chain has been successfully corrected prior to the STC measurements with and without DM. Subsequently, far field and INSIGHT measurements were conducted at low energy to examine the properties of the materials used in the spectral broadening experiment. These measurements revealed that the distortions introduced by the materials could be effectively compensated by adjusting the deformable mirror in the laser chain.

The measurements with the INSIGHT at low energy also suggest that the spatial chirp distortion introduced by the nonlinear optical material is negligible (see Table 4.2).

### 4.4.6 Energy loss

I assessed the energy losses caused by the presence of the materials, denoted as $E_{ratio}$, by calculating the ratio $E_{\text{material}}/E_{\text{no material}}$. This was accomplished by measuring the energy at the exit of the interaction chamber. These measurements were carried out using a Gentec energy meter, known for its RMS accuracy of less than 2%. During these measurements, the laser pulses covered approximately 75% of the detection surface.

The samples were positioned at a 30-degree incidence angle within the collimated HPLS full beam. In this configuration, the beam encompassed roughly 80% of the material's aperture. The losses observed were primarily attributed to Fresnel reflections (accounting for 5%) and nonlinear absorption within the materials. The energy losses, as presented

in Table 4.2, were subsequently used to calculate the measured B-integral, TSR, and the intensity in the focus.

The Chirped Mirrors (CMs) utilized in the setup, operating at fluences below 40 mJ/cm$^2$, were assumed not to introduce nonlinear absorption, as supported by a reference [15, 16]. I would like to emphasize that the study of nonlinear absorption in Chirped Mirrors (CMs) is a relatively recent field, and there is limited information available regarding this phenomenon.

It is important to note that in the case of the SF5 material, laser irradiation led to the formation of color centers and material degradation after more than 1000 shots. This degradation was evident in the energy measurement of BK7+SF5, where only 85% of the transmitted energy reached the detector.

To further mitigate these energy losses, options such as utilizing Brewster angles or implementing antireflection coatings were considered. These measures have the potential to reduce energy losses to less than 1%.

### 4.4.7 SPM simulations

In the previous sub-sections, we demonstrated through temporal (Spider) and spectral-temporal (SRS) measurements that at an input energy of 1 J, we successfully achieved a pulse duration of 11 fs, accompanied by a sufficiently broad bandwidth to obtain a FTL duration of 5.67 fs (See Figure 4.35).

Considering that at 1 J input energy, the fluence on the material was 40 mJ/cm$^2$, doubling the energy will result in an input fluence significantly below the Laser-Induced Damage Threshold (LIDT) of materials such as BK7, fused silica (FS), and even Zeonor film. This observation is supported by the threshold limit of nonlinear absorption (80 mJ/cm$^2$) in the chirped mirrors, where it's contribution is minimum.

Taking these results into account, I conducted simulations to predict the spectral broadening achievable both for 1 J and 2 J input energy. The outcome is depicted in Figure 4.38. These results highlight the potential to reach a pulse duration close to the single-cycle regime at the Joule-level input energy, with a maximum of a five-fold compression in pulse duration.

The simulations were conducted using the theory presented in Chapter 2, utilizing pyNLO Python functions and employing material parameters from Table 4.2 as input data. Two initial energy conditions were considered. The first condition was associated with an energy of 1 J, demonstrating the algorithm's efficiency in estimating both spectral and temporal profiles (see Figure 4.38 top). The second condition involved 2 J input energy, representing a single compression stage, where in the case of 2 mm BK7, the output pulse duration could be reduced to 5.25 fs.

In the figures, the spectral phase distortions (in radians) after interaction with the material are represented in green, while the temporal profile after passing through the material ($\tau_{out}$) is depicted in red. The final pulse duration with the necessary GDD compensation from the chirped mirrors was estimated at FWHM by considering both spectral and temporal profiles as Gaussian.

Additional software development involves incorporating a measured input spectrum and spectral phase, along with the GDD curve provided by the CMs manufacturers, as input data for the simulations.

### 4.4.8 Discussion

In this section, we investigated five different materials. The key parameters for each configuration have been summarized in **Table** 4.2, where we conducted comprehensive

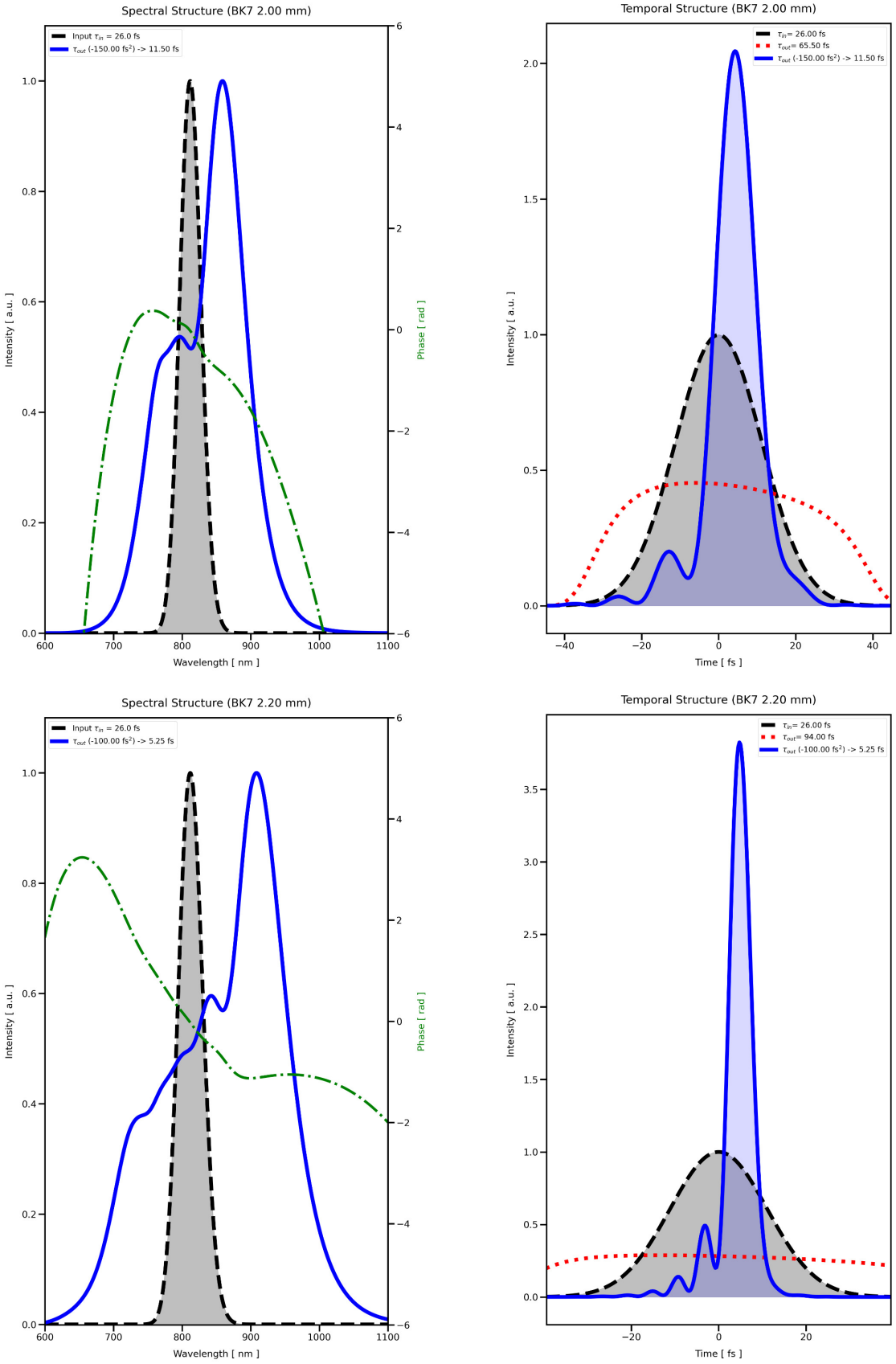


Figure 4.38: Temporal and spectral profiles for 2 mm of BK7 at 1 J (top) and 2 J (bottom) input energy. These profiles include the spectral phase (green), the output spectrum structure (blue), and the output temporal structure (filled, blue). The filled gray structures represent the input Gaussian spectrum and temporal profile.

analyses, including temporal, spectral, spatial, and spatio-temporal assessments.

A comprehensive statistical study of post compressed laser pulses has been performed. Compared with other research studies, this section concludes the results obtain from the mean value of 100 laser shots (temporal and spectral) and for the first time, spatio-temporal studies were included.

The results of the laser pulses metrology is presented below.

**Temporal** Using a single compression stage and 2 mm of BK7, placed ar 30°, I succeed to measure a stable pulse duration of 11 fs when both GDD and TOD was compensated. For the other materials configurations, just the GDD was optimized in the allocated beam time. Hence, the potential of using glasses, plastics or combination between them is still a subject of future research.

In the temporal studies, I introduced the Temporal Strehl Ratio and the factor $T_m/T_{FTL}$. Both parameters showed the potential to better estimate the spectral broadening $F_\omega$.

The B-integral can be better estimated while introducing new factors measured in this work (TSR and $E_{ratio}$ from Table 4.2) which are included in the Intensity value:

$$B_1 - int_m = \frac{2 * \pi * E * E_{ratio} * TSR_{in} * 4 * cos(\alpha)}{\lambda * T_{in} * \pi * d^2} \tag{4.7}$$

Therefore, the new B-integral for a second compression stage is given by:

$$B_2 - int_m = \frac{2 * \pi * E * E_{ratio} * TSR_m * 4 * cos(\alpha)}{\lambda * T_m * \pi * d^2} \tag{4.8}$$

Where $T_{in}$- input laser pulse duration, $\alpha$- input incidence angle and d- input beam diameter. $E_{ratio}$ denotes the losses in energy at the first surface while TSR denotes the losses in the temporal profile. This equation can be used as an input for further compression stages, to better estimate the B-integral and the broadening effect.

**Spectral** The spectral analysis was performed using both SRS and SPIDER spectrometers. The SPIDER measurements indicated sufficient bandwidth for achieving sub-10 fs laser pulse durations. On the other hand, the 2D spectrometer, with its wider spectral range, detected broadening capable of supporting sub-6 fs durations in the BK7+SF5 configuration. The 2D spectrograms data were processed and presented in Figure 4.32, demonstrating $T_{FTL}$ stability with a standard deviation (STD) of 4% for 2 mm BK7.

The broadening ratio, $F_\omega$, was estimated by performing a reverse Fourier transform on the measured pulse duration data obtained from SPIDER. It was observed that SPIDER encountered difficulties when dealing with irregular bandwidth profiles, particularly for spectral peaks with intensities exceeding 50%.

Conversely, for the data obtained from SRS, the spectral width ($\Delta_\omega$) was determined using the second-order momentum algorithm, which proved to be the most suitable choice for analyzing irregular spectra. The analysis of spectral broadening was conducted in both linear and logarithmic scales, with the logarithmic scale revealing the distinction between the signal and noise ranges.

Besides the B-integral$_m$, the factor $F_\omega$ denotes as the broadening ratio presented in Chapter 2 as Eq. 4.3, developed in Ref. [3] was investigated while considering the measured B-integral. The formula was further extended to estimate the $F_\omega$ at 2 J and the preliminary results are illustrated in Figure 4.39.

The experimental results aligned well with the theoretical predictions, and this figure highlights several key aspects: the $F_\omega$ values enable the extraction of the Nonlinear Refractive Index (NRI). Notably, for SF5, there are no reference values available. I estimated the

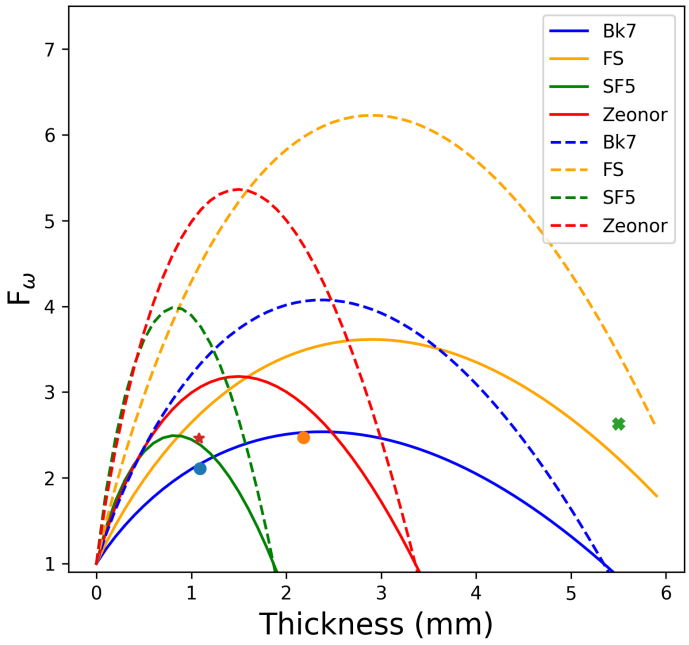


Figure 4.39: Estimated $F_\omega$ for 1 J (continuous curve) and for 2 J (dotted curve) where o,*, x denote the measured points for BK7, SF5 and FS.

NRI of SF5 at 7.2 $*10^{-20}$ $m^2/W$. Materials with a large Group Delay Dispersion and significant thickness (e.g., SF5 >1 mm) are not suitable for spectral broadening, as indicated by the inflection points for each material in Figure 4.39. Their potential lies in employing multiple thin plates.

Additionally, the figure includes results for Zeonor plastic material, emphasizing its potential for spectral broadening. Combining this with its previously measured wavefront qualities in Table 3.2, focal spot measurements (see Figure 4.40) demonstrate that this material yields comparable results to FS glass.

**Spatial** The preliminary spatial analysis of the far-field images was conducted in **four** configurations, encompassing both low and high energy regimes. These four configurations underscore the marked differences in focal spot quality, depending on the configuration used. It becomes evident that at high energy, all methods exhibit a degradation of the focus due to material quality, with the most prominent effect originating from nonlinear effects within the material. The nonlinear contribution was observed in the measured data under optimal compression conditions.

Moreover, it was demonstrated that at low energy, the deformable mirror is capable of improving the focal spot quality significantly (up to a factor of two in encircled energy). Other research papers have also underscored the potential of this mirror in compensating for nonlinearity-induced wavefront distortions [15].

The intensity in focus for post-compressed laser pulses can be estimated as:

$$I_{focus} = \frac{E^* E_{ratio} * TSR * 4 * SSR}{T_m * \pi * d^2 * calib_{DM}} \tag{4.9}$$

where SSR denotes the spatial Strehl Ratio measured, d is the diameter of the focal spot, while the TSR, the measured energy transmission coefficient of the glass plates ($E_{ratio}$), and

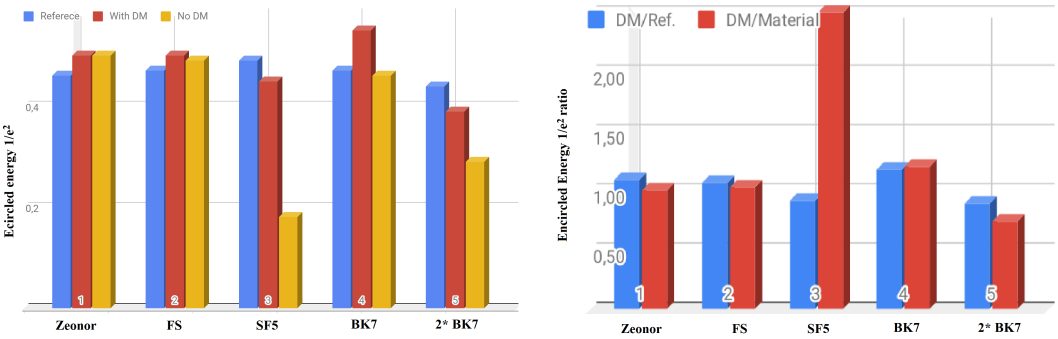


Figure 4.40: Left) Evolution of the focal spot at low energy for the reference, materials with and without DM correction and Right) The encircled energy ratio from where the factor $calib_{DM}$ was extracted

the measured pulse duration with the SPIDER ($T_m$) are listed in the comprehensive Table 4.2 as a function of material used. A new compensation factor $calib_{DM}$ is implemented to estimate the improvement in the focal spot of these parameters at high energy (HE) based on the DM measurements at low energy with and without deformable mirror (DM) as illustrated in Figure 4.40. The 15% error in both the reference and the value with DM ratio is associated with the optimization position, which was very close to the best-focusing parabola position.

The compensation factor $calib_{DM}$ for geometrical aberrations was calculated as:

$$calib_{DM} = Ampl._{DM}/Ampl._{Material} \tag{4.10}$$

For instance the $calib_{DM}$ factor showed a 75% compensation after the material (2 mm BK7) was inserted, therefore demonstrating the possibility to retrieve the initial focal spot.

The total energy losses (a. u.) factor on spatial profile (geometrical and nonlinear) was not fully covered during this experimental campaign. If I consider the experimental results of Ref. [15], where the compensation factor for both spatial losses was 84%, 16% Wavefront should be further compensated. In the case of 2 mm BK7, the cumulative losses resulting from a Gaussian energy distribution, Fresnel reflections, and wavefront distortions can be mitigated by the positive TSR (Temporal Strehl Ratio) and the $T_{ratio}$, which represents the ratio between the input and output pulse durations. When considering all these contributing factors the intensity in the focus can be significantly enhanced, which holds promise for future high-energy measurements.

$$Losses = -7\%Energy - 8\%Reflections - 16\%Wavefront + TSR\% + T_{ratio} \tag{4.11}$$

The main experimental results for each material are summarized in table 4.2. The yellow line on 2 mm BK7, denotes the trend of the presented data in this section.

Future perspectives involves improvements such as: contrast measurements; DM use at high energy; two sides polish glass for a better transmitted wavefront; nonlinear absorption measurements in CMs (topic discussed and planned to be studied with LaserOptik manufacturing team); STC analysis before experiment, dispersion and pulse durations measurements before and after each compression stage, energy increase to 1.5 and 2 J at 100 TW beam line followed by the implementation at 1 PW.

| Analysis | Material | Ref. | BK7 | BK7 | FS | SF5 | BK7 -SF5 |
|---|---|---|---|---|---|---|---|
| Material | Tk (mm) | - | 1 | 2 | 5 | 1 | 1+1 |
| | Tk_eff (mm) | - | 1,09 | 2,18 | 5,50 | 1,08 | 2,18 |
| | n (@810 nm) | - | 1,51 | 1,51 | 1,45 | 1,65 | 1,58 |
| | GDD ($fs^2$) | - | 44 | 44 | 36 | 126 | 170 |
| | $n_2$ ($m^2/W$) | - | 2,48 | 2,48 | 3,45 | 7,2* | 2,48+7,2 |
| Energy | E_ratio | 1,00 | 0,95 | 0,92 | 0,91 | 0,94 | 0,85 |
| Temporal SPIDER | $\lambda$ (nm) | 811 | 813 | 812 | 809 | 802 | 803 |
| | T_FTL (fs) | 23,00 | 10,66 | 10,26 | 9,65 | 9,17 | 10,13 |
| | T_m (fs) | 26,04 | 17,20 | 11,18 | 16,83 | 12,54 | 15,53 |
| | $\Delta\omega$_m (nm) | 37,10 | 56,50 | 86,70 | 57,20 | 75,45 | 61,07 |
| | $\Delta\omega$_FTL (nm) | 42,00 | 91,20 | 94,53 | 99,76 | 103,18 | 93,63 |
| | TSR | 1,00 | 0,87 | 1,45 | 0,47 | 0,87 | 0,87 |
| | T_m/T_FTL | 1,13 | 1,61 | 1,08 | 1,81 | 1,36 | 1,53 |
| Broadening | B-int_m | - | 3,13 | 6,06 | 10,31 | 5,98 | 9,11 |
| | hw | - | 1,50 | 1,50 | 1,50 | 1,50 | 1,50 |
| | gw | - | 0,91 | 0,91 | 0,91 | 0,91 | 0,91 |
| | D | - | 0,08 | 0,17 | 0,34 | 0,24 | 0,64 |
| | Fw_e | - | 2,61 | 3,14 | 2,17 | 2,46 | - |
| | Fw_s | - | 2,60 | 3,12 | 2,16 | 2,44 | - |
| Spectral SRS | $\Delta\omega$_m (nm) | 53 | 82 | 106 | 102 | 116 | 127 |
| | $\Delta\omega$_m/in | 1,00 | 1,55 | 2,00 | 1,92 | 2,19 | 2,40 |
| | T_FTL_m | 15,20 | 9,80 | 7,94 | 7,50 | 7,03 | 7,03 |
| | T_FTL_b | 14,70 | 9,99 | 8,01 | 8,12 | 7,40 | 5,74 |
| | $\Delta\omega$_m (nm) | 63,50 | 98,48 | 121,55 | 128,68 | 137,28 | 137,28 |
| | $\Delta\omega$_b (nm) | 68,93 | 96,50 | 120,64 | 118,85 | 130,42 | 168,14 |
| Spatial Far-Field | LE- Enc. 1 | 1,00 | 0,45 | 0,24 | 0,65 | 0,28 | 0,17 |
| | LE- Enc. 2 | 1,00 | 0,15 | 0,07 | 0,27 | 0,11 | 0,05 |
| | LE-PI | 1,00 | 0,64 | 0,34 | 0,95 | 0,43 | 0,22 |
| | LE-Eff. A | 1,00 | 0,55 | 0,25 | 1,05 | 0,44 | 0,20 |
| | HE-Enc 1 | 1,00 | 0,21 | 0,14 | 0,15 | 0,13 | 0,09 |
| | HE-Enc 2 | 1,00 | 0,11 | 0,05 | 0,05 | 0,05 | 0,03 |
| | HE-PI | 1,00 | 0,38 | 0,27 | 0,31 | 0,27 | 0,18 |
| | HE-Eff. A | 1,00 | 0,35 | 0,15 | 0,17 | 0,16 | 0,10 |
| Spatial- focus with DM | LE- Enc 1 | 1,00 | 1,17 | 0,89 | 1,06 | 0,92 | |
| | LE- Enc 2 | 1,00 | 1,21 | 0,81 | 1,08 | 0,80 | - |
| | LE-PI | 1,00 | 1,05 | 0,79 | 1,03 | 0,86 | - |
| | LE-Eff. A | 1,00 | 0,82 | 1,33 | 0,95 | 1,30 | - |
| STC (um/nm) | HE-SC_X | 0,38 | 0,42 | - | 0,52 | - | - |
| | HE-SC_Y | 0,01 | 0,03 | - | -0,09 | - | - |
| | LE-SC_X | -0,01 | 0,01 | 0,02 | 0,08 | 0,04 | - |
| | LE-SC_Y | -0,04 | -0,12 | -0,13 | -0,12 | 0,05 | - |
| STC_DM | LE-SC_X | -0,02 | 0,07 | -0,08 | 0,03 | 0 | - |
| | LE-SC_Y | -0,05 | -0,10 | -0,05 | -0,15 | -0,05 | - |

Table 4.2: Metrology of post compressed laser pulses Where: Tk-thickness, *E_ratio*-energy losses, B-int- B-integral, $\Delta\omega$ -Bandwidth (measured at FWHM for *Temporal* and at second order momentum for *Spectral*), $F_\omega$-Broadening ratio, Enc- encircled, Eff. A- Effective Area, TSR-Temporal Strehl Ratio, HE- high energy, LE- low energy, n-linear refractive index, PI- Peak Intensity, Tk -thickness, SC- spatial chirp, STC- spatio temporal couplings; The achronims denoted as *m*-measured, *b*- across the beam, *e*-estimated,*s*-simulated and '-' not measured. * $n_2$ for SF5 was estimated to fit the curve in Fig. 4.39.

| Laser | ELFIE | LASERIX | APOLLON | ELI-NP 100 TW |
|---|---|---|---|---|
| $\lambda$ (nm) | 1056 | 800 | 800 | 810 |
| Energy (J) | 5 | 0.16 | 7 | 1 |
| T_in (fs) | 350 | 45 | 22 | 26 |
| T_out_m (fs) | 200 | 23 | 15 | 11 |
| T_out_FTL (fs) | 124 | - | 9 | 10 |
| T_out_e (fs) | - | 9 | 9 | <6 |
| $F_{\omega}$_m | 2.60 | 2.04 | 1.8 | 3.14 |
| $F_{\omega}$_e | 2.66 | - | 1.9 | 3.12 |
| B-int | 1.78 | - | 1.8 | 3-12 |
| Analysis | B-int influence of the NF frequencies and FF-quality; FS and COP optical materials; Proof-of-principle for sub-picosecond post compression; | Development of a roller mechanism which allows up to 6 passes; FS and COP optical materials; $n_2$ estimation from spectral broadening; Broadening and fluence analysis; | PW scale post-compression; large optical materials; far-field studies; algorithm to estimate the broadening; wavefront measurement of the AF32eco materials | Complete metrology (spatial, temporal, spectral, spatio-temporal, energy loss) of post compressed laser pulses; GDD and TOD influence on the temporal and spatial profile; largest broadening. SPM for a range of B-int; possibility to reach 1-2 optical cycles at 2 J. |

Table 4.3: Comparison of the main results of the post-compression experiments. The achronims denoted as *m*-measured, *e*-estimated.

## 4.5 Discussion

This chapter presents the primary outcomes derived from four experimental campaigns in which the post-compression method was employed.

Throughout this chapter, I have detailed the implementation of the thin-film compression method across four distinct laser facilities. Four experimental setups were constructed and used to post-compress initial ultra-short laser pulses, reducing their duration from 350 fs to as low as 22 fs, culminating in output laser pulses with durations ranging from 200 fs down to a measured 11 fs. The most recent results, as discussed in Section 4.4, indicate the potential to achieve laser pulses close to the single-cycle regime with an input pulse duration of 26 fs and 2 J, thereby demonstrating a five-fold compression. The study encompasses input energy levels ranging from 150 mJ to 7 J, rendering this research pertinent to post-compression applications within the high-energy field.

The most relevant parameters and analysis is summarized in Table 4.3. The green cells denote the main improvements presented in the published papers and the last experimental results obtained at 100 TW laser of ELI-NP. The experimental campaigns presented in this work encompass aspects related to temporal, spectral, spatial, and spatio-temporal analysis. The most significant results are related to the temporal and spectral studies facilitated by the use of Dazzler and optical spectrometers. Additionally, the spatial profile (near-field, far-field, or focus) exhibited potential for improvement with the application of a deformable mirror. It was demonstrated through spatio-temporal measurements that the selected materials did not introduce spatial chirp.

Simulations indicated the feasibility of generating laser pulses approaching single-cycle duration at the J level using a 2 mm thick BK7 material. The realization of single-cycle pulses may require the incorporation of two compression stages. Furthermore, the intensity in focus, following spectral broadening, can be enhanced through the use of deformable mirrors (either the existing one or an additional deformable mirror after the initial post-compression stage), double-sided polished materials, and samples positioned at Brewster angle.

## 4.6 Publications of this chapter

*In publication process* : **P.-G. Bleotu**, A.M. Talposi, S. Popa, R. Ungureanu, D. Matei, S. Roder, V. Bagnoud, I. Dancus, S. Amarande, J. Fuchs, J. Wheeler, G. Mourou, D. Ursescu, "Four cycles, focused post-compressed 100 TW laser pulses", Optica.

[2]. **P.-G. Bleotu**, J. Wheeler, S.Yu. Mironov, V. Ginzburg, M. Masruri, A. Naziru, R. Secareanu, D.Ursescu, F. Perez, J. DeSousa, D. Badarau, E. Veuillot, P. Audebert, E. Khazanov, and G. Mourou, "Post-compression of high energy, sub-picosecond laser pulses", High Power Laser Science and Engineering, 11, 2023. https://doi.org/10.1017/hpl.2023.10

[9]. Wheeler, J.; **Bleotu, G.P.**; Naziru, A.; Fabbri, R.; Masruri, M.; Secareanu, R.; Farinella, D.M.; Cojocaru, G.; Ungureanu, R.; Baynard, E.; Demailly, J.; Pittman, M.; Dabu, R.; Dancus, I.; Ursescu, D.; Ros, D.; Tajima, T.; Mourou, G. Compressing High Energy Lasers through Optical Polymer Films. Photonics , 9, 715, 2022. https://doi.org/10.3390/photonics9100715

[13]. **Bleotu**, P., Wheeler, J., Papadopoulos, D., Chabanis, M., Prudent, J., Frotin, M.,..., Mourou, G., Spectral broadening for multi-Joule pulse compression in the APOLLON Long Focal Area facility. High Power Laser Science and Engineering, 10, E9, 2022, doi:10.1017/hpl.2021.61

[20]. I. Dancus, **P-G. Bleotu** et. al. "10 PW Peak Power Laser at the Extreme Light Infrastructure Nuclear Physics – status updates", EOSAM, 2022.

[21]. D. Ursescu, D. Matei, M. Talposi, V. Iancu, V. Aleksandrov, **P.G. Bleotu** et al., "First HPLS Experiments at ELI-NP: Spectral Broadening in Thin Films", Frontiers in Optics, 2020;

# Bibliography


[1] G. Mourou, S. Mironov, et al. "Single cycle thin film compressor opening the door to Zeptosecond-Exawatt physics". en. In: *The European Physical Journal Special Topics* 223.6 (May 2014), pp. 1181–1188. URL: http://link.springer.com/10.1140/epjst/e2014-02171-5 (visited on 02/06/2019).

[2] P.-G. Bleotu, J. Wheeler, et al. "Post-compression of high-energy, sub-picosecond laser pulses". en. In: *High Power Laser Science and Engineering* 11 (2023), e30. URL: https://www.cambridge.org/core/product/identifier/S2095471923000105/type/journal_article (visited on 05/02/2023).

[3] E. A. Khazanov, S. Yu Mironov, et al. "Nonlinear compression of high-power laser pulses: compression after compressor approach". en. In: *Physics-Uspekhi* 62.11 (Nov. 2019). Publisher: IOP Publishing, p. 1096. URL: https://iopscience.iop.org/article/10.3367/UFNe.2019.05.038564/meta (visited on 11/09/2020).

[4] Anatoly K. Potemkin, Efim A. Khazanov, et al. "Compact 300-J/300-GW Frequency-Doubled Neodymium Glass Laser—Part I: Limiting Power by Self-Focusing". In: *IEEE Journal of Quantum Electronics* 45.4 (Apr. 2009). Conference Name: IEEE Journal of Quantum Electronics, pp. 336–344.

[5] V. N. Ginzburg, A. A. Kochetkov, et al. "Suppression of small-scale self-focusing of high-power laser beams due to their self-filtration during propagation in free space". en. In: *Quantum Electronics* 48.4 (Apr. 2018). Publisher: IOP Publishing, p. 325. URL: https://iopscience.iop.org/article/10.1070/QEL16637/meta (visited on 03/07/2022).

[6] Sergey Mironov, Vladimir Lozhkarev, et al. "Suppression of small-scale self-focusing of high-intensity femtosecond radiation". en. In: *Applied Physics B* 113.1 (Oct. 2013), pp. 147–151. URL: https://doi.org/10.1007/s00340-013-5450-1 (visited on 11/01/2022).

[7] Ihsan Fsaifes, Louis Daniault, et al. "Coherent beam combining of 61 femtosecond fiber amplifiers". EN. In: *Optics Express* 28.14 (July 2020). Publisher: Optica Publishing Group, pp. 20152–20161. URL: https://opg.optica.org/oe/abstract.cfm?uri=oe-28-14-20152 (visited on 07/02/2023).

[8] Gerard Mourou, William Brocklesby, et al. "The future is fibre accelerators". In: *Nature Photonics* 7 (Apr. 2013), pp. 258–261.

[9] Jonathan Wheeler, Gabriel Petrişor Bleotu, et al. "Compressing High Energy Lasers through Optical Polymer Films". en. In: *Photonics* 9.10 (Oct. 2022). Number: 10 Publisher: Multidisciplinary Digital Publishing Institute, p. 715. URL: https://www.mdpi.com/2304-6732/9/10/715 (visited on 10/04/2022).

[10] Alexander M. Rubenchik, Sergey K. Turitsyn, et al. “Modulation instability in high power laser amplifiers”. en. In: *Optics Express* 18.2 (Jan. 2010), p. 1380. URL: https://www.osapublishing.org/oe/abstract.cfm?uri=oe-18-2-1380 (visited on 01/09/2022).

[11] D. M. Farinella, J. Wheeler, et al. “Focusability of laser pulses at petawatt transport intensities in thin-film compression”. en. In: *Journal of the Optical Society of America B* 36.2 (Feb. 2019), A28. URL: https://www.osapublishing.org/abstract.cfm?URI=josab-36-2-A28 (visited on 01/29/2020).

[12] M. Masruri, J. Wheeler, et al. “Optical Thin Film Compression for Laser Induced Plasma Diagnostics”. en. In: *Conference on Lasers and Electro-Optics*. San Jose, California: OSA, 2019, SW4E.3. URL: https://opg.optica.org/abstract.cfm?URI=CLEO_SI-2019-SW4E.3 (visited on 06/20/2023).

[13] P.-G. Bleotu, J. Wheeler, et al. “Spectral broadening for multi-Joule pulse compression in the APOLLON Long Focal Area facility”. en. In: *High Power Laser Science and Engineering* 10 (2022). Publisher: Cambridge University Press. URL: https://www.cambridge.org/core/journals/high-power-laser-science-and-engineering/article/spectral-broadening-for-multijoule-pulse-compression-in-the-apollon-long-focal-area-facility/62E91CE89219A83DCAC94BEE27CD4F6F (visited on 03/07/2022).

[14] Vladislav Ginzburg, Ivan Yakovlev, et al. “11 fs, 15 PW laser with nonlinear pulse compression”. en. In: *Optics Express* 29.18 (Aug. 2021), p. 28297. URL: https://www.osapublishing.org/abstract.cfm?URI=oe-29-18-28297 (visited on 08/23/2021).

[15] Ji In Kim, Ji In Kim, et al. “Wavefront-corrected post-compression of a 100-TW Ti:sapphire laser”. EN. In: *Optics Express* 30.15 (July 2022). Publisher: Optica Publishing Group, pp. 26212–26219. URL: https://opg.optica.org/oe/abstract.cfm?uri=oe-30-15-26212 (visited on 10/18/2022).

[16] Ji in Kim, Jin Woo Yoon, et al. “Post-compression of a 100-TW Ti:sapphire laser (Conference Presentation)”. In: *High-power, High-energy Lasers and Ultrafast Optical Technologies*. Vol. PC12577. SPIE, June 2023, PC125770G. URL: https://www.spiedigitallibrary.org/conference-proceedings-of-spie/PC12577/PC125770G/Post-compression-of-a-100-TW-Ti-sapphire-laser-Conference/10.1117/12.2669875.full (visited on 06/13/2023).

[17] Antonin Borot and Fabien Quéré. “Spatio-spectral metrology at focus of ultrashort lasers: a phase-retrieval approach”. EN. In: *Optics Express* 26.20 (Oct. 2018). Publisher: Optica Publishing Group, pp. 26444–26461. URL: https://opg.optica.org/oe/abstract.cfm?uri=oe-26-20-26444 (visited on 05/24/2023).

[18] Alexander Soloviev, Alexander Kotov, et al. “Improving focusability of post-compressed PW laser pulses using a deformable mirror”. EN. In: *Optics Express* 30.22 (Oct. 2022). Publisher: Optica Publishing Group, pp. 40584–40591. URL: https://opg.optica.org/oe/abstract.cfm?uri=oe-30-22-40584 (visited on 01/10/2023).

[19] Mikhail Martyanov, Sergey Mironov, et al. “Improvement of the focusability of petawatt laser pulses after nonlinear post-compression”. EN. In: *JOSA B* 39.7 (July 2022). Publisher: Optica Publishing Group, pp. 1936–1944. URL: https://opg.optica.org/josab/abstract.cfm?uri=josab-39-7-1936 (visited on 06/28/2022).

[20] Ioan Dancus, Gabriel Cojocaru, et al. “10 PW Peak Power Laser at the Extreme Light Infrastructure Nuclear Physics – status updates”. In: *EPJ Web of Conferences* 266 (Oct. 2022).

[21] Daniel Ursescu, Dan Matei, et al. “First HPLS Experiments at ELI-NP: Spectral Broadening in Thin Films”. en. In: *Frontiers in Optics* (2020), p. 2.

CHAPTER 5

# Chapter 5 Conclusions and perspectives

In this work, the Thin Film Compression (TFC) method was developed, applied, and characterized in four experimental campaigns, demonstrating its efficiency for use in facilities utilizing high-energy and ultrashort laser pulses to enhance their peak power.

To support this endeavor, a comprehensive study was conducted in *Introduction*, focusing on existing laser facilities, their amplification methods, and pulse durations, as outlined in Table 1.1. Additionally, the current status of post-compression at both low and high energy levels was explored. This work presents a glimpse (see Table 1.2) into the possibilities of achieving Exawatt-level peak power. The promising avenues include the development of novel grating technologies, the exploration of the $\lambda^3$ regime, plasma-based amplification and compression, and the groundbreaking integration of post-compression with amplification in nonlinear crystals.

Post-compression is rooted in two fundamental principles: dispersion management and nonlinear optics, encompassing nonlinearities ($n_2$) and self-phase modulation. These parameters were explored in depth to gain insight into how laser pulses can be intentionally modulated to achieve controlled broadening. The temporal shape of the pulse is further defined through the dispersion management system, a key component for attaining the single-cycle regime.

The optical materials used for spectral broadening underwent a comprehensive characterization that encompassed properties essential for this work. The characterization was focused on the measurements performed at central wavelength $\lambda_{central} = 800$ nm, which is typical for most Ti:Sapphire lasers, including those employed in this study.

The linear characterization included measurements related to dispersion (Group Delay Dispersion - GDD, Third Order Dispersion - TOD, and spectral phase), transmission, surface roughness, vacuum compatibility, and wavefront distortions.

Nonlinear characterization studies were conducted using established techniques such as Z-scan, along with methods aligned with ISO standards. I introduced novel techniques, such as Radius Z-scan and Image I-scan, specifically designed for measuring and characterizing the nonlinear refractive index of various optical materials. These materials included both traditional ones and novel options like Zeonor, Zeonex OKP, Apel film, Topas, PolyCarbonate, and PMMA. These novel techniques represented an improvement over the traditional Z-scan technique, offering benefits such as reduced standard deviation, enhanced stability, and improved reproducibility.

Moreover, the developed experimental setup presented in Figure 3.7 enabled the concurrent measurement of nonlinearities and of Laser-Induced Damage Threshold (LIDT), providing a versatile and efficient tool for optical material characterization.

I made significant contributions to the development of three complementary setups for

estimating LIDT, namely: spatial frequencies analysis, large beam analysis, and Langmuir Probe-Target Current (LPTC) analysis.

The original concept that I developed, behind spatial frequencies analysis, provides insights into any defects or modifications in the beam profile during laser irradiation. It can be employed to interpret the influence of spatial beam features on self-phase modulations and it was developed following LIDT ISO standards.

The second method involves the fitting of high-power laser beam profiles with different energy distributions across their surfaces. This unique feature was constructively leveraged to irradiate samples with N shots at a single spot, significantly increasing the statistical dataset. Each pixel in the beam profile represented an irradiated site, resulting in exposure of over $10^5$ sites to N-on-1 LIDT tests.

The third method represents an even more efficient technique in terms of sensitivity and the number of shots used. By implementing this method, it was demonstrated the ability to estimate the threshold for an infinite number of pulses using the R-on-1 test with a single laser shot, showcasing its superior sensitivity and potential.

The measured nonlinearities and damage thresholds were used to develop a software to simulate the spectral broadening in different materials. Hence, the broadening results were analyzed both in temporal and spectral domain followed by the simulation of the chirped mirrors effects on the output post-compressed laser pulse.

The expertise gained from both measurements and simulations was harnessed in the construction and utilization of four experimental setups. These setups were designed to achieve the post-compression of input ultrashort laser pulses, reducing their duration from 350 fs down to 22 fs, ultimately yielding output laser pulses as short as 11 fs, as demonstrated in the latest results of Section 4.4.

These results highlight the potential to attain the single-cycle regime, particularly for input pulse durations of 26 fs and 2 J, signifying a remarkable 5-fold compression. Importantly, this study covers a broad range of input energy levels, spanning from 150 mJ up to 7 J, underscoring the relevance of this research in the high-energy field.

In this work, I present the most comprehensive metrological approach for optical materials and high-energy post-compressed laser pulses. The cumulative impact of high optical quality materials, shortening pulse durations, deformable mirror correction for energy spread in the focus, and the two key factors - Temporal Strehl Ratio (TSR) and Spatial Strehl Ratio (SSR) - collectively contribute to the modification in focal spot intensity. It was shown that the shortest pulse duration with a TSR close to unity required both compensation of GDD and TOD. These results pave the way for the integration of this technique in future laser-matter interaction experiments, particularly those reliant on higher peak intensity.

In conclusion, my scientific endeavors over these years have encompassed various domains, including laser engineering, the development of experimental setups, laser pulse characterization, laser-matter interactions, materials characterization, and the detection of secondary sources.

The work presented here holds substantial potential for application in various laser facilities, with the demonstrated capacity to enhance peak power, as evidenced by four successful experimental campaigns. Additionally, the future prospects outlined will further reinforce the practicality and applicability of post-compressed laser pulses.

## 5.1 Perspectives

### 5.1.1 Next steps for post compression experiments

The forthcoming post-compression experiment will involve the development of the setup depicted in Figure 4.26, with applications for 100 TW and 1 PW class lasers as follows.

A combination of FS, BK7, and Zeonor materials with a total dispersion of 70 $fs^2$ or 140 $fs^2$ will be employed. The samples will have diameters of 15/40 cm and will undergo double-sided polishing, thus enhancing the transmitted wavefront (in collaboration with Manx Precision Optics). These samples will be positioned at the Brewster angle in dedicated mounts with minimal introduced stress. The new design for chirped mirrors will feature a GDD of -70 $fs^2$, a 45°angle of incidence, single-bounce use (minimizing the need for a CM pair), and a higher nonlinear absorption threshold based on the novel designs provided by UltrafastInovation. Preliminary GDD measurements will be conducted for millimeter-scale optical materials and 1" CMs (witness samples provided by the manufacturer) before the experiment.

Temporal distortions will be minimized through the use of the Dazzler and nonlinear absorption-reducing multilayer coatings, as documented in [1, 2], applied to the penultimate mirror before the post-compression setup. This type of coating will reduce peak intensities across the beam, functioning as a saturable absorber. This process will create a uniform beam prior to the first chirped mirror, preventing both nonlinear absorption and damage to the chirped mirror.

Spatial distortions will be mitigated by employing a deformable mirror ahead of the post-compression setup and using a spatial filter to optimize the cleanliness of the focused beam.

The existing temporal, spectral, spatial, and spatio-temporal analyses will be supplemented with contrast measurements, which have not yet been reported for post-compressed laser pulses.

The latest experiment showcases the ability to achieve laser pulses with durations ranging from 11 fs down to 3 fs when applying 2 J of input energy. Achieving this pulse duration will be demonstrated through the implementation of one or two compression stages. A comparative study will be performed for both one and two compression stages.

Following steps include the up-scaling to 1 PW showing a potential post compressed laser pulses of 2.5-5 temporal folding.

### 5.1.2 Secondary sources acceleration experiment

The cutting-edge results obtained during the ELI-NP campaign at 100 TW, 10 Hz repetition rate were used as input to investigate the potential of such pulses for efficient electron acceleration by means of large-scale particle-in-cell simulations. The Smilei particle-in-cell code [3] was used, exploiting its quasi-3D geometry with azimuthal mode decomposition of the fields. Two initial (laser parameters) conditions were considered:

- **A**: 11 fs, 1 J, 10 Hz, 90 TW and **B**: 6 fs, 1.5 J, 10 Hz, 250 TW

For both configurations, a scan over the various possible focusing, linking the spot size and the intensity in the focus was conducted. Assuming Gaussian profiles in both time and transverse coordinates, the laser intensity is related to its energy, duration, and focusing as $I = 0.598\frac{E}{\tau w_0^2}$. The plasma electron density was chosen to match the laser spot radius, using the condition described in Ref. [4]:

$$w_0 = \frac{\lambda_p \sqrt{\gamma}}{2} \tag{5.1}$$

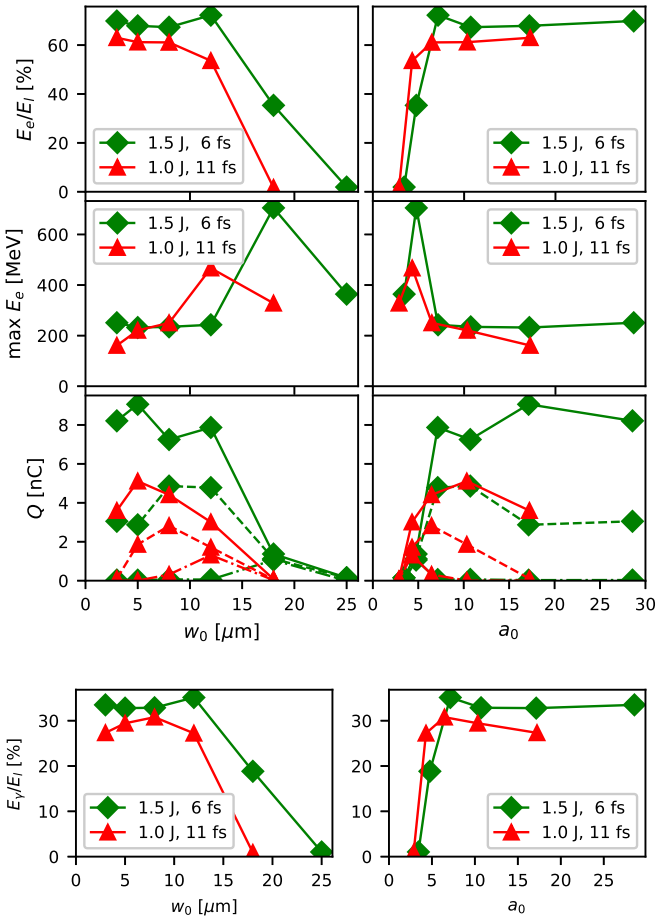


Figure 5.1: Properties of the laser-plasma accelerated electrons for the matching-condition-satisfying cases. Where solid - > 15 MeV, dashed - > 100 MeV, dashed-and-dot - > 200 MeV. Bottom: Conversion efficiency from laser pulse energy to Bremstrahlung radiation reaches up to 35%.

where $w_0$ is the laser waist, $\lambda_p = \frac{2\pi c}{\omega_p}$ is the plasma wavelength, $\omega_p = \sqrt{\frac{e^2 n_e}{m_e \epsilon_0}}$ is the plasma frequency, $\gamma = \sqrt{1 + \frac{a_0^2}{2}}$, $a_0 = 0.855\sqrt{I_{18}}\lambda_L$, $I$ is the intensity expressed in units of $10^{18}$ W/cm$^2$, $\lambda_L$ is the laser wavelength in microns. The numerical simulations predict the generation of electron bunches with energies in the hundreds of MeV range and charges of up to 4.9 nC above 100 MeV. The total conversion efficiency from laser pulse energy to electrons reaches up to 72%. Furthermore, the use of these electron bunches in generating secondary and tertiary sources of hard X-rays and neutrons through interactions with a high-$Z$ converter was explored in Figure 5.1.

In the proposed setup, the accelerated electrons emit hard X-rays via Bremsstrahlung radiation, and these X-rays, in turn, induce photonuclear reactions within the nuclei, resulting in the emission of neutrons. The optimized simulations suggest that up to 35% of the laser energy can be converted into hard X-rays, with an additional 1% being transformed into neutrons. This remarkable efficiency is achieved via two factors; first, the increased laser-to-electron conversion is facilitated by the short duration of the laser pulse and second, the high energy of the accelerated electrons translates into the higher conversion into X-rays.

## 5.2 List of personal contribution

This Ph.D. thesis was finalized with **6 papers** quoted by ISI, including total ranking factors: $\mathbf{AIS}_{total}$ **= 13.5;** $\mathbf{IF}_{total}$**= 38.6**, **22 presentations** at international conferences (9 as presenter) and **2 patents**. IF-denotes Impact Factor and AIS denotes Article Influence Score.

### 5.2.1 Publications

**P.-G. Bleotu**, A.M. Talposi, S. Popa, R. Ungureanu, D. Matei, S. Roder, V. Bagnoud, I. Dancus, S. Amarande, J. Fuchs, J. Wheeler, G. Mourou, D. Ursescu, "Four cycles, focused post-compressed 100 TW laser pulses", *Optica,in process.*

**P.-G. Bleotu**, S. Irimiciuc, A. Dumitru, D.G. Matei, R. Udrea, M.-D. Mihai, D. Craciun, O. Uteza, V. Craciun, D. Ursescu, "Exploring fs-laser irradiation damage sub-threshold behavior of dielectric mirrors via electrical measurements", *High Power Laser Science and Engineering*, *Submitted*

**P.-G. Bleotu**, J. Wheeler, S.Yu. Mironov, V. Ginzburg, M. Masruri, A. Naziru, R. Secareanu, D.Ursescu, F. Perez, J. DeSousa, D. Badarau, E. Veuillot, P. Audebert, E. Khazanov, and G. Mourou, "Post-compression of high energy, sub-picosecond laser pulses", *High Power Laser Science and Engineering*, 11, 2023. https://doi.org/10.1017/hpl.2023.10 **[AIS=1.01; IF= 4.8]**

**P.-G. Bleotu**, Mihai, L., Sporea, D., Sporea, A., Straticiuc, M., Burducea, I., "Impact of 3MeV Energy Proton Particles on Mid-IR QCLs", *Nanomaterials* 13, 677, 2023. https://doi.org/10.3390/nano13040677 **[AIS=0.71; IF= 5.3]**

Chien, A., Gao, L., Zhang, S., Ji, H., Blackman, E.G., Daughton, W., Stanier, A., Le, A., Guo, F., Follett, R., Chen, H., Fiksel, **G., Bleotu**, ... , Takizawa, R., "Non-thermal electron acceleration from magnetically driven reconnection in a laboratory plasma", *Nature Physics*, 19, 254–262, 2023. https://doi.org/10.1038/s41567-022-01839-x **[AIS=10.17; IF= 19.5]**

Wheeler, J.; **Bleotu, G.P.**; Naziru, A.; Fabbri, R.; Masruri, M.; Secareanu, R.; Farinella, D.M.; Cojocaru, G.; Ungureanu, R.; Baynard, E.; Demailly, J.; Pittman, M.; Dabu, R.; Dancus, I.; Ursescu, D.; Ros, D.; Tajima, T.; Mourou, G. Compressing High Energy Lasers through Optical Polymer Films. *Photonics* , 9, 715, 2022. https://doi.org/10.3390/photonics9100715 **[AIS=0.43; IF= 2.4]**

**P.-G. Bleotu**, Wheeler, J., Papadopoulos, D., Chabanis, M., Prudent, J., Frotin, M., Mourou, G., Spectral broadening for multi-Joule pulse compression in the APOLLON Long Focal Area facility. *High Power Laser Science and Engineering*, 10, E9, 2022, doi:10.1017/hpl.2021.61 **[AIS=1.01; IF= 4.8]**

V.Aleksandrov, **P-G. Bleotu**, R. Dabu, A. M Talposi, D. Matei, V. Iancu, A. lazar, I. Dancus, R. Fabri, R. Secareanu, D. Ursescu et. al., "Upgrading design of a multi-TW femtosecond laser", Romanian Reports in Physics, 72, 3, 2020.

### 5.2.2 Other relevant publications

**P.-G. Bleotu**, S. Irimiciuc, A. Dumitru, D.G. Matei, R. Udrea, D. Craciun, I. Dancus, V. Craciun, D. Ursescu, Target current and spatial modulations analysis for LIDT measurements using fs laser irradiation, in: Laser-Induced Damage in Optical Materials 2023, SPIE, Dublin/Livermore, United States, 2023: p. 81. https://doi.org/10.1117/12.2685157

**P.-G. Bleotu**, A. Naziru, A.H. Okukura, S. Popa, D. Matei, A. Dumitru, C. Alexe, V.P. Iancu, A.-M. Talposi, V.C. Musat, I. Dancus, L.P. Caratas, B. Boisdeffre, T. Samoskoi,

J. Takahisa, J. Wheeler, G. Mourou, D. Ursescu, LIDT station development with femtosecond pulses at ELI-NP, in: Laser-Induced Damage in Optical Materials 2022, SPIE, 2022. https://doi.org/10.1117/12.2641616.

D. Ursescu, D. Matei, M. Talposi, V. Iancu, V. Aleksandrov, **P.-G. Bleotu** et. al., "First HPLS Experiments at ELI-NP: Spectral Broadening in Thin Films", Frontier in Optics, 2020;

**P-G. Bleotu**, L. Mihai, D. Sporea, "Setup for quantum cascade lasers characterization using the labview programming environment" Romanian Reports in Physics 71, 901, 2019.

### 5.2.3 International conferences

P.Vasos, **P.-G. Bleotu** et al., "Magnetic resonance biomarkers for timely detection of high dose-rate radiation effects in cells", Flash Radiotherapy And Particle Therapy, 2023, Accepted.

G. Giubega, **P.-G. Bleotu**, et al., "Status of On-Going Experiments for Laser-Driven Bremsstrahlung Gamma Imaging at ELI-NP", PLASMA 2023, Poland, 2023.

L. Neagu, **P.-G. Bleotu** et al., "Diagnostics of ELI-NP - High Power Laser System including pulse front tilt correction using spatio-temporal metrology" LAPD20, Japan, 2023.

**P-G. Bleotu** et al., Metrology of high energy post-compressed laser pulses, Workshop STAMPLASS, Magurele, 2023. (*2nd price* -poster competition)

**P-G. Bleotu** et al., "LIDT station development with femtosecond pulses at ELI-NP", Rochester, New York, 2022.

I. Dancus, **P-G. Bleotu** et al., "10 PW Peak Power Laser at the Extreme Light Infrastructure Nuclear Physics – status updates", EOSAM, 2022.

I. Dancus, **P.-G. Bleotu** et al., "10 PW laser systems facility at ELI-NP", ICUIL conference, South Korea, 2022.

L. Gao, **P-G. Bleotu**, et al., "Direct measurement of non-thermal electron acceleration from magnetically driven reconnection in a laboratory plasma", APS conference, 2022

**P.-G. Bleotu** et al., "Post-compression experiments. Towards Exawatt lasers", ICLPR-ST conference, Romania, 2022.

A. Naziru, **P.-G. Bleotu**, et al., "Spectral Phase Characterization For Ultrashort Pulses Far From Fourier Limit Duration", ICLPR-ST conference, Romania, 2022

D. Ursescu, **P.-G. Bleotu** et al., "Prospective HPLS Developments: the Future of the Extreme Light Infrastructure", ICLPR-ST conference, Romania, 2022

**P.-G. Bleotu** et al., "Electron Beam Diagnosis Utilizing Fiber Bragg Gratings", PHOTOPTICS22, Virtual conference, 2022

**P.-G. Bleotu** et al.," Spectra broadening for post-compression experiments. Towards the next class of Exawatt lasers", ERICE Summer School, Sicily, 2022

Y. Nakamiya, **P-G. Bleotu** et al., "Experiment for mitigation of laser-induced contamination on the dielectric material with Oxygen injection at ELI-NP", IBWAP conference, 2022

A. Stancalie, **P-G. Bleotu** et al., " Charged particle beam diagnostics utilizing custom designed optical fiber sensors", ICLPR-ST conference, Romania, 2022

**P-G. Bleotu** et al., "Novel inspection technique for online determination of Laser Induced Damage Threshold", ELI Young Researchers DAYS conference, Magurele, 2022 (second place)

**P.-G. Bleotu** et al., "Experimental setup for fs-Laser Induced Damage Threshold measurements of optical films", 2022 Spring Meeting of the European Materials Research Society (E-MRS), VIRTUAL Conference, 2022

A. Naziru, **P.-G. Bleotu** et al., "Spectral Phase Characterization For Ultrashort Pulses Far From Fourier Limit Duration", High-Brightness Sources and Light-Driven Interactions Congress, 2022;

**P.-G. Bleotu**, et al., "Experimental setup for optical films Laser Induced Damage Threshold measurements", 13th International Conference on Physics of Advanced Materials (ICPAM-13) and the 4th Autumn School on Physics of Advanced Materials (PAMS-4) conference, Spain, 2021.

S. Zhang, **P.-G. Bleotu** et al.," Global field evolution in magnetic reconnection experiments using laser-powered capacitor coils", 62nd Annual Meeting of the APS Division of Plasma Physics conference, November 9-13, 2020 Memphis, Tennessee;

**P-G. Bleotu** et al.," Study of thin films Kerr non-linearity towards Exawatt lasers", 69th Lindau Nobel Laureate Metting conference, Germany, 2019;

V. Aleksandrov, **P.-G. Bleotu**, D. Ursescu, Femtosecond Pulse Shortening Using Cascaded Quadratic Nonlinearities for High Temporal Contrast, CLEO Europe conference, Munich, Germany, 23-27 June, 2019

### 5.2.4 Patents

The collaborative work within Langmuir Probe -Target Current (LPTC) for LIDT was finalized with submitted patents:

1. S. Irimiciuc, V. Craciun, D. Ursescu and **P.-G. Bleotu** "Technique for laser induced damage threshold through synchrony measurements of compensation current and Langmuir Probe (LPTC)", no. A00534/29.09.2023

2. L. Mihai, R. Mihalcea, **P.-G. Bleotu**, M. Serbanescu and A. Stancalie "Method and in-field validation apparatus for radiometric calibration of high-spectral-resolution dual-optics spectroradiometric systems used for vegetation monitoring", no. A00240/16.05.2023

# Bibliography


[1] Guan Gui, Amitava Adak, et al. "Measurement and control of optical nonlinearities in dispersive dielectric multilayers". EN. In: *Optics Express* 29.4 (Feb. 2021). Publisher: Optica Publishing Group, pp. 4947–4957. URL: https://opg.optica.org/oe/abstract.cfm?uri=oe-29-4-4947 (visited on 10/18/2022).

[2] Guan Gui, Amitava Adak, et al. "Supplementary document for Measurement and control of optical nonlinearities in dispersive dielectric multilayers - 5051811.pdf". en. In: (Feb. 2021). Publisher: Optica Publishing Group. URL: https://opticapublishing.figshare.com/articles/journal_contribution/Supplementary_document_for_Measurement_and_control_of_optical_nonlinearities_in_dispersive_dielectric_multilayers_-_5051811_pdf/13641095/2 (visited on 09/19/2023).

[3] J. Derouillat, A. Beck, et al. "SMILEI: a collaborative, open-source, multi-purpose particle-in-cell code for plasma simulation". In: *Computer Physics Communications* 222 (Jan. 2018). arXiv:1702.05128 [physics], pp. 351–373. URL: http://arxiv.org/abs/1702.05128 (visited on 10/23/2023).

[4] W. Lu, M. Tzoufras, et al. "Generating multi-GeV electron bunches using single stage laser wakefield acceleration in a 3D nonlinear regime". en. In: *Physical Review Special Topics - Accelerators and Beams* 10.6 (June 2007), p. 061301. URL: https://link.aps.org/doi/10.1103/PhysRevSTAB.10.061301 (visited on 10/23/2023).

# Acknowledgments

***Dear Reader,***
***My words are insignificant to express my thanks to all the people that raised me up in the scientific field and in life.***
***I dedicate this thesis to Nobel Laureate, Professor Gérard Mourou, the person who paved my road in this field and to my family who unconditionally support me to achieve my dreams.***
***I would like to express my sincere gratitude to the following people whose contributions, unwavering support, and expert guidance have played a pivotal role in the success of this doctoral thesis.***

**Coordinators of the thesis:**

Daniel Ursescu and Julien Fuchs for their valuable mentorship and direction throughout this research.

Daniel Ursescu, my supervisor for both my Master's and Ph.D. theses, has been an exceptional mentor. He not only explained complex concepts and taught me, but also played a pivotal role in shaping me into a more adept and accomplished scientist. I am deeply thankful for his involvement in the post-compression field, for entrusting me with the role of co-Principal Investigator in three experiments, and for guiding me towards innovative experimental directions.

I am also indebted to Julien Fuchs, whose support and collaboration made this thesis possible under the cotutelle framework between the University of Bucharest and Institut Polytechnique de Paris. He not only welcomed me as a Ph.D. student but also engaged me in laser-matter experiments, further enriching my academic journey.

**Professors and advisors:**

I would like to express my deep appreciation to two mentors who have been instrumental in this journey. The first is the person who believed in me, guided me, supported me unconditionally, and to whom I dedicate this work: Nobel Laureate, Professor Gérard Mourou.

I am also immensely thankful to Jonathan Wheeler, from whom I inherited the knowledge and expertise of the post-compression technique. He not only involved me in experiments but also dedicated countless hours to explain this intricate topic and assisted me in software development.

In addition, I extend my gratitude to Adrian Petris, Daniela Dragoman, Mihai Stafe, Niculae Puscas, Razvan Dabu, Virgil Baran, Emmanuel d'Humières for generously devoting their time and effort for reading and providing constructive feedback on this thesis. Their insights and support have been invaluable.

**Scientific discussions and guidance:**

I would like to thank to George Nemes, Jitsuno Takahisa, Vincent Bagnoud, Calin Ur, Victor Malka, Nicolae M. Marginean, Florin Negoita, Ovidiu Tesileanu, Cata Danil, Iani Mitu, Klaus Spohr, Marius Jurca, Veselin Aleksandrov, Moana Pitmann, Sebastien le

Pape, Eric Cormier for engaging in insightful scientific discussions that enriched or helped me to perform this work.

All of this work was made possible thanks to an exceptional team leader, Ioan Dancus, who facilitated travel for experiments, attendance at summer schools and conferences, support for this topic and additional days of beamtime.

I am grateful to my scientific parents Maria and Gheorghe Dinescu for their unconditional support, pieces of advice and materials for my ideas.

**Laboratory colleagues:**

This thesis represents the collaborative work with an exceptional team, and I am grateful to the following individuals:

Stefan Popa, Maria Talposi, and Razvan Ungureanu for their expertise and support in spatial measurement, spatio-temporal coupling, spectrometer results, and various technical aspects of the experiments. Simon Roder for his work with temporal data provided by SPIDER. Vicentiu Iancu for wavefront measurement. Andrei Naziru for his technical support, providing the thin film roller mechanism, and the long working distance imaging system.

Dan Matei for designing the interface of the experimental setup in the optics laboratory and for all the device integration and synchronization during the experiments. Laurentiu Rusen for ns LIDT measurements in ISOTEST laboratory. Ion Valentin for all the $TiO_2$ materials, measurement and fruitful discussions. Gabriel Cojocaru for our collaborative work on perovskite oxides LIDT. Madalin Rosu and Yoshihide Nakamiya for their technical support within LIDT and SPM beamtimes. Stefan Irimiciuc, Valentin Craciun and Radu Udrea for their support within LPTC LIDT method, experimental work and paper writing. Sergey Mironov, Efim Khazanov and Vladislav Ginzburg for their contribution in the ELFIE campaign, for all the scientific discussion and for their valuable contribution in the post-compression method.

Andrei Stancalie, Laura Mihai, and Razvan Mihalcea for their ongoing support and collaboration within novel detection systems.

My former students, Alice Dumitru, for her contribution and help in building the experimental setups for spectral broadening and LIDT, as well as data analysis. Saidbek Norbaev for his contribution within LIDT measurements and his valuable friendship. Andrew Okukura and Vlad Musat for improving the large beam LIDT and the online image analysis algorithms.

Cristina Gheorghiu, Stefania Ionescu, and Victor Leca for their exceptional contributions in optical materials cleaning, roughness measurements, and plasma cleaning. Vojtech Horny and Paolo Tomassini for their expertise and simulations related to the perspectives of my work on post-compressed laser pulses. Optics manufacturers: LaserOptik, UltrafastInnovation, and MGM teams for their support and fruitful discussions.

The experiments conducted in Chapter IV and all the others in which I participated were supported by multiple laser teams, including Thales, ELI-NP: Operation Team (LSD), Dosimetry laboratory, APOLLON, LASERIX, ELFIE, TITAN, CETAL, INFLPR, and GSI. Travel expenses were covered by the University of Bucharest, IZEST, IFIN-HH, ELI-NP, Institut Français, and other scholarships.

**Family and friends:**

To my family: Robert Marian, Constantin and Elena Bleotu for all their support, love and efforts. To all my relatives and for all the effort and challenges, to myself.

To my friends: Andreea S. Baltac, Ioana I. Fidel, Nataliia Tokareva, Marius Dragusin, Adrian Toader, Nicu Stan, Antonia Toma, Stefan Ataman, Alexandru Lazar, Mara Popovici, Corina Lungu, Andrei Gradinariu, Laurentiu Serban, Alexandra Carlig, Stefan and Cristina Gherghina, Andrei C. Tudor, Gabriel C. Apavaloae, Alexandru, Nicoleta and

Ilinca Diaconu, Emilia Matache, Stefan Ataman, Ana-Maria Lupu, Chloe Ho, Alok K. Pandey, Catherine Sarrazin, Chloé-Désirée Beugnies, Ghassan Zeraouli, Antoine Cavagna, Jaismeen Kaur, the Constantin, Cernat, Hoara, Mogos, Tanase, Marcu families, and to all the others.

In the end, the collective efforts of these people and many others have significantly contributed to the successful completion of this thesis, and I extend my deepest appreciation for their unwavering support and dedication.

The end.

**Petrișor Gabriel Bleotu**
Bucharest, 29 November 2023

ECOLE DOCTORALE

**Titre :** Étude de la réduction de la durée d'impulsion et de l'augmentation de l'intensité des systèmes laser de la classe Petawatt

**Mots clés :** Lasers femtoseconde, post-compression, lasers haute puissance

**Résumé :** L'augmentation de l'intensité et la réduction de la durée des impulsions laser à haute puissance sont hautement souhaitables pour un large éventail d'applications, car elles permettraient d'augmenter la luminosité des sources de rayonnement et de particules (électrons, ions, neutrons, etc.), qui à leur tour favoriser de nombreuses applications uniques. Une des directions pour y parvenir est d'étudier la compression efficace des impulsions laser petawatt, telles que celles devenant disponibles dans les installations laser du monde entier (par exemple Apollon en France), vers la limite fondamentale d'un cycle unique de leur longueur d'onde porteuse. Cette thèse prévoit d'abord d'étudier une méthode de post-compression qui repose sur le contrôle minutieux de la modulation de phase propre et de la compensation de vitesse de groupe des impulsions à large bande produites par l'interaction non linéaire des impulsions laser à haute intensité dans des supports transparents minces. Deuxièmement, il est également prévu d'étudier la possibilité de tester des impulsions de durée réduite pour piloter différents régimes de production de rayonnement et d'accélération des particules.

**Title :** Investigation of pulse duration reduction and intensity increase of Petawatt-class laser systems

**Keywords :** Femtosecond lasers, post compression, high power lasers

**Abstract :** Increasing the intensity and reducing the duration of high-power laser pulses is highly desirable for a wide range of applications, as it would allow to increase the brightness of radiation and particle sources (electrons, ions, neutrons, etc), which in turn would foster many unique applications. One direction to achieve this is to investigate efficient compression of petawatt laser pulses, such as those becoming available at laser facilities around the world (e.g. Apollon in France), toward the fundamental limit of a single-cycle of their carrier wavelength. This thesis plans first to study a method of post-compression that relies on the careful control of the self-phase modulation and group velocity compensation of the broadband pulses produced by the nonlinear interaction of high intense laser pulses within thin transparent media. Second, testing of achieved reduced duration pulses to drive different regimes of radiation production and particle acceleration is also planned to be investigated.

**Institut Polytechnique de Paris**
91120 Palaiseau, France